Navigating the lab-on-chip manufacturability roadblock: scalable, low-cost fluorescence detection for lab-on-chip instrumentation with rapid-prototyped microfluidics

by

Gordon Hiroshi Hall

A thesis
presented to the University Of Waterloo
in fulfilment of the
thesis requirement for the degree of
Doctor of Philosophy
in
Electrical and Computer Engineering

Waterloo, Ontario, Canada, 2018

Examining Committee Membership

The following served on the Examining Committee for this thesis. The decision of the Examining Committee is by majority vote.

External Examiner	NAME: Dr. Blanca Lapizco-Encinas
Supervisor	NAME: Dr. Christopher J. Backhouse
Internal Member	NAME: Dr. Karim S. Karim
Internal-External Member	NAME: Dr. Michael Pope
Other Member(s)	NAME: Dr. Peter M. Levine

Author's Declaration

I hereby declare that I am the sole author of this thesis. This is a true copy of the thesis, including any required final revisions, as accepted by my examiners.

I understand that my thesis may be made electronically available to the public.

Abstract

Miniaturisation and automation of laboratory testing protocols onto microfluidic chips (lab-on-chip technology) could revolutionise diagnostic testing, though the key challenge of integrating high levels of functionality at a low-cost has so far prevented widespread adoption both in industry and academia. Specifically, implementation of a cost-accessible fluorescence detection has eluded the field and ensured nearly all commercial and academic instruments are too costly for routine applications. The field also faces a manufacturability problem, as it is dominated by expensive and/or low-throughput fabrication approaches. This thesis aims to address core concerns on both the instrument and fluidic chip fronts through the development of a low-cost fluorescence detection module capable of executing standard molecular diagnostics. The detection was inherently designed to interface with a series of rapid-prototyped polymer fluidics that I designed and fabricated with direct-write methods (micromilling and laser ablation) and minimal processing, allowing for quick iterations of fluidic designs while retaining compatibility with high throughput manufacturing procedures such as injection moulding. The result is a sub-$1000 prototype capable of executing gold-standard diagnostic testing at sub-$10 per chip, though the specific protocol development is still on-going. Finally, these components have been designed in a scalable manner such that it is feasible for future manufacturing to be done in a standard CMOS compatible process, a process that also faces manufacturability issues and high development costs that could be avoided by utilising these designs as prototyping testbeds. Thus, this work provides a roadmap from interim low-cost instrumentation and rapid-prototyping methods, through standard high volume polymer processing techniques, to a true single-chip device where the entire instrument may one day be fabricated at high volume in a USB-key sized package.

Acknowledgements

There are many people who have contributed to my degree in both a professional and personal capacity that I would like to thank. First and foremost I would like to thank my supervisor, Professor Christopher J. Backhouse, for his ongoing support, guidance and witticisms. I'm sure that I will be using your analogies for years to come and I most certainly appreciate all you have done for me. I would like to extend a special thank you to my fellow graduate students Tianchi Ma, Victor Shadbolt and Collin Tittle. From the lab to the bar, you have all been wonderful friends and colleagues and I never would have gotten through this degree with success or sanity without you. To Professor D. Moira Glerum, thank you for always brightening my day with your humour and jovial nature. Both you, and your student Madeline H. Couse, were instrumental in providing the molecular biology support to this project and proving my instruments have real-world utility. I would like to thank Professor Duncan G. Elliott and his student David L. Sloan at the University of Alberta for their support on the CMOS-side of the project.

Finally, I would like to dedicate this thesis to my wonderful wife Sneha, without whom I would truly be lost.

Table of Contents

List of Figures

List of Tables

List of Acronyms

β2M	Beta-2-microglobulin gene
Δ-Σ	Delta-Sigma ADC
μTAS	miniaturised total analytical system
ADC	Analogue digital converter
AF532	Alexa Fluor 532
APD	Avalanche photodiode
BSA	Bovine Serum Albumin
BW	Bandwidth
CAD	Computer aided design
CAM	Computer aided machining
CCD	Charge coupled device
CE	Chip/capillary electrophoresis
CMOS	Complementary metal-oxide semiconductor
CNC	Computer numeric control
DAC	Digital analogue converter
DNA	Deoxyribonucleic acid
EDTA	Ethylenediaminetetraacetic acid
EOF	Electro-osmotic flow
EOP	Electro-osmotic pumping
EPDM	Ethylene propylene diene monomer
EWoD	Electrowetting on dielectric
FIR	Finite impulse response
FWHM	Full width at half maximum
GRIN	Gradient index lens
HV	High voltage
ICE	Input coupling efficiency
IP-CMOS	Intelligent packaged CMOS
LAMP	Loop-mediated isothermal amplification
LCE	Light collection efficiency
LED	Light emitting diode
LIF	Light induced fluorescence
LOC	Lab on chip
LOD	Limit of Detection
NGS	Next-generation sequencing
NRE	Non-recurring engineering
OD	Optical density
OLED	Organic LED
PCB	Printed circuit board
PCR	Polymerase chain reaction
PDMS	poly(dimethylsiloxane)
PGA	Programmable gain amplifier
PID	Proportional-integrator-derivative
PMMA	Polymethyl methacylate
PMT	Photomultiplier tube
PVC	Polyvinyl chloride
q-PCR	Quantitative polymerase chain reaction
QY	Quantum yield
RFLP	Restriction fragment length polymorphism
RMS	Root mean square
RPM	Rotations per minute
SAR	Successive approximation registerADC
SBR	Signal to baseline ratio
SI	Supplemental information
SIS	Staring into the sun
SNP	Single nucleotide polymorphism
SNR	Signal to noise ratio
SPAD	Single photon avalanche photodetector
SPI	Serial protocol interface
SRATE	Sampling rate
STR	Short tandem repeat
TB	Tris-borate
TBE	Tris-borate-EDTA acid
TE	Tris-EDTA acid
TIA	Transimpedance amplifier
USB	Universal serial bus

Chapter 1

Introduction

1.1 Motivation

Deoxyribonucleic acid (DNA) analysis is a crucial application of molecular biology with a broad spectrum of use-case scenarios including virus detection,[1] water quality analysis[2] and testing for disease susceptibility.[3] A typical protocol that could apply to any of these commercially relevant applications begins with DNA extraction and amplification using the polymerase chain reaction,(PCR), a process that selectively amplifies a target DNA sequence and concentrates it for further analysis. Next, the analyte is detected and verified through a method such as capillary electrophoresis (CE). The result, hereafter referred to as PCR-CE, combines the high sensitivity of PCR, which can amplify a target DNA sequence by six or more orders of magnitude, with the high selectivity afforded by CE[4] to form the gold-standard in molecular diagnostics[5]. However, conventional approaches to PCR-CE have a number of logistical drawbacks. Typical PCR and CE implementations require multiple expensive and bulky instruments in order to perform the analysis. Furthermore, due to the highly sensitive nature of PCR, best practices involve physical separations of pre- and post-PCR equipment in separate controlled environments.[6] Therefore, the facilities required to implement diagnostics are substantial, leading to the typical practice of transporting samples to a centralised laboratories for processing.[7] This status quo cannot readily adapt to certain critical scenarios. For example, in the case of a viral pandemic, such as SARS or a new bird flu strain, the rapid establishment of a quarantine to prevent the movement of infected individuals could be the difference between a small epidemic and depleting world's stock of emergency anti-virals.[8] Establishing a quarantine requires a technology that is field-deployable so that it can be performed at the checkpoint, reliable and sensitive such that it is an effective screening tool and cost-accessible for deployment to be financially feasible. So far, no technology has successfully filled this need. The solution pursued by this project was to develop inexpensive and integrated instrumentation to implement the standard PCR-CE technique, thus allowing for the miniaturisation of proven reliable and sensitive methods for field-deployable applications in a low-cost package.

As reviewed by Yager et al.,[9] there is a pressing need for low-cost diagnostic options for global public health issues. For example, in resource-poor environments this has led to the over-prescription of antibiotics as the test to determine the appropriate treatment is more costly than the treatment itself.[10] Low-cost alternatives are also important in the first

world, where reduced diagnostic costs can enable tests previously considered economically infeasible.[11] Diagnostic cost has two components: the per-test cost and the equipment cost. One excellent example of an affordable diagnostic is the standard pregnancy test. These tests are typically based on a lateral-flow mechanism where the analyte flows along a surface, first gathering deposited markers then flowing over capture regions. These tests have both low per-test cost, as they are typically based on inexpensive paper substrates,[12] and low equipment costs as they can be read-out by eye. For this reason, paper-based lateral-flow microfluidic devices have been the subject of much of the low-cost diagnostic research effort.[13] However, these devices suffer from very poor sensitivity, typically only capable of detecting analytes in the mM range.[14] This is suitable for many applications, for example blood glucose monitoring, but not for DNA applications. Some works implement additional readout capabilities, such as the electrochemical readout by Wang et al.,[15] to improve sensitivity. However, these methods remain three to four orders of magnitude less sensitive than a typical PCR application.[4] Lateral-flow devices also frequently require novel chemistry and precise reagent patterning[16] of unproven reliability. This is due to the fact that the simplistic nature of the device is not capable of implementing the standard multi-step procedures of conventional assays that have been verified as reproducible and sensitive. The reliance on novel chemistry also reduces the ability of the technology to be adapted to new targets as any new application would require extensive validation. This is a particular issue for mutating targets, such as viruses, where the target of the novel chemistry can become obsolete before reliability is established. This is not an issue for PCR-CE, which is typically the reference analytical technique for emerging threats[1]. Therefore, there is a need for a more advanced LOC technology capable of implementing the standard, reliable protocols.

The cost of LOC devices can be considered as a combination of the reagents, the microfluidic material used and the cost associated with manufacturing/assembly. One of the primary motivations for the development of μTAS was that miniaturisation of the experiment drastically reduces the volume of analytes and reagents required.[17] Thus, for a typical LOC device, the per-test cost will be dominated by the materials and processing of the fluidic chip. Initial work in the LOC field utilised glass as the primary material, due to its attractive surface properties and well-developed chemistry[18] and fabricated microchannels with photolithography. These methods, while effective, required expensive photomasks, time-consuming etching and cleanroom facilities,[19] leading to expensive and slow design iterations. More recently, soft lithography of, typically, poly(dimethylsiloxane) (PDMS)[20] has become very popular in academia as it has a low start-up cost and does not strictly require a cleanroom environment.[21] However, soft-lithography is a highly manual labour intensive process[22] with curing times generally in the minutes to hours per device[18] making it unsuitable for high volume manufacturing.[9,18,22] Commercial fabrication of LOC devices has since turned towards the use of injection moulding to form thermoplastic microfluidics,[18] an industry standard for high volume manufacturing, with several companies such as Microfluidic Chipshop[23] operating in this field. However, one issue with injection moulding is that iterations are slow and expensive, requiring new moulds for each design change.[24] This is the manufacturability roadblock,[22] a phrase used to convey the situation where a technology is either inexpensive in the initial development stages (i.e. soft-lithography) or in bulk manufacturing (i.e. injection moulding) but not both. Thus, bringing the technology to market is challenging, requiring either substantial capital to push through the development stages or limiting the application to situations where the per-unit cost is high. This motivated the focus of this project on rapid-prototyping methods for polymer fluidics, specifically in polymethyl methacrylate (PMMA). Rapid-prototyping allows for low-cost manufacturing of one-off devices, enabling quick and easy design changes, while ensuring material compatibility with injection moulding. Thus, designs can be iterated upon in this low-development cost environment with the option for scaled up manufacturing at a later date.

Having settled on a fabrication technique and material, attention must be turned towards the instrument used to execute the experiment on the LOC device. To unlock the true potential of LOC technology this instrument must be capable of the integrated functionality for standard applications[25] while also remaining low-cost.[9] This is a challenge that has not been well addressed to date. In industry, commercially available products for DNA analysis are prohibitively expensive in the $10,000 - $1,000,000 price range, unsuitable for many diagnostic applications. The primary challenge in developing low-cost instrumentation lies in the implementation of a detector. As elaborated upon below, for gold-standard DNA applications the detector must have a limit of detection (LOD) of 1 nM of analyte within a 1 nL test volume or better. There are a number of mechanisms that can be used for LOC detection including electrochemical, contactless conductivity and absorption/colourimetric mechanisms.[26] However, these methods have typical LODs in the μM to mM regimes[14,27,28] and are therefore unsuitable for implementing laboratory standard protocols. For this reason, molecular diagnostics have centred primarily on fluorescence[29] as it is capable of excellent LOD (down to single molecule detection[30]) and is readily integrated with standard molecular biology,[31] making it the detection mechanism of choice for the majority of the commercial and academic DNA analysis instruments[32–42]. The standard method of implementing fluorescence in the field is the confocal optics module pictured below in Figure 1.4a. This design is well optimised for high-performance with a typical LOD in the tens of pM,[41,43] however this performance requires several large and expensive components.[44] As such, these instruments are typically costly to the point that a recent review specifically excludes fluorescence detection from consideration for resource-poor usage scenarios.[45] Therefore, in order to implement cost-accessible LOC diagnostics there is a need for a new approach to detection. This was the primary motivation of this work.

The approach to fluorescence detection for LOC instruments described here takes advantage of two key concepts. Firstly the detection capabilities for a confocal module are typically much better than required for routine diagnostics. While impressive, clearly there is room for optimisation of a module designed specifically for the application that has lower, but sufficient, performance and lower cost. The second is that many LOC confocal optics modules are designed for flexible integration with a variety of microfluidic chip dimensions. For example, the commercial LOC instrument in the Backhouse laboratory by Micralyne (Microfluidic Toolkit, Micralyne) has a confocal optics module with a long working distance and three axes of movement such that it can conform to a variety of geometries. This not only adds cost, but also negatively impacts performance. There is an opportunity here for a fluorescence detection system that is specifically designed for a specific microfluidic technology. In summary, this project sought to design instrumentation optimised for both the application and the microfluidic technology, and exploit this optimisation to reduce the equipment costs.

One method of simultaneously addressing both the LOC fluidics and associated instrumentation cost is to combine both functions onto a single device. To this end, the long-term goal of this research project is to develop a device for PCR-CE where all of the instrumentation functionality is miniaturised to a single microelectronic chip, with the fluidics fabricated directly on top. This device could be made using a standard complementary metal oxide semiconductor (CMOS) process, a process that has been demonstrated by the microprocessor industry to be capable of manufacturing in very large volumes at a low per-unit cost. The core issue facing this monolithic single chip device is the very high NRE of CMOS development; even though the per-device cost is very low in bulk manufacturing, at low volumes design changes are very expensive. This is particularly problematic for research and development, leading to prohibitive costs and slow design iterations. Thus, much like the microfluidic chips, the instrumentation faces a manufacturability roadblock. Much work has been done to date on this project developing LOC instrumentation electronics[46–49] and

microfluidics on CMOS.[50] However, substantial development still remains to be done towards integration, especially with regards to fluorescence detection. This is a particular challenge because, as explored throughout this work, the detection performance is a function of the system geometry. Therefore, in contrast to the electronic and microfluidic aspects, which can largely be developed independently, the optics require an integrated device to be tested properly, and thus they face the brunt of the NRE costs. What is needed is a low-cost method of fluorescence detection development that can prototype the key issues of the design. To this end, one additional motivation for the detection instrumentation development was that it conform to the same constraints as a CMOS LOC design, making the instruments in this thesis functional testbeds for future integrated devices. This created a low-development cost environment for prototyping future designs, presenting a path through the instrumentation manufacturability roadblock.

1.2 PCR-CE: A Gold-Standard Molecular Diagnostic

The focus of this project was the implementation of the gold-standard PCR-CE protocol. In comparison to other DNA analysis methods, PCR-CE has three primary advantages. Firstly, it is a tried and true method and has been a mainstay of the field for decades. This means an instrument that implements this standard method has access to a library of well-established analysis protocols and its application can be rapidly re-targeted to a plethora of diverse fields. This is particularly important in fields such as virus detection where the target is continually mutating. Furthermore, the use of familiar, standard methods is effective in reducing the alienation of new users and promoting the adoption of the instrument in the diagnostics community. This has been cited as a common source of concern in the LOC field.[51] Finally, PCR-CE is a robust and sensitive technique with an inherent validating consistency check. Many works in the LOC field utilise PCR as a stand-alone analysis tool using what is called quantitative PCR (q-PCR). q-PCR experiments monitor the amount of DNA present during the amplification stages to establish the initial concentration of the target analyte. However, such experiments only indicate the presence of genetic amplification, not the identity of what was amplified. This makes the experiment highly susceptible to upstream sample processing and specificity issues,[52] leading to guidelines for laboratory best practices to explicitly require a consistency check.[5] Other genetic amplification methods have been applied in a similar fashion, for example loop-mediated isothermal amplification (LAMP), with similar specificity concerns. CE is an excellent technique to perform the consistency check as it accurately identifies the size of the amplified target, and, when combined with enzymatic analysis, can provide sequence-specific information.[3] Hence, this work has focused on PCR-CE.

PCR-CE poses a number of challenges over q-PCR. Firstly, PCR-CE requires more integrated functionality as the instrument must add high voltage (HV) control and switching to implement CE on top of the thermal instrumentation a PCR instrument contains. Figure 1.1 below details all of the key functions of a PCR-CE instrument. Fluid handling also becomes a more prominent issue. A simple q-PCR device can consist of only a single reaction chamber with reagent mixing as the only fluidic function required. In contrast, PCR-CE inherently requires multiple wells for CE with fluid transport in-between the PCR and CE aspects. Finally, as explored in more detail below, PCR-CE places more stringent requirements on the detection aspect of the instrument. This is due in part to moving the detection point from the fairly large (typically μL) PCR reaction chamber to a nL microchannel as well as a change in fluorescent labelling methods, resulting in the need for orders of magnitude more sensitivity. Thus, PCR-CE requires more functionality at a higher performance than q-PCR. For these reasons, there have been relatively few commercial or

academic implementations of PCR-CE. Furthermore, as reviewed below, none of these instruments are cost-accessible.

Developing a PCR-CE diagnostic system requires two components: the molecular biology protocol and the instrumentation to execute that protocol. This project has focused solely on the latter, with protocol development being outside the scope of this thesis. Instead, the focus has been on implementing instrumentation capable of executing the standard methods such that future work can build upon this platform for application demonstrations. Thus, the objective was to design instruments that meet the requirements representative of the molecular biology. This section will first review key concepts of and PCR and CE as standard analysis techniques. This allows for the establishment of metrics that the instrument must meet. Next, it will provide an overview of the literature in this field. From this analysis, it is clear that the primary opportunity for development lies in the implementation of fluorescence detection which is discussed in the subsequent section below.

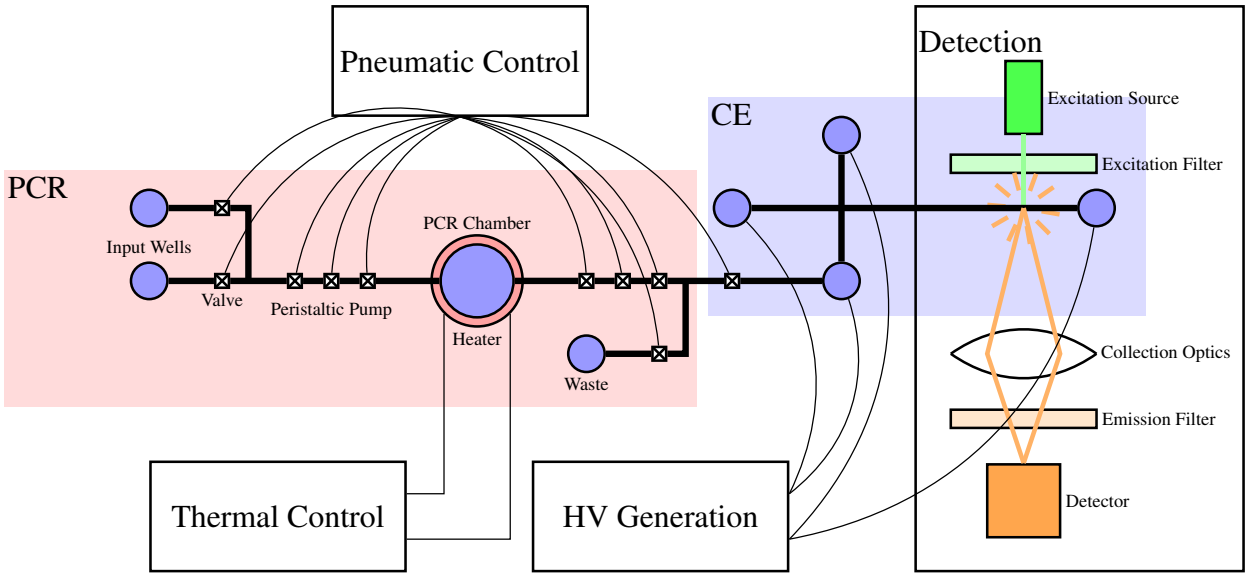

Figure 1.1: An overview of the functionality required to implement PCR-CE. The instrument must be capable of providing microfluidic valving and pumping for fluid actuation, thermal control for PCR, HV generation and switching for CE and fluorescence detection. Combining all of these functions with associated microfluidics enables a gold-standard molecular biology analysis of nucleic acids. Most of the instrumentation (HV, thermal control, fluidic valving and pumping) are discussed in Appendix A, the fabrication of microfluidics to perform these functions are discussed in Chapter 2 and the detector in Chapters 3 and 4.

1.2.1 Polymerase Chain Reaction (PCR)

PCR is a core molecular biology tool that is a part of nearly every DNA analysis protocol. One of the key problems in bioanalysis is acquiring a sample with a detectable concentration of the target analyte. For example, Voet and Voet[4] notes that in a saturated 10 L culture of *E. coli* only about 0.1 mg of DNA would be present, and purifying this small amount in the presence of confounding compounds is very challenging. PCR presents a method of specifically amplifying these trace analytes for further analysis. Broadly speaking, PCR begins with mixing a test volume which includes the sample to test, deoxynucleotides, short chains of DNA called primers that select the DNA sequence for

amplification and a polymerase, an enzyme that extends primers to copy the target DNA sequence. The volume is cycled between, typically, three set temperatures as shown in Figure 1.2. In the first step, a high temperature is set which causes the double stranded DNA sample to melt, or separate, into single strands. The reaction mixture is then cooled to a specific temperature, typically around 50 ^{o}C, at which the primers bind to the single-stranded DNA at a defined location. From here, the temperature is raised to optimise polymerase activity and the polymerase extends the primers to match the target DNA strand by incorporating the deoxynucleotides into the chain. The melt-anneal-extend cycle is then repeated. With each cycle, the PCR will extend a primer to match the target DNA sequence for each molecule of target present, theoretically doubling the analyte concentration. In practice, at very high cycle numbers other factors come into play, but nevertheless, the amount of amplification is over six orders of magnitude, amplifying as little as one copy of target to nM level concentrations.[4] In a PCR-CE instrument, the PCR output provides the concentration ranges expected for the CE subsection and thus defines the analyte concentration the detection module must be optimised for.

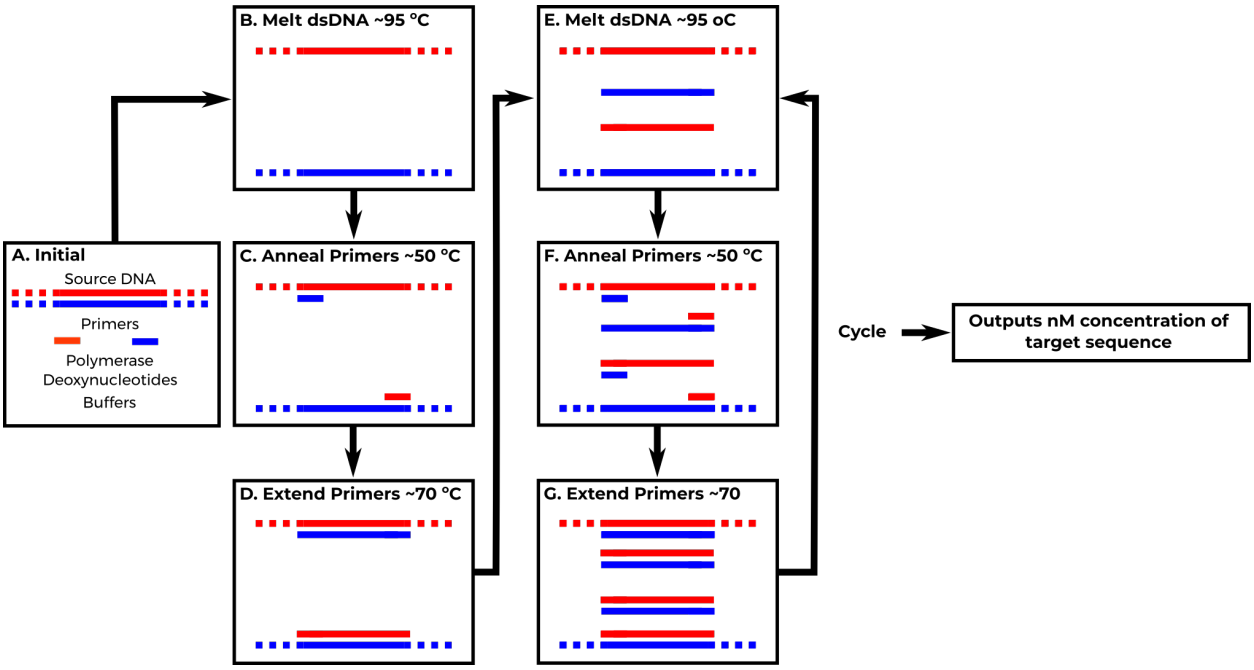

Figure 1.2: A diagram illustrating genetic amplification via polymerase chain reaction. A. An initial reaction will contain the source DNA, primers, polymerase, deoxynucleotides and buffers. B. In the first step the reaction mixture is brought to a high temperature (≈95 ^{o}C) which causes the double stranded DNA to separate. C. The temperature is reduced such that the primers selectively bind to the target region (typically ≈50 ^{o}C, depends heavily on primers/target). D. The temperature is raised to the optimum efficiency of the polymerase (≈70 ^{o}C) and the polymerase extends the primer chain to match the sample, creating exact copies. E-G. The sample is melted, annealed and extended again, doubling the concentration of target DNA. Steps E-G are repeated 35-40 times, amplifying the source DNA. While in theory each cycle will double the DNA present, other factors come into play. Ultimately, six or more orders of magnitude amplification is achieved, turning as few as one copy of sample to nM concentrations.

The primary requirement for a PCR reaction chamber is that the reaction volume temperature be highly uniform, typically within 1 ^{o}C.[53] Since the binding of primers to the target DNA sequence is a strictly thermodynamic process, this uniformity is crucial to ensure the appropriate sequence is being amplified. However, this requirement is predom-

inantly a function of the thermal design rather than the instrumentation, which was not the focus of this work. Instead, this thesis implements thermal instrumentation capable of driving a broad range of potential designs such that future work can utilise it for development. This is discussed in Appendix A.3, along with a preliminary PCR demonstration. This work was integrated into the an instrument in Section 5.5 for future PCR-CE demonstrations. However, this thesis focuses primarily on CE since the detection point is located in that section; for the purposes of this work it was important that the capability of future PCR integration was possible such that it could be integrated after the key issue of detection was implemented.

1.2.2 Capillary/Chip Electrophoresis (CE)

Electrophoresis, and its miniaturisation through the use of a capillary or microchannel in CE, is a standard molecular biology tool with a number of applications including DNA sequencing, protein analysis, nucleic acid mutation detection and more.[54] Broadly speaking, electrophoresis refers to the migration of charged species induced by an electric field. The velocity that the analyte moves is not only a function of the electric field applied, but also the charge and size of the species.[54] Thus, for molecules that have the same charge (such as DNA), a set field and time can be used to spatially separate analytes based on their size. A typical CE application will involve pushing a mixture of analytes through a sieving matrix, a polymer network the analyte passes through, with a set HV field. The HV field can also induce a electroosmotic flow (EOF), a bulk fluid flow, due to charge displacement between fixed and mobile species. In the applications considered here the EOF will result in a plug-like movement (i.e. the velocity of the sample is equal for the entire channel), either due to the EOF being suppressed/mitigated by the agarose sieving matrix, or the EOF being dominated by bulk EOF from the agarose itself. As a result, both EOF and the electrophoretic transport of the charged analyte are plug flows thus the ultimate flow-profile of an electrophoretic separation is also plug-like and can be described by a mobility. In comparison to the parabolic flow profile induced by an applied pressure, a plug flow is very advantageous as it ensures that the sample is kept concentrated and intact and not "stretched" out and diluted.[54] The target application of this work is to use CE to size DNA amplicons after a PCR in accordance with laboratory best practices.[5] This method can be extended by sizing the result of DNA after exposure to restriction enzymes. These enzymes selectively recognise a target DNA sequence and cleave the sample into multiple parts. By sizing the results one can readily determine if the enzyme acted, and thus be able to identify whether the sequence recognised by the enzyme is present. This provides sequence specific information and is capable of identifying single-point mutations which can identify clinically relevant information.[3]

Electrophoresis can be readily miniaturised from macroscale gels to capillaries or microchips. This thesis focuses on the latter, though the majority of the principles involved are similar. Hence CE in this work will refer to both capillary and chip electrophoresis. CE has a number of advantages over conventional methods including a reduction in reagent volume (and thus the cost per test) and an increased surface area to volume ratio leading to more efficient heat dissipation; conventional gel electrophoresis is quite slow because Joule heating of the gel limits the field that can be applied. As a result, CE can typically be run at one to two orders of magnitude higher fields and is thus much faster.[54] Another advantage to microchip based CE is the ability to perform the inject-separate technique as shown in Figure 1.3. In this technique, two channels are brought together into a cross with an intersection and terminated with wells. The sample is loaded into one well while all other wells are filled with buffer. In the injection phase (1.3a) a HV is applied to across the injection channel and the sample is pushed towards the intersection. In a second phase, the HV is switched

to across the separation channel and the sample components are separated based on size. This allows for the user to readily generate nL volume samples as compared to the 10+ μL sample volumes conventionally used, miniaturising the format of the microfluidic chip. In comparison to the typically cm-scale commercial instruments (such as the 28 cm long Applied Biosystems SeqStudio Genetic Analyzer[55]), the inject-separate technique can achieve usable performance at much smaller scales. For example, the Backhouse group has managed to reduce separation distance to 4mm.[56]

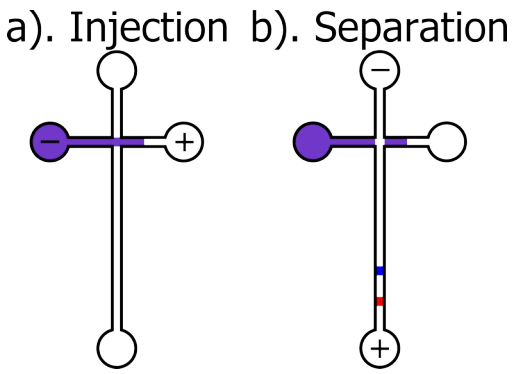

Figure 1.3: A diagram illustrating an inject-separate process for CE. a). An electric field is applied across the injection channel, pulling the charged DNA (purple) into the chip intersection b). The small sample plug created in the intersection is separated by an electric field applied across the separation channel. This separates the plug into its components (red+blue).

There are two primary assessment factors for CE: LOD and resolution. In this work, LOD is defined as the minimum concentration of fluorophore required to create a signal that is 3x higher than the noise (i.e. signal to noise ratio, SNR, of 3). For PCR-CE applications, the LOD must be at 1 nM or better to be capable of detecting trace amplicons. This corresponds to approximately 0.2-1% of the output of a well-executed PCR based on a typical primer concentration between 100 nM and 500 nM,[57] ensuring that analytes are robustly detected and low-level contaminants can be detected. This is important in a number of applications. For example, a short DNA contaminant with a concentration of 1-10% of the sample can cause significant seeding bias in next generation sequencing applications which, if left undetected, can result in incomplete data.[58] Therefore, 1 nM LOD is the requirement for diagnostically relevant CE detection.

The resolution is an assessment of how closely spaced in size two analytes can be differentiated, typically expressed in the number of base pairs (bp) of DNA. Ugaz et al.[59] has set a requirement of 10 bp resolution for most DNA applications, including PCR-CE. However, resolution is a complex assessment factor with a number of dependencies including the separation channel length, the injection channel width, the detection probing volume, electronic detection and the separation protocol used. Of these, the protocol is the most important.[60] As stated above, development of molecular biology protocols is beyond the scope of this work. Instead, focus has been on developing a platform upon which future experiments can be done, setting a series of instrumentation and fabrication requirements such that a future molecular biologist could readily implement protocols with sufficient resolution. Firstly, the HV generation and switching must meet a number of technical specifications including field, stability, reproducibility and current measurement. These are discussed in Appendix A.1. In terms of microfluidics, the channel dimensions must be on the order of 100 μm or smaller. Ugaz et al.[60] noted that when using the same instrument a sieving matrix change

from a cross-linked agarose gel to a pluronic gel improved the resolution from 100 bp to 4 bp. However, these high performance sieving matrices have lower viscosity making them more susceptible to pressure driven flow which would disrupt their network. For a given pressure, the Hagen-Poiseuille equation states a quadratic relationship between flow rate and radius. Thus, to ensure that pressure driven flow is minimized, the channel dimensions must be small and, conventionally, within 100 μm. The development of fabrication techniques is discussed in Chapter 2. Initially, the microfluidics produced had dimensions greater than 100 μm and thus were demonstrated with cross-linked agarose matrices that were viscous and resistant to flow (indeed, conventional applications of agarose electrophoresis use slabs on the cm scale). These interim demonstrations were intended to demonstrate the functionality of the instrument and the optical detection but were not expected to meet the resolution objective. Recent improvements to the fabrication have enabled channels that can support high performance linear polymers, presenting an opportunity for future demonstrations that meet the resolution target.

In addition to the HV instrumentation and microfluidic factors to resolution described above, there is a minor optical and electronic component. Firstly, the optical probing volume for the instrument must be the same size as the sample volume or smaller; if this probing volume is larger then two very tightly spaced samples will have overlapping signals and not be resolved. From a detection electronics standpoint, the circuit must respond faster than the typical transit time of a sample across the detectors. For most applications, the sample transit time is 1-2s, leading to a requirement of the detection electronics to detect signals at 1 Hz or higher.

1.2.3 PCR-CE Demonstrations in the Literature and Commercially Available Devices

There currently does not exist a low-cost instrument for PCR-CE. As stated above, PCR-CE execution is significantly more difficult than q-PCR. For this reason, the majority of commercial available DNA analysis instruments utilise simplified protocols to avoid CE integration, potentially introducing accuracy concerns. For example, consider the Alere i,[61] the first molecular diagnostic available for out of lab use, which targets point of care detection of influenza. This instrument avoids most of the functionality from Figure 1.1 by implementing an iso-thermal amplification reaction to avoid the need for thermal cycling, not extracting or purifying the DNA sample prior to analysis[62] to minimise fluid handling complexity and excluding CE entirely to eliminate the need for HV instrumentation. However, specificity concerns[63] prompted a recent recall[64] and post-recall the sensitivity of the instrument was found to be much lower than previously advertised.[62] Furthermore, the non-standard biochemical application and use of proprietary methods means that verification and extension of the application to other diagnostic applications is complicated. This highlights the challenges introduced by instrumentation "short-cuts". Other devices on the market add sample extraction and thermal cycling for a more standard q-PCR analysis including the Cepheid cartridge-style GeneXpert,[32] the Roche tube-style cobas liat,[34] the Biofire pouch-based FilmArray,[33] the Verdus PCB-style Vereplex[37] and the GenePOC disk-style Revogene.[38] However, the lack of a sequence specific consistency check (like CE) prevents these instruments from implementing gold-standard protocols that satisfy laboratory best practices.[5] Further, these instruments are still typically prohibitively expensive for resource-poor environments (the BioFire FilmArray is, for example, $39,500 per instrument[45]). The first and, to the best of my knowledge, only commercially available PCR-CE device is the Integen RapidHIT[65] targeted at forensic analysis applications. However, this instrument is very expensive, priced at $270,000 per instrument and $1,750 per test cartridge,[66] making it unsuitable for most diagnostic applications.

There have been a number of μTAS devices in the literature that have implemented and demonstrated PCR-CE. One very early example was the seminal work by Burns et al.,[67] who featured one of the first PCR-CE devices. The device was built on a silicon substrate with a deposited photodiode, interference filter, heater wires and glass, into which the microfluidics were etched. This tight integration eliminated much of the optics typically required for LOC instrumentation, opening the possibility for a low-cost demonstration. However, the instrument still required substantial external instrumentation including manually controlled air pressure lines for fluidic actuation, an LED and filter for fluorescence excitation and a high-end laboratory lock-in amplifier to read the fluorescent signal. These components push this work out of the low-cost regime. Exacerbating the cost was the use of an interference filter and glass followed by etching. This would lead to high material cost, slow fabrication times and a high NRE development environment. Therefore, both the instrument and per-test costs were not suitable for resource-poor environments. Furthermore, since the device featured no autonomous fluid handling capabilities it could only execute very simple functions with highly purified samples, and as such would see limited utility going forwards. The thermal system, while functional for their demonstration, featured too high a thermal load for rapid cycling (leading to slow experiment cycle times) and required substantial calibrations that would impede future developments.[53] The thermal difficulties (along with the high NRE environment) are likely why future designs omitted the PCR and focused exclusively on CE.[68,69] Finally, the optical detection of Burns et al.[67] was very marginal and highly insufficient for a practical PCR-CE application. While few details are given in the original work, similar designs in the follow-up work by Webster et al.[68] had the same 20 layer interference filter, blue LED and lock-in amplifier and featured a LOD in the μM regime, about 1000x too high for general-purpose applications. In the final publication from this group on these style of devices by Namasivayam et al.[69] which targeted CE applications, improvements to the detector and filter enhanced the LOD by an order of magnitude, however this still was too high for general purpose CE. Overall, while good for its time and a significant demonstration in the field, the instrument by Burns et al.[67] fell short of being a general-purpose molecular biology instrument.

Many of the PCR-CE instruments in the literature come from the Mathies group at the University of California, Berkley. Early work by Lagally et al.[70] featured a multi-layer glass device with integrated latex pneumatic valves for fluid actuation and pumping. This allowed for a much higher degree of complexity as compared to Burns et al..[67] Follow-up work demonstrated high-performance down to a single copy of analyte[71] and rapid analysis,[72] demonstrating a LOD at the limit of PCR[5] and the advantages to μTAS analysis. The group later integrated PDMS valves on-chip[73] leading to a high-performance instrument with all the functionality required for automated analysis.[74] For thermal control, all of the Mathies group demonstrations have on-chip heaters and on-chip resistive temperature sensors. However, there are two primary limitations to these works. Firstly, each device requires up to four discrete glass wafers, patterned through photolithography. This is not only expensive from a materials standpoint, but also faces high development costs due to reliance on photolithography. Furthermore, while heaters and valves are integrated on-chip, the rest of the instrumentation is external and generally expensive and bulky. The work by Scherer et al.[41] is the best and most well described instrument produced by this group, featuring all of the functionality demonstrated by proceeding papers while describing a well-executed but extremely expensive PMT-based confocal module. While this instrument had very high-performance and was capable of interesting applications (for example, autonomous sampling for life on Mars[75]), it was targeted at a very different application than this project; their focus on glass and high-cost instrumentation make them highly unsuitable for general-purpose molecular biology analysis.

The other primary group developing PCR-CE is the Landers group, who have produced one of the most impressive

PCR-CE demonstrations to date by Le Roux et al..[40] This tour de force presented a device that accepted injection moulded polymer chips manufactured by an industrial process and performed an automated DNA extraction, PCR and CE. The instrument performance was very high, capable of single bp resolution and a LOD substantially below the resultant PCR product concentration (though not discussed). Given these specifications, the instrument was demonstrated by performing sample in, answer out short tandem repeat (STR) analysis, one of the more demanding CE analyses.[59] However, even though attention has been paid to a low running cost by focusing on inexpensive, injection moulded fluidic chips, the instrument is far from a low-cost option with almost every sub-system being substantially more expensive than those used in this work. For fluidic actuation, the system employed a syringe pump, an effective but pricey option. For thermal cycling, the instrument used an IR laser to heat the sample and a second IR thermometer to measure the temperature. This provided a contact-free method of temperature control, but at considerable instrumentation cost. Finally, and most significantly, the optical detection was performed by a five colour confocal module with fibre optic coupling to the sampling point, a decidedly high-end design. Thus, while an impressive piece of technology, this instrument was similar to those produced by the Mathies group in that it is not relevant to the low-cost objective of this project.

In addition to the works described above, there have been a number of active valve-less PCR-CE demonstrations. However, by removing the ability to actively seal and unseal the PCR chamber these works are susceptible to diffusion of the PCR mixture into the surrounding channels and out of the thermally controlled zone. These devices would also be susceptible to erratic bubble formation from degassing of the heated reaction volume, potentially causing thermal and fluidic transport issues. Thus, these works are not expected to meet the strict 1 ^{o}C thermal requirement for robust PCR. Furthermore, the lack of a valving technology also typically requires the PCR product be injected directly into the CE channels without mixing with running buffer. This leaves the instruments highly susceptible to injection artefacts and is a deviation from best-practice protocols.[31] Valve-less PCR-CE demonstrations include the glass-based work by Pan et al.,[76] the polymer based work by Koh et al.[42] and the recent demonstration by Liu et al.[39] in polycarbonate. The latter was interesting in that they performed CE during the PCR such that the instrument could monitor the reaction in real-time. Thus, the instrument essentially performs a q-PCR experiment while sizing each step of the PCR, a process that has lots of potential for highly multiplex PCR-based analyses. However, while interesting, the lack of active valve prevents a standard protocol implementation. Furthermore, each of these works utilised high-cost optical detection components for fluorescent detection and were thus unsuitable for resource-poor environments.

Shaw et al.[77] and follow-up work that was not peer-reviewed by Docker et al.[78] present a lower-cost PCR-CE device, featuring DNA preparation, a Peltier thermal system and CE compatibility (though the CE-system was not demonstrated). Buccal cells were lysed on-chip and purified using silica monolith that was embedded on-chip, thus demonstrating DNA preparation without the use of valves. Fluid actuations were provided by electro-osmotic pumping (EOP). The works describe an optical detection system which leveraged moderate cost commercial products and avoided expensive lenses, filters and dichroic mirrors. The detection used a fibre optic-based reflection probe to transmit the laser excitation to the sample and collect the fluorescent signal for a commercially available spectrometer. However, the LOD of the instrument was not assessed (and based on the components, not expected to reach specification) and, while lower cost than other optical arrangements, this instrument is still multiple orders of magnitude more expensive than those designed in this thesis. Furthermore, while EOP was effective for the sample preparation they implemented, it has a number of drawbacks. Firstly, it faces the same active valve-less issues described above relating

to sample diffusion during the PCR. Furthermore, compared to pressure driven pumps used in other works, EOP is slow, does not provide good mixing and is susceptible to Joule heating and bubble formation.[79] Finally, this work was based on a glass microfluidic technology, and thus the technology remains too expensive from a per-test standpoint for resource-poor applications.

One of the best and lowest-cost μTAS implementation of PCR-CE was previously presented by the Backhouse group with the work by Kaigala et al.[80] being the most fully-functional. The microfluidic chip was quite similar to those of the Mathies group in that it was built in glass with on-chip PDMS valves and on-chip resistive heating and sensing. This enabled peristaltic pumping and effective sealing of the PCR chamber, as well as low-cost thermal control. The primary deviation from the Mathies implementations was in the optical detection. Where Scherer et al.[41] used a high-cost confocal, the design in Kaigala et al.[80] features laser illumination from the side while emission light was collected from below as discussed in detail in Section 3.1.1. This dropped the optical component count to one lens and one filter, enabling much lower-cost instrumentation than the works described above. However, as discussed above, the glass fabrication is expensive both in terms of the development cost as well as the on-going material cost of the devices. Furthermore, while lower-cost than the confocal modules described above, the fluorescence detection still remained a primary source of cost in this instrument and was much higher than the designs presented in this thesis.

Analysis of the field highlights three primary avenues of development for low-cost PCR-CE implementations. Firstly, there is a need for sufficient functionality. Almost all commercial DNA analysis equipment lacked the HV integration for CE, and of the PCR-CE demonstrations many did not include valving. Implementing all of these functions is primarily a technical issue that is discussed in Appendix A. Furthermore, there is a need to focus on polymer-based microfluidics to reduce the per-test cost. Of the PCR-CE instruments demonstrated to date, only Liu et al.,[39] Le Roux et al.[40] and Koh et al.[42] have avoided the high NRE of glass microfludic fabrication. To this end, Chapter 2 details efforts made towards low-cost rapid-prototyped microfluidics in the polymer PMMA. Finally, and most significantly, is the fluorescence detection instrumentation. Almost all of the above works, including the commercial Integen RapidHIT, rely on confocal optics. This is a high-cost approach which suggests that most of the above would carry costs comparable to the Integen RapidHIT (i.e. on the order of \$100,000[66]) if produced commercially. Of the exceptions, Pan et al.,[76] Shaw et al.[77] and Kaigala et al.[80] avoid the confocal arrangement but feature largely the same expensive components and as such cannot be considered cost-accessible for many applications. Finally, Burns et al.[67] does feature a low-cost detector but is multiple orders of magnitude below the LOD required to implement general purpose CE protocols. Thus, development of low-cost fluorescence detection with sufficient performance is the most important development required for affordable PCR-CE. This is introduced in the next section and discussed in detail in Chapters 3 and 4.

1.3 Light Induced Fluorescence (LIF) Instrumentation

Fluorescence is the primary detection principle behind all of the DNA analysis instruments surveyed in Section 1.2.3 above. Historically, fluorescence instrumentation used lasers to excite the fluorophores in what is termed laser induced fluorescence (frequently abbreviated to LIF). More recently, there have been efforts to replace the laser with a light emitting diode (LED),[81] such as in this thesis. Due to the comparable physics, LIF here will refer to light induced

fluorescence, whether that light originated from a laser or LED. LIF instrumentation can be considered in two stages: excitation and emission. Excitation begins with a source of light which is used to bring the fluorophore into an excited state. From this initial excited state, rapid vibrational and solvent relaxation processes reduce the excited energy followed by the fluorophore decaying to the ground state either non-radiatively or radiatively. In the case of the former, no signal is generated, while in the latter an emission photon is released. Due to the relaxation processes, the emission photon has a lower energy (and thus higher wavelength) than the excitation, a phenomenon called the Stokes Shift. This allows for the emitted photons to be spectrally distinguished from the excitation photons, enabling high specificity in a well-designed experiment. Furthermore, with good LIF instrumentation, selective amplification of the emission signal can enable high sensitivity. However, as stated above, typical implementations of fluorescence detection use expensive optics and electronics which constitute the bulk of the instrumentation cost, and this prices these devices out of many applications.[45] This forces typical cost-focused instruments to use low-performance detection techniques that can not perform the standard testing protocols. There is therefore a need for technology to avoid this compromise, implementing sensitive fluorescence detection but at low-cost.

The primary challenge to LIF detection is that the excitation power is typically multiple (eight or more) orders of magnitude larger than the power of the emitted light. This is due to a number of factors including power loss in the system, inefficiency of absorption of the excitation power, the aforementioned non-radiative decay processes and inefficient collection of the emission light. This creates two main issues. Firstly, it leads to low emission signals which are challenging to detect, typically in the fW-pW range. Secondly, this low emission signal is difficult to detect due to the presence of much more powerful excitation light. As stated previously, the typical approach to LIF detection is the confocal optical module. These designs, a sample schematic of which is shown in Figure 1.4a below, specifically target these issues. To address the low emission signal, a typical confocal module will utilise a high power laser for excitation, multiple lensing components to minimise power losses and a high-performance detector such as a photomultiplier tube (PMT), avalanche photodiode (APD) or charge coupled device (CCD). To reduce baseline the confocal module includes multiple high-end interference spectral filters, a dichroic mirror and a pinhole. The dichroic is a wavelength specific mirror that separates the excitation and emission light pathways, suppressing the amount of excitation light collected by the design while the pinhole reduces the volume probed by the optics to reduce the collection of scattered excitation light. All these factors result in a low-baseline and high-sensitivity, but also high-cost design. Conventional LIF instrumentation is discussed in more detail in Section 3.1.1.

The long-term objective of this overall research project was to develop a LOC device where the fluidics and instrumentation electronics are integrated monolithically onto the same substrate and fabricated in a CMOS process. In terms of the LIF detection, this goal imposes a number of stringent constraints on the instrument. These are justified in more detail in Section 3.1.3, though briefly they include replacement of the laser with a LED, the interference filters with polymer absorption filters and the PMT with a photodiode. This is depicted in Figure 1.4b which also removes the need for a dichroic mirror by separating the excitation and emission pathways on opposite sides of the chip and eliminates the need for lenses by bringing the LED and photodiode into close proximity. Overall, this design yields substantial cost and size savings, resulting in only a few dollars worth of optical components that can be readily miniaturised into a USB-key sized instrument. However, in order to realise this objective two primary challenges must be overcome. Firstly, each of the low-cost components used in Figure 1.4b introduces a reduction in the fluorescence signal, exacerbating a primary challenge of the field as established in more detail in Section 1.3.1 below. This requires careful design to ensure the design meets the performance requirements for PCR-CE. Another issue is that the design

inherently relies on the photodiode and sample being in tight proximity. As elaborated upon in Section 3.6.1, this proximity leads to very high collection efficiency of fluorescent light which can offset the performance issues of this design. However, practically implementing this proximity (on the order of tens of μm per Section 3.6) essentially makes prototyping of the design impossible without fabricating the monolithic LOC device.

Fully implementing the monolithic device is very difficult in the research and development phase as the design and manufacturing toolchain involved is both arduous and expensive to implement due to high NRE costs, leading to slow iteration rates and typically a limited number of test samples per design iteration. Furthermore, development is complicated by the tendency of biological reagents to foul surfaces,[82] limiting the re-use of the already limited test samples. Additionally, protocol development for biological processes is a complicated task with a number of variables that must be optimised and controlled, which typically requires a number of experiments to fully develop and reliable instrumentation. Thus, directly developing a monolithic device is a very risky proposition. On one hand, even in the unlikely scenario where all aspects of the design function perfectly, limited stock and the fouling problem might prevent protocol development and demonstration. On the other, fabricating a larger stock of devices for protocol development is not only expensive, but if the design does not function as expected it might still be impossible to develop protocols (regardless of the stock quantity) and significant resources would be wasted. Overall, even though the monolithic design could in the future realise low-cost diagnostics, it is prohibitively expensive to directly develop. This is an instrumentation manufacturability roadblock that must be overcome.

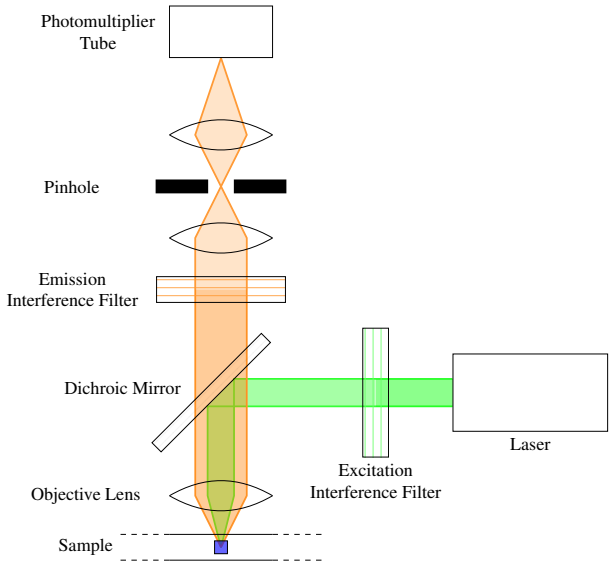

(a) A diagram of a confocal optics module. Both the light source and detector are present on the same side of the sample and share a single objective lens. The excitation path (green) and emission path (orange) are separated by a dichroic mirror which selectively reflects certain wavelengths. Additional lenses not pictured here are typically used to improve performance. The confocal module targets low-baseline, high-sensitivity applications and is the standard method for LIF detection in CE. However, it's size and cost preclude inclusion in low-cost instruments. Furthermore, reliance on multilayer interference filters, PMTs and dichroic mirrors prevent miniaturisation to a single chip as in Figure 1.4b.

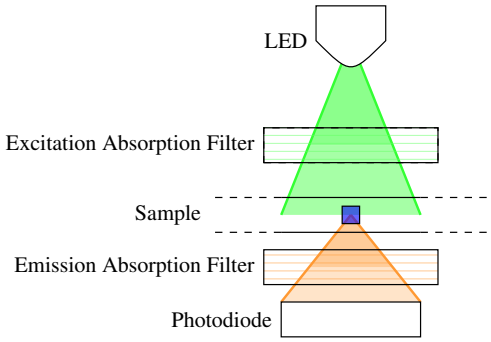

(b) A diagram of a miniaturised LIF detection system. This system uses low-cost LEDs and polymer absorption filters to drastically reduce cost while eliminating the lenses and dichroic mirrors by separating the excitation (cyan) and emission (orange) pathways and bringing all the components into tight proximity. Such a design would enable entire instruments to be fit within a USB-key sized device for ≈$20 and revolutionise diagnostics. However, this design has a number of challenges including the fact that it is entirely predicated on monolithic fabrication of the electronics, filter and fluidics which carries substantial NRE costs. Chapter 3 discusses methods of prototyping instruments that use the same components and have similar performance to this monolithic design but with short working distance lenses added to the emission path to enable use with the rapid prototyped fluidics from Chapter 2, avoiding the NRE issue.

Figure 1.4: LIF detection for CE

The solution to this problem pursued by this thesis was to develop a design methodology where the constraints of the monolithic design in Figure 1.4b were adhered to except with the addition of a short working distance lens. This lens stretched the sample-detector separation from 10's μm, a value that could not readily be achieved, to 100 μm, enabling the use of rapid-prototyped polymer fluidics designed for this module with thin channel caps. This allowed for the prototyping of optical designs with moderate cost (≈$100) that scaled directly to the proximity-based LIF instrument in Figure 1.4b while separating the microfluidic, optical and detection electronic design cycles such that they could be independently developed.

In summary, the overall goal of this work was to develop LIF detection that was both low-cost and scalable. This involved the fabrication challenge of designing polymer fluidics with 100 μm channels and 100 μm channel caps compatible with the short-working distance lens, the optical challenges of using a LED for illumination, a lens-free excitation pathway and absorption filters and the electronics challenge of amplifying low-level photodiode signals. This instrument must then be capable of reaching 1 nM LOD to implement PCR-CE applications. This is a difficult

goal that had not been addressed prior to this project. Scalable optical design is discussed in more detail Chapter 3, specifically in Section 3.1.3.

1.3.1 Reference Model for LIF Module Assessment

One of the difficulties in developing fluorescence detection is that the LOD is a function of the sample volume (which determines how many fluorophores are present), the LIF optics (which determines how much emission signal is collected) and the detection electronics (which determines the minimum signal that can be detected). This makes assessing the relative contributions of improvements to these individual aspects to the overall LOD difficult. To decouple the assessment of the microfluidics, optics and detection electronics a reference model representative of a low-cost instrument was generated based on the diagram in Figure 1.4b. This involved standardising on a sample size, sample concentration, optical geometry, filter performance and detection electronics. Next, a back of the envelope calculation was done to estimate the LOD of this reference system and assess the project feasibility. In later sections, the various optics and electronics iterations can be compared to this model as a reference point to assess their performance.

As described in Section 1.2.2, in order to reach 10 bp resolution a channel with a width and depth of 100 μm was needed. Based on the inject-separate procedure, this channel would create a sample volume defined by a 100 μm cube (1 nL). This sets a standard sample volume. The amount of light this sample absorbs can be estimated by the Beer-Lambert Law (discussed in more detail in Section 3.4.1) to be about 1×10^{-4} % of the excitation light incident. This absorption is largely independent of the optical design, illustrating the low-level signals expected for LIF detection in CE channels.

Next, we must define a standard optical system. The low-cost design in Figure 1.4b uses a LED for excitation, which has three notable effects on the signal. Firstly, a typical LED has a relatively low optical power output of about 1 mW. Furthermore, due to the wide-output angle of the LED and the lack of room for lenses in this system to focus this excitation light, all but 1% of this LED light is assumed to be lost. Finally, unlike lasers, LEDs are not monochromatic and have a relatively broad output spectrum. As a result, LED illumination does not excite fluorophores at their peak absorption efficiency, typically resulting in only about $^1/_3$ as much absorption as expected. These factors are discussed in more detail in Sections 3.3.1 and 3.4.1. To reduce baseline, spectral filters are used both to condition the excitation light and collect the emission light. The low-cost design in Figure 1.4b requires the use of absorption filters that are much less efficient than the high-performance interference sets used in a typical confocal, only transmitting about $^1/_4$ of the light incident upon them (discussed in more detail in Section 3.4). Finally, as explored in Section 3.6, the proximity of the photodiode to the channel is expected to collect about 5% of the emission light. In aggregate, this system would be expected to collect an optical signal of about 10 fW from the reference sample.

Finally, we must define a standard detector to convert the optical signal to an electrical readout. Unlike the typical PMT, APD or CCD used in conventional LIF detection, photodiodes do not have inherent gain and thus their ability to detect optical power is highly dependent on their readout circuit. First, the photodiode must convert the optical signal into a photocurrent. In the spectral region of interest (500-600 nm), a typical responsivity for a PIN photodiode is 0.33 $^{\mathrm{A}}/_{\mathrm{W}}$. Next, this photocurrent is typically converted to a voltage and amplified. The reference model used in this thesis is a design used previously by the Backhouse group, based on a Burr-Brown application note[83] and implemented in the

thesis of Alison Bidulock[84] and a published work by Kaigala et al..[85] This circuit had a bandwidth of 30 Hz, a gain of 10^9 $^{V}/_{A}$ and a measured noise of 114 μV.[84] Combining the responsivity, noise and gain the minimum detectable power, the power that results in a SNR of 3, can be estimated to be 1 pW.

Combining the back of the envelope assessments of the reference sample, optics and electronics results in an expected LOD of 100 nM, two orders of magnitude worse than required for implementing PCR-CE. This highlights the difficulties and trade-offs inherent in low-cost design and is likely the primary reason there has been relatively little development in this field. To the best of my knowledge, and per the reviews of LED-excitation based optics for CE applications by Macka et al.,[81] Xiao et al.[86] and Götz and Karst,[87] there has not been an optics module applied to CE that has met all of the above scalability constraints (LED, absorption filters, photodiode). Particularly, the use of absorption filters has been notably absent. The closest comparable work is by Yang et al.[88] (discussed in more detail in Section 3.1.1) who demonstrated an optics module with LED excitation, no lensing optics and photodiode detection. This work was cited by multiple reviews as being the state of the art for LED-excitation, photodiode detection LIF optics for CE.[26,81] However, it relied on an interference filter which, as described above, is both costly and non-scalable. Furthermore, the cited LOD for this device was 100 nM, very comparable to the reference model above and insufficient for general PCR-CE application. Thus, there remains a need for scalable designs and substantial upgrades to overall detection performance. This was one of the primary goals in this work, which demonstrated progressively improved optics and electronics, ultimately achieving the target of 1 nM while maintaining scalability towards future CMOS implementation.

1.4 Research Objectives

The primary research objective was to develop a low-cost instrument capable of PCR-CE that was stable, scalable to future miniaturised designs and met all performance requirements for future molecular biologist to execute a broad spectrum of standard bioanalysis protocols. This primary objective can be split into the following sub-objectives

- Design, build and test a series of technical modules that perform the core PCR-CE functions of HV generation and switching, microfluidic valving, pneumatic switching and thermal control. These modules are discussed in Appendix A.
- Develop a polymer-based microfluidic technology that can be rapid-prototyped for quick design, low-cost design development. Ensure the technology is capable of the following:
  - Patterning 100 μm wide and deep microfluidic channels to ensure compatibility with high-performance sieving matrices.
  - Compatible with bringing a short-working distance lens 100 μm away from the sampling point for compatibility with the low-cost, scalable optics.
- Develop a LIF detection system (optics and detection electronics) that is low-cost, scalable and capable of implementing gold-standard PCR-CE protocols. This requires the following performance requirements:
  - Achieving a LOD of 1 nM with a 1 nL sample to ensure adequate CE detection. This involves improving the combined performance of the optics and electronics by two orders of magnitude over the reference model developed above in Section 1.3.1.

  - Having a "spot-size" or probed optical volume on the order of a 100 μm cube to ensure the optics do not reduce CE resolution.
  - Capable of detecting a 1 Hz or greater frequency signal without artefacts to ensure the detection electronics do not reduce CE resolution.
  - Ensuring the optics and electronics meet the scalability constraints to ensure they accurately prototype a miniaturised, monolithic single-chip LOC instrument. These include the use of LED excitation, absorption filters for spectral filtering, lens-free fluorophore excitation and photodiode based detection.
- Design, build and test an integrated instrument that contains all of the instrumentation functionality required for PCR-CE on a single low-cost platform.
  - This includes HV generation and switching, microfluidic valving, pneumatic switching and thermal control as well as compatibility with the polymer-based microfluidic technology and the LIF detection system described in the objectives above. Note that this does not include thermal design, protocol development or application demonstration which are beyond the scope of this work.

1.5 Thesis Organisation

This thesis addresses some of the core concerns of the field to develop a low-cost PCR-CE instrument that is not only useful unto itself, but also features scalable LIF detection making it compatible with a future monolithic, single-chip LOC device. Furthermore, the instrument utilises low-development cost rapid-prototyped polymer fluidics and thus presents a route through both the microfluidic and instrumentation manufacturability roadblocks. The subsequent chapters detail the key advances to the fabrication and LIF detection modules.

Chapter 2: Fabrication discusses efforts put towards rapid-prototyped polymer microfluidics. The objective of this chapter was to develop reliable fabrication methods for channels that had a characteristic dimension of 100 μm (in both depth and width) which can implement general-purpose CE protocols while being capable of holding a lens 100 μm away from the channel to maintain compatibility with the low-cost, scalable optical designs. The focus of the chapter is first on the use of CNC milling for microfluidic fabrication and charts the progress from initially large channels to progressively smaller microfluidics as technique and equipment improved. Ultimately, a channel width of 127 μm was fabricated which is near the state of the art for such fluidics, though still slightly larger than typically used for CE. The micromilled fluidics, while larger than the target channels, were used heavily both in the application demonstrations contained in this thesis as well as by the Glerum molecular biology lab at the University of Waterloo for routine applications. Next, the chapter discusses bonding methods for capping the patterned channels, initially beginning with simple and fast, but low-performance adhesive methods before progressing to a new solvent-vapour bonding method that enables improved performance designs. The chapter culminates in the discussion of a new microfluidic fabrication process that utilises laser ablation, CNC milling and solvent bonding to form microfluidic channels that are triangular in shape with a depth of 75 μm, a base width of 180 μm (0.8 nL sample volume) and a capping layer of 85 μm. These new channels enable the use of general purpose CE separation matrices while retaining compatibility with the novel optical designs in this work and meet the research objectives for fabrication.

Chapter 3: Optical Design details the optical component to the LIF detection. The objective of the LIF detection

was to design a module implementing low-cost components that was compatible with miniaturisation to a monolithic-CMOS design and had performance metrics that comply with the desired CE application, notably a LOD of 1 nM and a spot-size of 100 μm. This chapter first details a calculation model to assess and estimate the impact of the design decisions on the resulting performance. This model is then used to guide a series of optics module iterations. With each iteration, key design changes were identified and implemented to push the development towards the detection goal. Ultimately, an optical design was developed that scales to higher levels of miniaturisation with an estimated signal of 56 fW from the desired sample size and a spot-size of 134 μm. This represents the limit of what can be achieved given the design constraints imposed by a low-cost and fabrication methods available at the time. In comparison to the back of the envelope reference model detailed above, this is a factor of 5.6x improved. However, even after optimisation the optical power collected by the design remains too low to be detectable with the reference detection electronics circuit, motivating development on this front.

Chapter 4: Detection Electronics describes the development of the electrical component to LIF detection. This involved developing a transimpedance amplifier circuit with a low bandwidth optimised for CE, a high gain to maximise signal to noise ratio and post-processing to reduce the circuit noise. The performance of the refined design had a minimum detectable power of 42 fW, 23x better than the reference electronics design. This enhancement was crucial as it, combined with the improved optics in Chapter 3, enabled a LOD below 1 nM, thus meeting the requirements of the LIF design.

Finally, Chapter 5: Instrument Demonstrations details the testing of a series of instruments which integrate a microfluidic technology from Chapter 2, an optics design from Chapter 3 and a detection electronics circuit from Chapter 4 along with associated technical instrumentation from Appendix A. These demonstrations focused on a series of electrophoretic applications based on relatively low-performance agarose and larger than 100 μm channels. As fabrication, optical and electronic improvements came online, the channels were progressively shrunk for enhanced separation performance. One notable application was the demonstration of the state of the art in low-cost LIF instruments for CE, the first sub-nM LOD LIF module in the literature with a photodiode and LED. In comparison to the work by Yang et al.,[88] this instrument was multiple orders of magnitude more sensitive in an even lower-cost format, with a reported detection limit of 0.15 nM[89] in 254 μm channels. However, the larger channels meant that the resolution of the separation was quite poor at 43 bp, above the 10 bp requirement for PCR-CE applications. The final instrument developed in this thesis improved upon that demonstration with refined optics and higher performance detection electronics developed in Chapters 3 and 4. This instrument has an expected 0.75 nM LOD from the reference 100 μm channels, thus it both meets the detection objective while enabling the use of higher-performance CE protocols. The instrument also integrated the functionality described in Appendix A which includes a thermal controller, thermocouple and resistive heater for PCR, 24 pneumatic lines for valving and fluidic actuation and improved HV electronics. This covers all the functionality required for PCR-CE as illustrated in Figure 1.1, making this instrument the first cost-accessible device capable of this gold-standard analysis technique. This functionality is combined with a highly flexible alignment interface and a design tool to enable future users to rapidly re-configure the instrument for a variety of application-relevant demonstrations.

In addition to the core problems addressed in the body, this thesis also contains a series of useful appendices. These cover the technical development of the remaining PCR-CE instrumentation functionality (i.e. excluding fabrication and LIF detection) (Appendix A), fabrication protocols for polymer fluidics (Appendices B and C), theoretical calculations

to assess the detection electronics (Appendix D) and a guide to the next-generation instrument (Appendix F). In addition to these appendices a supplemental information (SI) folder is available as a DVD. The SI contains all design files for fabricating all of the microfluidics and instrumentation, circuit schematics and board design files for all circuits discussed, software code for the various microcontrollers utilised, calculations for estimating the optical performance of the instrument (i.e. a refinement of the reference model above) and a series of reports that cover experimental protocols and guides to the fabrication equipment.

Chapter 2

Microfluidic Chip Fabrication

2.1 Introduction

The microfluidic chip itself, and the fabrication techniques used to produce it, are important aspects of any LOC technology due to their substantial impact on not only the process flows involved with the LOC research but also the technology's commercial relevance. Practically, the fabrication technique is also important as it relates to the fluorescence detection discussed in later chapters. Firstly, as detailed in Section 1.2.2 and 1.3.1, the sample volume is an important parameter in the performance of a PCR-CE application. This sample volume is defined by the channel width, which in turn is limited by the microfluidic fabrication. Furthermore, as discussed later in Section 3.8, the size and roughness of the channel have important consequences for the fluorescence detector design, especially related to the signal baseline. Therefore, it was important to the success of this project to develop and refine methods for producing microfluidic designs. This is the subject of this chapter.

One of the primary advantages to miniaturising to microfluidics is the substantial decrease in reagent volume, and at the μL and below the running cost become dominated by the cost of the fluidics. Thus, the LOC material and the fabrication methods used to make the fluidics are centrally important factors that determine the technology's cost and accessible applications.[11,12] Becker and Gärtner[18] have noted that the materials and methods used in academic pursuits are increasingly differing from those used in industry, and thus many works in the LOC field have limited market applicability. Specifically, as discussed in Section 2.1.1, much of the field is either based on photo-patterned glass, which carries too high a material cost for many applications,[9,12,90] or soft lithography of PDMS, which is not suitable for scale up manufacturing.[9,12,18,22] Thermoplastics are polymer materials that exhibit a softening above their glass-transition temperature, T_g, such that they can be formed into the desired geometry in this softened state then cooled to retain structural integrity. This enables techniques such as injection moulding, that is the formation of a part by forcing molten material into a cavity which defines the part features, which is a standard method used by many industries for high-throughput manufacturing. This method, combined with a low-cost thermoplastic, enables the high-volume fabrication of low-cost devices and has seen use in many LOC demonstrations.[18,39,91] However, it also requires expensive moulds to be produced, making it expensive in small batches.[24] Thus, in the research and development stage

where rapid iterations are needed, injection moulding's high NRE costs make it prohibitively expensive. This illustrates the "manufacturability roadblock" discussed by Bhattacharjee et al.,[22] which refers to the difficulty in the LOC field to develop technologies that are low-cost in both the research phase as well as in high-throughput production.

One method to circumvent the manufacturability roadblock is to develop the technology in a thermoplastic using rapid-prototyping methods for the initial development, then switch to injection moulding once the design has been locked down.[22] This is the approach taken in this thesis, where development has focused on laser ablation and micromilling, two direct-write fabrication methods. This means that designs can be readily changed from batch to batch, leading to high iteration rates. Comparing to the previous glass microfluidics used by the Backhouse group,[80] the development time for a new microfluidic geometry has been reduced from multiple weeks to only a few hours and the per-device cost has been dropped by multiple orders of magnitude. PMMA was selected as the polymer of choice because it is one to two orders of magnitude less expensive than glass,[90] has excellent optical clarity,[92] low autofluorescence,[93] good chemical properties for aqueous analysis[94] and PCR compatibility[95] and is easily processed using standard thermoplastic methods (injection moulding, hot embossing, micromilling, laser ablation).[18] By focusing on a material that can support both the developmental and mass manufacturing stages, the designs here can readily transfer to higher volumes of manufacturing.

The general structure of the fluidics used in this work are shown in Figure 2.1 and contain three key features: channels, wells and chambers. Channels refer to sub-mm features that are fully encased. These are the primary microfluidic feature and provide fluid transport throughout the device as well as form the channel for CE. Channels are the smallest feature patterned and the most challenging to fabricate, making them the primary focus of this work. Wells are here defined as reservoirs that connect to the microchannels and are open to the environment. These are a chip-to-world interface, allowing the user to access the microchannels and add fluids to the device. Finally, chambers are features that are encased like channels but are on the mm scale. These are reaction chambers for processes like PCR and interface only with channels and not the outside environment. Thus there is a need for both sub-mm and multiple-mm features. To make these features, there are two main types of patterning: "through-cuts" where the feature is patterned through the entirety of the substrate such that it is cut-out and "engrave" patterns where the feature is patterned partially into the substrate. To simplify processing, the procedures presented here pattern all fluidic features onto one substrate, called the fluidic layer, then cap it with a second layer, the capping layer. Thus, channels and chambers are made by engraving the fluidic layer and wells are made by patterning through-cuts in the fluidic layer. These features are encased by bonding to the capping layer as discussed in Section 2.3.

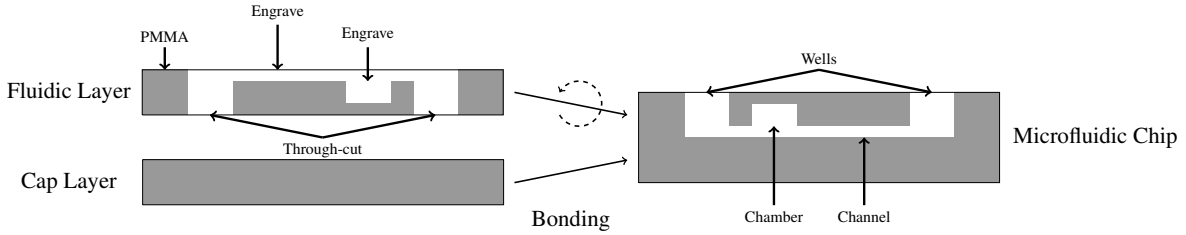

Figure 2.1: A cross-section diagram of the general microfluidic fabrication technique. Through-cut and engraved features are patterned into one layer (the Fluidic Layer) and supported with the surrounding chip material. The Fluidic and Capping Layer are then pressed together with a simple mechanical fixture to briefly (e.g. 30 min) provide alignment and pressure across the structure, after which it will have formed a single structure within which are wells, chambers and channels.

The assessment parameters for the fabrication output include the minimum feature size (which defines the channel geometry) and the channel surface roughness. The requirement on minimum feature size is highly dependent on the application. As assessed in Section 1.2.2, the requirement for implementing high-performance CE sieving matrices to reach the PCR-CE resolution target is that the channel dimensions are 100 μm or smaller, thus this defines a requirement on the minimum feature size. It should be noted that larger than 100 μm channels can still be useful for some CE applications if a cross-linked gel sieving matrix, such as polyacrylamide or agarose, is used as the typically high viscosity of these gels at room temperature resist pressure driven flow, though with lower separation resolution.[60] The use of agarose for demonstrating low-resolution CE applications with the larger than 100 μm channel iterations is detailed in Chapter 5. Surface roughness requirements were not explicitly set for a number of reasons. Firstly, assessing the roughness within a microchannel is a difficult task that required equipment that was not available at the time, precluding quantitative analysis. Furthermore, the effect of surface roughness on performance was also not well assessed. There are two potential performance impacts of rough channels. Firstly, we had previously observed that a high degree of surface roughness reduced the quality of CE separations.[96] However, the roughness of these channels was orders of magnitude higher than that exhibited in this work. High channel roughness also scatters more light, reducing the efficiency of the optical system. As explored later in Chapter 3, the scattering of light off of channel walls was a primary source of baseline for some designs. Therefore, the objective was to keep the surface roughness to an absolute minimum and to create channels as optically clear as possible for improved detection performance. Finally, one key requirement imposed by the optics in Chapter 3 is the need for a very thin ($\leq 100\mu$m) capping layer. While challenging, this enables a reduction in optical detection costs by multiple orders of magnitude.

This chapter details a brief overview of LOC fabrication methods typically used in academia in Section 2.1.1, followed by a discussion of polymer manufacturing methods including micromilling and laser ablation in Section 2.1.2. Micromilling was a convenient fabrication technique allowing for direct-write of microfluidics and rapid design turnarounds. This was a substantial enabling technology of the applications discussed in Chapter 5 and an important series of milestones in this research project. Development of the micromilling fabrication techniques is discussed in Section 2.2 which provides an overview of the total process as well as the various iterations of the micromilled channel. Through improved technique and equipment, the channel dimensions were decreased from the crude 381 μm first pass to 127 μm final designs. This represents a soft limit on the channel dimensions that can be readily CNC milled in-lab, as further reduction in channel size would require substantial increases in fabrication time and tooling-cost. Section 2.3 details work done on capping the microfluidic structures. This includes a rapid adhesive bond in Section 2.3.1 which was used in the applications in Chapter 5 as well as a new solvent-bonding technique for higher performance fluidics in Section 2.3.3. Finally, Section 2.4 presents the recently established next generation microfluidic technique for future work in the Backhouse group that involves laser ablation, CNC milling and solvent bonding. These new designs feature sub 100 μm fluidic layer caps for compatibility with the optics in Chapter 3 and smooth sub-100 μm dimension channels for compatibility with general purpose CE.

2.1.1 Traditional LOC Fabrication Methods

The fabrication method and material used for an LOC device are tightly coupled. Thus, these are both discussed simultaneously here. Early LOC systems used patterned silicon to form microchannels,[97] with patterning done using standard photolithography techniques. However, as a substrate silicon is a poor choice due to having a chemically

active surface, with a nominal conductivity precluding the use of electro-kinetic fluid actuation (and the exclusion of electrophoresis as an analysis method without surface modifications). Subsequently, substantial effort has gone towards glass based technologies, though the fabrication method remained mostly photolithographic based. Glass-based LOC technologies gained traction due to their lack of conductivity and well established surface chemistry.[73] This is specifically advantageous for CE, which is very surface sensitive. In fact, previous work in the Backhouse group has focused on glass-based LOC technology,[80] and, to the best of my knowledge, all current commercial CE devices still use glass chips.[98–100] However, there are a number of disadvantages to glass based devices. Firstly, glass is inherently more expensive as a material, with LOC grade glass being one to three orders of magnitude more expensive than polymers.[90] This makes it unsuitable as a disposable, and prices it out of many developing world applications.[9] In addition to being a more expensive material, glass is also much more expensive to develop for due to NRE issues. Photolithography requires the purchasing of new masks for every design change that needs to be introduced, leading to very slow iteration times and high development costs. Further, a clean room environment is needed, introducing processing and scheduling costs in a research environment. For these reasons, a move away from glass was one of the key objectives of this project.

The use of soft lithography to pattern PDMS microfluidics has become very popular in recent years[18,20,101] as it is much faster and easier to prototype with, which is very attractive in the academic environment. Soft lithography involves first developing a master stamp, then using the stamp to cast the microfluidic device in an elastomeric material. In comparison to glass photolithography, soft lithography has much lower start-up costs and does not strictly require a clean room environment.[21] PDMS is the most common soft lithography material due to its low surface energy (facilitating delamination of the finished device from the stamp), its transparency through the visible range for fluorescence applications and its moderate cost between polymers and glass.[20] However, soft lithography faces a number of challenges in both the prototyping and production stages of the technology. Firstly, while device replication does not need cleanroom facilities, the master stamp is still typically fabricated using a photolithographic technique.[20] Thus, design changes can still be cumbersome. In terms of commercial appeal, the curing time for soft lithography can take minutes to hours per device[18] and the overall process is very manual labour intensive.[22] Thus fabrication, while not capital intensive, is unsuitable for large volume manufacturing.[9] PDMS does not have forwards compatibility with high-throughput manufacturing, and thus a technology based on it cannot realise the full market potential of the LOC field. Finally, PDMS has some disadvantages as a material in that it is hydrophobic, typically requiring some surface treatments [92] and is gas permeable which can lead to air bubbles entering the fluidics, cross-contamination between channels and fluid loss.[102] Therefore, PDMS soft lithography was not seen as a viable technology to move towards. Due to the unsuitability of PDMS, glass and silicon, a focus was moved to polymer-based fluidics.

2.1.2 Polymer Microfluidics and Manufacturing Methods

Polymer microfluidics are very attractive due to their low unit cost and compatibility with industrial manufacturing,[18,103,104] specifically injection moulding. Injection moulding consists of first having a machined mould that molten polymer is injected into to form the fluidic device. There are a number of advantages to this technique including being able to form 3D geometries, good surface finish and very high throughput manufacturing. There are commercial services available like Microfluidic ChipShop[23] which provide custom injection moulded microfluidics for research purposes. Specifically, both Liu et al.[39] and Le Roux et al.[40] utilise injection-moulded polymer chips for PCR-CE

applications. However, there are a number of disadvantages to injection moulding in the research environment. Firstly, the equipment start-up cost is quite high.[18] This is further exacerbated by the need to machine very precise moulds. These NRE costs dominate in low quantities making prototyping expensive[24] with long turn-around times typically exceeding three weeks.[22] Hot embossing is another high throughput method for fabricating polymer microfluidics. This involves machining a stamp, heating the stamp to a high temperature and then imprinting the fluidic channels into the polymer substrate. This requires substantially simpler moulds to injection moulding (only one side needed), and thus lower NRE.[18,24] However, the need to make new moulds for each new design still presents a barrier to prototyping. Furthermore, some features (such as cross intersections used in electrophoresis) can be difficult to machine high accuracy moulds for, and not all features can be readily embossed (specifically, through-cuts present a challenge). Embossing and injection moulding are excellent techniques for high throughput and low cost per chip environments for a locked down design, but have not typically been adopted by the academic community due to the difficult in design iteration.[22] Rapid-prototyping methods are much more suited to this application. The objective is to use these methods to quickly and cheaply develop the desired microfluidics prior to a design freeze, after which the fabrication would be switched to one of the high throughput methods.

There exist a number of rapid-prototyping methods for polymer patterning of fluidics where the design is directly written into the material. Thus, each fabrication run can be readily adjusted to have different features and designs. There has been some interest in rapid-prototyping methods in the literature, with the notable review by Becker and Gärtner[18] providing an overview of a variety of methods. This work focuses on two key rapid-prototyping methods: laser ablation and micromilling. It should be noted that additive manufacturing and 3D printing could and have been used to fabricate polymer microfluidics. However, as recently reviewed by Au et al.[105] and Bhattacharjee et al.,[22] while the technology shows promise there are a number of technical challenges that need to be addressed before it can be readily applied to high performance microfluidics. Firstly, most conventional devices are limited in their ability to make small enclosed features, with 500 μm being a typical limit recently cited.[105] This is far too large for many microfluidic applications. A recent advance in resin development for stereolithography based 3D printing has recently demonstrated true microfluidic channels down to 60 μm x 108 μm.[106] However, stereolithography limits the potential channel materials to a few optically active resins, and the optical properties of the resin couple very strongly to the minimum feature size possible. Specifically, the resin used to fabricate these state-of-art channels was custom formulated and required adding Sudan I to increase the resin absorption. This limits optical clarity, and likely precludes optical detection. Depending on the 3D printing technology, the optical properties of the material can be very poor as many materials are fully opaque, and most stereolithographic printers use resins that set when exposed to light in the 380-480 nm range, similar to the optics in Section 3. Thus, in order to maintain compatibility with a wide range of materials (including PMMA, our selected polymer), focus has been kept on laser ablation and micromilling.

Laser ablation is a direct write technique where a laser is scanned over the material causing localised heating that ablates and removes material. This allows for a very clean design to fabrication work flow, and rapid iterations on designs.[104] Further, in comparison to other rapid-prototyping methods, patterning small features is comparatively quick.[18] However, there are a few specific disadvantages. Firstly, many lasers are pulsed in nature leading to uneven channel dimensions,[107] specifically "bumpy" channel bottoms from the laser pulses. This can be mitigated by defocusing the laser,[94] though this leads to wider channel dimensions. Another issue is that the laser ablation process involves a very localised point of high energy which can induce chemical modifications to the ablated edges, leading to surface control issues.[18] There is also the issue of redeposition of ablated material which leads to further surface

issues.[107] Practically, there are some logistical non-idealities that must be taken into account. Most notably, it is difficult to precisely control the dimensions of ablated microchannels. The depth of the channel is a function of the material being ablated, the laser dose (laser power and pulse time) as well as the focus of the laser at the material surface. Thus the channel depth is very specific to a given situation, meaning protocols from the literature cannot simply be imported and necessitating calibration and routine recalibration of the cutting parameters to get a given geometry. Channel width is a function of the laser spot size, which is related to the laser focus. Thus for a given focus, the user has very minimal control over the channel width which limits the design complexity. Finally, laser ablation is typically a 2D or 2.5D tool.[107] This means that features are cut to a given depth, and 3D surfacing is not generally feasible (for example, smooth ramps in channel depth). For most microfluidic applications this is not an issue, but it is still a constraint that injection moulding and micromilling do not impose. Laser ablation was previously the primary method of fabrication[96] and is used in the next generation of chips described below in Section 2.4.

The majority of the fabrication development in this work has focused on micromilling, which is a mechanical process where micrometer sized cutting tools are used to directly cut-out and pattern the fluidics. There are many examples of micromilling of polymers in the literature with a variety of equipment ranging from simple routers designed for circuit board manufacture[102,108,109] to specialised machining equipment[24,110] with channels ranging from 120 μm[108] to 650 μm.[109] Micromilling was the subject of a recent tutorial review in Lab on Chip by Guckenberger et al..[24] However, similar to the other literature works, the review lacks key details that prevent it from being used as a template for future development. Micromilling is quite sensitive tot he specific material, tools, equipment and parameters used. This not only makes comparisons with other works difficult (due to the scant details provided), it also requires that the user develop in-house laboratory processes from the ground up. The approach taken here was to iterate upon the micromilled channels, reducing dimensions and improving throughput and surface finish as fabrication techniques were refined. In contrast to laser ablation, micromilling removes a defined amount of material from the piece, making final channel dimensions much more deterministic and intuitive. A large variety of cutting tools are widely available ranging in the 100 μm range through to 10's of cm. This allows for a much wider variety of geometries as compared to laser ablation. It is possible to create complex 3D geometries with micromilling, and 4- and 5-axis machines can be used to form arbitrary complexity devices. Finally, micromilling can used on essentially any base material including metals, and thus is a generally more versatile fabrication method. However, there are a number of significant disadvantages to the use of micromilling fluidics. The most significant problem is the substantially higher complexity and learning curve of micromilling vs other rapid prototyping techniques. While laser ablation has only five key parameters (laser power, laser dwell time, laser pulse separation, laser focus, number of laser passes), micromilling has substantially more such as endmill diameter, number of endmill flutes, endmill material, tool deflection, tool speed (how fast the tool rotates), tool feed (how fast the tool moves through the material), tool plunge feed, tool depth per pass (how deep each pass of the tool is), tool pathing style, coolant, and the number of passes,[24] each of which can significantly impact the throughput and quality of the resulting piece. Further, while laser ablation systems have typically simplified software where designs can be merely "printed" directly to the device, milling typically requires the use of specialised software to program machine movements, adding a substantial expense and layer of complexity to the workflow. Another key disadvantage to milling is that the processes do not scale well to small dimensions; as the endmill diameter shrinks the tool becomes much more difficult to handle and easy to break.[107] This also necessitates substantially slower fabrication times.[18] Thus, in comparison to laser ablation, for microscale features micromilling is substantially slower. Micromilled fluidics have been the base for all of the applications demonstrated to date and are described below in Section 2.2.

2.2 Micromilled Fluidic Channel Development

Development of computer numeric control (CNC) micromilled fluidics in PMMA was one the core components of this project, enabling rapid-prototyping of fluidic designs without the surface modifications introduced through laser ablation previously used by this research group. As mentioned above, due to the general lack of available information the process flow for micromilled fluidics generally needs to be developed from the base up. The approach to milled channel development was highly iterative, beginning with comparatively large channels and progressively miniaturising as the milling techniques were developed and improved. These are presented here as a series of chip "generations" that were used and applied in various applications throughout the lab. Through improvements to the process flow and equipment smaller, smoother and higher throughput milled channels were developed. The minimum milled channel width is 127 μm wide. This represents a soft-limit on the minimum channel dimensions achievable in-lab with CNC milling due to the substantial cost increase in shrinking tool diameter and the machine limit milling parameters for this diameter (specifically, tool rotations per minute) . Due to a general lack of reported metrics in other works it is difficult to assess the position of these designs in the overall literature, though available information suggests that the most recent milled channels are at the state of the art. This suggests any improvements should involve other fabrication equipment.

The approach to milled channel development was highly iterative, beginning with comparatively large channels and progressively miniaturising as the milling techniques were developed and improved. One big change introduced towards the end of this project was an upgrade in the CNC milling machine. Initial work was done on the Microproto Systems MicroMill DSLS 3000, an economical hobby-level machine with limited power and rigidity. Furthermore, it lacked a coolant system, forcing all machining to be "dry". While an excellent starting point, this limited a number of the fabrication parameters and the quality of the microfluidics. The lab upgraded in 2015 to a Tormach PCNC 770, a machine targeted to low-throughput production and prototyping. This machine has much higher rigidity and horsepower (leading to improved cut accuracy) and flood cooling, which uses a pump and hose to spray synthetic coolant onto the workpiece during milling to wash away chips and debris while keeping the workpiece cool. The effect of these improved capabilities on the microfluidics is discussed below.

This section first provides an overview of the micromilling process before delving into the various chip "generations" that were used and applied in various applications throughout the lab. For each generation the motivation and potential for future improvements are assessed based on microscope images of the channel bottom and profile. Finally, the milling parameters are summarised and compared. All microscope images are obtained at either 4x, 10x or 40x using a microscope with digital camera (ZM-4TW3-FOR-9M, Amscope) in the lab. As discussed previously, the minimum dimension accessible for micromilling is 127 μm wide, above the target for this work. Therefore, while an important series of development milestones, reaching 100 μm channels required different processing techniques.

2.2.1 General Microfluidic Fabrication Procedure

The micromilled fluidic fabrication process begins with the computer aided design (CAD), which specifies the fluidic design to be made. A tool in the open-source 2D vector design software Asymptote[111] for producing microfluidics is available in the SI. Next, the design must be imported into a computer aided machining (CAM) software. This

software translates CAD file into machine operations for the CNC mill and involves the specification of all the machine movements. Sample CAM files for a variety of microfluidic chips are also available in the SI as well as a picture guide to the use of the CAM software SprutCAM v9 with Asymptote-based CAD files. After CAM, the design is ready to be fabricated. The general fabrication process has seen many adjustments in terms of milling parameters over the various chip generations, though it has consistently been split into six key stages: setup, through-cut patterning, flattening, channel milling, chip cut-out and thermal annealing. These steps are elaborated upon below, while a protocol is available in Appendix B.

Setting-up the CNC mill involves mill maintenance, work-holding and alignment. A maintenance guide is available in the SI. Work-holding is the method used to affix the material to be machined to the CNC mill table. This is difficult for microfluidics as the PMMA used cannot be conventionally clamped due to its thin and brittle nature. In this work, the PMMA was attached with thin, strong double-sided tape (410m, 3M) to a thicker sacrificial layer (which was then conventionally clamped to the CNC mill). After work-holding the CNC mill must be aligned to the workpiece. Typically, the top left corner is deemed the x=0, y=0, and the surface of the chip is z=0.

After setting up the mill according to best practices, and securing the chip with some workholding arrangement, the first step to chip fabrication is to pattern any through-cuts such as alignment pins or wells, typically with a drill. Next, the surface is flattened with a wide-tool to provide a surface that is flat and perfectly orthogonal to the CNC mill. In general, the wider the tool the smoother the finish[112] and the faster the throughput. After flattening, the channels are milled. Patterning in this order has a number of advantages. Firstly, during milling there is a tendency for the top edges to become rough from the tool cutting action with what are called burrs. Flattening after through-cuts ensures the burrs do not protrude upwards out of the chip, which would interfere with bonding. Flattening before channel milling is also important. The limiting factor in micromilling is the deflection of the cutting tool, which is a strong function of the depth of the cut, and it is therefore important that this depth be very finely controlled. Flattening the workpiece ensures that the surface of the PMMA chip is flat and orthogonal to the cutting tool, thus controlling the cut depth for surface variation or alignment error in the workpiece or support material. Finally, by patterning through-cuts before channels it is possible to start the channel milling from within a well, thus ensuring the micromill experiences forces in only x-y as opposed to if the endmill had to cut the surface of the plastic where it would experience forces in all three directions. This reduces tool wear and risk of tool breakage.

The final step to the chip fabrication is to cut-out the resulting chips. This can be done on the mill itself or, due to the compatibility of the 2D CAD path with the CO_2 laser, the chip can be cut-out on the laser. The advantage to the former is a more precise alignment between the channel and the chip edge, which leads to improved alignment with the optical detection module. On the other hand, cutting out the chip with the laser results in an outer edge that is much smoother. This allows the user to couple more light into the chip from the side, leading to improved detection parameters. Both methods have been used, though there is some preference towards using the mill for cut-out as optical alignment is crucial for good detection.

2.2.2 Generation 1 Milled Chips

The first generation of micromilled channels were a proof-of-concept to determine the viability of milling as a microfluidic fabrication technique. These channels were made on the MicroMill and were quite rough, both on the surface due to a poorly optimised flattening procedure as well as within the channels, and had wide 381 μm (0.015") channels. This relatively large diameter was chosen as a starting point as this is the width of the smallest available endmill produced by Sowa Tool, the primary tool supplier for the University of Waterloo machine shop and as such was readily sourced. Figure 2.2a is a microscope image of the channel bottom at a magnification of x40. Very pronounced circular patterns can be seen in this image. These are milling marks, implying that the z-axis was not perfectly orthogonal to the x-y table. This causes the endmill edge to be offset such that it preferentially cuts along one side, leading to more pronounced milling marks and poorer surface finish. Note that even though the flattening ensured the top of the workpiece is orthogonal to the cutting tool, this does not ensure the x-y-z axes are perfectly orthogonal. This is a particular problem with the MicroMill which has a removable z-axis. Despite the pronounced visual effect of the milling marks, they are, however, relatively minor in size compared to the channel dimensions and the channel roughness was considered adequate for early applications with agarose gels. Figure 2.2b shows the profile of a channel intersection after snapping the chip along the channel at a magnification of x4. The channel is quite large, and its aspect ratio is not quite as expected. The design parameters were 381 μm wide (as set by the endmill) and 381 μm deep. However, the channel depth here is notably larger than the width and estimated to be about 480 μm based on this image, a difference of 100 μm. This is well beyond the tolerances that should be possible using this equipment, indicating that an improvement in milling practices could be made. Also interesting is that there are very clear lines along the channel, indicating the depth of each mill pass. This is not an expected result, and has not generally been observed milling. There was no proposed hypothesis for this observation, however like the milling marks on the channel bottom it was not considered problematic for early agarose CE work.

There were many sources of improvement on the initial generation 1 chips. First and foremost, 381 μm wide x 381 μm deep channels are very large for CE applications and really constrained the currents and fields we could perform separations at. Thus, there was a pressing need to miniaturise the channels. The large channels were exacerbated by a poor control of channel depth as seen in Figure 2.2b. This suggested that procedure improvements were necessary to better control the z-axis. Finally, surface finish could be improved. Specifically, using a wider endmill for the flattening stage to improve throughput and reduce surface roughness was a good idea, as well as ensuring the mill was well trammed prior to fabrication. The generation 1 channels were used in the first application demonstration detailed in Section 5.2 and published.[48]

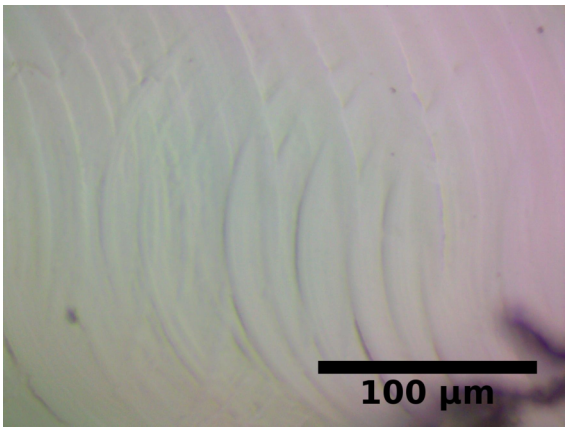

(a) Microscope image of the generation 1 channel bottom obtained at x40. The channel is 381 μm wide and 381 μm deep and cut with a high quality endmill from Sowa Tool. The concentric marks visible are from the cutting tool. These marks are very pronounced, indicating that the CNC mill was not trammed well. Thus, lower channel roughness can be achieved through improved fabrication procedures

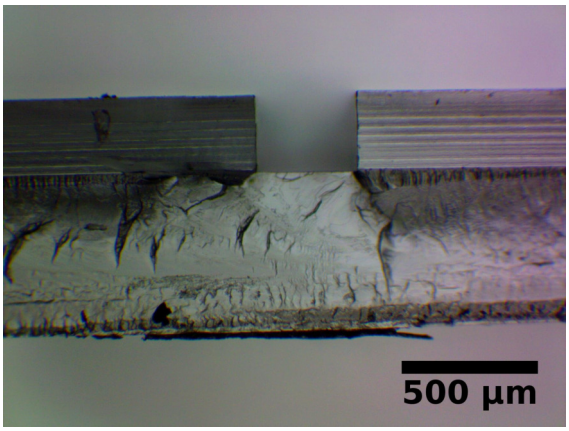

(b) Microscope image of the generation 1 channel and intersection profile, obtained by snapping a chip along its channel and taking the image at x4. The channel depth was notably deeper than expected (estimated at 480 μm instead of 381 μm), due to poorer control of the milling procedure at this early stage. The layered features on the channel wall were not expected, though were not considered problematic due to being relatively minor features.

Figure 2.2: Images of the generation 1 milled fluidics

2.2.3 Generation 2 Milled Chips

The objective of the second generation of milled fluidics was to reduce the channel dimension from 381 μm to 254 μm (0.010"). The channels were also made using the MicroMill and employed a new source of tooling. 254 μm is a common diameter used for routing mills for patterning printed circuit boards (PCB), and is widely available at very low cost (10 mills for about $14 CAD). This allowed for a lot of trial and error as the individual bits were over 10x less expensive than the 381 μm tool previously used and therefore expendable. Figure 2.3a shows a microscope image of the channel top at a zoom of x40. Unlike the generation 1 chips (Figure 2.2a), there are no discernible milling marks. However, the channel bottom was decidedly not smoother despite the lack of marks and was in fact very rough such that the x40 microscope lens depth of field was not able to resolve the whole channel bottom (hence the differing magnifications of Figures 2.3a and 2.2a). This implies a surface roughness between 1 μm and 6 μm,[113] which is very substantial and much larger than the previous generation 1 fluidics. Figure 2.3b shows the profile of a channel intersection obtained at a zoom of x4 of a chip snapped along its channel. Looking at the intersection, it is clear that the centre of the channel is cut slightly deeper than the edges, and that the channel profile is not flat. Further, the surface finish of the channel walls is also very poor and rough. The hypothesis for this roughness is that the cheap PCB endmills were not as sharp as the more expensive tool previously used. This changes the material removal mechanism from clean cuts to a more "rubbing" or abrasive mechanism and leads to poorer surface finish. This effect was further exacerbated by the extremely slow feed (rate of tool movement) used. The PCB endmill had a very long flute which caused very high tool deflection at the feeds previously designed for. Slowing down the feed substantially reduces the chip volume and introduces more friction.[114] Other potential issues arising from the tool include a non-flat mill bottom (leading to non-flat channel bottoms as seen in Figure 2.3b) and poorly patterned flutes that do not evacuate cut material well leading to more friction and surface roughness. This roughness would likely result in increased light

scattering and therefore have negative ramifications for the optical detection.

Despite the issues, there were some key improvements with this fluidic chip generation. Firstly, the aspect ratio of the channel is almost exactly 1:1 within the limits of the optical inspection. This demonstrates the improved milling techniques developed between the first and second generation of chip, specifically more attention to z-axis alignment, mill and workholding alignment. Another improvement over the previous generation was the reduction from 381 μm to 254 μm allowed for a substantial improvement in the CE protocols, enabling the use of CE fields that were previously inaccessible due to the low resistance of the large channels. Practically, reliable operation of agarose CE with these chips was achieved, suggesting that the surface roughness observed here was not a primary issue. The generation 2 channels were applied in an application detailed in Section 5.3 and published,[115] as well as were the general "workhouse" microfluidic chip for CE separations by the Glerum molecular biology lab from 2014 to 2015.

There were some notable issues with the second generation chips that required attention for subsequent development. The most important aspect was the very rough channel walls. While it was possible to achieve stable CE performance with these channels, the high roughness precludes the development of any potentially surface sensitive experiment. Further, while the agarose protocols being used did not exhibit any chip to chip variation, this roughness could cause issues with longer separation length/higher resolution applications. Finally, the rough channel walls scatter light, reducing the efficiency of the optical detection. To improve the channel roughness, a change in cutting tool was required, as the primary hypotheses for the roughness were all based on using a poor cutting tool. Another issue with the PCB endmill was that its flute length was far too long for the application, with only a very small portion of its length being used for patterning channels. This unused tool length made the endmill very prone to breakage and required very slow feeds and very shallow depths per pass, leading to poor cutting performance and low throughput. Thus, substantial improvements could be made by purchasing a higher quality, sharper tool with a flute length optimised for sub-mm cuts.

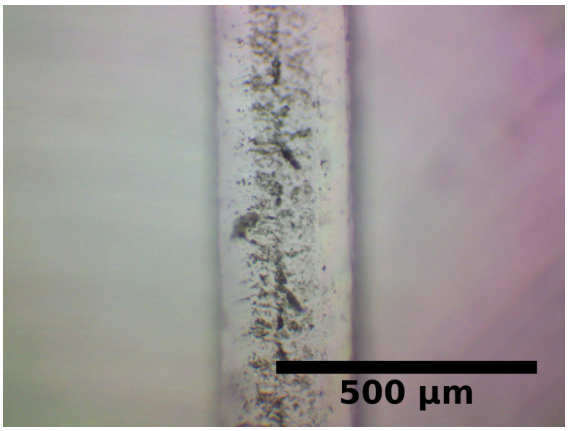

(a) Microscope image of the generation 2 channel bottom obtained at x10. The channel is 254 μm wide and 254 μm deep, cut with an inexpensive PCB endmill. The channel bottom does not have visible milling marks as in Figure 2.2a above, however instead it has a rough, random pattern with a substantial surface hight. The roughness exceeded the depth of field of the x40 lens, implying a roughness between 1 and 6 μm.[113] This is very high, and an issue that required improvement.

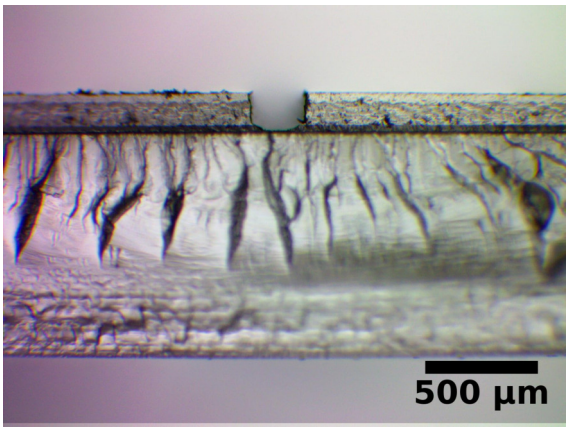

(b) Microscope image of the generation 2 channel and intersection profile, obtained by snapping a chip along its channel and taking the image at x4. As an improvement on the generation 1 chips, the aspect ratio of the width to depth is 1:1 implying improved control of channel depth due to refined milling technique. However, the channel walls are also very textured and rough which might preclude further development of this technology.

Figure 2.3: Images of the generation 2 milled fluidics

Generation 2.5 Milled Chips

The objective of the generation 2.5 milled fluidics was to use a new cutting tool to improve the surface finish and throughput of the 254 μm wide channels. These 254 μm channels with an agarose sieving matrix had become a standard fluidic technology within the Backhouse and Glerum laboratories. However, as detailed above, the previous cutting tool was leading to poor surface finish and throughput. Thus, a new cutting tool was selected (1610-0100.030, Kyocera Precision Tools). This tool was not only sharper, leading to smoother channels, but also had a flute length of only 760 μm which reduced the tool deflection substantially. This enabled higher feed rates and higher depths per pass, and substantially improved throughput. Figure 2.4a shows a microscope image of the top of the generation 2.5 channel at a magnification of 40x. In comparison to the generation 2 that used the PCB endmill, these channels are much smoother and the roughness can be fully resolved with the higher magnification. This implies a roughness below 1 μm. Faint milling marks can be seen (concentric rings), however these are notably less pronounced that in Figure 2.2a above. This is attributed to improved mill tram, as well as benefiting from the use of a sharp endmill. The channel side is shown in Figure 2.4b. The channel aspect ratio is as expected as the improvements in technique for controlling channel depth from the generation 2 channels were carried forwards. One interesting note is that some vertical texture is seen on the channel walls. This wall roughness is substantially less than previous chips, however, which suggests it will not have a notable effect going forwards. The wall roughness appears notably higher than the channel bottom roughness, though without physical measurements this cannot be readily assessed.

Improvements upon the generation 2.5 milled chips should focus on further miniaturisation of the channel. While 254 μm is quite narrow, it is still too large for general purpose CE applications. Further, the channel roughness could be

further improved, though the reliable performance of the very rough generation 2 channels suggests that the surface finish is more than sufficient for agarose CE applications. The generation 2.5 milled chips were used in the most recent application demonstration detailed in Section 5.4 and published. [89]

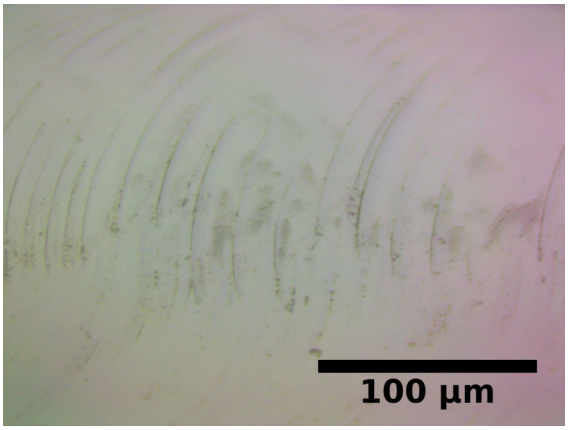

(a) Microscope image of the generation 2.5 channel bottom obtained at x40. The channel is 254 μm wide, and 254 μm deep and cut with a high quality endmill from Kyocera tool. In comparison to the generation 2 channels cut with a PCB endmill (Figure 2.3), these channels are substantially smoother. Faint concentric rings can be seen. These are marks from the milling procedure and estimated at sub 1 μm in height. They are substantially less pronounced than the generation 1 fluidics in Figure 2.2a indicating improved mill tram and fabrication procedures.

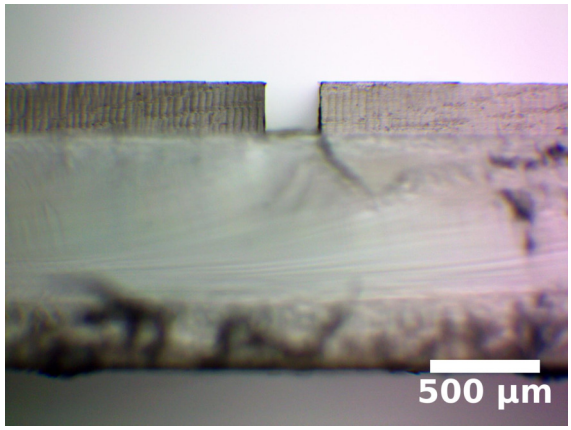

(b) Microscope image of the generation 2.5 channel and intersection profile, obtained by snapping a chip along its channel and taking the image at x4. The channel walls are much smoother than the previous generation 2 chips. A faint vertical texture can be seen, which suggests a wall roughness higher thant he channel bottom roughness.

Figure 2.4: Images of the generation 2.5 milled fluidics

2.2.4 Generation 3 Milled Chips

The objective of the generation 3 milled fluidics was to take advantage of newly available equipment to further improve surface finish and reduce channel dimensions to 127 μm. In 2015 the laboratory upgraded the CNC milling machine to the Tormach PCNC770. The biggest advantage to this upgrade was the introduction of flood coolant, which enables a number of process improvements. Firstly, flood coolant does a much better job removing milled material from the cut, extending tool lifetime and improving surface finish. Furthermore, previous chips had issues with the endmill imparting too much heat to the material, causing melting of the PMMA. Avoiding this melting required the use of non-optimal feeds and speeds. However, with the introduction of coolant, heat generation is no longer an issue and optimal feeds can now be used for improved surface finish. The effects of the milling machine change were assessed by manufacturing the generation 2.5 microfluidic chips but with the updated machine. Figure 2.5a is a microscope image at x40 zoom of a channel cut with the same endmill as Figure 2.4a, except with a lower feed rate (50.8 mm/min) and flood coolant. Comparing the two chips, the visibility of the milling marks in Figure 2.5a are much less pronounced. This shows a notable improvement in surface finish. Figure 2.5b shows a microscope image obtained at x4 of the channel wall after snapping the chip along the channel. This shows a very comparable wall roughness as Figure 2.4b. Thus, the change of CNC mill marginally improved channel quality by reducing channel bottom roughness, while having a minimal effect on channel walls. Therefore, especially since the MicroMill has been put into storage,

future users are recommended to use the Tormach CNC and can expect to replicate and improve upon previous chip generations.

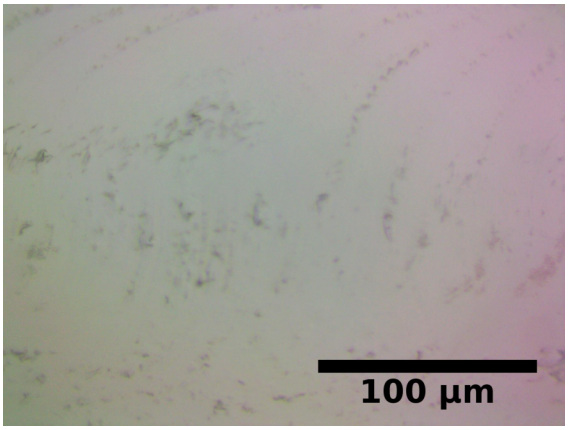

(a) Microscope image of a channel identical to the generation 2.5 channels (254 μm wide) but using the Tormach mill with flood coolant, obtained at x40. In comparison to the channel cut on the MicroMill (Figure 2.4a), this channel has even lower surface roughness and only barely discernible milling marks. This demonstrates the improvement of the new milling machine.

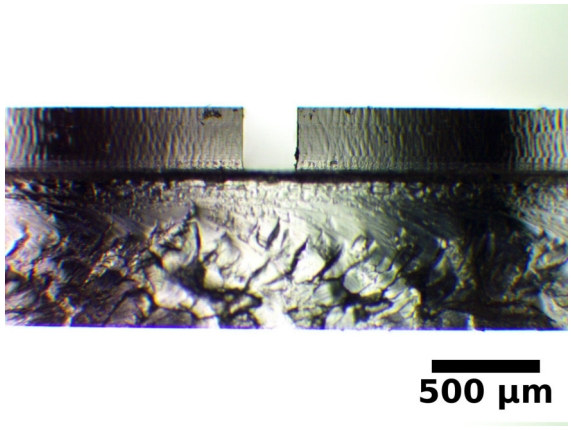

(b) Microscope image of the generation 2.5 channel side but using the Tormach mill with flood coolant, obtained at x4. The channel wall finish is highly comparable to Figure 2.4b

Figure 2.5: Images of the generation 2.5 milled fluidics

The milling machine upgrade coincided with the sourcing of even smaller milling tools, specifically a 127 μm diameter two flute carbide endmill (1610-0050.015, Kyocera Precision Tools). Figure 2.6 is a microscope image of the 127 μm wide channel at a zoom of x40. In this image, the channel roughness is almost impossible to see. This generation of fluidics therefore has the highest surface finish and lowest roughness of any produced to date. However, the throughput of the milled fluidics is very low due to a low work feed of 28.7 mm/min. For a CE separation chip, this is not necessarily an issue as there are only two channels, though scaling to more complex geometries such as PCR-CE could be problematic. As of writing, the generation 3 milled chips have not been demonstrated in an application.

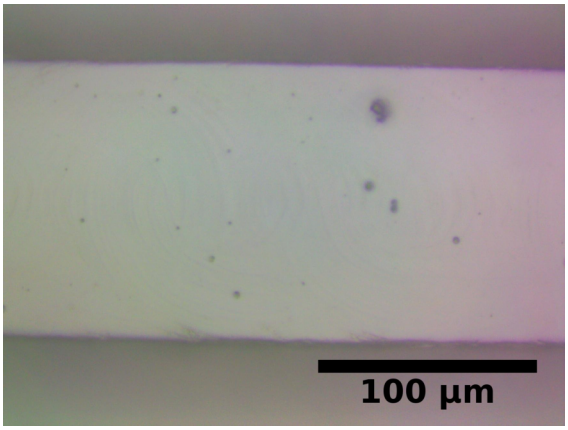

Figure 2.6: Microscope image of the generation 3 channel bottom obtained at x40. The channel is narrower at 127 μm wide, with a very good surface finish. This represents the best results obtained to date on the CNC mill.

2.2.5 Milled Channel Summary

Table 2.1 summarises the various generations of milled chip. As summarised above, each subsequent generation introduced throughput, surface finish and/or procedural improvements while reducing channel dimensions.

Parameter	Gen. 1	Gen. 2	Gen. 2.5	Gen. 3
Channel width (μm)	381	254	254	127
Channel depth (μm)	381	254	254	127
Channel Roughness	Good	Poor	Good	Excellent
Channel endmill manufacturer	Sowa Tool	PCB router	Kyocera	Kyocera
Mill used	MicroMill	MicroMill	MicroMill	Tormach
Speed (RPM)	10500	10500	10500	10000
Work Feed (mm/min)	177.8	50.8	127	28.7
Depth per pass (μm)	25.4	12.7	25.4	25.4
Applications	Hall et al.,[48] Section 5.2	Hall et al.,[115] Section 5.3	Hall et al.,[89] Section 5.4	None

Table 2.1: Table of parameters used for milling microfluidics. Successive generations reduced the channel dimensions, improved throughput and surface finish.

The generation 3 milled channel is a soft-limit for what can be produced in the lab with the tools available for two reasons. Firstly, 127 μm is the smallest diameter endmill that could be readily sourced at moderate cost ($CAD 15 per tool) with smaller diameters being either unavailable or 3^{+}x more expensive. Smaller tools would also have have higher deflections requiring higher RPMs to maintain low runout and lower depths per pass. However, the RPM was at the Tormach PCNC 770 maximum. Thus, a smaller endmill is likely to experience higher tool deflection and be prone to breakage. Further, the work-feed and depth per pass for the generation 3 milled fluidics was very low at 28.7 mm/min and 25.4 μm respectively. These would have to be reduced for smaller endmills. Thus, even if the smaller endmill could survive the RPM limitation, the throughput would be further reduced. This reduction is not linear[114] and has a few implications. Firstly, the longer the machine requires to fabricate the part, the more thermal expansion can interfere with the design tolerance. Further, long run times lead to increased tool-wear, increasing running costs and decreasing channel quality as seen in the generation 2 channels which used poor endmills. Finally, while lower throughput is an issue with the CE microfluidics used in Chapter 5, it would be a bigger issue for more complicated fluidics. Therefore, it is recommended that for smaller than 127 μm features an alternative fabrication technique be adopted such as laser ablation. This is discussed in more detail in Section 2.4 below.

It is difficult to compare the milled microfluidics with the state of the art due to a general lack of reported details. The 127 μm channel feature is the minimum size reported in the review by Guckenberger et al.[24] and in the application by Chen et al.[108] and smaller than works by Ogilvie et al.[102] (160 μm), Chen et al.[110] (250 μm) and Rahmanian and DeVoe[109] (650 μm). Thus, from a purely geometric perspective, these channels are typical of the state of the art in academia. Channel roughness is difficult to assess as good microscope images for the majority of these works are not available. Many works in academia use small-format machines targeted at PCB production such as the popular LPKF Protomat[102] or hobby-oriented machines such as the Roland MDX-650A[108,109] which do not have flood cooling and

have lower machine rigidity for poorer alignment. Thus, compared to these works one would expect the channels described here to have improved surface finish. Two notable exceptions include Chen et al.[110] who use an industrial level machine from Haas automation and Guckenberger et al.[24] who use the same Tormach machine used here. Guckenberger et al.[24] cites sub-0.42 μm surface roughness for PMMA channels. A comparison of images taken of the channels between those in Guckenberger et al.[24] and Figure 2.6 suggests that the roughness of the channels discussed in this thesis are comparable or better than this value they reported. In general, lack of reporting of methods of alignment, work-holding, tool-choice, coolant method and milling parameters in this field make comparison between works difficult to impossible. However, overall these micro-milled channels should be considered at or near the state of the art in this field.

The most important conclusion of the micro-milled fluidics is that a method has been developed for reliable fabrication of fluidic channels in a variety of dimensions. This allowed for rapid fabrication of microfluidics that were applied both to the instruments described in this thesis as well as a series of experiments in the Glerum molecular biology lab at the University of Waterloo. Thus, this was a key enabling technology for testing the microfluidic instrumentation in Chapter 5. However, overall the micro-milled processes were not able to miniaturise down to the target 100 μm dimension. This prompted increased attention to laser-ablation which is discussed briefly in Section 2.4 below.

2.3 Microfluidic Bonding

In addition to the method of patterning the microfluidic channels, there needs to be a method for capping the layers patterned with channels to make enclosed structures. The objective of this project was to develop rapid-prototyping methods for polymer fluidics that are readily implemented without high-cost equipment with short turnaround times. Bonding techniques broadly speaking follow a few standard strategies that includes the use of adhesives, thermal bonding, localised welding and surface treatment/modification.[116] Adhesive bonding is one of the simplest approaches where the capping layer and substrate are attached with a glue or tape. This is the fastest capping method and requires no external equipment, however, care must be taken to ensure that the adhesive does not affect the properties of the microchannel or plug the fluidic systems. Thermal bonding uses heat to fuse the cap and substrate together. This method also uses no outside reagents and thus has a reduced risk of contamination or channel plugging. The primary challenge with thermal bonding is that it is difficult to optimise the pressure-heat used such that the bond is strong and the channel does not warp. Further, thermal bonds are typically weak, which might limit downstream processing of the chip.[117] Localised welding involves using ultrasonic, microwave or laser power to apply energy to the interface between two layers in a very specific spot. However, it requires very specific chip designs to ensure that the energy is properly directed to the interface and thus a protocol cannot be developed for an arbitrary chip design. This makes it unsuitable for rapid-prototyping methods and thus localised welding was not pursued for this project. Surface treatment is a very common method used in the literature that is often used in conjunction with pressure or heat. These activate the microfluidic chip surfaces to assist the formation of a bond. The advantage of these approaches is the bonds can be made at typically lower temperatures and the resulting bond strength is typically higher. Plasma treatment is commonly used[102] to clean and activate a PMMA surface for improved bonding strength. However, in comparison to thermal only bonds, this requires specialised equipment that was unavailable fort his project. Another common surface treatment is to use a solvent to weaken surface bonds and increase bonding strength. This approach

was pursued as discussed below to enable higher bond strengths for the development of next-generation chips.

Three main approaches to bonding were developed in the Backhouse lab: capping the fluidics with a strong tape (Section 2.3.1), a thermal PMMA-PMMA bond (Section 2.3.2) and a solvent vapour assisted bond (Section 2.3.3). Each of these technologies has advantages and disadvantages that are described below. There are a few key assessment criteria for a bonding technology. First and foremost is reproducibility, as this is central to any LOC technology that hopes to succeed. Next, the composition of the bond must be considered. Many biological processes are very surface sensitive including PCR (surface contaminants can substantially decrease reaction efficiency) and electrophoresis (surface effects affect the zeta potential, and thus the rate of fluid flow). In an ideal world, the surfaces are PCR compatible, homogeneous and reproducible. The throughput of the bonding process is considered, as the process should be compatible with the rapid prototyping ideology that permeates the rest of this work. Finally, the bond strength of the procedure must be sufficient such that chips made can be fabricated and operated reliably up to 100 ^{o}C (PCR temperature). The following sections discuss these three bonding methods, including the new solvent vapour assisted method that the next generation microfluidics described in Section 2.4 are based on.

2.3.1 Tape bonded chips

Initial bonding designs made use of a simple PCR tape (AB1170) to cap the channels. There were many advantages to this approach. First and foremost, the method was very quick and easy leading to very high throughput. The tape can be applied directly to milled chips immediately after fabrication, which compares very favourably to the previously used thermal bond which required upwards of six hours of processing.[96] Further, the tape could be easily removed and replaced, which simplified channel cleaning after use. In terms of material compatibility, since the tape is designed for PCR and q-PCR applications, we know it is surface compatible with our target biological processes and functions up to 100 ^{o}C. Finally, the tape has excellent optical clarity and has a well specified thickness of 100 μm which not only conforms to the alignment constraints of the optics but is also a convenient thickness for thermal systems. All of the applications detailed in Chapter 5, both electrophoretic and PCR, used this bonding method.[48,89,115]

There were a number of disadvantages to the tape bonded approach. Firstly, while the thickness of the tape is 100 μm, this thickness is distributed between the adhesive and the polypropylene backing with the former composing a substantial amount of the thickness. This is a problem with fluidic channels as there is a tendency for the adhesive to be pushed into the channel, causing variability of the channel dimensions. This was not considered a substantial issue with the relatively deep generation 1-3 channels (381 μm and 254 μm deep) used to date, but proved to be very problematic when shrinking to 127 μm depths. Variation in the observed pressure required to flow fluid through these thinner channels suggests that the tape is not a good strategy for more miniaturised fluidics. The use of tape also introduces a heterogeneous channel composition where three walls are PMMA and the last is adhesive/polypropylene. This means that the zeta potential of the channel surface is not the same on all four walls, which can lead to interesting and unpredictable electrophoretic behaviour. To date, all of the demonstrations have used agarose as the sieving matrix, which has the advantage in that it is relatively insensitive to pressure driven flows and surface effects due to its viscous nature and heavily interlinked pore structure. This alleviated concerns not only of the fairly large channels but also the inhomogeneous nature of the channels. However, as described in Section 5.4, we have approached the resolution limit for the agarose gels we use and this limit is still short of the desired resolution targets set by Ugaz et al..[59] In order

to overcome this barrier, a smaller channel with homogeneous composition is required, and tape simply precludes that development. Overall, the tape method was a good strategy for early designs due to the rapid processing and ability to readily re-use microfluidics. However, future designs will require an adhesive-free approach with homogeneous channel composition.

2.3.2 Thermal PMMA-PMMA bonded chips

A second method of microfluidic bonding was developed by Tianchi Ma and described in his thesis.[118] This method uses only heat and pressure to form PMMA-PMMA bonds that are fluid-tight and consistent. Thus, in contrast to the tape, this method forms homogeneous channels. Further, in comparison to previous methods,[96] by avoiding the need for an ethanol soak the amount of processing time has been cut from about six hours to roughly three. However, one issue is that this method bonds a 1.5 mm thick piece of PMMA to cap the channels, and this is far too thick to be used with the optical designs in Chapter 3. Thus, there is a need to reduce the thickness of the PMMA cap. One approach is to use a thinner piece of PMMA. However, the thinnest that was sourced at the time was 200 μm thick, still too thick to meet the fabrication requirements. Beyond the issue of sourcing, it is also unclear that directly bonding 100 μm PMMA is possible in-lab due to practical processing issues. These include the handling difficulties as well as the issue of how to apply and distribute appropriate pressure across thin layers. Finally, it is unknown if this PMMA would have equivalent surface properties to the PMMA currently used, which means that the effort towards developing new fabrication processes might not achieve the desired results. Thus, the thin PMMA was ruled out due to being a high risk development process.

An alternative approach was to bond the thick 1.5 mm PMMA to the chip, then use the CNC mill to shave this layer down to the desired thickness. However, it was found that while the thermal bonding forms interfaces that are robust against the pressures experienced in microfluidic applications, they could not resist the sheer force applied during milling. This resulted in nearly $^5/_6$ microfluidic chips delaminating during the thinning process. Therefore, the thermal bond force was deemed insufficient for this application, demonstrating the need for a more robust PMMA-PMMA bond to allow for the additional processing with the mill.

2.3.3 Solvent vapour assisted PMMA-PMMA bonding

To address the need for a robust PMMA-PMMA bond that could reliably withstand milling forces a method that used chloroform vapour to soften the PMMA before bonding with pressure was developed. Chloroform has a profound effect on the structural integrity of PMMA, and even exposure to just the vapour can cause substantial re-flowing of the PMMA surface. Thus, the key issues to overcome with this method all relate to controlling all of the bonding parameters. This method was based on the work by Ogilvie et al.,[117] though it differed in a number of regards due to equipment, processing and material changes. Briefly, this method uses custom milled blocks to apply the bonding pressure to replace the thermal press, operates at room temperature as compared to 65 ^{o}C and introduced minor changes to the timing to account for changes in the polymer used, chloroform used and bonding conditions (this is summarised in the protocol in Appendix C). With sufficient control, a very strong PMMA-PMMA bond was reproducibly achieved, stronger than the thermal only technique described above. While the strength of this bond

was not assessed directly, it was determined empirically that it was strong enough to resist the milling forces that were problematic for the thermal-only bond. This was a very important advance for the next generation microfluidics described in Section 2.4 below.

The first variable that required attention was the dose of chloroform introduced into the PMMA. Ogilvie et al.[117] controlled this by specifying the separation distance of the PMMA from liquid chloroform in a sealed environment, and controlling the time of the exposure. A similar approach was taken here, although to do so a Polytetrafluoroethylene (PTFE) bath and chip holding jig was developed. This jig is chemically resistant to the chloroform, and allows the user to easily control the vapour exposure; upon adding 10 mL of chloroform to the bath, the fluid level will be held 3 mm from the chip surface. The second variable to control was the bonding pressure. This was done with a special bonding jig. The jig contains two pockets, one on the lid and one on the base. The total pocket depth was 0.1800" deep, and accommodated the two PMMA pieces being bonded (0.06" each) and two thin layers of nitrile ($^1/_{32}$" each). The jig was then tightened with six screws until the lid and base were completely in contact, resulting in a compression of 0.0025" or a strain of 0.04. The nitrile used has a hardness of shore 40A, which gives it an estimated Young's modulus of 1.3 MPa. Thus, the bonding pressure can be controlled to 52 kPa, or 176 N across the 1.5" x 3.5" chip. The final issue was ensuring tight timing for the exposure, and for the time between exposure and bonding. Details can be found in Step 5 of the preliminary protocol detailed in Appendix C. Figure 2.7 shows the required components for this procedure. In the front right are two PTFE pieces. The top piece contains recesses for holding the PMMA chips, while the bottom is a bath for the chloroform. A lid is also used to cover the assembly during exposure. On the right is the aluminum bonding jig.

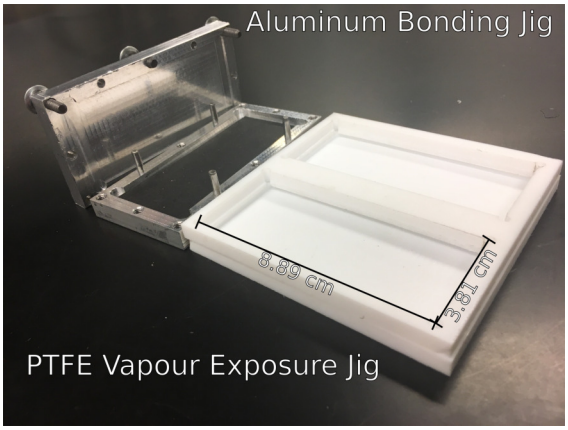

Figure 2.7: Components required for the solvent bonding of PMMA. In the front right are two PTFE pieces. The top piece contains recesses for holding the PMMA chips, while the bottom is a bath for the chloroform. A lid is also used to cover the assembly during exposure. On the left is the aluminum bonding jig for applying pressure to the bond by sandwiching the PMMA between two nitrile sheets and compressing the assembly with screws.

Using this procedure, a bond that can withstand milling forces is possible. This enabled the next-generation microfluidic chip described in Section 2.4 below.

2.4 Next generation laser processed chips

The next generation microfluidics combine laser ablation, CNC milling and solvent bonding for rapid prototyping of PMMA microfluidic channels compatible with the optics detailed in Chapter 3 and general purpose CE protocols. The requirements of the new design were fully homogeneous in composition, channel dimensions of approximately 100 μm x 100 μm and capping layer thickness of 100 μm or less. As described in Section 2.2, micromilling fluidics is a low-throughput method that cannot readily access 100 μm channel widths. Thus, the channel fabrication method was switched to laser ablation. This was used to create channels 75 μm deep and 180 μm wide. However, in comparison to micromilling, laser ablated channels are not square. Instead, they have a triangular appearance. Thus, while the maximum width was 180 μm the majority of the channel was much thinner with an overall volume of 0.81 nL. The next key advance was to utilise the solvent bonding technique in Section 2.3.3 to create a strong PMMA-PMMA capping layer bond. The capping layer was then thinned using the CNC mill to 85 μm. This in turn required the development of an in-house built vacuum table for workholding. The result is a microfluidic chip with 0.8 nL sample volume composed of homogeneous PMMA with a 85 μm thick capping layer accurate to 15 μm. These channels are suitable for a broad spectrum of conventional CE sieving matrices and fit perfectly with the optics designed in Chapter 3.

2.4.1 Design

The microfluidic chip designs for this protocol have two added design features. The first was a sacrificial border of 0.25" (6.35 mm) around the outside of the chip. During the milling step, delamination and chipping of the capping layer around the edges was observed in approximately one in six fabricated chips. This could interfere with fluidic functions near the chip edge. The sacrificial border ensures that the edge effects are kept away from any fluidic features, increasing the process yield. The sacrificial border increased the chip size to 1.5"x3.5", though after removal the final dimensions are 1" x 3", the same as a microscope slide. The second design feature is to add some through-holes to the capping layer in non-critical areas. These through-holes are to allow the user to access the fluidic layer with the CNC mill and enables the user to zero the mill on the patterned side. By aligning to the base layer, any variations in the thickness of the capping layer material is calibrated out resulting in a more reproducible capping layer thickness. Furthermore, this allowed for the development of a universal milling program that cuts the capping layer to the desired thickness assuming the capping layer material is less than 2 mm thick (substantially above the tolerance in thickness of the raw material). Without this alignment feature, the user would have to measure the capping layer material for each individual microfluidic chip and re-program the CNC mill to accommodate any changes. The universal milling program available in the SI.

2.4.2 Protocol Overview

A preliminary protocol can be found in Appendix C, though it is described briefly here.

1. Pattern the fluidic chips using a CO_2 laser (VLS 2.3 with 30 W laser tube). The parameters used were 1.4%

power, 5% speed, 1000 PPI and focused 3.5 mm above the PMMA surface. The resulting channels have a Gaussian profile and extremely low channel roughness. The defocussing in particular results in wide channels, but smooths out the laser pulses for flat channel bottoms. The channels are 180 μm wide at their widest point and 75 μm deep. This is seen in Figure 2.8a. These parameters were optimised by Rob Bennett

2. Thoroughly anneal the laser patterned chips in a forced air convection oven at 80 ^{o}C for a minimum of 2 hours. This annealing relaxes stresses induced by the laser patterning and is crucial to the procedure. Failure to anneal will result in the channels immediately crazing.

3. Bond the patterned PMMA to a capping PMMA layer using the solvent bonding protocol. This is done at room temperature and takes about 30 minutes.

4. Load the bonded PMMA chip into the CNC vacuum table. This holds the chip very flat and avoids the introduction of tape.

5. Zero the CNC mill to the height of the bottom PMMA layer. The CNC mill will then shave off from 1.6 mm to 0.1 mm of the chip in two steps. In the first step a large endmill is used for throughput reasons, while in the final step a very fine finish is done. This fine finish is crucial to ensure that the chip surface is clear and to reduce the force on the capping layer such that it does not delaminate

6. Clean up the microfluidic chip. The edges can now be trimmed either with the CNC mill or the CO_2 laser.

2.4.3 Preliminary Results

A large number of test chips were made by Rob Bennett to develop the laser parameters for the microfluidic channels presented here. One of the key issues with the use of laser ablation is the pulsed nature of the laser, and the effect of the pulses on the channel bottom. The maximum pulse density is 1000 PPI which results in a channel bottom that oscillates with this pulse density (pulses every 25.4 μm). These oscillations can be reduced through de-focusing the laser such that the pulses overlap substantially. This is potentially problematic for CE applications where the variations in channel dimensions would couple into a variation in analyte current with unknown and potentially unreliable effects. However this results in a wider channel. Ultimately, since the channel shape is Gaussian a channel width above 100 μm still results in miniaturised sample volumes compatible with general purpose CE, thus optimisation on very smooth channels was done. Figure 2.8a shows a laser patterned channel intersection before bonding, obtained using a microscope and a x4 objective. This channel exhibits no undulations along the bottom due to laser pulses. Figure 2.8b shows the same laser channel after completing the above fabrication procedure and snapping perpendicular to the channel, with a x40 objective. It is interesting to note that the channel profile has changed. Specifically, it has become slightly shallower and much narrower, which results in a higher aspect ratio. This is likely due to re-flow of PMMA during the chloroform vapour exposure. The cap thickness in this image is 85 μm, and the channel is measured to be 180 μm at its widest point and 76 μm deep. The channel dimensions are representative of the protocol, though the cap thickness varies by 15 μm from chip to chip. In a CE application, the sample volume defined by these channels would be 0.8 nL. Thus, this sample is comparable to the target 100 μm x 100 μm channels. Further, these dimensions are resistant to pressure driven flows due to their small size and aspect ratio and thus are compatible with general purpose

CE matrices.Finally, the sub-100 μm capping layer ensures compatibility of these fluidic chips with the short working distance optics discussed in Chapter 3.

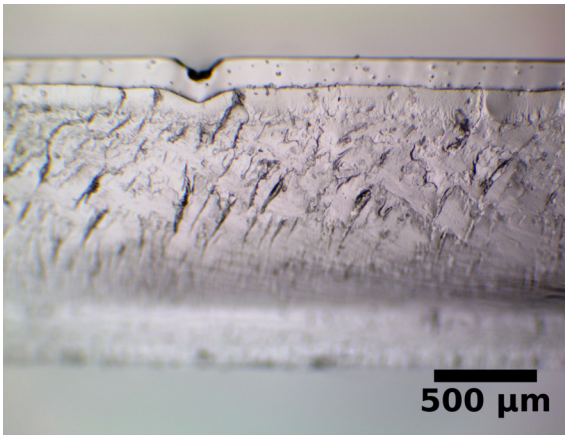

(a) Microscope image of the microchannel intersection patterned by laser ablation prior to any solvent exposure, obtained by snapping the microfluidic chip along a channel and using an x4 objective. The channel passes along the top of the PMMA pictured with a smooth channel bottom and no evidence of laser pulses. This demonstrates the effectiveness of a de-focused laser. The intersection of the snapped channel can be seen in the middle.

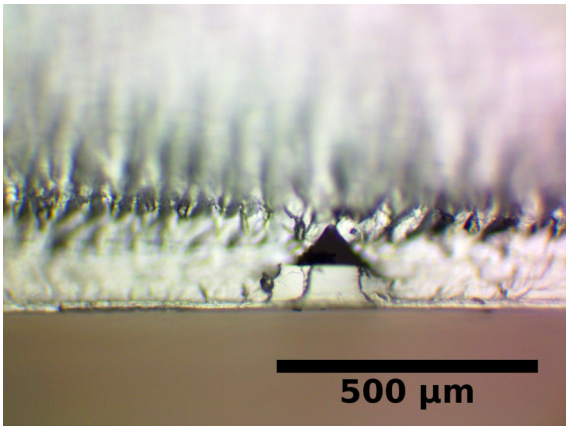

(b) Microscope image of the microchannel after solvent exposure, bonding and cap thinning at x40 magnification. Comparing to Figure 2.8a, the channel dimensions have shrunk slightly and the aspect shape of the channel has changed. This is likely due to re-flow of the PMMA from the chloroform vapour exposure. The channel dimensions are measured to be 180 μm at its widest point, 75 μm deep with a 85 μm thick cap. The estimated sample volume for a CE application is 0.8 nL

Figure 2.8: Images of the next generation laser processed microfluidics

Chapter 3

Optics Design

3.1 Introduction

LIF has been a mainstay of the biochemical field since the 1960's[119] and is particularly suited to DNA analysis due to its high sensitivity (typical implementations have pM LODs[41,43]) and high selectivity [54] due to well established labelling chemistry as described below in Section 3.1.2. As a result, LIF is the detection mechanism of choice for DNA analysis, from q-PCR[120] and CE[98] to next-generation sequencing (NGS),[121] nearly every commercial DNA diagnostic instrument[32–34,61,65] and all of the PCR-CE demonstrations summarised in the literature review in Section 1.2.3.[39–42,76,77,80] However, while high performance, typical implementations of fluorescence detection use expensive optics and electronics which prices them out of many applications.[45] Currently, the field requires users make a choice, either opt for a low-cost option with detection specifications that are non-standard and below the desired target or implement the tried and tested analysis protocols with high-cost instruments. This chapter has two objectives. First, it demonstrates a design methodology for low-cost LIF detection optics that enable established protocols without expensive components. Furthermore, this chapter will demonstrate how this design methodology can be readily scaled towards a miniaturised, monolithic LOC device where the fluidics and electronics are fabricated in a CMOS-compatible process. This scalability enables interim prototyping of the optical detection in a low-development cost environment, thus addressing the CMOS manufacturability roadblock. This is discussed in more detail in Section 3.1.3 below.

As detailed in the Introduction, the LOD must be 1 nM or better from a 1 nL sample to enable standard PCR-CE applications. The LOD is a function of both the optical design, which determines the amount of signal present, and the detection electronics, which determines the detector noise. This chapter discusses only the former and thus focuses primarily on the signal generated, while the latter is described in detail in Chapter 4. To decouple the analysis of these two aspects to a LIF module, the reference model in Section 1.3.1 was developed which specified a standard optical design with an estimated signal of 10 fW for the 1 nM, 1 nL sample and a reference detection electronic circuit with a minimum detectable power of 1 pW. These combined to form a LOD of 100 nM, nearly two orders of magnitude higher than required, thus motivating optimisation of both the optics and electronics to close this gap. This chapter

discusses how the various optical components to the system affect the fluorescent signal and presents an optimised design. Later, Chapter 5 combines the optics with detection electronics and microfluidic chips to form instruments to implement CE and provide measured results.

Another important assessment factor for LIF instrumentation is the spot-size, which refers to the volume that is being optically probed by the instrument. In this work, the spot-size is defined as the distance from the detector centre where the signal from an infinite sample drops to half of the maximum. Typically, this is limited by the size of the focused excitation light beam. However, as explored below, in this work the spot-size is instead limited by the collection efficiency of the emission signal. As stated in Section 1.2.2, for CE the requirement of the spot-size is that it be on the order of the same size as the sample to ensure the optics are not a limiting factor in the electrophoretic resolution. The spot-size and signal are also related in that for smaller probed volumes there are fewer fluorophores and therefore smaller signals. Thus, there is a need to optimise the spot-size to be as close to the sample size as possible (100 μm for standard CE applications) to maximise signal without impacting resolution. In this work, early iterations prioritised LOD over resolutions for the simple reason that in a design with inadequate LOD where the sample cannot be detected it is very difficult to assess other performance parameters. Therefore, the initial approach focused on LOD, leaving spot-size a secondary concern. As the designs were developed, increasing attention was paid to spot-size as discussed in Sections 3.6 and 3.8.

The final assessment factor to consider is the signal to baseline ratio (SBR). The SBR is a measure of the efficiency with which the instrument separates non-fluorescent sources of light (baseline) from the emitted fluorescent signal of interest. This is challenging as the typical excitation light is orders of magnitude more powerful than the resultant emission.[44] The SBR does not directly relate to the LIF instrument performance, though it does have a number of LOD-related ramifications. Firstly, for some instruments (typically using lasers[122]) high baselines directly contribute to signal noise. In these situations, improving the SBR directly improves the LOD by improving the SNR. Another aspect of SBR that can improve detection relates to the practical implementation of the detection electronics. These electronics have a limited dynamic range, typically in the 12-24 bit range and the SBR must therefore be sufficient such that the signal, baseline and detector noise can all fit comfortably within that range. Poor SBR requires the detection circuit to adjust its signal gain to accommodate the high baseline, which negatively impacts the detection. This is discussed in more detail in Chapter 4. The reference model in Section 1.3.1 shows that for the 1 nL, 1 nM sample the difference between the excitation power and emission power is at least 10 orders of magnitude simply due to the minimal amount of power that can be absorbed by the small sample. Uncontrolled, the excitation power would clearly create an overwhelming baseline. This highlights the need for attention to SBR.

The approach to LIF design taken in this thesis was to develop around LED illumination and photodiode detection to maintain a low instrumentation cost while ensuring future scalability to single-chip instruments. The crux of the design was to leverage the high stability of LEDs[81] such that the baseline signal no longer directly relates to the noise, thus decoupling the SBR from the LOD. Low-cost absorption filters were then chosen to limit the baseline to the dynamic range of the detection electronics. The result are a series of instruments with nominal, but manageable, baselines on a low-cost, scalable technology platform. Initially, these instruments were designed with larger spot-sizes and samples for initial prototypes for higher signals. Subsequent iterations featured targeted improvement of the designs and smaller channels. These iterations are described in Section 3.8. The model developed over the course of this chapter was then used to correct these designs to the standard sample volume of 1 nL for comparison with the

reference model from Section 1.3.1.

This chapter first provides a background on LIF detection that motivated this research. This includes discussions of approaches to LIF from the literature and industry (Section 3.1.1), how fluorescence can be integrated with molecular biology (Section 3.1.2) and a more detailed justification of the constraints required for implementing a scalable testbed (Section 3.1.3)). Next, the chapter develops a theoretical framework of how LIF detection functions and a model to estimate the performance of a LIF design. This begins with an overall equation (Section 3.2) that is composed of a number of factors relating to the various stages of fluorescence which are described in subsequent sections, notably excitation (Section 3.3), spectral filtering 3.4, fluorophore considerations (Section 3.5) and emission light collection (Section 3.6). For each, a model is described for how design decisions made affect the signal and how they compare with conventional instrumentation. Finally Section 3.8 outlines the performance of the various optics modules that were developed. The ultimate design discussed in Section 3.8.4 leverages excellent filter selection and the high signal stability from LEDs to implement an optical arrangement where the LED and detector are aligned on the same axis (termed staring-into-the-sun or SIS) which is directly compatible with monolithic single-chip designs. The model estimates a 56 fW signal from a 1 nM sample in 100 μm x 100 μm channels. This is only a factor of 5.6 improvement over the reference model in Section 1.3.1, insufficient on its own for achieving the LOD detection target with the reference electronics. This proves the need for the development of improved detection electronics as discussed in the next chapter. Section 3.8.5 then discusses an extension of the model to a feasible proposal for a monolithic-CMOS LOC device with an estimated signal of 91 fW. This shows that the testbed designed here has comparable, though slightly underestimated, performance as compared to future integrated designs, making it an excellent proof of concept for what would otherwise be a near impossible device to develop.

3.1.1 Approaches to Fluorescence Detection

Revisiting the Confocal Design

The standard LIF optics approach for PCR-CE, as discussed in Section 1.3 and Figure 1.4a, is the confocal optics module. At this stage it is instructive to analyse these designs in more detail to identify a few more nuances of the design that have made it the optical arrangement used in the majority of the molecular biology instruments in both industry and academia to implement LIF detection. Firstly, as mentioned previously, confocal modules have typically excellent spot-size, SBR and LOD performance. The spot-size is tuned with the use of a pinhole within the emission light collection optics. For example, the confocal used by the Mathies group and described by Scherer et al.[41] has a spot-size of 3-10 μm. Baseline control is accomplished in a confocal in two ways. First, the baseline is spectrally controlled not only with an excitation and emission filter, but the dichroic mirror that is used to split the excitation and emission pathways provides additional baseline suppression. Furthermore, the limited spot-size ensures that the collection of scattered emission light (for example, from the channel walls) is minimised. In terms of LOD, we can perform a back of the envelope calculation to estimate the performance of a representative design in a similar vein to the reference model in Section 1.3.1. A confocal optics module uses a laser for excitation that emits about 100 mW. This light is filtered by a well-optimised, high performance interference filter with near-unity efficiency. Furthermore, due to the collimated nature of the excitation laser and the beam-shaping optical components, most of the excitation light is transmitted into the sample. After emission, the objective lens collects the fluorescent light. However, due

to the small spot-size, only a small portion of the sample is collected from leading to a collection efficiency of about 0.1 %. This light is then reduced by about half due to the limited spectral width of the emission filter. Assuming the same absorption as the 1 nL, 1 nM reference sample from Section 1.3.1 (1×10^{-4} %), this results in a signal of about 44 pW. This is over three orders of magnitude better than the reference model. This is consistent with the literature where confocal optics typically report LODs in the tens of pM[41,43] compared to the 100 nM reference model result from Section 1.3.1. Excellent performance metrics are one of the primary advantages to a confocal design.

In addition to performance, there are a number of logistical advantages to this arrangement afforded by the use of the dichroic mirror to split the excitation and emission light pathways. This allows the confocal optics module to place all optical components on the same side of the device. Furthermore, both the excitation and emission light pathways share the same objective lens, ensuring that both pathways are focused on the same spot and making the module inherently aligned. These two factors allow the LIF optics to be isolated to a single, contained module, simplifying the interface between the optics and the sample. Furthermore, this allows for one optical design to be readily adapted to different scenarios. For example, the confocal optics module in the Backhouse lab (Microfluidic Toolkit, Micralyne Inc.[123]) has a working distance of several mm and a tunable z-stage such that it can be accommodate a wide variety of microfluidic chips. These practical factors simplify the optics design and promote adoption of this arrangement.

There are, however, a number of issues with the confocal design that require development. Firstly, there is the aforementioned trade-off between the spot-size and the signal. In some designs, the spot-size is increased by removing the pinhole from the design. This is typically referred to as a colinear optical module (or epi-illuminated design in microscopy). These modules carry the same logistical and most of the performance advantages of the confocal design, but with lower cost (due to fewer components and alignment constraints) and higher signals. Possibly the most impressive example is the work by Ahrberg et al.[124] who reduced the size of the colinear design into a hand-held package. However, the larger spot-size and increased baseline signal from scattered light make this less suitable for CE applications. Furthermore, in the case of laser illumination, the higher baseline results in higher noise, impacting the LOD. As a result, colinear optics are typically applied towards less demanding applications with larger sample volumes and higher sample concentrations such as q-PCR. [120,124,125] A second challenge that faces both confocal and colinear optics relates to the presence of the dichroic mirror which requires collimated light to operate effectively. This reduces the ability of the designer to replace the laser with lower-cost LEDs, which are not collimated, without the additional lenses which offset the cost savings. Thus, the ability to reduce the instrument cost is limited. Finally, and most important towards the objectives of this thesis, the dichroic mirror inhibits the miniaturisation towards single-chip devices as its location, composition and angular requirement are inconsistent with standard microprocessing. Therefore, for cost and scalability reasons an alternative to the confocal/colinear design is required.

Alternative Optics: Orthogonal, Axial and Staring-into-the-Sun (SIS) Arrangements

In a review by Xiao et al.[86] on LED-based fluorescence detectors they note two alternative optical arrangements to the confocal/colinear design above: the orthogonal and axial arrangements. These designs operate by separating the excitation and emission pathways, a function previously performed by a dichroic mirror. This reduces the component count of the design, relaxes the collimation requirements and enables the possibility of scalability. The orthogonal and axial arrangements are named based on the relative position of the light source, sample and detector. Both arrangements

have been pursued in this thesis.

The orthogonal arrangement is an optical design where the excitation and emission paths are at or near 90^o to each other. The most common implementation of this arrangement has the excitation light coming from the side of the chip, with a collection lens either above or below the detection point. Since the excitation and emission pathways are not coincident, the baseline in the orthogonal approach is dominated by the scattering of light from the channel edges and sample. Therefore, this arrangement can boost the SBR, though not as much as a good dichroic mirror which has typically two to three orders of magnitude baseline rejection. However, there are two notable disadvantages to the approach. Firstly, by separating the excitation and emission pathways there is now a need to align them to the same sample spot. This is not an issue in colinear/confocal optics where the two paths share an objective and thus a focal point. The alignment issue is typically solved by increasing the spot size of the instrument and thus, in general the resolution would be expected to be worse than for a confocal module. Furthermore, in this arrangement at least one of the excitation or emission pathways (typically, excitation) is coupled through a chip edge. As a result, the orthogonal approach is more susceptible to fabrication concerns, notably the and chip and channel edge roughness now affect how much excitation light is present at the detection point. Since the baseline is dominated by the scattering of light from the channel walls, fabrication changes can also introduce a variation here. This variation is also highly sensitive to the chip placement. Thus, in general strict reproducibility is more challenging. Furthermore, the orthogonal arrangement introduces a number of design constraints to the system. Since the input light is edge-coupled, this requires the detection point to be close to the chip edge for efficient excitation. Not only does this limit the design flexibility, it means that the orthogonal approach is not readily arrayed for multiple detection points due to each point needing edge-access. These issues can be somewhat mitigated by embedding an optical fibre into the chip to perform this coupling,[126,127] however this complicates the fabrication of the fluidics. The most significant downside to orthogonal approaches is that it is difficult to implement in miniaturised systems. For the large, mm scale chips the microfluidics are patterned into, an LED, lens or fibre can be readily used to couple light into the channel. However, as the vertical size of the chip shrinks, the amount of light being wave-guided in is also reduced. In the case of the monolithic, CMOS chip, there are also bond wires to consider which can interfere with the optical coupling. One solution to this would be to implement waveguides, however this would further complicate an already difficult fabrication problem, take up valuable chip surface area in a constrained system and introduces the challenge of effective waveguide coupling.

The orthogonal arrangement has been used extensively in the literature. Miyaki et al.[127] placed an LED very close to the channel to illuminate the sample, while using an optical fibre to collect emitted light and conduct it to a filter and PMT. While good for its time, the poor collection efficiency of fluorescent light by the bare fibre optic led to a LOD in the 100's of nM, insufficient for general purpose analysis. Furthermore, while a more simplified set of optics than a confocal, this work still required an expensive PMT and interference filters to operate. Diao et al.[126] performed the opposite approach in that they used an embedded optical fibre to conduct LED light to the detection point and used a high performance objective, an interference filter and PMT for detection. Their 0.3 nM LOD was impressive, however similar to Miyaki et al.,[127] the reliance on the design on expensive components does not address the core concern of low-cost, scalable detection. Possibly the most notable work in the literature using this arrangement was done by Chabinyc et al.[128] who integrated an LED light source guided by an optical fibre, polymeric filters and APD detector with PDMS fluidics to demonstrate a CE instrument with a LOD of 25 nM. This design was notable in that it is one of the only optical modules demonstrated for CE that utilise polymeric filters, meaning it is generally lower cost than other literature examples. However, the LOD and use of an APD do not meet the research objectives of this work,

the spot-size of the design was not assessed and the need to embed the optical fibre into the PDMS device precluded scale-up manufacturing of the microfluidics. The Backhouse group has previously used the orthogonal approach with lasers in Kaigala et al.[80] with the optics shown in Figure 3.1b. This design eliminated the excitation filter and dichroic and used a GRIN collection lens for a relatively low-cost demonstration with a good LOD of 0.7 nM. However, the laser and interference filters are not suited for true low-cost applications. Most of the optical modules demonstrated in this thesis also use the orthogonal approach, including our recent demonstration of the state of art in CE fluorescence detection using LEDs and PDs, the optics of which are described in Section 3.8.3, the electronics in Section 4.5 and the application demonstration in Section 5.4.

The axial approach to LIF instrumentation places the excitation and emission pathways on either side of the fluidic chip on the same axis. This results in a very high baseline as the only suppression mechanism are the optical filters, and thus this design is more commonly used for absorption based detection than fluorescence. To mitigate this effect somewhat, many axial arrangements angle their detector slightly to separate their excitation and emission pathways. There are no strict guidelines as to what constitutes an axial vs. an orthogonal arrangement, however in this work a truly axial design where the excitation and emission pathways are perfectly aligned will be termed "staring-into-the-sun" (SIS), named because the strong excitation light background is akin to the sun. Axial and SIS arrangements, in general, carry the same advantages (no dichroic, less lensing required, less expensive components) and disadvantages (alignment, spot size) of the orthogonal arrangement, but avoid the edge-coupling related problems. Specifically, there is no longer a need to have the sampling point close to a chip edge, the detection is readily arrayed provided more light sources/detectors are used and the chip to chip reproducibility is improved. The baseline in such instruments comes from direct illumination of the detector by the light source and thus fabrication features have a less pronounced effect. The most important factor, however, is the SIS arrangement is relatively easy to implement and can be readily miniaturised to any arbitrary system, including a monolithic CMOS based instrument. Thus, this provides a fully scalable approach as detailed in Section 3.1.3. However, substantial challenges exist that have so far prevented application of this design to LIF detection in CE, and exploring solutions to this challenge has been a significant component to this work. Firstly, as already mentioned, this arrangement has a very high baseline. This puts very stringent limitations on the optical filters and excitation source stability. The arrangement also requires fully transparent chips, which can limit the substrates used.

There have been relatively fewer demonstrations of CE optics with a SIS arrangement. Yao et al.[129] and Nakajima et al.[130] are examples that both used organic LEDs (OLED) and interference filters in well integrated devices. However, these approaches both had very poor LOD in the μM levels and relied on the expensive filters for baseline control. As mentioned previously, the work by Yang et al.[88] has been cited by many [26,81] as the state of art in LED + PD based fluorescence detection for CE. This demonstration used an axial arrangement with an angled detector to demonstrate 100 nM LOD with an approximately 1 mm spot size as shown in Figure 3.1c. While a good demonstration of low-cost and easy to integrate optical detection, and applied to an application demonstration,[131] the LOD for this instrument was 100x worse than the requirement for nucleic acid applications. Furthermore, the spot-size of 1 mm is well above the 100 μm target. Finally, the Yang et al.[88] work relied upon both an off-axis detector and an interference filter for baseline suppression such that it did not meet the scalability constraints. Therefore, there remains a need for the development of similar low-cost designs but with improved detection performance and scalable designs. This is the subject of Section 3.8.4 which describes the most recent optical module that can implement an axial SIS optics configuration that meets all scalability requirements.

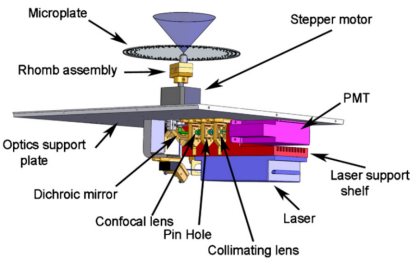

(a) A confocal optics module used by the Mathies group with glass microfluidics. This is a high performance, high cost system with a heat-sunk 75 mW, 488 nm laser, dichroic mirror and interference filters, confocal lensing and a PMT. The pinhole is 200 μm and the reported LOD is 30 pM, making it an excellent option for CE analysis. However, this optical arrangement carries considerable expense and does not miniaturise well, necessitating further development. Image taken from Scherer et al. [41]

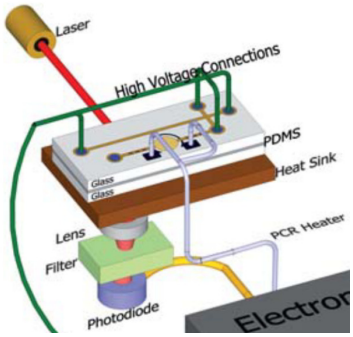

(b) The orthogonal optics used in previous instruments by the Backhouse group. These optics feature a side-illuminating 5 mW, 632 nm laser for excitation, a GRIN lens for emussion collection, an interference filter for baseline suppresssion and a photodiode. The optics have a reduced cost as compared to confocal/colinear optics, though still carry notable costs due to the laser and filter. The reported LOD is 700 pM, which is about an order of magnitude worse than the confocal module by Scherer et al. [41] but still sufficient for robust DNA analysis. Image taken from Kaigala et al.. [80]

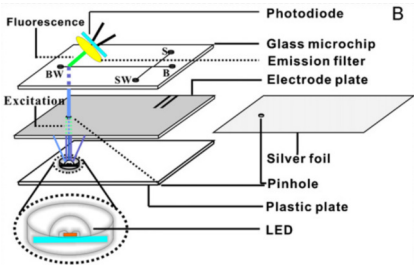

(c) The axial optics arrangement, cited as the state of the art in low-cost LIF detection. The work uses a 1mm pinhole in some silver foil to mask off the detection region from a high power LED. Baseline is suppressed using an interference filter and holding the photodiode and filter at an angle as compared to the LED illumination. This instrument has a reported LOD of 100 nM, which is sufficient for many applications but 100x too high for general purpose DNA analysis. Image taken from Yang et al.. [88]

Figure 3.1: Selected LIF implementations in the literature. These are compared later in Table 6.1

3.1.2 Fluorescence Labelling Techniques

There are two main methods of implementing fluorescent labels in CE: end-labelling and intercalating dyes. [31] End-labelling refers to the binding of a fluorescent tag to one of the primers used to generate the DNA sample to test. This results in a single fluorophore being bound to each strand of DNA, and thus the concentration of fluorophores directly tracks that of DNA. The other method is to use intercalating dyes. These are fluorescent molecules that have very low, near negligible quantum yield when loose in solution. When these molecules bind to double stranded DNA the quantum yield jumps substantially and they begin to fluoresce. [132] Intercalators have the advantage of higher signals as they can bind to one in four base pairs. [133] For a 300 bp product, this results in 75-300 fluorophores per DNA molecule as compared to the single fluorophore per molecule of a typical end-label. For this reason, many instruments both in industry use intercalators and cite LOD values accordingly. These LODs are not representative of end-labelled applications, potentially precluding such analyses. For example, the work by Namasivayam et al. [69] who performed a DNA analysis with CE report a LOD of 0.9 $^{ng}/_{\mu L}$, which corresponds to roughly 341 nM based on their reported intercalating binding. Thus, while their DNA separation data was sufficient for their application, the instrument LOD was over two orders of magnitude off the research requirements of this work.

End-labels were targeted for this work due to their higher CE separation performance. The multi-fluorophore binding of intercalators to DNA causes changes in the conformation of the DNA molecule, resulting in alterations during electrophoresis. Perhaps more importantly, the intercalation reduces the net charge of the DNA molecule and thereby

also reduces its mobility. Since the number of fluorophores per molecule is not strictly controlled, this causes a variable effect on the CE separation. As discussed by Barron and Blanch,[134] this altered migration would render futile any attempts to quantify differences in DNA fragment mobilities between samples. For example, an assay designed to detect slight differences in the size of PCR fragments, such as those associated with small deletions or insertions, would not be reliable given the effects of the intercalator on DNA mobility. The variable binding also makes complicates quantitative analysis of the CE peaks.[31] This is not a problem in end-labels as there is only one fluorophore per molecule. End-labels enable higher performance applications than intercalators at the expense of signal, thus requiring a higher standard for LOD. In order to ensure the system is compatible with the gold-standard end-labelled methods, the LOD requirements detailed in Chapter 1 are based on a concentration of fluorophore. Thus, detectors that meet the specifications will be able to execute the high-performance end-labelled separations standard for many analyses.

3.1.3 Scalable Designs

The long-term objective of the research project is to monolithically fabricate the microfluidics atop the electronics on a single chip made in a CMOS process. CMOS here refers to the standard processing methods used by the microelectronics industry, thus designing for CMOS means you are inherently designing for mass manufacturing. By including the fluidics onboard as well, the resulting device could cost on the order of $10 based on high-volume CMOS running costs, two to five orders of magnitude less expensive than today's standard instruments, and fit within a USB-key sized instrument. This would be a substantial advance to the field, eliminating the need for equipment to run the LOC device by integrating that equipment within it. There are many approaches to CMOS-based biology detection as reviewed by Datta-Chaudhuri et al.,[135] using the CMOS as an imaging unit[136] or performing electrochemical measurements.[137] These are good demonstrations, but tend to focus on specific binding-based assays that face many challenges such as limited functionality, LOD and reproducibility. The approach taken by this research project was to develop towards multi-functional CMOS chips that perform the standard molecular biology operations of PCR and CE. This project was done in collaboration with the Elliott VLSI design group at the University of Alberta, with the CMOS instrumentation development provided by the Elliott group and optics, fluidics and testing provided by the Backhouse group. To this end, much work has been done developing CE-scale microchannels for CMOS processing,[50] developing HV electronics for CE separations[46,138] and developing a CMOS-compatible heater for PCR.[53] There are two primary aspects that require development: integration/packaging and optical detection. These are tightly related concepts, as the optical detection is highly dependent on the geometry of the system, and hence it can only be tested after integration and packaging have been done. Integration is a substantial challenge that faces the whole field [82,135,139] which is further complicated by the high NRE costs of CMOS processing. The tendency of fluids, especially biological samples, to foul and contaminate surfaces (and the sensitivity of techniques like PCR to those contaminants) is a particular issue. Another difficulty is that the prototype CMOS electronics developed by the University of Alberta might not always function as expected due to each iteration implementing novel features that might not have been previously tested. It is therefore crucial that before integration is attempted, the design is frozen for extensive testing. However, this presents a catch-22; it is not possible to lock-down the integration without solid optical detection, yet it is not possible to test the optical detection without locked-down integration. The approach of this research project was outlined in an early publication,[48] which was to develop a low-cost testbed that retained most of the same limitations and physics of a

CMOS device such that the optics could be iterated upon without the locked-down integration. Fluorescence detection on a monolithic CMOS instrument is an interesting problem. On one hand, the miniaturisation of the channels reduces the signal, as it reduces the number of fluorophores present. However, this signal reduction is offset by a much higher collection efficiency of the emission light. Consider the situation illustrated by Figure 3.2a, which depicts a finite sized sample in contact with an infinitely large detector. Since fluorescence emits in all directions, this situation would be expected to collect half the fluorescent light, the practical maximum for such systems. To compare, as described in Section 3.6 below, a typical confocal collects much less than 1% of a typical CE channel. Thus, while miniaturisation typically makes LIF detection more difficult, high levels of integration can offset this signal decrease in the form of collection efficiency. However, the Figure 3.2a is not a practical design as the detector size must be comparable to the sample size (due to spot-size requirements) and the channel must be separated from the photodiode by some nominal thickness to ensure reliable fluidics. In this work, the CMOS channel dimensions used will be equivalent to those by Gutierrez-Rivera et al.[50] at 100 μm wide and 40 μm thick. The photodiode will be assumed to also be 100 μm x 100 μm and a 15 μm separation between the channel bottom and the photodiode will be set. This reduces the amount of fluorescence light collected to 6%, much lower than Figure 3.2a but still much higher than a typical confocal. These designs are described in more detail in Sections 3.6.1 and 3.8.5 below. The primary challenge, as described above, is that prototyping this instrument is very difficult. The approach taken in this work was to use short working distance GRIN lenses to imitate as close as possible the monolithic performance, while physically separating the microfluidics from the CMOS electronics as shown in Figure 3.2b. This provides a number of advantages. Firstly, as described in Section 4.2, some of the early work used a prototype multi-functional CMOS chip for optical detection. However, interfacing optically with that chip is challenging due to the presence of fragile bond wires.[135] The optical relay separates the chip from the fluidics by multiple mm, allowing for the protection of the bond wires. Most importantly, however, it decouples the microfluidics (which can now be rapid-prototyped PMMA as in Chapter 2) from the electronics. One of the primary challenges in CMOS fluidics development is that biological fluids readily foul interfaces,[82] which exacerbates the already problematic CMOS development pathway. The optical relay allows for replaceable fluidics on the same electronics, eliminating the fouling problem. Further details on the GRIN relay are described in Section 3.6.2 and in Hall et al..[48]

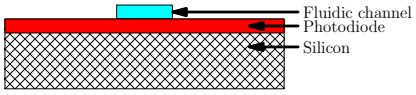

(a) Illustrating the a situation where a sample is atop an infinite detector. This system would reach the theoretical maximum collection efficiency of emission light of 50% (i.e. half of the light will go up and be lost, the other half down and be collected). Miniaturising the distance between the detector and channel can vastly improve the instrument performance.

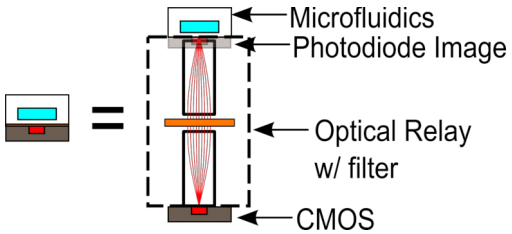

(b) Figure demonstrating the optical relay. a). shows monolithic CMOS LOC instrument with optical proximity that cannot be readily prototyped due to NRE. It is approximately equivalent to b). which shows the optical relay created by two GRIN lenses to image the detector directly below the channels. This approximates proximity while physically separating the fluidics and electronics, avoiding the NRE issue.

Figure 3.2: Approaches to scalable light collection. Figures taken from Hall et al.[48]

As previously described, there are three key components to LIF detection instrumentation. The optical relay takes care of one of those components, emission light collection, leaving the excitation and baseline rejection as remaining issues. For excitation, there are a few important considerations. Firstly, the objective of a $25 USB-key suggests not only low-cost but also low power. For this application, LEDs are well suited at over an order of magnitude lower cost than lasers with simpler drive electronics and lower power consumption. The other excitation consideration is the method of excitation light coupling into the sample. Three methods are described in Section 3.1.1: colinear, orthogonal and axial/SIS. Colinear optics are not compatible with a monolithic CMOS chip as the dichroic mirror must be placed in the light path between the sample and the detector. Since these are fabricated on the same substrate, there is no room in this design for this element. Orthogonal configurations are also challenging for this design as the fluidic layers are very thin as compared to typical LEDs (40 μm thick as compared to mm scale commercial LEDs) and it is difficult practically to assemble a device with the side-illumination in a USB-key sized package. This leaves the SIS mode of excitation where the source, sample and detector lie in the same axis. This typically results in a very high baseline leading to two key challenges. Firstly, the baseline rejection must be very high to limit the baseline and signal to within the electronics dynamic range. Secondly, the baseline must be very stable such that it can be effectively managed. This, too, suggests an LED as the best option.[81] Therefore, for a scalable design, the excitation source must be an LED.

As discussed in Section 3.4.4, the baseline rejection is a key component to LIF design. In general, there are two methods of accomplishing this. One method takes advantage of the finite time the fluorophore remains excited before emission to eliminate the baseline. These "temporal" based instruments blink the excitation source on and off rapidly while analysing the fluorescence only when the source is off. This method has been previously demonstrated with CMOS microelectronics by the Shepard group at Columbia University,[140,141] however these solutions have required high-end lasers and have had quite poor LOD as described below. A more standard method is to use spectral filtering. The standard methods in the field are to use interference filters due to their high performance and tunability, however in a CMOS-based process where high yield and throughput are paramount the excessive number of highly controlled layers ($\approx$ 40 with nm precision [44]) for these filters is very problematic. A prominent example in the field is the work by Webster et al.[68] who integrated a photodiode, interference filter and fluidics atop the same silicon die, essentially implementing the monolithic detection system that is the ultimate objective of this work. This landmark publication was a continuation of the PCR-CE work by Burns et al.[67] targeting optical detection for CE (and eliminating the PCR to simplify device iterations). However, there remained two key issues. Firstly, it contained an interference filter, complicating mass production. It is telling that in their subsequent work they separated the fluidics from the filter, likely to simplify development.[69] Furthermore, the LOD remained poor, relying on intercalating dyes to image the DNA and several orders of magnitude off the 1 nM research objective. Here again, the in-house fabricated interference filter appears to be an issue as they cite that their improved filter only blocks 95% of light below its cut-off wavelength (about four orders of magnitude worse than a high-performance commercial offering), likely due to inaccuracies in the layer thicknesses.[44] This highlights the scalability issues inherent in interference filter usage. Absorption filters, on the other hand, are much more readily implemented into microprocessing methods as they only require a single, relatively uncontrolled deposition. Therefore, the use of absorption filters is another constraint imposed for reasons of scalable designs.

There are two prominent CMOS DNA demonstrations that bear mentioning. Illumina, the current market leader in DNA sequencing, has been targeting a CMOS-based instrument under the title "Project Firefly" for quite some time

and have recently released their new iSeq device.[142] In a project that followed their acquisition of the pyrosequencing company Avantome in 2008, Illumina has been seeking to develop a CMOS based NGS device that enters at a much lower price point than their previous offerings, while educing the footprint from a full-size photocopier to a small desktop.[143] The key advance of this instrument was to pattern the standard Illumina flowcells above an array of CMOS imaging pixels. This contains all the emission light collection optics on-chip, similar to the monolithic design suggested in this work. The excitation design is not described well, however it can be inferred that it is based on LED illumination as per its specification sheet[144] and in a near-SIS style arrangement based on the dimensions of the flowcells (which are several cm wide, precluding side illumination). Therefore, the optical design would appear to be highly similar to the designs posited here. However, there remain a number of issues that remain unsolved. Firstly, the list price of the instrument is $20,000 USD.[142] This is an order of magnitude less than their premium offering and over 2x lower than their MiniSeq instrument released last year, however it still remains much too high for resource-poor applications. One potential reason could lie in the method of excitation light filtering, which is unstated but likely interference filter based. Furthermore, Illumina is listing their chips at $650 USD per device. This is also much higher cost than targeted by this thesis, both in terms of polymeric fluidics in Chapter 2 as well as fully monolithic designs which are expected to be over an order of magnitude less. This price discrepancy is due to the fact that while the detection is done in CMOS, the microfluidics remain glass which is both expensive unto itself as well as to process. In summary, the Illumina instrument demonstrates the feasibility and cost savings of miniaturisation. However, it remains tied to certain designs (glass microfluidics, for example) that prevent resource poor applications as targeted by this work.

In academia, to the best of my knowledge, the only CMOS molecular diagnostic implemented has been the excellent work by Norian et al..[141] This work used a multi-functional microelectronic chip that contained high voltage generation and switching, single photon avalanche photodetectors (SPAD) and micro heaters. The group then fabricated an electrowetting on dielectric (EWoD) fluidic device directly onto the chip to form a device capable of q-PCR. The SPAD detector work was particularly interesting as they implemented a temporal baseline suppression method, toggling their laser/detector at 1 MHz. For fluidic actuation the instrument uses EWoD, which allows for the individual moving and mixing of droplets. Through focusing on droplets, Norian et al.[141] have avoided many of the more difficult aspects of LOC development (channels, valves, pumps, etc). While an elegant solution, the volumes and complexity possible with this instrument are highly limited. The system contains only four reservoirs and a grid of 56 pads; the limited number of pads limits the complexity of fluid movement possible, while the limited number of reservoirs highly limits the complexity of the protocol. It is therefore not possible to implement robust sample preparation on this platform. Further, the entirety of the chip surface is taken up by the EWoD + reservoir, which limits the expandability of the platform without drastically increasing the size of the CMOS die which would add to the cost. The system implements only a q-PCR, which leaves the instrument open to a number of issues and does not satisfy laboratory best practices.[5] The LOD of the instrument is in the μM regime, suitable for their q-PCR application with intercalators but much too high for end-labelled CE detection. Finally, and most importantly, the instrument optics relied on a very high end laser that was external to the system. This laser adds substantially not only to the cost and bulk of the instrument (likely much more costly than the CMOS chip), precluding miniaturisation to a USB-key diagnostic, but also introduces operator alignment as a requirement for executing an experiment. This contrasts directly with this project's focus on CMOS scalable optics that eschew expensive lasers for LEDs that require less alignment and can be integrated much more closely with the instrument for a true LOC solution. Thus the work by Norian et al.[141] was a technical marvel and a demonstration on CMOS of most of a diagnostic platform, but left key questions of channels, valving, pumping

and excitation light unsolved.

3.2 Estimating signal power

In order to design optimised optics it is important to develop a model to determine the effect of the various design decisions. Figure 3.3 shows a flow chart depicting the various stages of fluorescence detection. At each step, there is an associated efficiency and loss of optical power. A model for LIF detection performance can be made by assessing each of these efficiency losses and combining them to estimate the resulting fluorescent signal. The first step is to determine the amount of power input into the system. This is discussed in Section 3.3 and includes calculation of the LED optical power (P_{input}) and efficiency of coupling into the sample(input coupling efficiency ICE). Next, one must analyse the spectra of the various optical elements as described in Section 3.4. This includes the efficiency the excitation filter transmits the excitation light (T_{exfilt}), the amount of power absorbed by the fluorophore as calculated by the Beer-Lambert law $\left(1-10^{E_{absorption}\varepsilon_{max}Ct}\right)$ where $E_{absorption}$ is an efficiency correction for the wavelength of excitation light, ε_{max} is the absorption coefficient maximum of the fluorophore, C is the concentration of the fluorophore and t is the thickness of the sample) and finally the transmission efficiency of the emission light through the emission filter (T_{emfilt}). After absorbance, the fluorophore undergoes two power losses as discussed in Section 3.5: the energy loss due to non-radiative relaxation as expressed by the fluorophore quantum yield (QY) and the energy loss due to vibrational relaxation in the form of the Stokes shift (SS). Finally, the light collection efficiency of the emitted fluorescence light (LCE) is discussed in Section 3.6. The product of all these factors and efficiencies estimates the amount of fluorescent light detected as shown in Equation 3.1, assuming that the fluorophore concentration and the excitation power P_{input} are both low such that the sample is optically thin, there is no photodegradation and the fluorophore excited states are not saturated.

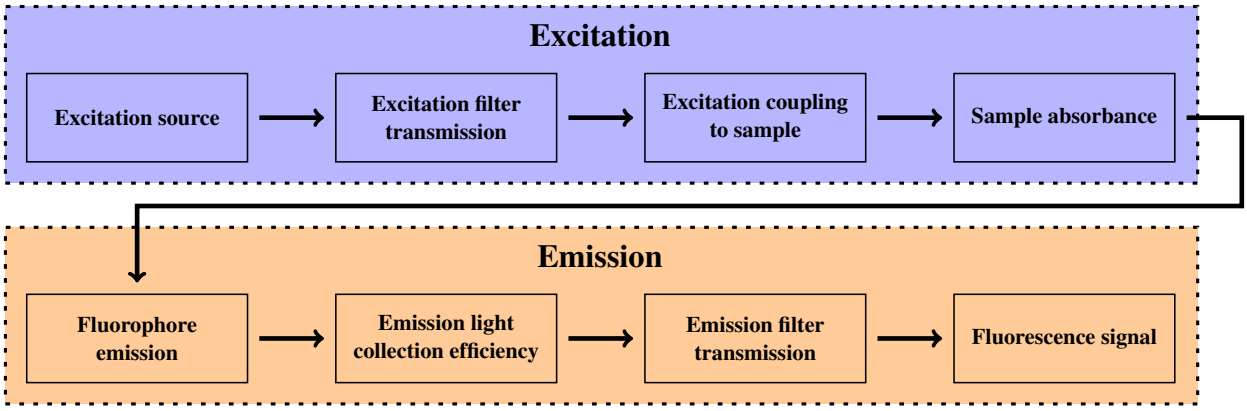

Figure 3.3: A flow chart depicting the parameters that contribute to the fluorescence signal. Signal estimation begins with the excitation source power which is then filtered by an excitation filter to remove baseline. Next, only a portion of this excitation light will be coupled into the sample. Of the light incident on the sample, only some of this will be absorbed to excite the fluorophore. After excitation, energy is lost within the fluorophore due to its Stokes Shift and non-radiative relaxation processes. The radiative energy is then emitted in all directions, of which a portion is collected by the optical system. The collected light is then filtered with an emission filter. After these processes, the remaining signal is then detected. Typically, the fluorescence signal is eight or more orders of magnitude lower in power than the excitation source. Maximising and detecting this low signal is the primary challenge of a LIF instrument.

$$P_{opt} = P_{input} \times ICE \times T_{exfilt} \left(1 - 10^{E_{absorption} \varepsilon_{max} Ct}\right) \times T_{emfilt} \times QY \times SS \times LCE \tag{3.1}$$

The following sections detail the model used for the optical modules were designed. These modules assume LED illumination, no lenses on the excitation path, absorption filters (i.e. no collimation requirements) and no reflections. As a point of comparison, a discussion of lasers and interference filters is also included to illustrate where the impact of the low cost design is hindering the detection. Using this model the effect of the design decisions between optics iterations discussed in Section 3.8 can be assessed and compared.

3.3 Excitation

The first step in the fluorescence instrumentation tool chain is determining the amount of optical power input into the sample. This excitation light can be provided by filtering a band of broadband light (such as a spectrophotometer), a laser (an approach followed by most conventional microchip electrophoresis instruments such as the BioRad Experion[98]), or a LED (an approach followed by many q-PCR instruments such as the BioRad CFX[120]). Broadband light sources are good for instruments that require a tunable excitation wavelength, however they are not very appealing to miniaturised systems due to the large size, high cost and the thermal issues that accompany the use of xenon bulbs. Thus, focus will be placed on laser and LED excitation sources.

Light sources are assessed generally on how much optical power the source can couple into the sample and their stability. In an ideal instrument, the sample will experience the highest possible optical power as the signal scales linearly according to Equation 3.1. Practically, there are limits due to the onset of saturation and photodegradation, though these are expected to become significant at irradiances much higher than those experienced here ($10^5 \frac{W}{cm^2}$ and above).[122] Maximizing the amount of optical power into the sample amounts to having an initially powerful source and concentrating the optical power both spectrally and physically into the sample. Thus, the three main criteria that determine the optical power of the source are the absolute output, the spectral full-width at half max (FWHM) and the étendue (i.e. how spread out the light emitted from the source is, or how uncollimated it is). For LED based light sources, the absolute output is expressed in terms of luminosity rather than watts, thus a conversion must take place. This process is described below in Section 3.3.1. Spectral considerations are discussed in more detail in Section 3.4.1, but briefly the more narrow the FWHM, the more efficiently the excitation light can excite a fluorophore. Furthermore, wide FWHM sources can lead to baseline issues as discussed in Section 3.4.4 if not properly contained and filtered. There are two components to étendue: the area of the source and the angle of emission. For the ideal excitation source, the étendue would be minimised, thus the excitation light can be more effectively used to probe a small spot size and the "waste" of light is minimised. The étendue problem can be mitigated somewhat by the use of high numerical aperture lenses, though it remains limited by the initial étendue of the source.

In terms of the two main excitation sources, there are advantages and disadvantages to each. Lasers are effective light sources for high performance applications for several reasons. Firstly, lasers are typically collimated and thus have low étendue. This allows for the design of systems where most of the source intensity is effectively coupled into the sample as well as compatibility with standard dichroic/interference filter based designs. Furthermore, lasers have a very narrow spectral width; a typical semiconductor laser will have all of its intensity confined within a few nm. Thus,

for fluorescence instrumentation a laser will typically have the strongest signal for a given source power. This is why most high performance instruments use laser illumination. However, there are a number of drawbacks to laser use. Firstly, in order to get reliable operation out of a laser the instrument would need to control both the power delivered to the laser as well as its thermal properties. Thus, more extensive drive electronics and instrumentation is required, along with a heat sink making the laser typically larger and less miniaturisable than LEDs. Even in the case of a well controlled laser the power stability still varies typically by about 5%.[145] This variation means that the resultant LIF signal will also vary by an amount proportional to the baseline, which is highly problematic when the baseline is high such as in SIS configurations or when using lower-performance absorption filters as was done in this work. For example, previous work by Kaigala et al.[80] contained a laser module whose signal variation was comparable to PCR product signals (i.e. 100 nM), causing substantial complications when identifying signals from the noise. A move to LED illumination addresses this issue.

LEDs are becoming a more popular source for fluorescence instrumentation, being used in a number of applications including the BioRad CFX[120] q-PCR machine and the entry level Illumina Miniseq and iSeq systems.[144,146] There are a number of advantages LEDs have over lasers including being substantially lower cost, requiring simpler drive electronics, having longer lifetimes, using less power, and having higher signal stability and lower temporal noise.[81,147] For low current LEDs (i.e. under 100 mA), heat sinks are not necessary leading to improved miniaturisation and simpler integration.[147] However, LEDs do have a number of drawbacks. LED light has a typical FWHM that is 10x higher than a diode laser (typically about 25nm), which severely limits the potential efficiency of the system and typically resulting in a higher baseline. The baseline issue is further compounded by the LED light containing a significant thermal component that extends through the red and into the IR range[81] (see Section 3.4.4). Thus, LED illumination systems typically require excitation filtering.[81] LEDs also have typically poor étendue with viewing angles of 20^o through to 180^o.[147] In comparison to lasers, a LED source power is substantially more spread out both in terms of spectra and physical space. This limits both the spacial resolution of the optics as well as the signal, and as such most commercial applications that use LEDs are limited to less demanding applications such as q-PCR. As reviewed by Götz and Karst[87] in 2007, Xiao et al.[86] in 2009, Macka et al.[81] in 2014 and Castro and Manz[26] in 2015, LED based optics for CE are rare. The following sections detail a model to estimate the efficiency of using LEDs vs. lasers, showing how even a low power 5 mW laser can couple multiple orders of magnitude more light into the sample. This lower power couples directly into the expected signal, and is one of the primary reasons for the dearth in LED-based CE optics.

This work has focused on LED illumination. As the project evolved it became clear that the LED stability was a crucial component to this projects success. The inexpensive polymer filters described later in Section 3.4 and the SIS optical arrangement described in Section 3.8.4 have created a scenario with a relatively high baseline. For laser-based instruments, this baseline would dominate the instrument noise, substantially impacting detection. Thus, the choice of LED illumination is not only important as it is lower-cost and more scalable than lasers as discussed above, but it also is a crucial factor in enabling the scalable filters and optical arrangements as well.

3.3.1 Estimating excitation power for LEDs

Estimating the excitation power input into the sample for LEDs is typically a two step process. Most LEDs report the amount of light they emit in photometric units, usually either in luminous intensity in candelas (cd). The first step is to use the luminous intensity and angular distribution of it to estimate the luminous flux into the sample. This is measured in lumens (lm) and is calculated from the product of the luminous intensity and the solid angle the sample subtends from the source. The second step is to convert the photometric units to radiometric units (i.e. convert from lumens to watts) using the 1931 C.I.E. Standard colorimetric observer.[148] These two steps are described below.

Estimating luminous flux into the sample

To estimate the amount of luminous flux into the sample the solid angle subtended from the LED must be calculated. In this calculation the sample area that faces the LED is considered to be a square defined by the channel depth and width (i.e. the area of the cross section of the electrophoretic device). The solid angle of a rectangular aperture with one corner directly above the light source is given by the equation from Khadjavi[149]:

$$\Omega_{\frac{1}{4}} = \sin^{-1}\left(\frac{ab}{(a^2+c^2)^{\frac{1}{2}}\,(b^2+c^2)^{\frac{1}{2}}}\right) \tag{3.2}$$

Where a and b are the rectangle lengths and c is the distance of the rectangle from the source. From the variable definitions, this calculates the solid angle of one quadrant of a rectangle centred directly above the source. The solid angle of the sample can thus be calculated by multiplying the above by four, setting $a = b = \frac{\text{Channel Width}}{2}$ and $c =$ Channel-LED Separation. This is expressed in Equation 3.3

$$\Omega = 4\sin^{-1}\left(\frac{\left(\frac{\text{Channel Width}}{2}\right)^2}{\left(\left(\frac{\text{Channel Width}}{2}\right)^2 + (\text{Channel-LED Separation})^2\right)}\right) \tag{3.3}$$

The solid angle, multiplied by the luminous intensity, will give the luminous flux. LED datasheets specify the peak luminous intensity, as well as a graph of how that intensity is distributed across various emission angles. Based on the datasheet for a through-hole LED and a solid angle below 10^{-3}str (1^o) typical for the systems described here, the output intensity of the LED across the angle of interest varies from ≈ 0.98 and 1. This will be assumed to be unity to simplify the calculation. Thus the luminous intensity is simply expressed in Equation 3.4. It should be noted that this takes into account both the LED output power as well as the input coupling efficiency.

$$\text{Flux} = \Omega \times \text{cd} \tag{3.4}$$

Conversion of luminous flux to optical power

The second step to estimating the excitation power of the LED is to convert from the luminous flux units LED datasheets typically use to an optical power.[147] This calculation is done with Equation 3.5 based on the 1931 C.I.E. Standard Colorimetric Observer[148]:

$$I_e(\lambda) = \frac{I_v(\lambda)}{683.002 \times \bar{y}(\lambda)} \tag{3.5}$$

Where $I_e(\lambda)$ is the radiant intensity in Watts per steradian, $I_v(\lambda)$ is the luminous intensity in candelas and $\bar{y}(\lambda)$ is the 1931 C.I.E. Standard colorimetric observer factor. This can be estimated based on the maximum intensity wavelength from the LED datasheet, however this does not take into account the spectral width of the LED. To do so, the following procedure was done:

1. Obtain a reference spectrum for the LED using a spectrometer (USB-4000, Ocean Optics)
2. Correct the reference spectrum for the CCD dark current
3. Convert this spectrum from power intensity to luminous intensity using a re-arrangement of Equation 3.5
4. Normalize the area under the curve to the reported luminous intensity of the LED
5. Multiple this normalised curve by the Flux calculated in Equation 3.4
6. Convert this normalized spectrum back to a radiant power using Equation 3.5
7. Integrate the radiant power spectrum to calculate the total power

Finally, depending on the current used in the LED an additional modifier is used. In this work standard indication LEDs were operated at 30 mA, which introduces a factor of 1.5 increase in luminous intensity based on the datasheet (most LEDs have a nominal drive current of 20 mA). Thus, for an LED running at 30 mA the output optical power coupled into the sample can be expressed in Equation 3.6

$$P_{input} \times ICE = 1.5 \times \int \frac{\text{Flux} \times \frac{I_m(\lambda) \times 683.002 \times \bar{y}(\lambda)}{\int I_m(\lambda) \times 683.002 \times \bar{y}(\lambda) d\lambda}}{683.002 \times \bar{y}(\lambda)} d\lambda \tag{3.6}$$

Where $I_m(\lambda)$ is the measured intensity profile of the LED from the spectrometer and Flux is calculated in Equation 3.4.

3.3.2 Estimating excitation power for lasers

Estimating the excitation power of a laser is comparatively simple as the output is expressed typically in terms of radiometric units. Thus, the only factor to consider is the beam divergence and estimate how much of the laser input is incident on the sample. For this comparison, the laser used in previous work[80] will be compared to. This was a 5 mW output red laser[150] that was focused to a 200 μm spot.[80] If we assume that the power distribution is completely even across the spot and the focused spot is larger than the channel, the input power for this laser can be estimated in Equation 3.7.

$$P_{input} \times ICE = 5\text{mW} \times \left(\frac{\text{Channel Width} \times \text{Channel Height}}{\pi \times \left(\frac{200\mu\text{m}}{2}\right)^2} \right) \tag{3.7}$$

3.3.3 Comparison of Excitation Sources

Figure 3.4 shows the normalised output of the two LEDs that were used in this work and the laser from Kaigala et al..[80] The wide distribution of energy for LEDs drastically reduces the efficiency of excitation, though this is discussed in more detail in Section 3.4.

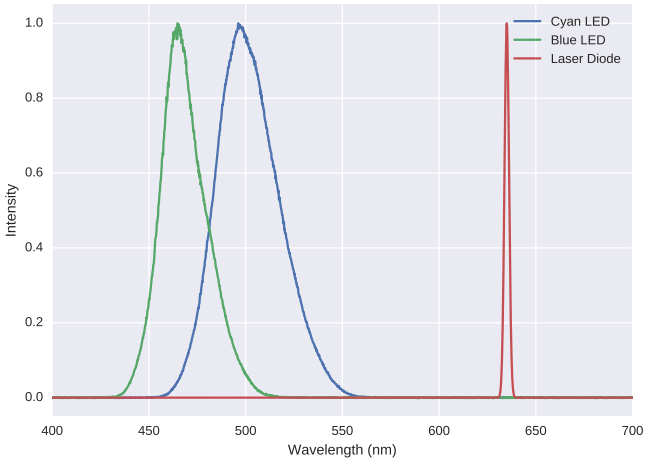

Figure 3.4: Output spectra for the blue LED, cyan LED and red laser described in Table 3.1 obtained with an Ocean Optics spectrometer. The substantially lower FWHM of the laser spectrally concentrates the excitation energy, which typically leads to much higher signals and efficiencies. Peak heights have been normalised to one for display purposes

Table 3.1 compares the specification for the LEDs and laser, and assesses the amount of power the sources can couple into a a 100 μm x 100 μm sample held 3.5 mm away from the source and no additional optics. Also included was an estimate of the *ICE*, the proportion of generated optical power that excites the sample. For the LEDs this was estimated as the ratio between the solid angle of viewing reported by the datasheet and the solid angle of the sample

calculated as above in Equation 3.3. Since the viewing angle is defined as the angle the intensity drops to half its peak value, there is still substantial light outside the cone defined by this angle. Thus, this calculation overestimates the *ICE* of the LED. For lasers, the *ICE* is the factor multiplied by 5 mW in Equation 3.7.

	Blue LED	Cyan LED	Red Laser
Product Number	WP710A10QBC/G	WP710A10WG1C	M635-5
Cost per unit (USD)	0.84	0.84	93
Drive Current	30 mA	30 mA	50 mA
λ_{max}	470 nm	505 nm	635 nm
Luminous Intensity	2.5 cnd	5.8 cnd	-
Radiant Flux	-	-	5 mW
Viewing Angle	20^o	34^o	-
Solid Angle of Viewing	0.3789 str	1.0742	-
Solid Angle of Sample	0.000816 str	0.000816 str	0.000816 str
Estimated *ICE*	0.22%	0.076%	32%
Power Into Sample	45.3 μW	25.9 μW	1.59 mW

Table 3.1: Table comparing two of the LEDs currently in use with the laser diode module used in Kaigala et al..[80] Despite having similar drive currents, the amount of power coupled into the sample is 35-61x lower for LEDs as compared to a laser diode module. This is predominantly due to poor input coupling efficiency (*ICE*).

Comparing the relatively inexpensive laser diode to the LEDs it is clear that the signal is expected to be substantially (35-61x) lower for the LED based module than the laser. This is primarily due to the fact that 32% of the laser light is coupled into the sample as compared to the sub-1% *ICE* for the LEDs, illustrating the difference between a collimated and focused laser and the poor étendue of an LED. One method to mitigate this issue is to reduce the LED-sample distance. For example, a 1 mm separation (as in a more integrated USB-key style device) the excitation power from the blue and cyan LEDs would jump to 0.6 and 0.6 mW respectively, which is only a factor of three to five different from the laser diode. This illustrates the benefit of miniaturisation for LEDs.

In conclusion, LED excitation in the absence of input lenses leads to poor excitation efficiency and low excitation powers as compared to a typical laser. However, this issue is offset by the reduced cost, reduced size, simpler implementation, scalability and signal stability. The signal stability is particularly important when considering the rest of the low-cost design detailed here, specifically the baseline considerations in the subsequent section. When considered as a holistic system with scalability and low-cost as primary drivers, LEDs become the best option for excitation. However, the lowered signal resulting from lower excitation power is a key challenge to be mitigated by the rest of the design.

3.4 Spectral considerations

In optical filter based fluorescence instrumentation, balancing the various spectral considerations is paramount to the success of the module. There are a number of different spectral components that determine the instrument's

performance. The first is the transmission efficiency of the excitation light through the excitation filter. Excitation filters are a crucial component to any LED-based fluorescence detection module to suppress the baseline from the very wide spectral FWHM of the LED,[81] though excitation filters are frequently applied to laser based systems as well.[122] After the excitation filters, the absorption of the excitation light by the fluorophore must be calculated. This too has a spectral component due to the wavelength dependence of the molar extinction coefficient. Finally, the transmission efficiency of the fluorescent light through the emission filter needs to be calculated. An ideal optical design would allow 100% of the excitation light through, excitation wavelengths coincide perfectly with the optimum absorption of the fluorophore and the emission filter transmits 100% of the emission light and 0% of the excitation light. However, this is not feasible for practical systems. The mechanism that allows for fluorescence instrumentation is the separation of the excitation and emission light from the Stokes shift of the fluorophore, which can be as little as 10 nm,[44] resulting in the overlap of excitation and emission spectra. This precludes 100% efficiency systems as it is thus impossible to both excite the fluorophore at its peak absorption wavelength while also transmitting 100% of the resulting emission light. This is illustrated in Figure 3.5 which depicts two common fluorophores used in our lab: Alexa Fluor 532 (AF532) and Rhodamine B and the notable overlap of their absorption and emission spectra.

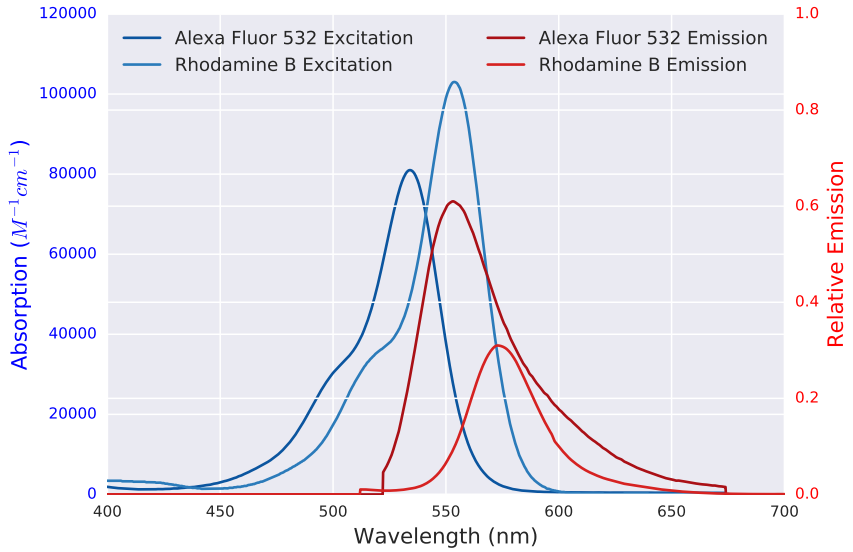

Figure 3.5: Plot of the excitation and emission spectra for two fluorophores: AF532 and Rhodamine B based on data from the ThermoFisher Spectral Viewer.[151] The excitation intensity is weighted by the absorption coefficient, while the relative emission is weighted by the quantum yield of the fluorophore. The effective fluorescence of both dyes is comparable; AF532 has a higher yield but lower absorption than Rhodamine B.The Stokes shift for both fluorophores is also similar at about 20 nm.

Another factor that limits practical optics are non-idealities in the spectral filters used. There are three primary attributes of an optical filter set that determine its suitability for use. The first is the optical density (OD) or the amount of unwanted light the filter will suppress. This value should be as high as possible to suppress the baseline. The next is the transmission of the filter in the wanted wavelengths. Here, this should be as high as possible to allow the passage of excitation/emission light where appropriate. Finally, there is the slope with which the filter transitions from

suppression to transmission. This slope should be as high as possible to maximize efficiency. A high on-off slope allows for a tighter match between the filter set and the fluorophore excitation/emission.

Most conventional fluorescence instruments use interference filters due to their high performance.[44] These filters consist of multiple $^1/_4$ wavelength thick layers of alternative material deposited with high accuracy, suppressing unwanted wavelengths with destructive interference. This allows for the design of filters with arbitrary cut-off wavelengths, thus allowing for optimised design of filters to match a specific application. Furthermore, a commercial interference filter has very high performance with an OD of six or greater, a pass-band transmission of about 98% and a high on-off slope where the stop-band to pass-band transition is within 5-10 nm. These factors lead to maximised signal and minimise the baseline light. However, there are a number of disadvantages to interference filters. Firstly, they can be quite costly, as detailed in Section 3.1.1 above, between USD $450-$900 per set.[152] This exceeds the entire cost of instrumentation for many of the instruments described here. Furthermore, due to the interference phenomenon being leveraged, there is a significant angular dependence to the performance. Thus, collimated light is typically needed. This is not an issue when using lasers, but does suggest that lensing of some sort be used for LED-based systems. Finally, interference filters do not miniaturise well to the CMOS-process compatible monolithic instrument that is the ultimate objective of this research. A good interference filter will typically require at least 40 layers deposited, each layer with a thickness error of less than 5% (or a couple nm).[44] This is a strenuous task that is not consistent with a CMOS manufacturing objective. As previously discussed in Section 3.1.3, Webster et al.[68] integrated an interference filter onto a LOC device, though this resulted poor LOD in the μM regime. One of the reasons for this poor LOD was an inexact interference filter, and it is telling that future work separated this interference filter from the LOC device, leading to 100x improvement in LOD.[69] This demonstrates the scalability issue with interference filters. Most commercial and academic demonstrations use these devices, including previous work by the Backhouse group.[80] However, due to the cost and lack of scalability these designs are not suitable for this research project.

The second type of optical filtering is to use absorption filters. These filters operate essentially according to the Beer-Lambert law and simply have absorption coefficients that are very high in the undesired wavelengths, and very low in the desired. Absorption filters are typically substantially less expensive than interference filters, with some based on coloured polymers at 10^4x lower cost than interference filters.[153] Further, when miniaturising, absorption filters have substantially relaxed deposition requirements and thus could be readily integrated into a scaled up manufacturing process. Absorption filters are also easier to design for with no angular component to their performance. This makes them a good option for non-collimated sources, such as LEDs. For these reasons, this research has focused on using low cost polymer absorption filters. However, there are a number of performance disadvantages. Firstly, and most significantly, the on-off slope for absorption filters is typically much worse than interference filters. The low on-off slope means that the excitation filter transmission and emission filter transmission bands must be separated, typically more than the Stokes shift of the fluorophore. This substantially reduces the system performance. System performance is also reduced by the relatively lower transmission efficiencies of absorption filters vs. interference filters. Absorption filters also typically have limited OD, especially in the IR region. This leads to typically higher baselines. Commercial absorption filters are available in a wide variety of formats, from standard coloured plastic, to filter films designed for photography and even dedicated glass filters for microscopes. One notable use of absorption filters for CE was published by Chabinyc et al.[128] where filter films were integrated with a blue LED and a APD. This was a good CE demonstration, however the LOD of 25 nM did not meet the requirements for end-labelled DNA analysis. This thesis has improved upon that work by further improving the LOD, and replacing the APD with a lower cost, easier to

integrate photodiode.

This section details the calculation methods and optimisation of the spectral performance of some selected polymer absorption filters. A pool of over 500 potential filters from various photography lighting and plastics manufacturers were analysed based on their reported transmission spectra. The objective was to find an excitation filter with a defined pass band in wavelengths below 550 nm, a long-pass emission filter with a pass band that started from around 550 nm and finding combinations where the two pass bands did not overlap. Most filters were excluded as they did not have well defined pass-bands as they were optimised for their attractive colour, not spectral purity, had incomplete reported information or were not readily available. From the initial pool of filters, twelve excitation and five emission filters were identified as likely candidates for future instruments. However, while spectra for these filters was available, the available details were insufficient (notably, OD in the stop-band of the filter). Thus, their performance was then quantified in-lab as described below.This analysis is presented here for the spectral filter sets used in the optics iterations in Section3.8 and applications in Chapter 5, while the performance of unused filters is available in the SI.

This section first details the calculation methods for calculating excitation filter efficiency (Section 3.4.1), fluorophore absorption efficiency (Section 3.4.2) and emission filter efficiency (Section 3.4.3). These factors determine the effect of the filter on the signal and baseline of the optical module. Baseline considerations are presented in Section 3.4.4 detailing that the ultimate designs are limited by the IR-transmission of polymer filters. Section 3.4.5 details the optimisation of the spectral filters, targeting the standard molecular biology fluorophore AF532. This final section also compares the selected filter sets to a recommended laser interference filter set from Chroma. Comparing the best absorption filters with an interference filter set, the baseline rejection is comparable though the expected signal is nearly two orders of magnitude less. Thus, the overall SBR of these modules are notably less than for a high performance instrument. However, the total filter cost is drastically reduced from $825 from Chroma to under 3 cents. Further, the use of absorption filters improves the feasibility of scaling the optical system to monolithic CMOS devices.

3.4.1 Excitation filtering

In order to get appropriately high baseline rejection, an excitation filter is needed,[81] especially given that typical LEDs are designed for lighting applications, not spectral purity. In order to determine the amount of power lost to the excitation filter output spectrum were obtained of the LED including and excluding the excitation filter with a spectrometer (USB-4000, Ocean Optics). The power transmitted can be expressed as the ratio of the areas under the curves, corrected for any change in integration time.

$$T_{exfilt} = \frac{AOC_{exfilt}}{AOC_{LED}} \times \frac{t_{int,LED}}{t_{int,exfilt}} \tag{3.8}$$

Where AOC_{exfilt} is the area under the excitation filter spectrum, AOC_{LED} is the area under the LED output spectrum and $t_{int,x}$ is the integration time for either just the LED or LED with excitation filter. Areas under curves are assessed with trapezoidal integration. This method is more accurate than obtaining a transmission spectra and multiplying it with the initial LED spectra, and requires the same amount of effort. Furthermore, by saving the spectra after excitation filtering further calculations can be readily done.

Due to the low slope of the on-off curve of absorption filters and LEDs, the excitation and emission bands have to be more separated for these optics as compared to conventional interference filters. This results in an excitation band in the blue/cyan region. Of the 12 primary candidates for polymer absorption filters for LED excitation, three were selected for use in applications. At time of design, each of these filters was the best option used, though over the course of this project the pool of filters analysed expanded resulting in more optimised designs. The first filter used was Laird 2424 Blue, a blue acrylic that was readily available at the time. Subsequently, a more in-depth analysis of filters was done. Roscolux Sapphire Blue, a thin photography filter, was the second excitation filter used. This was determined to be highest performance filter for blue LED excitation. It should be noted that Chabinyc et al. [128] also used a Roscolux filters, though the Congo Blue filter used there was deemed lower-performance with both a lower signal and poorer baseline rejection. Finally, a recent move to cyan LEDs necessitated the move to Lee 729, another thin photography filter that was determined to be the best for this new excitation wavelength. Other excitation filters considered are the SI.

Figure 3.6 shows the excitation spectra before and after filtering with the intensity normalised to a pre-filter height of one. Each of the absorption filters discussed above are shown along with a high performance interference filter from Chroma (ET470/40X). The amount of excitation light lost due to the excitation filter is quantified in Table 3.2.

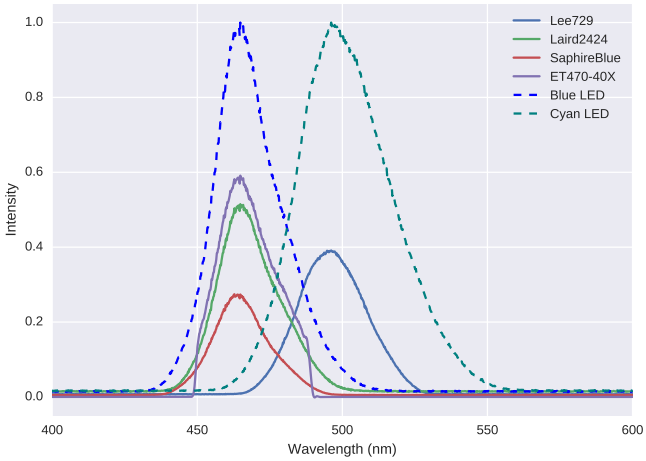

Figure 3.6: Spectra comparing the pre-filtered output of the LEDs with the result after filtering with three selected polymer absorption filters (Laird 2424 Blue, Roscolux Sapphire Blue, Lee 729) and a representative interference filter (ET470/40X, Chroma) as shown in Table 3.2. Peak heights have been normalised to the pre-filtered LED maximum intensity. Substantial excitation light is lost in all options. However, the excitation filter attenuates some of the ”tail” to the LED, shaping the spectra to be more suitable for emission filtering and reducing the baseline. The amount of LED light transmitted is comparable between absorption and interference filters, thought the on-off slope is much higher for the latter. This can affect other aspects of the design detailed in Section 3.4.5

Parameter	Chroma ET470/40X	Laird 2424 Blue	Roscolux Sapphire Blue	Lee 729
Thickness	3 mm	3 mm	85μm	85μm
LED	Blue (WP710A10QBC/G)			Cyan (WP710A10WG1C)
Transmission of Excitation Light	38.0%	61.8%	26.8%	32.5%

Table 3.2: Table comparing the transmission efficiencies for the three filters used in applications. The excitation filters substantially reduce the amount of excitation light, but reduce the baseline much more to realise improved SBR. This is explored in more detail in Section 3.4.4.

Each of these filters provides substantial attenuation of the LED light, leading to a reduction in excitation power. However, most of the light attenuated is from the edges of the LED output, especially at the higher wavelength edge. Thus, while these filters do reduce the excitation power, they reduce the baseline more leading to improved SBR. This is discussed in more detail in Section 3.4.4. There is not a substantial difference in transmission efficiencies between the filters with a factor of roughly two separating the lowest expected signal (Roscolux Sapphire Blue) from the highest (Laird 2424 Blue). However, this analysis only considers absolute light transmitted and omits two key factors: how useful is the light that is transmitted and how well does the filter attenuate baseline. Determination which of these filters is the best must therefore take into account the rest of the filter set. This is done in Section 3.4.5. It should be noted that in the case where a laser and interference filter is used, the transmission efficiency would be 90+% due to the very narrow FWHM of the laser fitting well within an interference filter pass band.

3.4.2 Fluorophore absorption

The amount of energy absorbed by the fluorophore can be expressed with the Beer-Lambert Law:

$$I = I_0 \times 10^{-\varepsilon \times L \times C} \tag{3.9}$$

$$A = I - I_0 = I_0 \left(1 - 10^{-\varepsilon \times L \times C}\right) \tag{3.10}$$

Where I is the intensity of light after passing through the sample, I_0 is the incident intensity of light on the sample, ε is the extinction coefficient, L is the sample length and C is the concentration. For these calculations, C will be set to 1 nM to determine per nM signals. L is equal to the sample thickness, t_{samp}, which is either the channel width or height depending on the optical arrangement. ε is more complicated, and a function of the wavelength. Most fluorophores report ε for only the maximum wavelength (ε_{max}) which is not representative of the system in most cases as the excitation wavelength is not at the maximum. Further, the LED illumination used here is broadband and this also needs to be taken into account. To do so, a multiplication was done. First, the desired fluorophore excitation spectrum was downloaded.[151] This spectrum was first normalised to a height of 1, then multiplied with the spectrum obtained from the LED passed through the excitation filter as presented in Figure 3.6, also normalized to a height of 1. The

multiplied spectrum is the relative efficiency with which the excitation light maps onto the excitation spectrum, and the ratio of the area under the curve of the multiplied spectrum to the area under the curve of the excitation light spectrum gives a correction coefficient for the efficiency with which the fluorophore absorbs light of a given wavelength.

$$E_{absorption} = \frac{AOC_{abs,norm \times exfilt,norm}}{AOC_{exfilt,norm}} \tag{3.11}$$

Where $AOC_{abs,norm \times exfilt,norm}$ is the area under the curve of the spectrum obtained by multiplying the absorption spectrum of the fluorophore with the transmission spectrum of the excitation filter and $AOC_{exfilt,norm}$ is the area under the excitation filter spectrum. All spectra are normalised. The area under curve was calculated using trapezoidal integration. The $E_{absorption}$ factor is multiplied to the peak absorption coefficient, ε_{max}, within the Beer-Lambert Law to determine the amount of power absorbed as in Equation 3.12.

$$A = \left(1 - 10^{-E_{absorption} \times \varepsilon_{max} \times t_{samp} \times 10^{-9}}\right) \tag{3.12}$$

per nM of fluorophore. Table 3.3 details the excitation efficiency for two common fluorophores (AF532 and Rhodamine B) used in our lab for the three main excitation sources + excitation filters described in Figure 3.6 and Table 3.2. Note that the interference filter + blue LED option has been replaced by a green laser + interference filter. This filter set is one recommended by Chroma specifically for AF532 and represents the optimum performance for this system

Light Source	Green Laser	Blue LED ()			Cyan LED ()	
Filter	Chroma ET470/40X	None	Laird 2424 Blue	Rosecolux Saphire Blue	None	Lee 729
AF532 $E_{Absorption}$	98.4%	10.8%	10.3%	8.8%	41.3 %	33.8%
Rhodamine B $E_{Absorption}$	43.9%	4.0%	3.7%	3.2%	20.8 %	15.9%

Table 3.3: Table of excitation efficiencies and $\varepsilon_{effective}$ for the excitation sources and filters used in this work, as well as a comparison to a standard green laser. LED based illumination has notably lower efficiency due to poorer spectral overlap. This results in LED-based LIF optics having a reduced signal as compared to lasers.

It is not surprising that the excitation efficiency of a 532nm green laser is very high for AF532, as this is precisely the usage scenario the fluorophore was designed for. Excitation with LEDs is spectrally less efficient than the laser, and this too is expected. Combining the poorer transmission efficiency in Section 3.4.1, and the overall lower power of LEDs vs. lasers in Section 3.3, it is clear the signal from LED-based optics is substantially less. The cyan system in Table 3.3 is notably more efficient at excitation than the blue based optics, however as seen in Section 3.4.5, this ultimately leads to other trade-offs down the chain. There are some other fluorophore specific factors to consider, and these are described in Section 3.5.

3.4.3 Emission filtering

Emission filtering is crucial for baseline suppression in any filter based fluorescence detection instrument. In an ideal instrument, the emission filter will suppress all of the excitation light (post-excitation filter) and allow all of the fluorescent light through. The two primary assessment factors for a good emission filter are thus having a very high OD in the "off" region, which results in higher baseline suppression, and a high transmission in the "on", which maximizes the amount of fluorescent light detected by the system. The ultimate baseline and transmission efficiencies are thus dependent on the excitation source, excitation filter and fluorophore used. This section details the emission filter's effect on the fluorescent signal (i.e. transmission efficiency) while baseline considerations are discussed in detail in Section 3.4.4.

There are many options for interference filters that could be used for any given fluorophore. However, for absorption filters the options are more limited. From the initial pool of filters surveyed above, five were identified as potential polymer absorption filters due to their clean long-pass behaviour compatible with the excitation filters discussed above. These five were then tested to estimate their baseline rejection performance (detailed below in Section 3.4.5), resulting in two good filters for these applications. The first is Acrylite 2C04, an orange coloured acrylic that is widely available and has been previously alluded to in the literature.[153] The majority of the early work on this project was based on this plastic. Later, the photography filter Lee 507 was used. Of the filters tested, Lee 507 had the highest OD and lowest baseline as discussed in Section 3.4.4.

The transmission of emission light through the emission filter was calculated by first finding the transmission spectra of the filter. This was done using a spectrometer (USB-4000, Ocean Optics) and a pulsed xenon light source (PX-2, Ocean Optics) that was attenuated with an OD 0.9 neutral filter to prevent saturation of the spectrometer CCD. The integration time and pulsed light duration were matched such that each acquisition contained a single xenon pulse. 200 μm diameter optical fibres were used to make all optical connections. The resultant transmission spectra was multiplied with the emission spectra of the fluorophore obtained either from the Life Technologies website[151] for AF532 or measured directly with a spectrophotometer (RF1501, Shimadzu) for Rhodamine B, and the ratio of the area under the curve of the multiplied spectra to the fluorophore emission spectra was assessed. This corresponds to the amount of emission light that transmits through the emission filter as shown in Equation 3.13.

$$T_{em} = \frac{AOC_{emission,norm \times emfilt,norm}}{AOC_{emission,norm}} \tag{3.13}$$

Where $AOC_{emission,norm \times emfilt,norm}$ is the area under the curve of the spectrum obtained from multiplying the fluorophore emission spectrum with the transmission spectrum of the emission filter, both normalised, and $AOC_{emission,norm}$ is the area under the fluorophore emission spectrum. Figure 3.7 shows the transmission spectra for the two filters used as well as the recommended interference filter for AF532 from Chroma and the emission spectra of the two main fluorophores, and Table 3.4 shows their quantified transmission efficiencies.

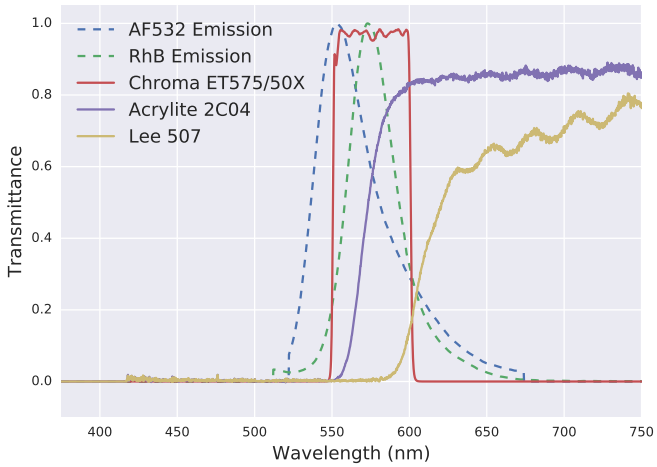

Figure 3.7: Transmission spectra for the two absorption filters used and the recommended interference filter from Chroma for AF532, along with the emission spectra of both AF532 and Rhodamine B. The transmission spectra were obtained as detailed above while the emission spectra were exported from the ThermoFisher Spectral Viewer. [151] While each of the emission filters attenuates the fluorescent light to some degree, the Lee 507 filter transmits substantially less than the other two options.

Filter	Chroma ET575/50X	Acrylite 2C04	Lee 507
Cutoff Wavelength 1	546 nm	552 nm	581 nm
Cutoff Wavelength 2	607 nm	-	-
Transmission of AF532	56.5%	33.5%	7.5%
Transmission of Rhodamine B	78.0%	51.8%	7.4%

Table 3.4: Table of transmission efficiencies for AF532 and Rhodamine B emitted light through selected optical filters. The high end Chroma interference filter has the highest performance, though Acrylite 2C04 also has good transmission efficiency. Lee 507 significantly attenuates the fluorescent light

From the table and graph above, it is clear that Lee 507 has by far the worst performance of the three filters in terms of the magnitude of the fluorescent signal. However, a filter needs to be considered as part of its entire set. This is done below in terms of the baseline (Section 3.4.4) and signal (Section 3.4.5).

3.4.4 Baseline considerations

Baseline suppression is one of the key challenges in designing fluorescence detection instrumentation, where baseline refers to optical signal that does not originate from the fluorescence of the sample. There are three main sources of

baseline in the system, assuming the system is well sealed from the environment with no leakage light entering. The first potential source of baseline is autofluorescence in the system, from the microfluidic chip material, fingerprint contamination, sieving matrix, etc. We have selected PMMA as a chip material partially due to its low autofluorescence.[93] Other sources of fluorescence that are not the sample are limited through careful handling of the system and chips. The second is from Raman scattering of the excitation light, either from the chip material or the fluidic sample. Based on measurements made by others, Raman scattering is comparable in intensity to roughly 1 pM or less of fluorophore emission.[122] This is relatively negligible both compared to the baselines in the system described here as well as the target LOD. Finally, there is Rayleigh scattering of excitation light, the primary source of baseline. In contrast to autofluorescence and Raman scattering, Rayleigh scattering has the same wavelength as the excitation light. Thus, it can be removed with spectral filtering.

Depending on the excitation source and filters used, the baseline performance can be limited by one of three factors. The first limiting factor is the OD of the filter set used. For example, a 5 mW laser with an effective filter OD of six would have a baseline signal of 5 nW. Though low, this is not an uncommon signal in fluorescence and is multiple orders of magnitude higher than the signals encountered in the LED-based instruments here. Most laser/interference filter applications would be OD limited, and improved performance can be had by increasing the number of filters used. The second limitation regime is the presence of high wavelength excitation light that is not absorbed by either filter. Most polymer absorbing filters do not absorb in the red/infra-red, thus any light in this region will be passed directly into the detector. Figure 3.8a presents the absorption spectra for excitation filters Roscolux Sapphire Blue and Lee 729 along with the emission filters Acrylite 2C04 and Lee 507 illustrates this phenomenon in that none of the four filters absorbs well in the red region. Thus, long wavelength light is not attenuated at all. This ”bleed-through” light is distinct from the OD limitation in that more filtering will fundamentally not improve the baseline (as the filters are having no effect). This regime is common in LED applications where there is noticeable amounts of parasitic light in the red and infra-red regions of the spectra.[81] Figure 3.8b shows blue LED light transmitted through Acrylite 2C04 and two comparable Schott glass filters from Edmund Optics (OG570 and OG590). The transmission spectra of each approaches the same curve, strongly suggesting the source of this light is the LED itself and not some sort of autofluorescent filter material. Further, there is not an appreciable difference in the amount of LED light suppressed other than the cut-off wavelength between these three filters. Despite the similar performance for this application, the polymeric Acrylite 2C04 is orders of magnitude less expensive than the glass filters. This effect was observed for multiple blue, cyan and green LEDs tested.

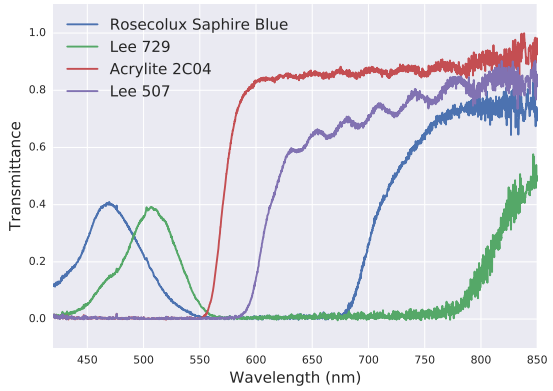

(a) Transmission spectra obtained using a pulsed xenon lightsource and spectrometer. None of these polymer filters have a high optical density above 800 nm, thus any excitation light in this region will be present as baseline

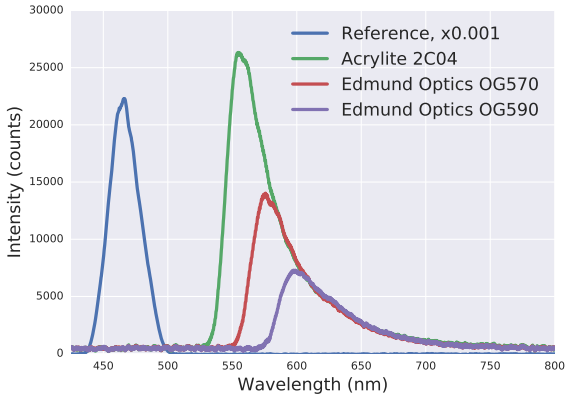

(b) Spectra showing a blue LED reference, and the amplified light visible after shining the blue LED through a series of commercially available filters. The light from each filter converges to the same curve, suggesting the source of this "tail" is from the LED and not from autofluorescence of the filter material. This parasitic light in high wavelengths is typical of LEDs and well documented in the literature [81,147]

Figure 3.8: Filter performance of select absorption filters

This subsection will first detail the method of baseline assessment, followed by a discussion of the baseline for the various filters and excitation sources discussed above.

Calculating baseline rejection

Baseline rejection is defined here as the overall OD of the excitation light through both the excitation and emission filters. Interference filter providers detail the OD of the filter as a function of wavelength. This is not true for the absorption filters used in this work. Further, measuring absorption spectra for the filters is not sufficient for determining the OD due to the limited dynamic range of the spectrometer. To address this issue a method was developed to measure the overall effective OD of the entire excitation + filter system. Two spectra obtained using a spectrometer (USB-4000, Ocean Optics) were used. The first is the same one from Section 3.4.1 of the excitation source though the excitation filter. The second spectra used is of the excitation source through both the excitation and emission filters. The ratio of the area under the curves adjusted for integration time gives the relative baseline light as compared to the light used to excite the fluorophore in terms of only spectral effects. This is shown in Equation 3.14.

$$BL_{rejection} = \left(\frac{AOC_{bothfilters}}{AOC_{exfilt}} \times \frac{t_{int,exfilt}}{t_{int,bothfilters}} \right)^{-1} \tag{3.14}$$

Where $AOC_{bothfilters}$ is the area under the curve of the spectrum obtained through both filters, AOC_{exfilt} is the area under the curve of the spectrum obtained from the excitation filtered LED light and t_x is the integration time associated with those spectra. The advantage of this method is that the integration time on the spectrometer can be increased substantially when measuring the excitation source through both filters. This allows for a better determination of the

spectral shape of the baseline (which in turn allows for the determination of the dominant baseline source), and extends the dynamic range of the experiment.

Baseline rejection for filter combinations

Table 3.5 shows the the results of the calculation described above for a few specific filter combinations that were used in instruments as compared to a laser/interference filters used in a conventional instrument. Other filter combinations described in the SI. The spectra shape of the excitation light and baseline light is shown in Figure 3.9

Light Source	Excitation Filter	Emission Filter	Baseline Rejection	Effective OD
Green Laser	Chroma ZET532/10x	Chroma ET575/50X	$> 10^6$ †	6+ †
Blue LED	None	2C04	2.4×10^3	3.4
Blue LED	Laird 2424 Blue	2C04	4.1×10^4	4.6
Blue LED	Roscolux Sapphire Blue	2C04	1.1×10^5	5.0
Cyan LED	Lee 729	Lee 507	2.1×10^6‡	6.3

Table 3.5: Table of baseline performance for a variety of excitation source, excitation filter and emission filters used in this work. As the optical design was iterated, higher baseline rejection was required. The recent cyan LED + Lee filters did not have measurable baseline with the current instrumentation, thus the baseline rejection was estimated using a higher power LED.
†: obtained from Chroma website.[152] Each filter is independently OD 6+.
‡: determined with a high power LED

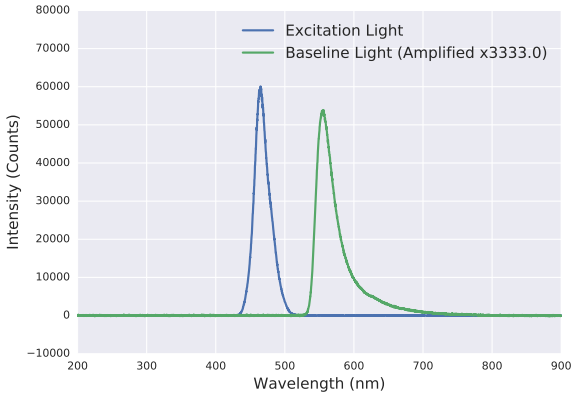

(a) Blue LED, no excitation filter, 2c04 emission filter

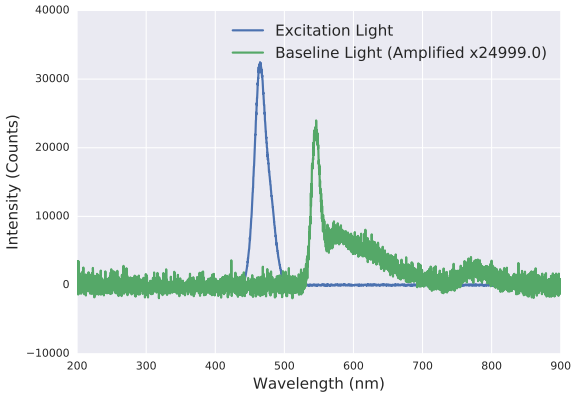

(b) Blue LED, Laird2424 Blue excitation filter, 2c04 emission filter

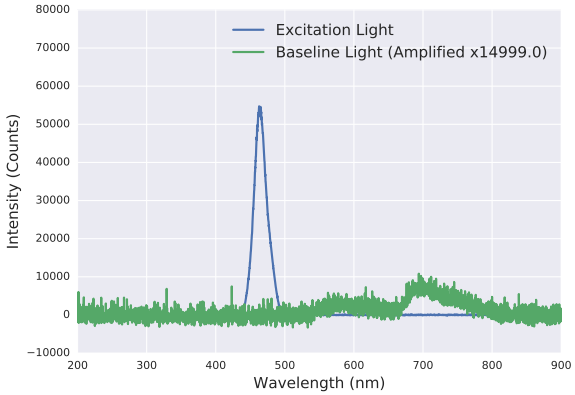

(c) Blue LED, Sapphire Blue excitation filter, 2c04 emission filter

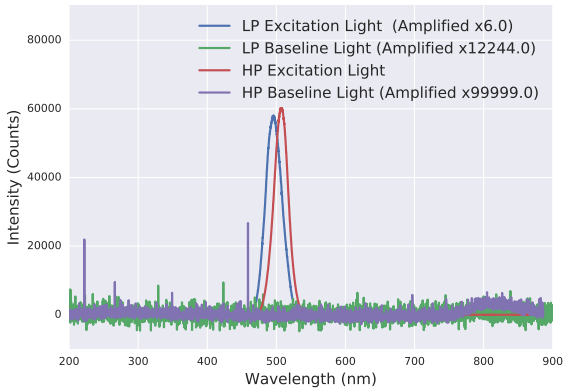

(d) Cyan LED, Lee 729 excitation filter, Lee 507 emission filter

Figure 3.9: Spectra of the excitation light (LED light filtered with an excitation filter) and the amplified spectra of the baseline light (LED light filtered with both an excitation and emission filter). The red/IR "bleed-through" dominates the baseline of the blue LED based sets and is easiest seen in Figure 3.9a. The Laird 2424 Blue filter attenuates the baseline substantially, but there is a noticeable peak at 545 nm where the excitation and emission filters overlap slightly. Roscolux Sapphire Blue absorption spectra does not overlap with Acrylite 2C04 at all and thus there is no strong peak under 550 nm. Instead, this filter set is limited by the IR absorption of the excitation filter and limited OD around 550 nm. The cyan LED + Lee729 + Lee 507 filter set baseline was not measurable with the equipment used as shown in the blue and green curves of Figure 3.9d. To estimate the filter performance, a high power LED was tested. The baseline light is above 780 nm, consistent with the transmission spectra of the Lee 729 filter in Figure 3.8a, though at a much lower intensity relative to the raw LED light than other filter sets. Thus Lee 729+Lee507 filter set has the best baseline performance.

As seen in both Table 3.5 and comparing Figure 3.9a to the other figures in Figure 3.9, adding an excitation filter to the system can substantially suppress the baseline. For the case of Figure 3.9a where no excitation filter is used, the baseline is quite high. The effective OD of the system to baseline light is just over three, making high gain/high sensitivity applications difficult. The first excitation filter used, Laird 2424 blue in Figure 3.9b increased the baseline suppression by an additional order of magnitude, despite the fact that the pass-band of the excitation and emission

filters overlap a little around 545 nm. This causes the interesting peak in the baseline spectra. To address this, an excitation filter a with a slightly earlier cut-off wavelength was needed. Roscolux Sapphire Blue filled that need well. Figure 3.9c shows a slight bump in the baseline around 575 nm, then a second larger bump around 700 nm. Based on Figure 3.8a, the Roscolux Sapphire Blue filter does not stop any light beyond approximately 675 nm. Thus the second larger bump is from IR-bleed through of both filters. The first bump is barely present in the Laird 2424 blue spectra as well, suggesting this is from insufficient OD in the Acrylite 2C04. Thus this excitation filter is within a factor of three of the performance limit of Acrylite 2C04, and any more substantial reductions would need to change both filters. Initial tests of the cyan LED based optical system with the two Lee filters yielded a baseline that was not measurable with the spectrometer (green curve in Figure 3.9d). In order to estimate the baseline rejection, the typical cyan LED was replaced with a high power LED used for lighting applications (LXZ1-PE01, Lumileds). This LED was effectively 6x brighter and slightly red-shifted in its emission spectra as compared to the low power LED typically used. This red-shifting and higher intensity allowed for the determination of the weak point in the filter set. The effective OD of the Lee filter set was estimated to be 6.3 for cyan LED excitation, a value much higher than previous filters and comparable to interference filters. The high power LED experiment also found that, like the Roscolux filter, the Lee filter set is limited by the high wavelength LED light above 780 nm. Thus, again, IR block material might prove useful in future designs.

3.4.5 Spectral optimisation

The spectral performance of the instrument is optimised by the SBR, which in turn requires attention to the effect of the filters on both the signal and the baseline. To this end, three key figures of merit are proposed: $Sig_{relative}$, $BL_{rejection}$ and Q_{filt}. $Sig_{relative}$ is a measure of how the filters affect the fluorescent signal. This is shown in Equation 3.15 and is the product of the transmission efficiency of the excitation light, the transmission efficiency of the emission light and the relative efficiency the filtered light is absorbed by the fluorophore.

$$Sig_{relative} = T_{exfilt} \times E_{absorption} \times T_{em} \tag{3.15}$$

Where T_{exfilt} is calculated in Equation 3.8 above, T_{em} is calculated in Equation 3.13 above and $E_{absorption}$ is the relative efficiency of fluorophore absorption of the excitation filtered light as calculated in Equation 3.11. $Sig_{relative}$ is therefore specific to the excitation filter used, the emission filter used and the fluorophore in question. The second factor, $BL_{rejection}$ is an assessment of how well the filter set attenuates the baseline and is a function of the two filters used. This is calculated in Equation 3.14 in the Section above. Finally, Q_{filt} is the product of the signal and baseline rejection as shown in Equation 3.16. Q_{filt} is a measure of how well a certain filter set improves the SBR of the instrument from a spectral point of view for a given fluorophore.

$$Q_{filt} = Sig_{relative} \times BL_{rejection} \tag{3.16}$$

$Sig_{relative}$, $BL_{rejection}$ and Q_{filt} were used to assess a number of filter combinations which are presented in the SI. The best filters combinations (i.e. highest Q_{filt}), and those used in the optics modules developed later in this chapter, are

presented in Table 3.6 for the fluorophore AF532.

Excitation Source	Excitation Filter	Emission Filter	T_{exfilt}	Excitation Efficiency ($E_{absorption}$)	T_{em}	$BL_{rejection}$	$Sig_{relative}$ (x100)	Q_{filt}
Blue LED	None	2C04	1	0.108	0.335	2.4×10^3	3.62	87
Blue LED	Laird 2424 Blue	2C04	0.455	0.103	0.335	4.1×10^4	1.57	644
Blue LED	Roscolux Sapphire Blue	2C04	0.234	0.088	0.335	1.1×10^5	0.69	759
Cyan LED	Lee 729	Lee 507	0.292	0.338	0.075	2.1×10^6	0.74	15586
Green Laser	Chroma ZET532/10x	Chroma ET575/50X	0.9	0.984	0.565	$> 10^6$	50.04	> 500000

Table 3.6: Table summarising filter performances. While the baseline performance of the cyan LED optics is comparable to interference filters, the efficiency losses that occur from the spectral separation of the excitation and emission transmissions leads to a substantially lower performance as compared to a state of art laser+interference filter system. This difference is estimated as being at least an order of magnitude. However, such a system is not scalable, and many orders of magnitude more costly.
†: obtained from Chroma website [152]

Based on Table 3.6, as well as further analysis in the SI, the best performance from the absorption filters tested is Cyan LED + Lee 729 + Lee 507 set with a Q_{filt} value one to two orders of magnitude higher than any other option tested. This high Q_{filt} value comes from the very high baseline rejection. This was one of the motivating factors towards switching the excitation LED to cyan and the increased baseline attenuation of this set was the primary enabling technology of the SIS optical implementation described in Section 3.8.4. This filter set was used in the most recent generation of optics described in Section 3.8.4 below.

Of the blue-LED based filter sets the Roscolux Sapphire Blue + 2C04 was the highest performing. The introduction of the Roscolux Sapphire Blue filter over the Laird 2424 Blue filter improved the baseline dramatically, enabling the higher instrument gain discussed in the detection electronics chapter (Section 4.5). This filter set was used in the OPT3 optics which demonstrated the best LOD for a LED and photodiode based CE instrument. This is discussed more in Section 3.8.3 below and in the application discussion in Section 5.4

3.5 Other fluorophore considerations

In addition to the spectral considerations above, there are two other factors that are fluorophore dependent in the system. The first is the QY. This factor takes into account the efficiency with which an excited state results in a radiative emission and is typically reported for the fluorophore in use. The second factor is to take into account the energy lost by the excited state to various relaxation processes that cause the Stokes Shift. This factor is estimated by finding the average excitation wavelength and dividing it by the average emission wavelength. The average excitation

wavelength is the average wavelength of the multiplication of the spectrum of the excitation light (i.e. LED light after filtering) and the excitation spectrum of the fluorophore. This is shown in Equation 3.17

$$SS = \frac{\int_{300}^{1000} S_{exfilt} \times S_{excitation} d\lambda}{\int_{300}^{1000} S_{emission} d\lambda} \tag{3.17}$$

The values for these parameters for AF532 and Rhodamine B are shown in Table 3.7. There is a very minimal difference between the various excitation sources used in the Stokes Shift calculation. The quantum yield of AF532 was readily obtained from the source,[154] though that for Rhodamine B was more complicated. The value of 0.31 is for the Rhodamine B zwitterion form that occurs in basic solutions. This form can be differentiated from the acid form based on the maximum absorption and emission wavelength. These wavelengths were measured for samples in the lab. Thus, the value of 0.31 reported by Lopez Arbeloa et al.[155] was used.

Fluorophore	LED	Excitation Filter	Quantum Yield (QY)	Stokes Shift Factor (SS)
AF532	Blue	None	0.61 [154]	0.836
	Blue	Laird 2424 Blue		0.832
	Blue	Roscolux Sapphire Blue		0.823
	Cyan	Lee 729		0.878
Rhodamine B	Blue	None	0.31 [155]	0.823
	Blue	Laird 2424 Blue		0.817
	Blue	Roscolux Sapphire Blue		0.81
	Cyan	Lee 729		0.865

Table 3.7: Table of the quantum yield and Stokes Shift parameters for the two main fluorophores used in the lab and the various excitation sources discussed.

3.6 Light collection efficiency

The final component to estimating the optical signal is the light collection efficiency (LCE) which is the proportion of light emitted by the sample that is collected by the optics and detected. There are two main components to this: the proportion of the sample the collection optics probe and the proportion of the fluorescent light emitted by this probed volume that is collected. For example, consider a confocal optical module with an objective lens with a numerical aperture of 0.75 and a spot size of 10 μm probing a 100 μm channel (for example, the Nikon lens used in the Illumina HiSeq2000[156,157]), a top of the line objective lens for such systems. To estimate the proportion of the sample probed, the ratio of the spot size volume to the sample volume can be calculated. To determine the proportion of fluorescent light collected is more difficult. If we assume the lens is in perfect focus, the limiting factor is the input angle into the lens. This input angle maximum is defined by the numerical aperture. Fluorescence from a sample that contains a number of fluorophores, such as in CE, is typically assumed to be an isotropic phenomenon, thus the collection

efficiency can be estimated as the ratio of the solid angle of this maximum input angle to a sphere as in Equation 3.18

$$
\begin{aligned}
LCE &= \frac{\Omega}{4\pi} \\
LCE &= \frac{2 * \pi * (1 - \cos(\theta))}{4\pi} \\
LCE &= \frac{2\pi \left(1 - \cos\left(\sin^{-1}(NA)\right)\right)}{4\pi}
\end{aligned}
\tag{3.18}
$$

Thus, this objective would probe only 0.4% of the sample volume and collect 18% of the emitted light, resulting in an overall efficiency for the sample of 0.068%. This very low value is largely due to the very minimal sample volume being probed. A larger spot-size would increase this signal though at the expense of decreasing the optical resolution of the system. However, for CE systems this change in optical resolution might not have an effect on the separation resolution. Thus, decreasing the probed volume would not have result in an improved separation while decreasing the LIF signal. Instead, the probed volume must be roughly equivalent to the size of the sample to maximize the detection while maintaining comparable resolution.

There are two methods of collecting the emission light described here. The first is a system where the fluidics and electronics are held in close proximity with no lenses. This is the situation representative of a monolithic LOC system. However, as discussed previously, the NRE issues prevent the prototyping of this instrument directly. To circumvent this issue an optical system composed of two short working distance, cylindrical GRIN lenses was made. This optical system allows the use of the polymer microfluidics discussed in Chapter 2 while maintaining the same *LCE* as a future monolithic instrument. Thus, this serves as a testbed from which optical designs and fluidic protocols can be verified for future miniaturisation, thus making this a scalable optical design. In terms of prototyping cost, the use of GRIN lenses maintains a high *LCE* without resorting to very expensive and bulky microscope objectives as found in most commercial equipment.

3.6.1 Proximity calculation

In a monolithic CMOS instrument, the collection of fluorescent light is a strictly geometrical argument, dependent on the size of the sample, the size of the detector and their separation. In the limit of infinitesimal sample (i.e. a single point) directly in contact with the detector, the LCE reaches its theoretical maximum of 50% as described in Figure 3.2a above. Practically, there must exist some separation between the two as shown in Figure 3.10 below, which results in a decrease in the LCE as described by Equation 3.19.

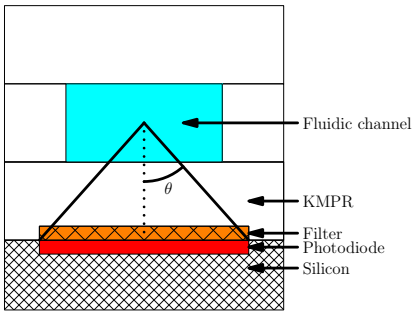

Figure 3.10: Illustrating the *LCE* for a system where a finite detector is placed a finite distance from the sample. The angle θ can be used to calculate the *LCE* as per Equation 3.19. Figure taken from Hall et al.[48]

$$
\begin{aligned}
LCE &= \frac{\Omega}{4\pi} \\
LCE &= \frac{2\pi(1-\cos(\theta))}{4\pi} \\
LCE &= \frac{\left(1-\frac{d}{\sqrt{d^2+r^2}}\right)}{2}
\end{aligned}
\tag{3.19}
$$

where d is the distance from the sample to the detector and r is the radius of the detector, assuming a circular detector and a point sample directly above the detector. However, when considering an entire sample plug above a detector this equation will substantially overestimate the *LCE*. To address this a simple model was developed that first determines the solid angle of a circular detector from an arbitrary point in the well then calculates an average weighted on radius to estimate the *LCE*.

Consider a simple triangle where the base is the photodiode with a diameter a and having two other sides b and c that connect the edges of the photodiode to the sample point. This triangle has a height h that is the vertical distance of the sample point above the base and has a value r which is the horizontal distance from the sample point to the detector centre. The sides b and c define an angle 2θ which is used to calculate the solid angle. This model is shown in Figure 3.11

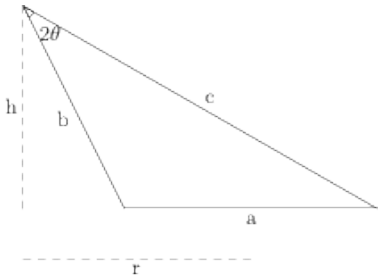

Figure 3.11: Diagram of Triangle used in the calculation. This allows for the solid angle to be expressed in terms of the radial distance from the photodiode centre, the photodiode size and the vertical distance from the photodiode top.

The angle 2θ can be calculated:

$$
\begin{aligned}
b^2 &= h^2 + (r - \frac{a}{2})^2 \\
b &= \sqrt{h^2 + r^2 - ar + \frac{a^2}{4}} \\
c^2 &= h^2 + (r + \frac{a}{2})^2 \\
c &= \sqrt{h^2 + r^2 + ar + \frac{a^2}{4}}
\end{aligned}
\tag{3.20}
$$

Using the Rule of Cosines:

$$
\begin{aligned}
cos(2\theta) &= \frac{c^2 + b^2 - a^2}{2bc} \\
cos(2\theta) &= \frac{h^2 + (r + \frac{a}{2})^2 + h^2 + (r - \frac{a}{2})^2 - a^2}{2 \times \sqrt{h^2 + r^2 - ar + \frac{a^2}{4}} \times \sqrt{h^2 + r^2 + ar + \frac{a^2}{4}}} \\
cos(2\theta) &= \frac{2 \times h^2 + 2 \times r^2 - \frac{a^2}{2}}{2 \times \sqrt{h^2 + r^2 - ar + \frac{a^2}{4}} \times \sqrt{h^2 + r^2 + ar + \frac{a^2}{4}}}
\end{aligned}
\tag{3.21}
$$

The *LCE* can be calculated from the solid angle as in Equation 3.18 and 3.19, and, using an identity converted, expressed in terms of h, r and a

$$
\begin{aligned}
LCE &= \frac{2\pi(1 - \cos(\theta))}{4\pi} \\
LCE &= \frac{1 - \sqrt{\frac{1 + \cos(2\theta)}{2}}}{2} \\
LCE &= \frac{1 - \sqrt{\frac{1 + \frac{2 * h^2 + 2 * r^2 - \frac{a^2}{2}}{2 * \sqrt{h^2 + r^2 - ar + \frac{a^2}{4}} * \sqrt{h^2 + r^2 + ar + \frac{a^2}{4}}}}{2}}}{2}
\end{aligned}
\tag{3.22}
$$

The LCE scaling in both r and h directions can be determined and plotted from this equation. The total LCE is the average LCE of the volume weighted by the radius to account for the cylindrical coordinates. Considering a monolithic LOC system where a 100 μm photodiode is placed directly below photoresist channels which are 100 μm wide and 40μm deep as in previously published work[50] with 15 μm separation between the channel and detector. According to Equation 3.19, the *LCE* would be 36%. This is the point of maximum collection and compares very favourably to the numerical aperture limited lens,being equivalent to a 0.98 numerical aperture in terms of collection angle. The total *LCE* of the sample can be calculated according to Equation 3.22 to be 6.2%. For the confocal lens the *LCE* would be

estimated to be 0.068%. This is an improvement of over an order of magnitude and illustrates the primary advantage of the miniaturisation for fluorescence detectors.

This calculation approach can also be used to estimate the spot-size of the system. As detailed above, the spot-size here is defined as the distance from the centre axis where the *LCE* drops to half of its maximum. This is a function of the photodiode size and and separation of the sample from the photodiode, with the spot-size increasing with either of these parameters. The effect of sample-photodiode separation is illustrated in Figure 3.12 which shows the trend of *LCE* vs. radial distance from the plug centre for a 100 μm photodiode at various distances from the sample. The approach taken in this work was to first set the photodiode size to the same as the channel for good *LCE*, then determine the maximum channel separation such that the spot-size remains below the target of 100 μm. For a 100 μm photodiode, the the spot-size remains below 100 μm provided the sample-photodiode separation remains below 50 μm. A typical value provided by our collaborators at the University of Alberta is 15 μm. This gives a spot-size estimate of 89 μm which meets the target requirements.

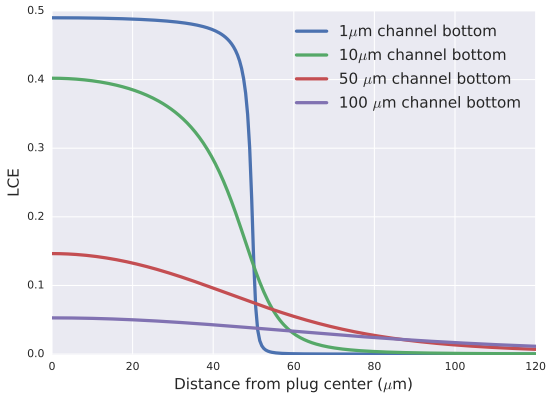

Figure 3.12: Plot of the *LCE* as a function of radial distance from the plug centre for a 100 μm diameter photodiode held at various distances from the sample. As the sample-detector distance shrinks, the *LCE* approaches the theoretical maximum of 50% and the spot size approaches the size of the photodiode. This suggests to maintain the 100μm spot size requirement the photodiode must be less than 50μm away from the sample.

3.6.2 GRIN lenses based optics

The proximity approach to *LCE* of a monolithic CMOS LOC device is very good for detection, but as described in Section 3.1.3 this is difficult to prototype due to the high NRE costs of CMOS development. This project focused on designing testbeds that imitated the monolithic performance as close as possible but provided a physical separation of the microfluidics and CMOS electronics. This allowed for separate electronic and fluidic design cycles, and re-use of the CMOS without fear of fouling. As described in Hall et al.,[48] the testbed was implemented with GRIN lenses. GRIN lenses are cylindrical optical elements that have a refractive index that varies quadratically with radius which confines light within the lens with periodic oscillations in space. The advantage to using GRINs is that their short working distance is similar to a proximity situation for light collection. This is further assisted by their flat surface which can be brought very close to a fluidic chip. Further, they have low aberrations, which allows for high

performance with a low-lens count. A GRIN lens has four main parameters: its diameter, its length, its gradient index and its refractive index in the centre.[158] Lenses are often spoken of in terms of pitch, which is a fraction of the periodic oscillations and related to the gradient index and lens length. Two GRIN based optical systems were developed: one for interfacing multifunctional CMOS chips with polymer fluidics and one for use in discrete instrumentation systems. Both will be discussed below.

GRIN Optical Relay

In order to avoid the NRE issue but also test and apply prototype CMOS devices a "packaged CMOS" instrument was developed. The primary challenge for this project was the interface, determining how to bring chips in close contact to the CMOS without disturbing the bond wires in the package. This was further complicated by the fact that in a fully integrated system a high density absorption filter can be deposited with only a few microns, but adding a comparable discrete filter can take multiple millimetres. To address this, an optical system (shown in Figure 3.2b in Section 3.1.3) was developed where 0.25 pitch GRIN lenses (#64-519, Edmund Optics) were separated by an absorption filter. A 0.25 pitch lens has a focal point directly on its surface, thus this system essentially mirrored a proximity system as close as possible with as few elements as possible, while physically separating the optical plane from the CMOS. This allowed for the decoupling of fluidic and CMOS design cycles and the prototyping of demonstrations that leveraged the prototype CMOS chips. However, with the introduction of lenses, the *LCE* was again limited by the numerical aperture which, at 0.46, resulted in an estimate of 5.6%. This optical system was used to demonstrate the application in Chapter 5, Section 5.2 and published in detail in Hall et al..[48]

Focusing GRIN lenses

Due to multiple reasons discussed in more detail in Section 4.2 and Section 5.3, the prototype CMOS chip used in the optical relay was unsuitable for future LIF detectors. Thus, there was a need to create a similar optical relay system, but with commercially available photodiodes. The best candidate that was readily available was the OSRAM semiconductor SFH 2701 which has a 300 μm acrylic protective layer over its active area. This is substantially more than the negligible thickness protective insulator deposited on the CMOS chip, thus the 0 working distance GRIN relay could no longer be used. Instead, we opted to move to a 0.23 pitch GRIN (2306A, Thorlabs) which is designed to collimate light from its working distance (here 234 μm). Thus, while not exact, this lens operates similarly with the discrete photodiode as the previous 0.25 pitch lens operated with the CMOS chip. The other popular GRIN lens pitch available, and the one used in the previous Backhouse group optics module, is 0.29 pitch. However, since the 0.29 pitch is greater than 0.25 it does not collimate and therefore would require completely different designs. The lens manufacturer was also changed from Edmund Optics to ThorLabs. This was done as Thorlabs reports the optical constants used for adjusting the GRIN specifications to non-design wavelengths in a process described below. This allowed for more accurate designs. The collection optics of all of the optical systems that were designed are based on the two GRIN system shown above, and the majority were using the discrete photodiode + 0.23 pitch lenses.

GRIN lens chromatic adjustment

Adjusting the GRIN parameters to take into account wavelengths beyond the explicit design wavelengths is a necessity as there is no commercial provider of GRIN lenses at the visible wavelengths that these fluorescence systems target. The three main parameters of a gradient index lens are the refractive index at the centre, the gradient constant and the pitch. The refractive index at the centre can be expressed as:

$$n_0 = B + \frac{C}{\lambda^2} \tag{3.23}$$

Where B and C are constants and λ is the wavelength. The gradient index can be expressed as:

$$g = K0 + \frac{K1}{\lambda^2} + \frac{K2}{\lambda^4} \tag{3.24}$$

Where $K0$, $K1$ and $K2$ are constants. From these parameters the refractive index across the lens can be calculated:

$$n(r) = n_0 \left(1 - \frac{rg}{2}\right) \tag{3.25}$$

The pitch is expressed as:

$$P = \frac{gZ}{2\pi} \tag{3.26}$$

Where P is the pitch, and Z is the lens length. The lens working distance can also be expressed[158]:

$$h = \frac{1}{n_0 g \tan(gZ)} \tag{3.27}$$

Where h is the working distance. Therefore, given the lens length (from the datasheet) and the constants B, C, $K0$, $K1$ and $K2$ all relevant GRIN lens parameters can be calculated. Thorlabs provides files for use in the popular ray tracing software Zemax for their lenses specifying the material (SL1.8 glass, gradient9), and thus the above parameters can be extracted from Zemax itself. These parameters are shown in Table 3.8

Parameter	Value
Material	SL1.8 glass with gradient9
B	1.5868
C	$8.14 \times 10^{-3} \mu\text{m}^2$
$K0$	0.3238 mm^{-1}
$K1$	$5.364 \times 10^{-3} \text{mm}^{-1} \mu\text{m}^2$
$K2$	$2.626 \times 10^{-4} \text{mm}^{-1} \mu\text{m}^4$

Table 3.8: Constants for wavelength corrections to GRIN lens parameters.

Since this development, all lenses used have been the Thorlabs 2306A lenses as the wavelength correction can be applied. Unfortunately, Thorlabs does not market a 0.25 pitch lens and optical relay such as those above cannot be

made. Table 3.9 shows the effect of wavelength change on the centre index n_0, gradient index g and working distance as estimated based on the above equations.

λ (nm)	n_0	g (mm^{-1})	Working Distance (mm)
630	1.6073	0.339	0.2337
591	1.6101	0.341	0.2135
575	1.6114	0.342	0.2075

Table 3.9: Calculated values for the GRIN lens for various wavelengths. The lenses are designed for 630 nm, and the 630 nm calculations are fully consistent with those on the Thorlabs datasheet

There are three main conclusions to draw from Table 3.9. The first is that the calculated values for 630 nm (the design wavelength of the lenses) is fully consistent with the values from the datasheet, verifying the method above. Further, the working distance does not change very much and the lens remains focusing with a positive working distance. The working distance will remain positive provided $g < 0.368$ mm^{-1}, which is true for all the visible wavelengths we are dealing with. However, it should be noted that the working distance decreases with decreasing wavelength. While parameters are not given for the Edmund Optics lens used in the relay, this does suggest that the relay is actually diverging at the lens surface and thus less efficient than anticipated.

GRIN ray tracing tool

The values in Table 3.9 can be used to design systems where both the emission source and photodiode are at the working distance of the first and second GRIN lens. However, in order to visualise this design and provide a rough estimation of *LCE* a GRIN ray tracing tool was developed based on the equations in Yariv and Yeh.[158] Equation 3.28 shows the ray matrix for a two GRIN lens system.

$$\begin{bmatrix} r_{out} \\ r'_{out} \end{bmatrix} = \begin{bmatrix} 1 & d_{det} \\ 0 & 1 \end{bmatrix} \begin{bmatrix} 1 & 0 \\ 0 & n_{grin} \end{bmatrix} \begin{bmatrix} cos(g_2 z_2) & \frac{sin(g_2 z_2)}{g_2} \\ -g_2 sin(g_2 z_2) & cos(g_2 z_2) \end{bmatrix} \begin{bmatrix} 1 & 0 \\ 0 & \frac{1}{n_{grin}} \end{bmatrix} \begin{bmatrix} 1 & d_{sep} \\ 0 & 1 \end{bmatrix} \ldots \\ \ldots \begin{bmatrix} 1 & 0 \\ 0 & n_{grin} \end{bmatrix} \begin{bmatrix} cos(g_1 z_1) & \frac{sin(g_1 z_1)}{g_1} \\ -g_2 sin(g_1 z_1) & cos(g_1 z_1) \end{bmatrix} \begin{bmatrix} 1 & 0 \\ 0 & \frac{1}{n_{grin}} \end{bmatrix} \begin{bmatrix} 1 & d_{work} \\ 0 & 1 \end{bmatrix} \begin{bmatrix} r_{in} \\ r'_{in} \end{bmatrix} \tag{3.28}$$

where r_{out} is the radial position of the output beam, r'_{out} is the angle of output, d_{det} is the distance from the output lens to the detector, g_x is the gradient constant of lens $_1$ or $_2$, z_x is the length of lens $_1$ or $_2$, n_{grin} is the refractive index of the GRIN lens, d_{sep} is the distance between lenses, d_{work} is the distance from the sample point to the lens, r_{in} is the radial position of the sample point and r'_{in} is the angle output from the sample. The ray tracing tool is based on this equation with two key changes to reduce the number of assumptions made. The first is the small angle approximation of $tan(\theta) = \theta$. This assumption does not hold true for some of the wide acceptance angles of the system and thus was changed. The second assumption is that the refractive index of the GRIN n_{grin} can be approximated by a single vale. This is fundamentally not true of GRIN lenses where $n_{grin} = n_1 \left(1 - \frac{(rg_x)^2}{2}\right)$. The ray tracing tool updates the

GRIN refractive index based on the radius according to the lens parameters. These changes to Equation 3.28 are made possible by breaking the ray matrix calculation into a series of discrete steps such that the n_{grin} and angles can be appropriately adjusted. The model was verified by entering the design wavelength of the lens (630 nm) and verifying the ray-traced working distance matched the lens data sheet.

There are some key assumptions that the tool does make. The first and foremost is that it does not calculate skew rays. This is an issue as these rays dominate the system due to the isotropic emission of fluorescent light. Further, the tool assumes no refractions or reflections within the system, and thus overestimates the transmission efficiency of the lenses. The ray-tracing algorithm is used to make figures as well as predict the focal length for designing the pinhole placement above.

Two tools were made for ray tracing. The first was made in Asymptote[111] and is used to visualise the ray tracing through the lens with a vector graphic file of the model results as the output. This visual tool is also useful for determining the lens focal point of the lens system. A second tool was developed in Python for estimating the spot-size and *LCE* of GRIN based systems. It performs the same iterations as the ray-tracing tool, but due to the higher efficiency a larger number of rays can be calculated. This tool divides the sample into a grid. For each point in the grid the radial positions r_{in} and working distances d_{work} are set and the tool simulates output rays with a variety of angles. The *LCE* is estimated by first determining the maximum and minimum angles of acceptance of the emitted rays from each point, defining an acceptance angle cone, and then taking the ratio of the solid angle defined by this cone to that of a sphere. The the overall *LCE* of the optics is the average of these points weighted by radius. The tool also estimates the spot-size by taking a plane through the middle of the channel height and finding the distance from the centre where the *LCE* drops to half of its maximum. This method assumes that skew rays are collected at a similar efficiency as meridional rays, and thus slightly over-estimates the *LCE*. The magnitude of this over-estimation is not quantified, thus this tool is recommended for rough estimates only.

Even though the GRIN ray-tracing tool was able to estimate the spot-size of an optical system, the tool gives few options for tuning the design due to the large number of variables present. This was implemented with the introduction of a pinhole. The GRIN ray-tracing tool was then modified to limit accepted rays based on the location and diameter of this pinhole. As this project progressed, the fabrication complexity that could be undertaken was also improved. Early optics modules (OPT1 and OPT2 modules discussed in Sections 3.8.1 and 3.8.2) did not have any pinhole and thus had spot-sizes much larger than the 100 μm target. The primary challenge in implementing a pinhole is ensuring its tight alignment to the rest of the optics. The first pinhole (OPT3 discussed in Section 3.8.3) implemented was made by drilling a 200 μm hole in an aluminised tape attached to the optics part-way through fabrication (200 μm being the thinnest drill bit available at the time). This allowed the module to be milled in a single fabrication step, simplifying the alignment of all the features. However, this pinhole functioned more as an aperture and, while it did reduce the spot-size somewhat, it was far from optimised, resulting in a drop in *LCE* (and signal). The final design (OPT4 discussed in Section 3.8.4) leveraged the ray-tracing tool to place a pinhole at the focal point of the optics system. This necessitated a two-step milling procedure with a re-alignment process in-between. To ensure the pinhole and lens were centred they were fabricated in the same step, however this necessitated the widening of the pinhole to 300 μm as a longer and more robust drill was required. Each of these pinhole options was analysed with the GRIN ray-tracing tool with results presented below in Table 3.10.

In summary, a ray tracing model was developed to assess the performance of the GRIN-based light collection optics.

The inputs to the model were the wavelength, sample width, sample height, lens separation, pinhole diameter and pinhole placement. In the case where there was no pinhole used, the photodiode active area width and photodiode capping thickness were used instead. The simulation was run with a "mesh" of 2 μm for spot-size estimation and a 1 μm spacing for *LCE* estimation. Test rays were output with 1^o increments from a 120^o output cone. These parameters ensured the calculation was as accurate as possible while managing the computational complexity of the tool. Both the asymptote and python calculation tools are available in the SI.

3.6.3 Light Collection Summary

Two styles of light collection optics have been proposed: a proximity based system where the sample and detector are fabricated monolithically as in a future CMOS LOC device and a GRIN-lens based system with comparable performance for prototyping scalable designs. Of the GRIN-based instruments, three different designs were proposed with various pinholes to modify the spot-size of the instrument: a system with no pinhole, a system with a pinhole pressed against the output lens (i.e. an aperture) that was easy to fabricate but unoptimised and an optimised pinhole at the focal point of the centre of the channel. For each of the proximity and GRIN-based optics systems the *LCE* and spot-size were estimated, with Section 3.6.1 discussing the methods used for proximity based collection systems and Section 3.6.2 discussing the GRIN-based systems. The results are shown in Table 3.10 for a 100 μm channel and Figure 3.13 shows the representative ray diagrams for the GRIN-based instruments.

	Pinhole/Photodiode Diameter (μm)	Pinhole offset or Detector Spacing (μm)	Spot size (μm)	*LCE*
Proximity	150	15	89	6.2%
GRIN, no pinhole	600	300	323	6.2%
GRIN, aperture pinhole	200	0	152	3.1%
GRIN, optimized pinhole	300	321	134	6.2%

Table 3.10: Spot size and *LCE* estimations for a monolithic CMOS system as per Equation 3.22 and a variety of GRIN based designs. While the mechanism and physics of the systems are different, the optimised pinhole GRIN design and proximity systems both have similar *LCE* and spot-sizes of 6.2% and near 100 μm spot size. Note: two different channels are presented

Of the GRIN designs, the no-pinhole instrument has a spot-size over 300 μm, much larger than the 100 μm requirement. The introduction of an aperture-pinhole successfully reduced the spot-size to 152 μm, though at the expense of a factor of two in *LCE*. Moving the pinhole to the optimal placement recovered the *LCE* to the no-pinhole design and further reduced the spot-size to 134 μm despite the larger pinhole. Future designs can reduce this further with improved tooling.

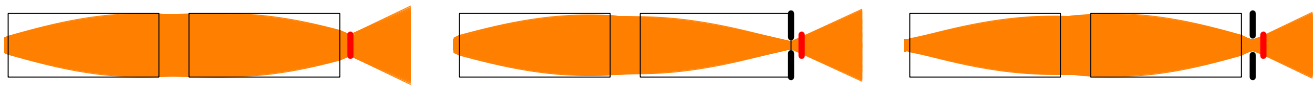

(a) No pinhole (b) 200 μm pinhole on lens face (c) 300 μm pinhole held 321 μm from lens face

Figure 3.13: Ray trace diagrams for three GRIN based collection optics. GRIN lenses are in thin black lines, the pinhole is drawn in thick black lines, the photodiode is a thick red line and rays are drawn in orange. Without a pinhole the spot-size of the optics are too large for high performance applications. Adding a pinhole directly on the lens surface constricts the spot-size, though it also restricts the transmission efficiency. A higher performing option is to introduce a pinhole at the focus spot. For small channels this is equivalent to the no-pinhole efficiency, though with a reduced spot-size. Quantification of the *LCE* and spot-size is done in Table 3.10

Table 3.10 illustrates the primary advantage to the use of short-working distance GRIN lenses in these designs in that the instrument performance can be tuned to be as close as possible to a Proximity-based light collection system with identical *LCE* and comparable spot-sizes. This allows the readily built GRIN-based optics used here to be used as a testbed to prove the feasibility of optical detection in future monolithic CMOS-based LOC designs without undergoing the NRE costs associated with those prototypes. Thus, these designs have light collection that is scalable to future miniaturisation.

Table 3.10 also demonstrates the motivations behind the various pinhole iterations build. The initial, no-pinhole design had a very large spot-size of 323 μm, much larger than the 100 μm requirement. It is interesting to note that the spot-size here is much less than the photodiode width (600 μm). This suggests that the limit on the spot-size is the acceptance angle of the GRIN lens. However, this was not a parameter that was readily tuned. Further, while photodiodes with smaller active areas are available, few are readily integrated into optics like the small surface mount (SFH2701, Osram Semiconductor) used. Thus, while minor manipulation of the spot size might be possible, it was not readily tuned with the no-pinhole design. Introduction of a pinhole was successful in changing the spot-size. The initial pinhole tested was an aperture style in that it was placed directly on the second GRIN lens as shown in Figure 3.13b. This pinhole did reduce the spot size (152 μm from 323 μm) but at the expense of the *LCE* which fell by a factor of two. This illustrated the need for improved optimisation. Using the GRIN ray-tracing tool, the focal point of the optics were determined to be 321 μm. With improved fabrication procedures, a pinhole was fabricated into the aluminum optics mount at this location. This optimised pinhole, despite being larger in diameter than the aperture, had an improved spot-size of 134 μm. This is close to the 100 μm requirement of the design. More importantly, the optimised design did not impact the *LCE* of light from within the channel as compared to the no-pinhole design.

The 134 μm spot-size realised by the optimised pinhole is close to the 100 μm requirement, though slightly bigger. This size was limited by the minimum diameter drill that was compatible with the optics fabrication process that was available at the time. Future designs might find improved tooling that can reduce this diameter to reduce the spot-size. For the optimised location, reducing the pinhole to 225 μm diameter would reduce the spot-size to 97 μm, below the target requirement. However, in the interim, the current design is very close to this requirement and is not likely to affect the CE resolution substantially. During a CE experiment, the sample is first defined by the channel dimensions as detailed in Section A.1 earlier. However, after the experiment begins this initial sample size increases due to diffusion. A typical diffusion coefficient for DNA is $\approx 1 \times 10^{-11} m^2/s$,[54] and with both edges of the sample diffusing outwards the sample will increase in size to 134 μm within 60s. This is much shorter than the experiments run to date ($\approx$ 300s).

Therefore, while future designs should refine the fabrication to reduce the spot-size, the current implementation is sufficient for many analyses.

3.7 Light Detection

The final step to the optical system is converting the optical power of light to an electrical signal. This is performed with a photodiode and associated amplification electronics which are discussed in Chapter 4. In this chapter, the optical designs will be discussed within the context of the reference electronics outlined in Section 1.3.1 and detailed in a Burr-Brown application note,[83] Kaigala et al.[85] and the thesis of Alison Bidulock.[84] Briefly, the reference electronics feature a gain of 10^9 $^{V}/_{A}$, a responsivity of 0.33 $^{A}/_{W}$ and noise of 114 μV_{RMS} for a minimum detectable power of 1 pW. This allows for the estimation of the LOD of an optics module.

3.8 Optics Module Designs

The development of the optics module was done through a series of design iterations that identified and solved the key challenges to low-cost, nM level LIF detection. An optical module must bring together each of the various components discussed above. This includes an excitation source (Section 3.3), appropriate spectral filters (Section 3.4) and a method of collecting the fluorescent light (Section 3.6). These components were then combined and arranged into an optical geometry, giving all the parameters required to model the expected optical performance. As discussed previously, a LIF module must take into account the microfluidics, the optics and the detection electronics. Therefore, all these aspects must be integrated for testing. This is done later in Chapter 5. To decouple the optics discussion from the other interrelated components, this chapter will focus primarily on the parameters estimated from the model discussed above. First, the estimated signal from a 1 nM sample is assessed based Equation 3.1 and the various parameters discussed in the chapter above. Next, the spot-size is assessed based on the discussion in Section 3.6. Estimating the baseline is problematic due to its source being primarily scattered light, therefore this parameters was assessed by measuring the signal from a microfluidic chip with no fluorophore present in the channels. The signal was measured with one of the available detection electronics designs from Chapter 4 and converted to optical power based on a responsivity of 0.33 $^{A}/_{W}$ and the gain of the circuit used. Based on the signal and baseline, an estimated LOD (eLOD) based on the reference detection electronics and an estimated SBR (eSBR) can be assessed and compared.

Four optics designs were developed (OPT1-OPT4) with each module iteration identifying key parameters that were then integrated into future designs. OPT1 was a first pass at a scalable optical design, though based on a prototype CMOS microelectronic chip for detection that was unsuitable for future work (as discussed in Sections 4.2). OPT2 adapted the OPT1 design for use with a discrete photodiode and introduced excitation filtering for improved baseline performance. However, the spot-size for this design was much larger than anticipated, identifying spot-size reduction as a key issue. OPT3 introduced a pinhole for spot-size control as well as improved filtering. This design was a vast improvement over previous iterations and was used to demonstrate the state of the art in low-cost CE LIF design in Section 5.4. Finally, OPT4 adjusted the optics and implemented new filters to execute a SIS configuration. The OPT4 module implements the all of the scalable design principles from Section 3.1.3 (LED excitation, SIS illumination with

no lenses, 1 nL sample, absorption filter), making it the first fully scalable LIF design. This model was then used to extrapolate the OPT4 module to a feasible monolithic CMOS design. Table 3.11 summarises all of the design and calculated parameters for each of the iterations, with discussion regarding the optics modules and their development presented in Sections 3.8.1 to 3.8.5 below.

	Parameter	OPT1	OPT2	OPT3	OPT4	Monolithic CMOS
Design Parameters	LED Part Used	WP710A10QBC/G			WP710A10WG1C	
	LED Luminous Flux	2.5 cnd			5.8 cnd	
	LED Dominant Wavelength	470 nm			505 nm	
	LED Drive Current (mA)	20	30	30	30	30
	Number of LEDs	2	2	2	1	1
	Excitation Style	Side-Illumination			Staring-into-Sun	
	Excitation Filter	None	Laird 2424 Blue	Rosecolux Sapphire Blue	Lee 729	
	Excitation Filter Thickness (mm)	N/A	3	0.1	0.085	
	Emission filter	Acrylite 2C04			Lee 507	
	Emission filter thickness	3 mm			0.085 mm	<3 μm
	Design	GRIN based				Proximity
	GRIN Lens pitch	0.25	0.23			None
	Pinhole	None	None	Aperture	Optimised	None
	Pinhole Diameter	N/A	N/A	200 μm	300 μm	N/A
	Photodiode	CMOS	OSRAM SFH 2701			CMOS
	Photodiode active width/length(μm)	150	600			100
	Channel Width (μm)	381	254	254	100	100
	Channel Depth (μm)	381	254	254	100	40
	LED-Channel space (mm)	11	6.5	3.6	1.5	0.8
	Channel-Lens space (μm)	100	100	100	100	15
Calculated Parameters	Sample solid angle ($\times 10^{-3}$ sr) (Section 3.3.1)	1.2	1.53	5.01	3.98	15.6
	Excitation Power (μW) (Section 3.3.1)	133	84.4	283	126	494
	T_{exfilt} (Section 3.4.1)	100 %	45.5 %	23.4%	29.2%	29.2%
	E_{abs} (Section 3.4.2)	10.8%	10.3%	8.8 %	33.8 %	33.8 %
	A (nM^{-1}) (Section 3.4.2)	8764	486	418	639	252
	T_{em} (Section 3.4.3)	33.5%	33.5%	33.5%	7.5%	7.5%
	QY (Section 3.5)	61%	61%	61%	61%	61%
	SS (Section 3.5)	83.6%	83.2%	82.6%	87.8%	87.8%
	LCE (Sections 3.6.1 and 3.6.2)	$\approx$ 6%	6.0 %	2.7%	6.2 %	6.2 %
Assessment	Effective OD (Section 3.4.4)	3.4	4.6	5	6.3	6.3
	Estimated Signal ($^{\text{fW}}/_{\text{nM}}$) (Equation 3.1)	1050	380	250	56	91
	Spot Size (μm) (Sections 3.6.1 and 3.6.2)	$\approx$150	323	152	134	89
	Measured Baseline (pW)	†	6900	160	263	204‡
	eSBR ($\times 10^{-4}$)	†	0.6	15.6	2.1	4.5‡
	eLOD (nM)	1.0	2.6	4.0	17.9	11.0

Table 3.11: Summary of estimated performances for each of the optics module iterations that were built and tested in Chapter 5. As the iterations progressed the baseline was improved, spot-size and channel dimensions were reduced and overall performance refined as improved filters, electronics and fabrication were developed. However, due tot he sample volume changes, it is not possible to directly assess these modules based on the above parameters. Therefore, Table 3.12 was developed with normalised metrics. The ultimate module has an estimated 56 fW from a 1 nM sample in 100 μm channels and a 134 μm spot size in a SIS configuration. Extension of this model to a monolithic CMOS design estimates a 91 fW signal. Thus, the OPT4 design provides not only optimised low-cost LIF optics but also approximates the performance of future systems, making it an excellent testbed for prototyping.
†: Due to an unknown responsivity, the SBR for the OPT1 design is measured, not estimated
‡: The baseline was estimated from the model as a CE experiment has not been performed yet

Table 3.11 details the models results for the channel dimensions the modules were designed, built and tested for. However, the channel sizes built were unavoidably varied as the microfluidic fabrication techniques were iterated upon and improved (as discussed previously in Chapter 2), preventing direct comparison of the modules. Further, these channels were mostly larger than the 100 μm requirement and thus the signals estimated were larger than a general purpose CE application. To address this issue, a new metric called normalised signal (nSc) was developed which corresponds to the signal estimated by the model for each module but for 100 μm x 100 μm samples (i.e. the reference sample from Section 1.3.1). Similarly, a normalised eSBR (nSBR) was also calculated based on the measured baseline in Table 3.11 and nSc. Finally, the normalised eLOD (nLOD) is the estimated LOD based on the nSc and assuming use of the reference detection electronics. One important assumption made in this calculation is that the measured baseline detailed in Table 3.11 is representative of the baseline that should be expected for the miniaturised designs. As discussed in Section 3.8.2 below, this is not typically the case as channel miniaturisation typically results in increased baseline. Therefore, nSBR values presented here are likely vastly overestimated, potentially making the practical implementation of 100 μm channels with the OPT1-OPT3 designs impossible. The SIS arrangement of the OPT4 design does not have this issue, making the nSBR estimate for this module more representative.

In a direct comparison of nSc, nSBR and nLOD values, the OPT4 design is clearly the best performing of the scalable optics designs with both the lowest nLOD and highest nSBR. Furthermore, it is the only one of the four capable of implementing a SIS optical arrangement and thus is the only fully scalable design to CMOS. Analysis of the proposed monolithic optical design suggests that miniaturisation will further improve the nLOD and nSBR beyond the scalable testbeds. Thus, any experiment that is proven viable using the OPT4 design would be expected to work even better when miniaturised to a single-chip instrument, validating the use of scalable optics for prototyping designs that would otherwise be inaccessible due to NRE and high development costs. Comparing the monolithic CMOS design with the reference model from Section 1.3.1 suggests the refined calculations presented in this chapter and optimisations present should improve the performance by a factor of nine compared to the previous back of the envelope calculations. However, the nLOD of the proposed monolithic design is still 11 nM. This is an improvement on the 100 nM LOD demonstrated in the literature as the state of the art in low-cost LIF instrumentation, but still a significant step from the 1 nM requirement for PCR-CE. This design, however, was well-optimised suggesting that reaching this objective purely with optical improvements is not feasible. Chapter 4 discusses the development of detection electronics and data processing to improve the minimum detectable power. Chapter 5 then presents the results of combining the optics described here with improved detection electronics. With both optical and electrical improvements, both the OPT4 and monolithic CMOS designs realise sub-nM predicted LODs for the 1 nL target sample. To the best of my knowledge, these would be the first such designs to meet the requirements for general purpose PCR-CE analysis.

	Reference Model	OPT1	OPT2	OPT3	OPT4	Monolithic CMOS
Excitation Power (μW) (Section 3.3.1)	2.5	9	26	86	126	494
Spot-Size (μm)	N/A	$\approx$150	323	152	134	89
Measured Baseline (pW)	N/A	N/A	6900	160	263	204‡
nSc (fW)	10	19	23	15	56	91
nSBR ($\times 10^{-4}$)	N/A	N/A	0.03	0.95	2.13	4.5‡
nLOD (nM)	100	53	43	66	18	11

Table 3.12: Model estimated performance for 100 μm channels for all optical designs. While Table 3.11 shows the OPT4 design having the lowest signal (and thus lowest expected LOD), normalising the model such that all designs are tested with the same channels demonstrates the substantial improvement over the other scalable optics. These improvements include an optimised pinhole for improved *LCE* and spot-size, optimised filters for improved SBR and close LED-sample coupling. Each of these modules exceeds the performance of the back of the envelope calculations presented as part of the reference model in Section 1.3.1. However, the nLOD values predicted still remain too high suggesting that electrical improvements are also necessary.
‡: These parameters are estimated from the model as this design has not yet been fabricated

3.8.1 OPT1- Scalable light collection, LED illumination and Absorption Filters

The OPT1 design was a first pass at developing scalable light collection optics (the GRIN lens system from Section 3.6.2) and was designed around prototype multi-functional CMOS microelectronics from our collaborators at the University of Alberta. The key advance was the implementation of the two GRIN lens light collection system that imitates as close as possible the collection in a fully integrated monolithic design as shown in Figure 3.2b in Section 3.1.3. This lens system enabled the use of the polymer fluidics discussed in Chapter 2 with the prototype CMOS microelectronics for optical detection (discussed in Section 4.2), decoupling the microfluidic and microelectronic design cycles while matching light collection performance as close as possible to a fully monolithic design. The OPT1 design also initiated the orthogonal, two-LED excitation arrangement as shown in Figure 3.14a. The use of two LEDs amplified the excitation power by a factor of two, while the orthogonal arrangement reduced the baseline as no excitation light was directly incident on the detector. The design was tested with generation 1 milled fluidics (381 μm wide and deep channels), discussed in Section 2.2.2, resulting in a boosted eLOD of 1 nM. However, these were a first-pass at micromilled fluidics and were therefore much larger than the target channels resulting in a boosted signal from the larger sample volume. To decouple the analysis of the optics from changes to other aspects of the design, the normalised values in Table 3.12 should be used. These show that for a 1 nL sample representative of a general purpose CE application the nLOD would 53 nM, nearly a factor of two better than the reference model but still over an order of magnitude above the instrument requirements. Thus, more optical development was required. The OPT1 optics were featured in publications[48,115] as discussed in more detail in Section 5.2. The OPT1 design laid the groundwork upon which future designs were built but deficiencies in LOD and the need to implement a discrete photodiode motivated future developments. The specific parameters of the design are shown in Table 3.11 with specific features discussed below.

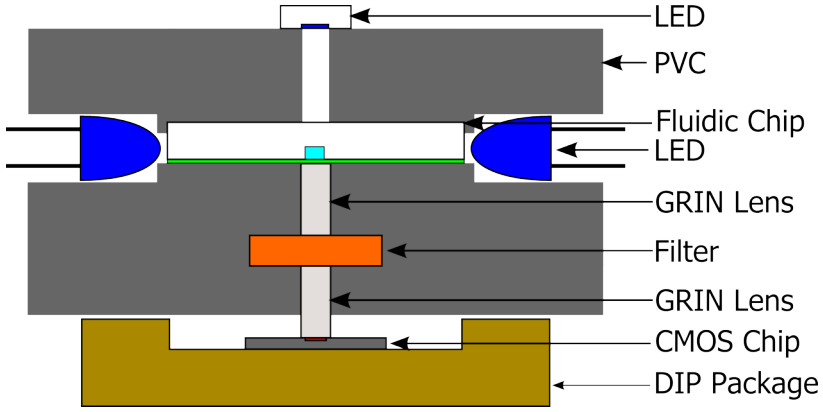

(a) Diagram of the OPT1 optics. The design consists of a fluidic chip, two LED's in an orthogonal arrangement, a third LED for offsetting the baseline and a GRIN lens collectino system with an emission filter in between. The design was attached to a multi-functional CMOS microelectronic chip in a DIP package. This design ultimately proved to have insufficient performance for general purpose PCR-CE analysis, however it did introduce a number of important design features that were later used in subsequent designs. Figure from [48]

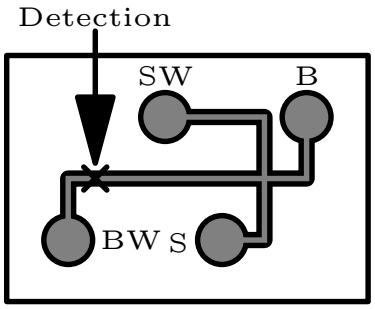

(b) A diagram of the microfluidic chip used with the OPT1 optics. The design was the same as used previously to allow for interoperability of the fluidics with both this instrument and a commercially available CE instrument to verify the fluidics. However, the design led to poor input light coupling and thus lower signals.

Figure 3.14: Diagram of the OPT1 optics and associated microfluidic chip. This design formed the basis for future iterations, though it did not meet the optics module requirements itself.

The OPT1 design initiated a number of the principles that were carried through to future designs. Firstly, the general optical arrangement with two side-illuminating LEDs proved to be a good approach. This orthogonal arrangement reduced the baseline, an important design feature as the lack of excitation filter led to poor baseline suppression in this design. Further, the use of two LEDs doubled the excitation power to offset the low excitation power of LED illumination as compared to lasers as discussed in Section 3.3.3. This two-LED arrangement was carried forwards to OPT2 and OPT3 for this reason. Another important feature was the two-GRIN lens optical relay design. This design was advantageous as the very short working distance of the GRIN lenses combined with thin channel bottoms (100 μm of tape as discussed in Section 2.3.1) led to collection efficiencies on the order of 6%. This mirrors closely the refined prediction of the *LCE* of the monolithic CMOS design. Further, as discussed in Section 3.6.2, this design places the sample and detector at the working distances of the lenses. This means the light between the lenses is collimated and thus the light lost within the lens system due to reflection is minimized, making the optical system relatively insensitive to the thickness of the emission filter. This is particularly important for designs that used the 3 mm acrylic filter (OPT1 and OPT2) as this material has a relatively low concentration of absorbing material as it is optimised for visual appeal and transparent display applications. The expected filter thickness deposited in a fully integrated, monolithic device is on the order of a few microns, a thickness not easily handled absent as an independent optical entity. Thus, this optical system allows the thick filter used to stand in for the deposited filter and makes for a more scalable design. Thus, the GRIN lens arrangement was used in each of the scalable optical testbeds.

The LIF model estimates the OPT1 optics would collect about 1 pW of fluorescent light from a 1 nM sample as shown in Table 3.11. This is a very substantial signal, though this is in part due to the very large microfluidics. At the time of design, micromilling fluidics was a very new technique to the lab and the protocols were only just being developed. The 381 μm width was chosen as this is 0.015", the smallest tool readily available through the engineering machine

shop at the University of Waterloo. As described in Section 2.2, this relatively wide channel was more readily built as wider endmills are less likely to break and can accommodate more milling forces than thinner endmills. However, 381 μm is substantially larger than the target 100 μm channels. Thus, while 1 pW is a substantial amount of optical power, it is not representative of a usable LOC device.

One issue with the OPT1 module was that it was designed specifically for use with the CMOS detection electronics which did not have a known responsivity. Therefore, the optical power of the baseline could not be readily assessed. Section 5.2 details a practical experiment to assess the LOD of these optics. In this experiment, the measured SBR was 2.8×10^{-4}. This is, in comparison to other values in Table 3.11, a relatively good SBR for such systems. Furthermore, as described in Section 4.2, this prototype CMOS chip was only functional when the signal incident upon it was within a certain range and had limited available gain. Thus, it required a nominal baseline. However, the SBR was determined to be such that even with relatively poor baseline suppression (OD 3.4 or 2400x per Table 3.6) the signal did not reach the threshold for reliable operation. Thus, a third LED was added to perform the baseline offset with a minimal (1-3 μA) current. This suggests that the orthogonal arrangement used had a very profound effect on reducing the signal baseline.

Previous work by the Backhouse group integrating prototype CMOS into LOC instruments by Behnam et al.[47] has many similarities to this work, including orthogonal excitation of the sample and the use of GRIN lenses, however this design featured a number of key changes that greatly improved upon the scalability of the design. Firstly, this design features a two-GRIN light collection design as compared to the single-GRIN design previously used. As mentioned above, this allowed for a shorter working distance, enabling a *LCE* more representative of final monolithic designs and making the design more readily scaled to future integration. The filter used in the OPT1 design was an absorption filter, Acrylite 2C04, which replaced the Chroma interference filter used previously. As detailed in Section 3.4, interference filters are substantially more expensive than absorption filters both as discrete components used in this instrument and Behnam et al.[47] as well as when integrated into monolithic devices where the need to deposit 40+ layers with sub-nm accuracy for an interference filter compares poorly to the single deposition of a few microns of absorption filter. Therefore, the filter change not only reduced instrument cost but also enabled improved scalability towards future designs. Finally, the OPT1 design switched the excitation source from a laser to a LED. This reduced the alignment tolerance requirements of the optical design as the LEDs used here did not require focusing as they illuminated an area much larger than the sample, reduced the power consumption of the instrument, reduced the instrumentation costs ($93 to $1) and reduced the size of the instrument both by using a smaller component and by eliminating the need for a laser heat sink. Each of these parameters greatly improves the scalability of the optical design to future instruments.

The OPT1 optics provided a good starting point but featured a number of easily addressed issues. Firstly, the lack of excitation filter meant that the baseline suppression was not well optimised. This was necessary for the instrument built around the prototype CMOS microelectronics but is a notable drawback for future instruments that do not have the baseline requirement and can access more signal gain. In such unconstrained systems, reducing the baseline enables more of the instrument dynamic range to be used for signal and improved detection. Further, the microfluidics used were not suitable for many applications with a poorly optimised layout and large dimensions. The general microfluidic chip layout used was the same as that in previous work[56,96] which allowed for the same microfluidics to be used on both this instrument as well as a commercial CE instrument with confocal optics (Microfluidic ToolKit, Micralyne Inc.) for separation verification. This was particularly important in the early stages of the project while the fluidic

protocols were being developed. However, as shown in Figure 3.14b this design had the separation channel in the centre of the chip and far from the edges. This led to decreased input coupling efficiency. The design also featured twisted channels to maximize channel length in a small format. This was advantageous with previous glass fluidics which carried a high material cost, though is less necessary with the inexpensive PMMA fluidics used here. The twisted channels caused the BW well in particular to partially occlude the detection point, likely reducing the signal. Thus, the microfluidics in general required attention. Finally, as discussed in Section 4.2, the CMOS microelectronics ultimately were unsuitable for future development. This required the change from a photodiode that was microns below the surface of the chip to one with hundreds of microns of protective acrylic above it, thus requiring a change in optical design as the 0.25 pitch GRIN lens would no longer be appropriate. These improvements and changes are discussed below.

3.8.2 OPT2 - excitation filters and discrete photodiode integration

The primary objective of the OPT2 design was to convert the optics from using the prototype CMOS chip for detection to a discrete detection electronics setup using a commercially available photodiode. As such, the OPT2 design used a similar concept to the OPT1 but with a change in GRIN lens to accommodate the new photodiode. Further, some added optical improvements were introduced which included an excitation filter and new microfluidics. As described in Section 4.2, there was a need to move from the prototype CMOS detection electronics to in-house designs based on discrete electrical components. This necessitated a change in the GRIN lens from the 0-working distance 0.25 pitch lenses to the 234 μm working distance 0.23 pitch lens. Furthermore, the move away from the prototype CMOS design meant that the third LED for baseline offsetting was no longer required and was removed. The final change to the optical design was the introduction of the Laird 2424 Blue excitation filter to improve the baseline rejection. These adjustments can be seen in Figure 3.16, though the OPT2 module did not have a pinhole (the second GRIN rested directly on top of the photodiode). Changes were also made to the microfluidics. The channel dimensions used were shrunk from 381 μm to 254 μm as the fabrication techniques were refined (the generation 2 parameters from Section 2.2.3 were used). Another improvement to the fluidics was the introduction of the ”neck” design where the fluidic chip narrows as much as possible near the detection region. This allowed for the LEDs to be brought closer to the chip, improving the coupling efficiency of the excitation light into the sample and increasing the resulting signal. This chip is shown in Figure 3.15. Based on these channels, geometry and optical components, the eLOD for the instrument was 2.6 nM. Thus, even for larger channels, the optics did not meet the research objectives. An application of these optics combined with the PDE electronics (discussed in Section 4.4)) to perform a CE separation of DNA that had been enzymatically digested is detailed in Section 5.3, though it was not published due to poor LOD and unstable detection electronics.

Analysis of the normalised metrics in Table 3.12 show a slight improvement from OPT1 to OPT2 in terms of nSc and nLOD. The nLOD for the design was 43 nM, still well above the target objective. Thus, while the ”neck” should have improved the signal by bringing the LED closer to the sample, this improvement only resulted in a marginal signal improvement and the design remains significantly worse than required. Another key issue is the SBR. The eSBR here of 2.2×10^{-4} and the nSBR of 0.03×10^{-4} are quite poor, even when compared to the OPT1 design which did not have any excitation filters. This is an unusual phenomenon that is explored in more detail below.

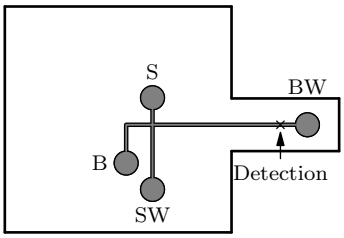

Figure 3.15: Diagram of the microfluidic chip design used in the OPT2 and OPT3 designs. The chip edges narrow before the detection point creating a ”neck”. This allows for the excitation LEDs to be brought closer to the detection point, increasing the amount of excitation power coupled into the sample and increasing the signal.

The photodiode used (SFH2701, OSRAM Semiconductor) features a 300 μm protective cover of acrylic over the photodiode active area in comparison to the few microns of dielectric that capped the previously used prototype CMOS microelectronics. By switching from a 0.25 pitch GRIN to a 0.23 pitch GRIN with a nominal working distance of 234 μm, the effect of this cover could be mitigated. Further, since with this design all of the lenses were from Thorlabs (who include Zemax simulation data for their lenses) the calculations in Section 3.6.2 could be done to perform chromatic corrections to the lens parameters. Thus, estimates for the OPT2 *LCE* are more accurate than for the OPT1. This is estimated at 6% across the entire sample, which is almost two orders of magnitude higher than would be expected from a commercial confocal instrument and almost exactly the same as the *LCE* for a proximity-based monolithic design. Thus, the OPT2 design retains the scalable light collection of the OPT1 design while allowing for prototyping with commercially available photodiodes.

The new microfluidics narrowed the distance from the chip edge to the start of the optics from 11 mm to 3.5 mm. The efficiency of coupling has a roughly $^1/_{r^2}$ dependence on distance, so the ”neck” design should increase signal by nearly an order of magnitude. Ideally, this distance would be further reduced. However, practically the width of the well and the need for structurally sound microfluidic chips prevents any further shrinking of the ”neck”. This demonstrates a deficiency in the orthogonal arrangement.

The excitation filter used was Laird 2424 Blue, a 3 mm thick coloured acrylic similar to the Acrylite 2C04 emission filter used. This material was readily available at the time and the model predicts an improved baseline rejection by a factor of 16 as compared to the filter-less design. Analysis of the filter combination used in Section 3.4.5 shows that the Laird 2424 Blue and Acrylite 2C04 transmissions actually overlap slightly around 550 nm as seen in Figure 3.9b. Therefore, this is not an optimised design and one would expect more baseline rejection with a different excitation filter. Absorption filters have much lower pass/stop ratios than interference filters and typically also attenuate the excitation light. For Laird 2424 Blue this attenuation was a factor of 2.2. Overall, despite not being optimised, the introduction of this filter was expected to improve the overall SBR performance by a factor of 7.4 as per the Q_{filt} metric in Table 3.6. However, Q_{filt} overlooks one important factor which is the excitation filter thickness. By placing the filter between the microfluidic chip edge and the LED, the LED-sample separation had to be increased by 3 mm leading to an additional factor of 3.4 reduction in excitation light. This mitigates the overall improvement of the filter such that only a 2.2x improvement in SBR is expected from the filter introduction. However, overall the SBR would be expected to be improved by a much larger factor over the OPT1 design due to the ”neck” introduction and removal of the baseline offset LED.

One unexpected results is that after measuring the signal baseline it was found that the SBR did not improve significantly. In fact, as discussed later in Section 5.3, the measured SBR for these optics is actually worse than the OPT1 design, even after adjusting for channel size reductions. This illustrates one of the difficulties in designing orthogonal LIF detection systems in that it is difficult to deterministically estimate the baseline. The primary hypothesis for this behaviour was the relationship between the spot-size, channel width and the baseline. In orthogonal arrangements such as the OPT1-OPT3 designs, the baseline source is primarily excitation light scattered off the walls and into the detection system. In the OPT1 design the spot-size was small at about 150 μm x 150 μm, the size of the photodiode on the multifunctional CMOS chip, and the channels were very wide at 381 μm. This meant that the OPT1 design collected much less light scattered off the channel walls. One overlooked feature of the OPT2 design was that the photodiode used, while a small active area compared to most readily commercial devices, was much larger than the CMOS chip at 600 μm x 600 μm. This led to a much larger spot-size of 323 μm, larger than the 254 μm channels. This suggests that the OPT2 design would collect light scattered off the channel walls much better than the previous design and resulted in a SBR reduction despite the introduction of an excitation filter. The poor SBR and limited dynamic range of the detection electronics meant that the amount of signal gain that could be applied was limited, leading to the poor LOD. The objective of the OPT2 design was to focus on attaining LOD with resolution (and therefore spot-size) being a secondary objective to be addressed with a future design. However, the results of the OPT2 analysis suggested that in the orthogonal arrangement attention to the spot-size was crucially important not only to the CE separation performance but also to the detection performance. A reduction in spot-size was thus the primary objective for future iterations.

In summary, the OPT2 module did not meet the performance requirements with a too-large spot-size, too poor SBR for high performing detection electronics and overall too poor LOD (2 nM) in too large channels (254 μm x 254 μm). The nLOD of 43 nM shows a slight improvement over the OPT1 design due to improved input light coupling but was not sufficient to realise the final objective. The primary reasons for these issues included a poor excitation filter that provided only marginal improvements and, especially, a spot-size that was much larger than the channels which caused both baseline and resolution issues. This prompted a thorough survey of excitation filters as well as development of pinhole fabrication techniques in future iterations.

3.8.3 OPT3 - state-of-art low cost LIF CE detection

The objective of the OPT3 design was to address the key issues of baseline and spot-size identified in the previous iteration. Specifically, this involved a more thorough survey of excitation filters to replace the poorly optimised choice from the OPT2 design and the implementation of a pinhole to control the spot-size as shown in Figure 3.16. The module was tested with nearly the same fluidics as the OPT2 design, as shown in Figure 3.15 above, with 254 μm x 254 μm micromilled channels and a ”neck” style detection point. However, the micromilling process was improved slightly to the generation 2.5 parameters from Section 2.2.3 with lower channel wall roughness. Combining all of these factors, the measured baseline of the optics module was reduced significantly. Analysis of the values in Table 3.12 shows that the nSBR improved dramatically in this module, over an order of magnitude higher than the OPT2 design, validating these design changes. However, these changes also resulted in a slight reduction in nSc and thus slightly worse nLOD at 66 nM. Therefore, this module identified boosting the signal as a primary concern going forwards. However, despite the lower optical signal, the detection performance from this module was improved significantly

in practice as the SBR improvements enabled higher performance detection electronics (discussed in Section 4.5). Testing of this module as part of the state of the art in LED and photodiode based CE detection described in Section 5.4 and an associated publication.[89]

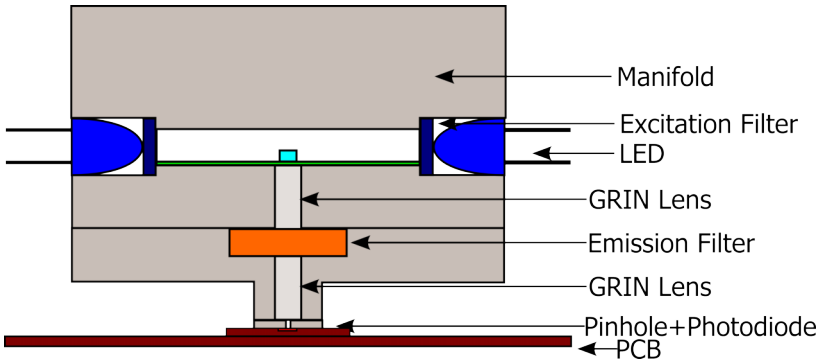

Figure 3.16: Diagram of the OPT3 design which consists of a fluidic chip, two LEDs that illuminate the chip from the side through excitation filter, a GRIN lens collection system with an emission filter in between and a pinhole to limit the spot-size. The OPT2 design is identical except that it lacks a pinhole. Figure adapted from Hall et al..[89]

The introduction of a pinhole in the emission light collection was successful in reducing the spot-size of the module, though the lack of optimisation of the pinhole location meant that it reduced the *LCE* of the instrument as well. Due to fabrication difficulties and to ensure proper alignment of the pinhole to the optical system as described in Section 3.6.3, the pinhole in the OPT3 design was implemented in an aperture style where it was pressed directly against the bottom GRIN lens from Figure 3.16. The pinhole diameter was 200 μm, the minimum sized drill bit that could be sourced at time of design. Simulations estimated this spot-size at 152 μm, which is now smaller than the 254 μm channel width. As discussed above, if the spot-size is less than the target channel it does not affect the CE separation resolution. Thus, this size reduction was crucial to the instrument performance. However, this is only true of the 254 μm channels used in this prototype. The objective of the optical design is to implement 100 μm channels that have broad compatibility for standard CE applications. Thus, while an improvement, the spot-size of the OPT3 design is not compatible with high-resolution CE sieving matrices and does not meet the research objectives outlined in Section 1.4. Nevertheless, as a first pass it demonstrates that tuning the spot-size with a pinhole in the emission light collection is a viable strategy going forwards. A second issue with the OPT3 pinhole is that the aperture style design attenuated the *LCE* by a factor of about two. A better strategy would be to place the pinhole at the focal point of the instrument to minimize the loss of useful emission light. However, this would require improved fabrication ability; at the time of design the ability to hold the required tolerances between multiple angles of the same piece, especially in the z-axis, was not yet achieved. Therefore, one potential improvement to this design would be to optimise the pinhole placement and reduce the pinhole diameter for optimised *LCE* in spot-sizes comparable to 100 μm channels.

The excitation filter was changed from the Laird 2424 Blue acrylic filter to the Rosecolux Sapphire Blue PET filter. In terms of spectral changes, as discussed in Section 3.4.5, the new filter increased the baseline rejection from 4.06×10^4 to 1.1×10^5 at the expense of poorer transmission efficiency (23.4% vs 45.5%) and excitation efficiency (8.8% vs 10.3%). Combining all these factors results in a reduction in the signal by a factor of 2.3 and a reduction in baseline by a factor of 2.7 compared to the previous design and an overall marginal SBR improvement. However, the new filter

is also substantially thinner at 100 μm compared to the 3 mm previously used. This allowed from the LEDs to be brought much closer to the sample, increasing the excitation power from 84.4 μW to 283 μW. Overall, combining the geometric and spectral parameters the new excitation filter is expected to result in a 1.7x increase in overall signal with a 2.7x reduction in baseline for 4.6x improvement to SBR. Practically, the eSBR values from Table 3.11 show an improvement by a factor of 28. This is much greater than can be explained by the filter change above and is attributed to the reduction in spot-size and reduced collection of scattered light from the smoother microchannel walls. The substantial improvement in SBR was crucially important as it enabled a higher gain on the detection electronics, resulting in improved LOD as discussed later in Section 5.4.

Overall, the OPT3 design succeeded in the objective of improving the SBR with both spectral and spot-size improvements. This improvement made for a design well suited to 254 μm channels as tested in Section 5.4. However, these improvements came at the expense of signal with a nLOD value of 66 nM, clearly well above the research objective. Furthermore, while the spot-size of 154 μm was sufficient for the channels tested, it is not optimised for the 100 μm required for standard CE protocols. This would not only cause the optics to limit the resolution, though this would be a relatively minor effect as the spot-size is only 50% larger than the channel and is therefore less important to the results than other protocol related effects, but also would affect the SBR. Therefore, to reach the research objectives a design optimised for 100 μm channels is needed.

3.8.4 OPT4 - staring into the sun, scalable and meets specifications

There were two objectives of the OPT4 design. The first was to take all the lessons learned from the previous designs to implement an optimised collection system. This includes robust filter analysis and spot-size control with a pinhole. The second objective was to solve an unaddressed issue with the scalability of the designs by implementing an axial SIS optical arrangement. This new optical arrangement allows simplifies the microfluidic design of the PMMA chips used in the works to date while also ensuring scalability to future miniaturised designs. These concepts are explored in more detail below. The SIS design was enabled through improvements in both the excitation and emission filtering; of the pool of over 500 filters surveyed this module implements by far the highest performing combination as per Section 3.4.5. The pinhole location was also optimised in comparison to the OPT3 design to increase the collection of fluorescent light while maintaining a small spot-size. The optical arrangement is shown in Figure 3.17. The instrument has been built with preliminary baseline testing completed (results shown later in Section 4.6) though CE testing of the LOD has not yet been done. The model predicts a signal of 56 fW from a 1 nM sample in 100 μm x 100 μm channels with a spot-size of 134 μm. In comparison to previous designs, since the target channels are the correct size the nSc as shown in Table 3.12 is the same as the estimated signal in Table 3.11. The model predicts this OPT4 design to have the highest signal and best nLOD of the four designs presented so far with a nLOD of 18 nM. However, this remains above the 1 nM research objective. Since this design is well optimised, this suggests that in order to reach the objective improvements to the detection electronics are necessary.

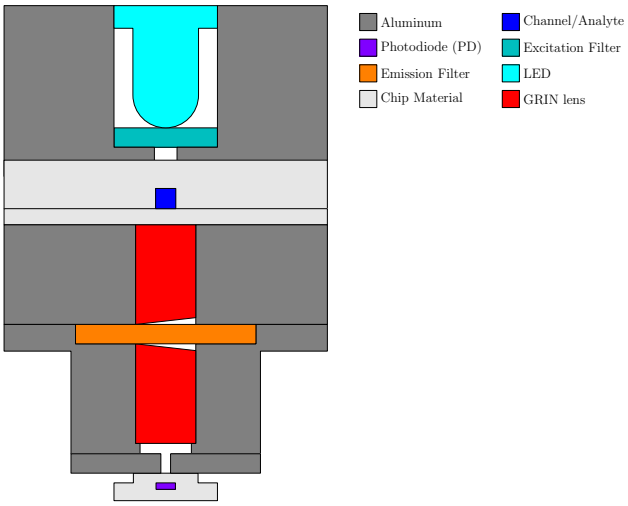

Figure 3.17: Diagram of the OPT4 optics featuring a SIS LED with excitation filter, GRIN lens emission light collection, optimised pinhole location and a photodiode along the same optical axis. This design is directly compatible with further miniaturisation, can be more readily arrayed, simplifies fluidic chip design and has a more deterministic baseline. However, by directly illuminating the detector the baseline performance is worse. Thus, this arrangement requires excellent filter design and stable LED excitation light.

There are many advantages to implementing a SIS design. Firstly, it simplifies the fluidic design by allowing the detection point to be placed at an arbitrary location in the microfluidic chip without drastically changing the performance. This also eliminates the need for the ”neck” design of fluidics shown above in Figure 3.15, relaxing design constraints on the microfluidics. Furthermore, an SIS design can be readily arrayed with multiple detection points within the same design. This was not readily done with the orthogonal design as it required detection points to be proximate to a chip edge. The baseline in a SIS design is also more deterministic and no longer a function of the channel dimensions. As discussed above, the baseline signal in previous designs was a function of the spot-size and microfluidic channel width. This meant that miniaturisation of the channels for these optical designs would increase the baseline by an unknown amount, likely requiring a change in detection electronics for various fluidic channel sizes. Not only is this inconvenient, it makes it generally impossible to predict the performance of previous optical designs with small channels. In the SIS design, the baseline comes from direct illumination of the detector by the LED. Thus, provided the LED, detector and LED-detector distance do not change, the baseline will remain relatively consistent. Different microfluidic channel dimensions and designs can therefore be readily used on the same instrument with similar baselines and performance. Finally, and most importantly, the SIS design solves a key issue by being a scalable excitation design. As discussed in Sections 3.1.3, 3.6 and 3.8.1 above, the GRIN-lens collection design is a scalable approach to collection fluorescent light. However, a scalable method of excitation light coupling into the sample had not yet been demonstrated. In the orthogonal designs previously discussed, the excitation light is coupled from the side through the chip material. This works as both the chip (1.5 mm thick) and LED (3 mm wide) are of similar dimensions. However, in a miniaturised monolithic design the chips themselves become much thinner. For example, previous work on CMOS-compatible fluidic channels featured a maximum channel depth of 40 μm.[50] If these channels are built upon a CMOS substrate, the total chip thickness would be less than 100 μm. The ramifications of this change are not easily assessed. Input light coupling would be further complicated by the need for bond-wires to interface with the

microelectronics. In comparison, the SIS arrangement in Figure 3.17 can be used with any arbitrary thickness channel and any arbitrary thickness chip. However, all these benefits come at the expense of a high baseline as the excitation light directly illuminates the detector.

One alternative to the SIS arrangement is to offset the angle of the LED such that it is somewhat between an orthogonal and SIS design, reducing the baseline of the design without changing the signal and thus improving the SBR. This is the approach taken by the previous state of the art in low-cost CE LIF design by Yang et al..[88] However, this angled design is not a feasible strategy for monolithic designs. Firstly, LEDs output uncollimated light that illuminates a relatively wide area. This makes selective illumination of the sample and not the detector very challenging from a practical perspective. This challenge becomes more pronounced by the very thin layers in a CMOS-based LOC design where the separation between the sample and the detector is about 15 μm which would make it nearly impossible to avoid directly illuminating the detector. Thus, there is a risk that an angled axial optical design like the one in Yang et al.[88] would become a SIS design when miniaturised and the baseline rejection previously expected would be gone, meaning the design is not scalable. A laser might be able to perform this task, however that would add expense, lasing noise and time consuming alignment to the device precluding low-cost applications. Thus, for scalability reasons there is a need for implementing SIS designs. These designs are enabled through careful control of the baseline.

The baseline in the OPT4 design is addressed in two ways. Firstly, as discussed elsewhere, by using LED illumination the baseline can be controlled with very high stability.[81] The other strategy is to implement as robust as possible of an optical filter. In Section 3.4.4 above it was shown that the primary limiting factor in the suppression of LED baseline with absorption filters comes from the parasitic ”bleed-through” light in the high wavelengths. Thus, there is a need for an excitation filter that attenuates strongly to as high a wavelength as possible. The Lee 729 filter was found to have the highest potential for this application, however this filter was cyan rather than blue. Therefore, the LED was also changed from a 470 nm blue LED to a 500 nm cyan LED. Another issue is that the Lee 729 transmission spectra overlapped with that of the Acrylite 2C04 absorption filter previously used. Therefore the emission filter also had to be changed. The Lee 507 filter was found to have a compatible stop-band. This filter combination has over an order of magnitude more baseline suppression with a slight improvement in expected signal as compared to the combination used in the OPT3 design as shown in Table 3.6. This added baseline suppression, combined with the stable LED excitation, led to a baseline that did not affect the LOD of the instrument with a signal that fits within the dynamic range of the detection electronics. Comparing the expected SBR of this design (based on the measured baseline in Section 4.6 and estimated signal from the model) with the nSBR of the other optical designs, the OPT4 is expected to have the highest performance at 2.13×10^{-4}, over double the OPT3 design and nearly two orders of magnitude improved over OPT2. Practically, the largest expected measurement for this device would correspond to the baseline (263 pW) and 400 nM of signal (i.e. a concentrated PCR primer that has not been amplified at all). This corresponds to a total signal of 285 pW, which is 87 mV with the reference detection electronics and 1.9 V with the DEV2 detection electronics in Section 4.6. In either case, this fits within the standard dynamic range of the circuit, confirming the viability of the approach.

Another key improvement in the OPT4 design was the implementation of an optimised pinhole location. Through use of a more rigid and accurate CNC mill, improved alignment tools and refined milling techniques the ability to hold 25 μm tolerances across multiple milling steps was achieved. This allowed for the optics to be fabricated in two steps and the placement of the GRIN lens above a pinhole at a defined distance. However, one consequence of the

design was that the pinhole diameter had to be increased as the previously used drill would not be capable of executing this strategy. This resulted in a 300 μm pinhole as described in Section 3.6.3. Despite the larger pinhole diameter, the estimated spot-size based on the ray-tracing approach from Section 3.6.2 actually shrank slightly to 134 μm. However, this remains higher than the 100 μm channels. Thus, this optics module does not quite meet the research objectives and can be expected to have some effect on the CE resolution. However, this effect is expected to be quite small for two reasons. Firstly, 134 μm is not very much larger than the 100 μm sample. Furthermore, one effect that has not been discussed is that while CE utilised plug flow to maintain a small, well-controlled sample, this sample diffuses during the experiment and becomes larger. Based on the work by Nkodo et al.,[159] under electrophoretic motion DNA has a diffusion coefficient for a 300 bp product is 1.77×10^{-7} cm^{2}s^{-1}. Therefore, a 100 μm sample can be expected to increase in size to 134 μm within 16s. This is a rough estimate, but it suggests that depending on the CE experiment many would have no measurable resolution impact due to the optics. For previous designs, the spot-size was crucially important as it affected the baseline of the instrument. However, for this SIS design the baseline is no longer a function of the spot-size/channel-size difference. Therefore, while a 134 μm spot-size and 100 μm channel would be a poor strategy for an orthogonal arrangement, it is much less so for this design. Future work might further refine the fabrication to reduce the pinhole diameter to less than 224 μm (the limit for a 100 μm spot-size) to improve the instrument CE resolution. This reduction in spot-size would not change the *LCE* for a 100 μm sample, suggesting the LOD would remain relatively unchanged.

Using the model described above, the OPT4 design is expected to collect 56 fW from a 1 nM sample in 100 μm x 100 μm channels. This is a lower power than previous designs in Table 3.11 by a significant margin. However, after correction of the model to 100 μm channels shown in Table 3.12 it is clear that the newest design has both the best nSBR and nLOD. Deconstructing the parameters in the model is instructive as to where these improvements are occurring. Comparing the OPT4 and the early designs, the new filters attenuate the signal by factors up to 4.9 as shown in Table 3.6. Further, the use of only a single LED halves the potential excitation power. However, these reductions are more than offset by the substantially closer LED-sample spacing leading afforded by using a thin filter in a SIS arrangement; the edge-coupling of previous designs forced the LED-sample spacing to be greater. Thus, the excitation power in the newest design is the highest after controlling for the channel size.

The nLOD for this design is 18 nM. Due to the high level of optimisation, this module can be considered at or near the practical limit for performance for a scalable, low-cost optical design, with a nLOD 3.7x higher than the demonstrated state of the art in the field[89] (i.e. OPT3 above). Thus, improvements to the electronics are necessary for reaching the 1 nM LOD goal in a scalable system. Section 5.5 discusses a next generation instrument that combines the OPT4 optics with new detection electronics that exceed the reference model performance as detailed in Section 4.6. This combined design has an expected LOD of 0.75 nM, thus meeting the detection goal. As a demonstration of the scalability, the next subsection will discuss a similar SIS design to this, but based around a fully integrated, monolithic design.

3.8.5 Future Work- Monolithic CMOS Fluorescent Design

The designs and estimation model developed above can be extended to predict the performance of a feasible monolithic LOC design where the microfluidics are fabricated in the same process above a CMOS microelectronic chip that contains all the required instrumentation for a diagnostic. The design parameters are shown in Table 3.11 above and

are based upon the OPT4 design and the microfluidic channels previously developed by Gutierrez-Rivera et al..[50] The optics are based on the OPT4 design with the same arrangement, excitation filter and emission filter demonstrating the scalability of the OPT4 design. The key difference is that instead of a GRIN lens emission light collection system the design places the photodiode in tight proximity with the sample. This is covered in detail in Section 3.6.1 above. Another key difference is a shrinking of the channel thickness from 100 μm to the 40 μm previously demonstrated in a CMOS compatible process.[50] Thus, the channel dimensions used have already been practically implemented in a CMOS compatible process before, making this a highly feasible design. A diagram of the proposed optics is shown in Figure 3.18.

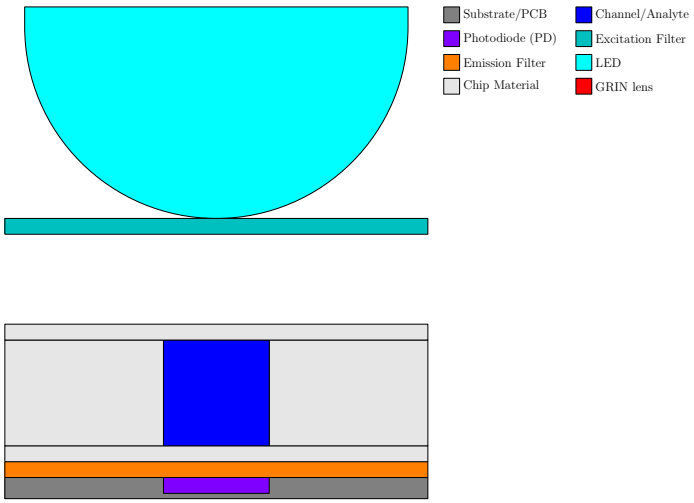

Figure 3.18: Diagram of a monolithic CMOS-LOC device optics. The design features the same SIS optics as the OPT4 design in Figure 3.17 but without the GRIN lens collection. Instead, the spot-size and fluorescent light collection are tuned with the separation between the channel and the photodiode and the photodiode size. The expected performance of this design is slightly improved as compared to the prototype optics, suggesting that LIF detection in a monolithic chip can now feasibly be designed.

The LIF signal estimation model was applied to this design resulting in an estimated 91 fW of fluorescent light collected for a 1 nM sample. Compared to the reference model, this is an increase by a factor of nine. More importantly, this is 1.6x higher than the OPT4 design suggesting that OPT4 can provide a reasonable testbed that approximates the performance of the monolithic design with a slight underestimation. Thus, OPT4 can be used to demonstrate the viability of the design and protocols for later translation to a more miniaturised instrument. The difference in signal arises from the fact that when monolithically fabricating microfluidics above detection electronics the fluidic structure is much thinner. Thus, the LED can be brought much closer to the sampling point (increasing the excitation power from 126 μW for OPT4 to 494 μW) to increase the signal while the thinner (40 μm vs. 100 μm) channel decreases the number of fluorophore. The end result is a modest increase in signal.

Differing from previous iterations, the baseline can also be readily estimated in the monolithic design by employing the same equations used to estimate the excitation power (Equations 3.3 and 3.6) and substituting the photodiode dimensions for the sample dimensions. This results in an estimated a baseline of 204 pW. Based on both the signal and the baseline estimations, the required dynamic range of the electronics can be estimated. Assuming the average noise

from the previously demonstrated CMOS microelectronic chip of 2.4 counts, a signal of 7.2 counts is the minimum detectable signal. The maximum signal expected is 400 nM plus any signal from the baseline. This can be used to calculate the minimum number of ADC bits required as below.

$$\text{ENOB} = \log_2\left(\frac{\text{Baseline} + 400 \times \text{Signal(1 nM)}}{\frac{\text{Signal (1 nM)}}{7.1}}\right)$$

$$\text{ENOB} = \log_2\left(\frac{204 \times 10^{-12} + 400 \times 91 \times 10^{-15}}{\frac{91 \times 10^{-15}}{7.1}}\right)$$

$$\text{ENOB} = 14.2$$

This gives a required number of bits of 14.2. This is slightly more than the 14 ENOB from the most recent prototype CMOS microelectronics chip[49,160] used in the application discussed in Section 5.2, though is a very attainable value going forwards. For example, 24-bit $\Delta - \Sigma$ ADCs are readily available on the market as used in Section 4.6. This demonstrates the need for the high OD absorption filters first used in the OPT4 design as well as the overall feasibility of the design.

There remain a number of challenges to implementing this design. Firstly, there is still a need for improved detection electronics. Neither the demonstrated detection electronics on the prototype CMOS chip discussed in Section 4.2, nor the reference detection electronics design are sufficient for reaching a 1 nM LOD with this optical design. Furthermore, the number of ADC bits needs to be slightly extended to take into account the dynamic range requirements. A number of micro-fabrication issues must also be solved including verifying the procedures from Gutierrez-Rivera et al.[50] and ensuring process compatibility with the underlying layers. The emission filter requires deposition. In these calculations the filter used is assumed to be the same as the Lee 507 filter demonstrated in the OPT4 design. This filter is 85 μm thick and thus seemingly incompatible with the thin-bottomed monolithic design. However, it was found that this thickness is almost entirely composed of a clear plastic carrier with the active layer being negligibly thick and readily removed with a solvent such as acetone. Thus, it is highly feasible that the active material could be removed and redeposited with an evaporation process. These fabrication and electronics challenges are beyond the scope of this work. However, this work does show that if these challenges can be individually addressed a full optical design can be readily built and expected to work. While integrated devices by Webster et al.,[68] Chabinyc et al.[128] and Norian et al.[141] that are described in Sections 3.1.1 and 3.1.3 above exist, they rely upon optical components that precluded low-cost, high-throughput manufacturing, whether that be interference filters, fabrication techniques or external lasers. These components have all been removed with the design presented here in Figure 3.18. Thus, while this design might appear deceptively simple, it is only through a strict attention to each parameter of a LIF system that it could become feasible. These LIF design parameters themselves were verified and developed through progressive iterations on the optics design. Thus, this thesis presents the roadmap from the early, crude OPT1 design through to something that might enable a revolution in LOC instrumentation.

Chapter 4

Detection Electronics

4.1 Introduction

A LIF detection module is composed of both optical and electrical components with the former being discussed previously in Chapter 3 and the latter being the subject of this chapter. Previously, in Section 1.3.1 a reference model was developed which featured scalable optics with an estimated 10 fW of signal from a 1 nM, 1 nL sample and a reference detection circuit previously used by the Backhouse research group with a minimum detectable signal of 1 pW. This model resulted in a predicted LOD of 100 nM, well above the 1 nM research objective. In the previous chapter, an optimised design was outlined in Section 3.8.4 which was estimated to collect 56 fW from the sample, a factor of 5.6x improved over the reference model. However, this was an insufficient improvement towards the detection goal, despite the optimisation. Therefore, the remaining performance gap must be made-up with improvements to the detection electronics. The approach taken in this chapter was to implement photodiode detection with a high gain, low bandwidth amplifier circuit as the time-scale of a CE sample is very low (on the order of 1-2s per Section 1.2.2). This approach, combined with judicious selection of components, good PCB design and a high amount of oversampling of the signal to introduce averaging, has enabled a circuit with a minimum detectable power (P_{min}) of 42 fW, below the signal for a 1 nM, 1 nL sample from the optimised optics, thus meeting the requirements for PCR-CE detection. Similar to the optics, this approach yields a low-cost instrument that is useful unto itself while being scalable to future single-chip designs currently inaccessible due to NRE considerations.

Detection begins with a method of collecting the optical power and converting it to an electrical signal. As detailed previously, for scalability reasons this work focuses on photodiode detection over the typical PMTs, APDs or CCDs used in conventional LIF instruments. However, unlike the conventional detectors, photodiodes do not have inherent gain necessitating additional circuit design. This involves first converting the photocurrent generated by the photodiode into a voltage signal and amplification of this low-level signal. In this work, a transimpedance amplifier (TIA) design was used to provide both these functions as shown in the right of Figure 4.1 below. After conversion to a voltage signal, this signal must be digitised with an analogue to digital converter (ADC) such that the data can be analysed on a computer. This is provided by an ADC. Finally, the digital signal can then be post-processed to remove noise prior

to analysis.

This chapter will first convert the primary research objectives (1 nM LOD, detection of a 1 Hz signal) into specific metrics for the detection electronics assessment. Next, it will briefly discuss two circuits implemented by others to frame the development environment. The first involves a prototype multi-functional CMOS microelectronic chip designed by the Elliott VLSI group at the University of Alberta. This chip was used in some early demonstrations and is discussed briefly in Section 4.2. This design nearly exactly matched the performance of the reference design (a P_{min} of $\approx$1 pW) and thus did not have sufficient performance to reach the detection goal, and instability of the electronics made them a poor foundation for reliable instruments. This demonstrated the need for circuits using discrete components (i.e. not built on prototype CMOS) for future instrument development. The second design by others discussed is a TIA design by Victor Shadbolt titled Previous Detection Electronics (PDE). This design is detailed in his thesis [161] and is discussed briefly in Section 4.4. Though the P_{min} for this design was worse than the reference design at 2.6 pW and too high to implement CE applications, this design provided a convenient starting point for future optimisation. Following discussion of previous designs, the chapter details two design iterations that were implemented for this thesis. The first was based on the same circuit board and schematic as the PDE design but with targeted optimisations to address key issues. This circuit, titled Detection Electronics Version 1 (DEV1) is discussed in Section 4.5 and had a much improved P_{min} of 122 fW, nearly an order of magnitude improved over the reference design. Although much improved, this P_{min} remained above the estimated optical power for the optimised designs in Chapter 3, thus more development was required. The second circuit, DEV2, details a circuit fully designed for this application with a P_{min} of 42 fW. Thus, this was the first design implemented in the Backhouse group capable of reaching the detection goals, combining with the recent OPT4 optics in Section 3.8.4 to enable a LOD of 0.75 nM of fluorophore in a 100 μm sample, satisfying the design requirements of the LIF detection subsystem. The DEV2 electronics and OPT4 optics are both included in the next generation instrument in Section 5.5.

4.1.1 Requirements

In Section 1.4, the research objectives that pertain to the detection electronics were stated to be a LOD of 1 nM from a 1 nL sample and the ability to detect a 1 Hz or greater signal frequency. This section clarifies and expands upon these objectives to form a series of requirements specific to the detection electronics. Specifically, four primary assessment factors are discussed: bandwidth (BW), sampling rate (SRATE), signal stability and P_{min}. Definitions and requirements for each of these factors is discussed below.

BW here refers to the analogue bandwidth of the TIA, the highest frequency signal the detection circuit can pass as measured in Hz. The requirement on BW is that it be sufficient to detect a CE sample without distortion or a reduction in intensity. Section 1.2.2 states that a typical CE sample will transit the detector in 1-2s, or 1 Hz. The BW must therefore be high enough to monitor this signal without distortion. The seminal textbook by Horrowitz and Hill [162] recommends a safety factor of five for setting circuit bandwidths, which puts the requirement for this circuit at 5 Hz. A BW higher than the expected peak is also important in the case where cosmic rays impinge on the detector as the resultant signals clear away at time-scales faster than a CE sample and thus can be removed in processing. It should be noted that a BW above 5 Hz is acceptable as it, too, would not interfere with the signal detection. However, higher than 5 Hz BW would not afford any improvement towards the target CE application. Thus, 5 Hz is a minimum value

the analogue circuit must exceed.

SRATE is defined as the number of times the ADC samples the signal per second. The primary concern for SRATE is aliasing of the signal, implying the SRATE must be over 2x the frequency in question as defined by the Nyquist rate. In the TIA design, all relevant signals are confined within the BW. Therefore, the SRATE requirement is set at 2 x BW. For example, a 5 Hz BW would suggest a minimum SRATE of 10 samples per second (sps) such that features at the BW are not corrupted. It should be noted that there is a substantial advantage to oversampling the signal. As described below, the P_{min} of the instrument is specified after processing with a moving average with a period of 1s. Thus, the number of data points in the moving average post-process scales directly with the sampling rate, suppressing broadband noise. This improvement scales with $\sqrt{n}$ where n is the number of sps, assuming normally distributed noise. To this end, each of the electronics iterations discussed here sample at a much higher rate than the strict Nyquist imposed requirement.

Signal stability is a core component to the development of the low-cost optics modules in Chapter 3 as a stable baseline is needed for signal analysis. One of the primary variations observed refers to the change in LED light output with LED temperature[81] which has empirically been found to go through three phases. After turning on the LED the signal begins to decrease rapidly in an exponential fashion as the LED junction heats up. This takes between 30 and 100s depending on the thermal environment the LED is in. This decay is on the order of 1% or lower of the baseline signal, though this level is still relevant given the stringent P_{min} requirements and must be removed. Following the rapid decline, the signal decreases linearly over the course of about 1 hr. Finally the signal stabilised to a steady value. Since the time period of interest for a typical CE experiment is 1-300s, only the first two phases are important to these designs. In the first phase, the magnitude of the signal decrease is on the order of 1% or lower of the baseline signal and is thus quite low. However, this is still relevant for these systems due to the stringent P_{min} requirements and must be accounted for. The approach followed here was to avoid the exponential decline phase with a "warm-up" protocol. The second phase is reproducibly linear and thus easily removed during processing. However, non-linear variations in noise would be very problematic, especially if the time-scale of these variations is within the same range as the signal. Another requirement is that the signal be reproducible as variations or bursts in noise can complicate data processing. For example, previous work by the Backhouse group had sporadic bursts of noise that required each experiment to be run in triplicate with a protocol for discounting any "noisy" runs.[84] In summary, the signal stability here is defined here as any non-linear variation in the signal after the warm-up period. A signal is considered stable if there are no such non-linear variations in a 300s time period.

Finally, as described above, the most important assessment factor is P_{min}, here defined as the optical power incident on the photodiode that causes a signal 3x greater than the total measured circuit noise (N_T). As detailed in Section 3.8.4 and mentioned above, the fluorescent power expected from an optimized optical system for 1 nM from a 100 μm x 100 μm channel is 56 fW, setting a P_{min} requirement for the circuit. This requires a factor of nearly 18x improvement over the reference detection circuit from Section 1.3.1. The P_{min} is a function of the circuit signal amplification, the signal noise and the amount of data processing that is done. Two functions are provided in post-processing. First, a linear drift removal is performed to address the thermal effects detailed above. Next, a moving average is applied as described above. In this chapter the noise is defined as the standard deviation of the baseline signal after processing, a

value representative of noise in a CE application. This can be used to calculate P_{min} as per Equation 4.1 below.

$$P_{min} = \frac{3 \times N_T}{G \times R} \tag{4.1}$$

Where N_T is the noise after processing, the factor of 3 sets a SNR of 3, G is the overall circuit gain (in $^{V}/_{A}$)and R is the circuit responsivity (in $^{A}/_{W}$). This definition of P_{min} makes it a practical figure of merit that reflects the circuit performance in a real world scenario. There are many sources of noise in the detection circuit. These include the TIA amplifier noise (defined as N_{TIA} and discussed in more detail in Appendix D), the excitation source noise, power supply ripple coupling (proven to be minor based on interpretation of Figures 4.2b and 4.5b), ADC noise and pick-up noise. Assessing the relative contributions of these sources is difficult and, ultimately, not relevant towards the practical implementation. In this work, noise will typically refer to the total measured noise N_T which includes all of these sources, with the exception of Section 4.3.1 which discusses the N_{TIA} in the context of optimising the TIA design.

Figure 4.1 summarises the LIF detection system and requirements. A mW level LED is used to excite a 1 nM sample with 100 μm width, height and depth. This sample emits fluorescent light, of which 56 fW is collected and brought to the photodiode. These factors were previously covered in Chapter 3. A TIA converts the photocurrent to a voltage which is then digitised by an ADC. After the ADC, the signal undergoes processing which includes a linear drift removal and a moving average corresponding to 1s of signal. Three of the four requirements of the circuit are annotated: the BW must be greater than 5 Hz, the SRATE greater than 2x the BW and the SNR greater than 3 for a 56 fW signal after processing such that P_{min} is less than 56 fW. Not annotated is the signal stability, which requires the signal baseline exhibit only linear variations on a timescale less than 300s.

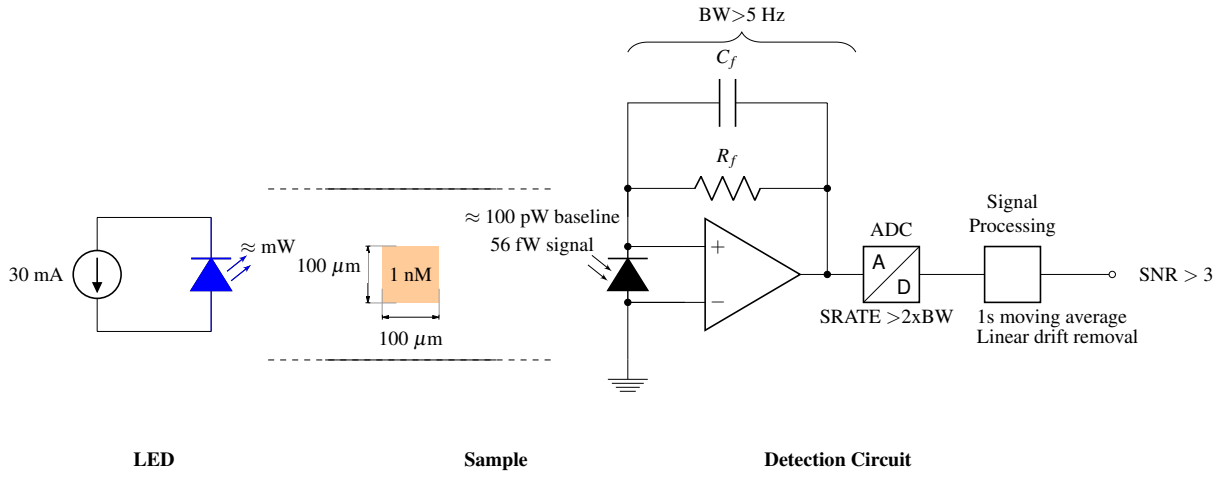

Figure 4.1: Schematic for the LIF detection system being considered. For a LED-excited fluorescent sample in a 100 μm x 100 μm channel representative of general purpose CE applications, the expected signal is 56 fW of fluorescent light within 0.5-1 Hz. The TIA design must be capable of converting this light to a signal with a bandwidth greater than 5 Hz and be sampled at double the bandwidth. The SNR after digitisation and a 1s moving average must be greater than 3 for this signal to ensure the P_{min} of the circuit is sufficient for CE applications.

4.2 CMOS detection electronics

The first detection electronics used were those integrated on-board a prototype multi-functional CMOS electronic chip designed by the Elliott VLSI group at the University of Alberta, capable of not only detection as detailed here but also HV generation.[48,49,160] In terms of optical detection, the instrument featured a 150 μm x 150 μm photodiode which fed into a programmable integrator. This integrator could be run up to 23.6 ms/sample and discharged into a second order delta sigma ($\Delta - \Sigma$) ADC with 14 effective bits. This instrumentation was contained within a 5 mm x 5 mm die wire bonded to a 64-pin package (Kyocera Corporation, CSB06428). Communication with the chip was performed by an off-board microprocessor (Parallax Propeller prototype board) which in turns communicated with a laptop via a universal serial bus interface (USB).

In practice, the integrator was run at the maximum integration time for the highest signal gain. This results in a BW of 43 Hz, satisfying the requirements of the circuit. The SRATE was, however, only 38 sps. This is sufficient for the expected 1 Hz signal, however since the SRATE is less than 2x the BW there is the possibility of aliased signals in this design as the circuit BW can pass any signal features between 19 Hz and 43 Hz. Therefore, this did not meet the circuit requirements. However, since no frequency specific noise sources were identified by the University of Alberta, this circuit was not precluded from use at the time. The circuit had a P_{min} of approximately 900 pW, which was much above the required 56 fW required for miniaturised channels. The CMOS detection electronics were tested with the OPT1 module (described in Section 3.8.1) with an electrophoretic analysis described in Section 5.2, measuring a LOD of 0.9 nM in 381 μm channels. Due to an unknown responsivity, it was difficult to correlate this LOD to the minimum optical power detectable by the circuit. To do this, the model in Section 3.8.1 was used which estimates the signal from 1 nM to be 1 pW of optical power, suggesting the CMOS microelectronics P_{min} was 924 fW. This is approximately identical to the reference circuit from Section 1.3.1, but still significantly worse than needed to reach the detection objective. Therefore, neither the SRATE nor the P_{min} of the circuit met requirements, requiring the need for on-going development. This was a particular problem for this design as the integration time (i.e. signal amplification) was already maximised, suggesting a new design was required.

In addition to the performance issues, there were two additional problems encountered with the prototype CMOS microelectronics. The first was that the on-chip ADC required a signal at $^1/_3$ of its dynamic range to operate (signals below this threshold behaved non-linearly). The absolute baseline level was not well controlled in the early optics modules due to the side-illuminating arrangement as described in Sections 3.8.1 and 3.8.2. Thus, re-tuning of the baseline between microfluidic geometries and optics modules would be needed, and this sensitive adjustment was both practically challenging as well as lacking in the rigour required for implementing robust protocols. Furthermore, as described in Section 5.2.3, the HV subsection to the CMOS caused irreparable damage to the low-voltage detection subsection and the demise of the CMOS chip. This prompted development at the University of Alberta on the CMOS microelectronics. Due to the high NRE of CMOS development, the turnaround time for the CMOS microelectronics was slow. Further, due to the prototype nature of the designs, it was difficult to rely on these devices as a reliable foundation for the optical detection. Thus, attention was turned towards the development of detection electronics made from discrete components on printed circuit boards (PCB) designed in-lab. This allowed for design and modification of circuits while avoiding the CMOS NRE.

4.3 Transimpedance Amplifier (TIA) Circuits

There was a need for detection electronics based on discrete components (i.e. not on-board prototype CMOS micro-electronics) to allow for design modifications to improve the P_{min} of the CMOS designs above. The approach taken by the lab was to implement a TIA design as shown in right of Figure 4.1 above, which uses a feedback resistor R_f to convert the photocurrent generated by the photodiode (typically sub-pA) to an a voltage that can then be readily read by an ADC. The photodiode is connected in photovoltaic mode with no applied bias, dropping the photodiode dark current to negligible levels. This is a standard method of improving the circuit sensitivity of PIN photodiodes to low photocurrent levels at the expense of response time.[162–164] A TIA design was chosen over the integrator approach used in the CMOS designs for a number of reasons including a wider variety of design guidelines in the literature[162–164] and a straightforward transfer function for simplified back-calculation of the incident optical power to verify the models in Chapter 3.

Despite the relative simplicity of the circuit, a good TIA implementation has a number of challenges in both the design and assembly. The design aspect centres heavily on controlling the noise introduced by the TIA amplifier and gain (N_{TIA}). This involves ensuring the noise gain response of the op-amp is rolled off sufficiently to prevent signal oscillation while optimising for a desired bandwidth, gain and noise level. A P_{min} less than the target of 56 fW requires the measurement of fA level currents. There exist a number of design documents pertaining to TIA design including the excellent book on photodiode amplifiers by Graeme[163] which was used for the basis of much of this analysis, the circuits textbook by Horrowitz and Hill,[162] a series of application notes[83,164–166] and web tools.[167,168] However, most of the advanced designs in these resources optimise for higher bandwidth applications (for example, telecommunications applications) and involve higher signals. These designs are not useful for this application. Further, adapting the designs to the particularly low-BW, high-gain situation used here requires typically very high capacitances that are not trivial to integrate and are often not available in high-performance materials, introducing other issues such as dielectric soakage. Furthermore, as discussed below in Section 4.6.4, introducing additional design complexity would introduce very minimal performance changes due to the high resistor noise introduced by the gain in these designs. Therefore, a simple TIA design was adopted and optimised based on the theoretical base for estimating the RMS voltage noise analysis provided by Graeme.[163] It should be noted that since the design was implemented, Analog Devices released an in-depth application note for their recently released ADA5430 op-amp.[166] The circuit design and discussion here is fully consistent with this application note. For fA current levels the schematic design is only part of the issue as the practical implementation of the circuit becomes crucially important.[169] This poses a number of challenges including the need to isolate the sensitive front end from external noise sources, provide well-regulated power, keep input capacitances to a minimum and guard against leakage currents. To reach the lofty goal of 56 fW the design, implementation and assembly must all be done carefully.

This section discusses first some general aspects of TIA design before delving into detail on three specific circuits. The first of these, PDE, was a previous circuit design by another student, Victor Shadbolt. This circuit did not have the requisite performance to meet the design objectives but is included here as motivation for improved electronics design. Next, the DEV1 circuit is discussed, which was a modification of Victor's design to test the hypotheses for previous design's shortcomings. It was built using the same PCB and schematic as the PDE circuit which, while constraining, allowed for a rapid design turnaround. This circuit was applied in Section 5.4 as part of an application demonstration. Finally, the DEV2 circuit is discussed which was re-designed to address the shortcomings in the

previous two designs. For each circuit, the key design parameters are detailed and the circuit noise to calculate the P_{min} of the design is assessed. This is followed by a discussion of the performance and assessment of what can be improved. The performance of the three circuits is summarised in Section 4.7 below. The DEV2 circuit exhibits the best performance of the three designs with a P_{min} of 42 fW at a BW of 16-32 Hz (estimated based on parasitic capacitance levels after assembly[162–164] as detailed in the circuit discussion), a SRATE of 1000sps and a highly reproducible and stable baseline, thus exceeding all of the requirements detailed in Section 4.1.1. This circuit is the first one designed in the Backhouse group that meets these requirements for application relevant CE detection.

4.3.1 TIA Design

The objective of TIA design is to reach a P_{min} of 56 fW with a 5 Hz or greater BW, which revolves around maximizing the circuit gain and minimizing N_{TIA} while maintaining the BW requirement. In order to reach high sensitivity the circuit must have high gain. For the TIA, this is equal to the feedback resistor, R_f. The BW of a TIA can be calculated by Equation 4.2.

$$\text{BW} = \frac{1}{2\pi R_f C_f} \tag{4.2}$$

Where R_f is the feedback resistance and C_f is the total feedback capacitance which includes both a set feedback capacitor as per Figure 4.1, which includes any stray capacitance. There is, therefore, a relationship between the BW and the gain. As discussed in the requirements in Section 4.1.1, the BW of the circuit must be above 5 Hz. This is quite low, potentially enabling a very large gain which is advantageous for low-level signal detection.

The standard approach to N_{TIA} analysis has been presented by Graeme in his book on TIA design[163] as well as more recently by Bonnie Baker, a prolific senior engineer at Texas instruments[167]. This analysis is performed in Appendix D for the three circuits in this chapter with general observations discussed here and the results discussed in the specific circuit subsections below. N_{TIA} refers to a root mean square (RMS) noise produced at the output of the TIA circuit. Therefore N_{TIA} is a significant component to the total measured noise N_T, and optimisation of the TIA to maximise signal and reduce N_{TIA} relates directly to the instrument performance. N_{TIA} can, in general, be considered as three distinct components: Johnson noise from the resistor, input current noise and input voltage noise. Of these three, the input current noise (proportional to the square root of the input bias current) can be considered negligible due to the very low bias currents of the op-amps used here, as is common in this field[162,167]. Thus, we are left with input voltage noise and Johnson noise.

Johnson noise, or thermal noise, is a wide-band noise with a nearly flat spectrum[162] due to the resistor used in the circuit that is limited by the circuit bandwidth. In a TIA, this is proportional to $\sqrt{R_f}$ and has the same bandwidth as the signal described by Equation 4.2. This means the Johnson noise is independent of the op-amp used to implement the TIA and can be considered the ”base” noise that can only be changed by adjusting the feedback resistor or circuit bandwidth. In general, optimising the Johnson noise involves increasing R_f as high as possible.[162–164] This might seem counter-intuitive at first, but since the Johnson noise scales with $\sqrt{R_f}$ and the signal scales with the gain at R_f, the overall SNR also scales with $\sqrt{R_f}$. In other words, the Johnson noise will increase in this scenario, but slower

than the signal. The limit on increasing R_f is the bandwidth. As detailed in Equation 4.2, the bandwidth is inversely proportional to the product of R_f and C_f. Thus, for a given bandwidth and gain, the upper limit on the gain is set by C_f which includes both feedback and parasitic capacitances. This typically varies from 0.5 pF to 2 pF depending on the circuit's implementation.[163,164] Therefore, for a 5 Hz bandwidth the parasitic components limit R_f to 10-60 GΩ based on Equation 4.2.

Input voltage noise is another broadband source of TIA noise, though its magnitude is highly dependent on the target frequency and op-amp used. At low frequencies, it is dominated by the "pink noise" or $^1/_f$ noise of the op-amp while at higher frequencies the various input capacitances cause amplification of the op-amp noise floor. In general, there are a few aspects to consider. First, the majority of the input voltage noise is proportional to the op-amp noise floor,[163] thus picking a low-noise op-amp should improve performance. However, this is not always true. The key variable when considering the input voltage noise is the amount of frequency spectrum that noise is stretched over. This noise is not limited to the same bandwidth as the signal and instead can stretch all the way to the unity-gain crossover frequency which can be in the MHz or higher. Considering that the pink noise of an op-amp only exists up to 100 or so Hz, it is clear that the overall noise is typically dominated by the high-frequency component. Therefore, the input voltage noise can be reduced by using an op-amp with a lower unity-gain crossover frequency. Finally, since the input voltage noise occupies spectrum that is typically much beyond the BW,[163] filtering can be a very effective tool to reduce this noise without perturbing the signal. This is a strategy pursued by DEV2 with more in-depth justification in Appendix D. It should be noted that sources such as Graeme[163] and Horowitz and Hill[162] suggest various composite amplifier designs where the high frequency filtering is performed during the current-voltage conversion. While elegant, they target applications in the 100s of kHz. Adjusting these designs to the Hz regime would require very high capacitances which can have a negative impact the signal stability by exceeding the op-amp's ability to drive their load and adding dielectric soakage (hysteresis) to the signal. Furthermore, the objective of these designs is to reduce the signal offset which is not a concern due to then nominal baseline from the optical design. Therefore, a post-TIA filter would have the same results with lower risk of error and simpler design. Overall, the approach to reducing input voltage noise used was to select an op-amp with a low unity-gain bandwidth and/or a low noise floor, with a post-TIA low pass filter.

The input voltage noise can also cause a phenomenon called gain-peaking which causes signal oscillation (and a great increase in noise). This is covered in more detail by an application note by Texas Instruments[165] and avoided through the use of a feedback capacitance in parallel with the feedback resistor. The equation to calculate this minimum required feedback capacitance is in Appendix D. However, for the high-gain systems described here, the minimum capacitances are very small, often smaller than the expected parasitic capacitance (in the fF regime). As such, gain-peaking is not a primary concern of these circuits.

In addition to input voltage noise, another factor in op-amp selection is the input bias current. There are three key issues with the input bias current. Firstly, this current provides a signal offset to the system. This is not a particular cause for concern as the LIF detection systems in this thesis already have a substantial baseline. The input bias current is also a source of noise in the TIA design. This, too, is not a particular cause for concern as the magnitude of this noise is negligible as compared to the other noise sources as shown in the calculations in Appendix D. The final, and most important, issue is that the input bias current is highly susceptible to environmental factors.[166] This makes it a substantial source of signal instability. Therefore, in order to meet the stability requirements of the circuit it is crucial that the input bias current of the op amp is low as compared to the signal. This is particularly difficult in the fW regime

as the typical photodiode will generate fA level currents. There are still a few suitable op-amps available that optimise for this purpose, such as the LMC6082 and LMP7721 op-amps used in DEV1 and DEV2.

Finally, the layout of a low-noise TIA is crucially important. First, the input stage must be well guarded against leakage currents. This can be done by air-wiring as in DEV1 or by using a guard trace as in DEV2. Next, the TIA input (i.e. everything before R_f) must be designed with as low as possible parasitic capacitance. This has not only an affect on the bandwidth as described in Equation 4.2 but also causes slight increases in the input voltage noise. Strategies undertaken to do this are detailed in the DEV2 design description in Section 4.6. Finally, good low-noise board design principles should be followed such as the use of ground planes, good power regulation, the use of decoupling capacitors and the separation of digital and analogue signals. At very high gains the circuit is also very sensitive to pick-up noise and thus good shielding is also important.

4.4 Previous Detection Electronics

The PDE design was developed by another student, Victor Shadbolt, with more details available in his thesis.[161] Even though this circuit was designed by others, a discussion is included here as motivation for the improvements implemented in subsequent iterations. The PDE circuit was a first foray into TIA design with a measured P_{min} of 2600 fW. This was notably worse than both the CMOS detection electronics ($\approx$ 900fW) as well as the reference circuit demonstrated previously by the Backhouse group (1000 fW) and did not meet the requirements of the module (56 fW). More importantly, the signal stability in this circuit was often poor, leading to phantom features in experiments. This work was combined with the OPT2 module (Section 3.8.2) in an instrument targeting DNA applications described in Section 5.3, though this work was not published due to poor LOD. While this circuit did not meet the performance requirements of the application, it provided a convenient starting point and the basis for circuit optimisation.

4.4.1 Design

The PDE design consists of a TIA followed by a non-inverting voltage amplifier and a resistive divider. An inexpensive op-amp (TLV272, Texas Instruments) was used to provide both the TIA and voltage amplifier stages. The TIA gain was set with a 100 MΩ resistor with a set feedback capacitance of 1 nF resulting in a BW of 1.59 Hz. At the time of design the safety factor on the BW was not implemented, and thus a lower BW was chosen for better noise performance. However, as explored below, this did not have the desired effect. Following the TIA a voltage amplifier with a gain of 32.6 was applied. Since the voltage amplifier will roughly amplify both the signal and noise by comparable amounts, it does not have a profound effect on the SNR of the design. Instead, it is used to map the first stage output to the dynamic range of the circuit to reduce the need for a higher bit ADC. In order to avoid over-voltage issues with the ADC, the signal was put through a voltage divider (factor of x0.223) to match the maximum op-amp output to the ADC voltage rail. This prevents any op-amp output from damaging the ADC input. The total transfer function of the circuit was 7.27×10^8 $^{\mathrm{V}}/_{\mathrm{A}}$. The ADC used was a 12-bit successive approximation register (SAR) (MCP3202, Microchip Technologies). The entire circuit was single-ended and powered by a 20 V, 0.5 A input. This was regulated down to 15 V to power the op-amp and down to 3.3 V as a reference for the ADC. The ADC was probed using SPI from a

microcontroller (LabJack U6, LabJack Corporation). The SRATE was limited to about 160 sps by the slow LabJack software SPI, though this was not well controlled and varying from 80 sps to 205 sps throughout the acquisition. A schematic is available in Appendix D with more details in Victor's thesis. [161]

Appendix D estimates N_{TIA} to be $\approx 400\ \mu$V. Provided normally distributed noise and a 100 point moving average, this suggests a P_{min} of 550 fW could be achieved. This analysis assumes that N_T is composed of only N_{TIA} (i.e. all other noise sources are negligible). Furthermore, the expected reduction with averaging assumes white noise and no baseline variation. Even with these assumptions, the 550 fW post-processed P_{min} is clearly above the 56 fW target and thus this circuit cannot meet the detection requirements. Analysis of the N_{TIA} breakdown illustrates that one of the primary reasons for the insufficient performance of the design was that the circuit was not well optimised for this particular gain. The $N_{TIA}$is heavily dominated by the input voltage noise in the region between 1.59 Hz (the BW) and 3 kHz, over an order of magnitude higher than the Johnson noise. As mentioned in Section 4.3.1 above, the Johnson noise is component agnostic and a "base" noise inherent in the TIA design for a given gain. Since this noise is insignificant, it points to poor component optimisation. Furthermore, this suggests that the strategy of limiting the BW to limit noise was not effective for this circuit as most of the noise is not confined to the BW. This demonstrates the need either for a lower unity gain bandwidth op-amp or a post-TIA low-pass filter.

4.4.2 Testing and Data Processing

This circuit was attached to the OPT2 optics discussed in Section 3.8.2 which featured an uncontrolled spot size (estimated 323 μm) and 254 μm wide and 254 μm deep channels. Illumination was provided by two side-illuminating LEDs run at 30 mA using a constant current source (LT3092, Linear Technologies). CE was performed on this instrument with details discussed with the application in Section 5.3. The circuit N_T was assessed by measuring the standard deviation of the baseline signal of eight different electrophoretic separations and applying the standard data processing of a linear fit to remove drift and a moving average. The moving average was applied across 100 data points. Due to the high variability of the SRATE, the moving average was intentionally set below the nominal value of 160sps to avoid over-averaging. This should be considered preliminary testing (as the sample size for noise analysis is small). However, due to the relatively poor performance, a robust analysis was not considered necessary.

In addition to the above analysis, a baseline run was done with the LabJack U6 ADC attached in place of the detection circuit ADC. This allowed for a controlled SRATE of 1000 sps and therefore a frequency analysis of the baseline, though it did involve routing the signals externally to the LabJack. The external routing made the design more susceptible to pick-up noise. Further, the use of the LabJack U6 ADC in streaming mode interfered with the microcontroller's ability to both measure the optical signal and control the other aspects of the instrument (such as valves and high voltage). Thus, this connection was best suited for a short experiment to perform analysis on the frequency domain of the signal and not routine use. This frequency analysis was performed to check for 60 Hz noise coupled from mains power which had been identified as an issue in previous work.

4.4.3 Preliminary Testing Results

The preliminary testing results in a N_T of 0.21 mV after processing and a P_{min} of 2600 fW. This does not meet the detection requirements of the design. More importantly, the signal stability of this instrument proved to be quite poor suggesting that the P_{min} calculated overestimates the circuit's ability to detect fluorophore. Figure 4.2a below depicts the worst of the eight runs in terms of instability. This is a separation of two fluorescently DNA fragments of about 200 nM concentrations with peaks at 57s and 67s (as inferred by other experimental data). However, in addition to these two peaks, the data features an unusual shift in the drift below 30s, a sudden drop in signal at 38s and another subtle drift shift at 120s. The drop at 38s is particularly bad as, when combined with the change in drift, it appears peak-like. Subsequent experimentation on both this instrument and a commercial CE instrument verify that this is a signal artefact introduced by the electronics and not the sample. These phantom features are very problematic for data analysis and are not fully encapsulated by the noise assessment. Therefore, the PDE circuit meets neither the P_{min} nor the stability requirements.

Figure 4.2b shows the fast fourier transform with a uniform window of the baseline signal acquired by the LabJack ADC at 1 kHz. The most important observation is that there were no peaks corresponding to 60 Hz noise coupled from the mains power, an issue that faced previous instruments. Figure 4.2b also confirms that there are no expected features in the 80-500 Hz region that would cause aliasing in the data when sampled at 160 sps, and that a moving average filter is an effective noise reduction technique (as there is no dominant frequency component to the noise). This suggests the power regulation circuit being used is suitable for this application

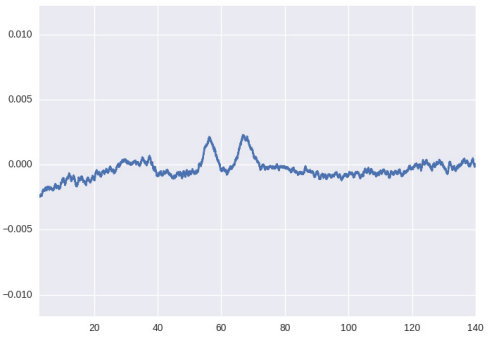

(a) A sample run using the PDE circuit with the OPT2 optics with 254 μm x 254 μm channels. The plot presents the electrophoretic separation of two fluorescently labelled DNA products that arrive at 57s and 67s. These products have an estimated concentration of 200 nM. The P_{min} is clearly insufficient for 1 nM analysis. Further, the instability of the signal (notably around 38s) creates false features that obscure the data analysis and preclude the use of this circuit for sensitive applications.

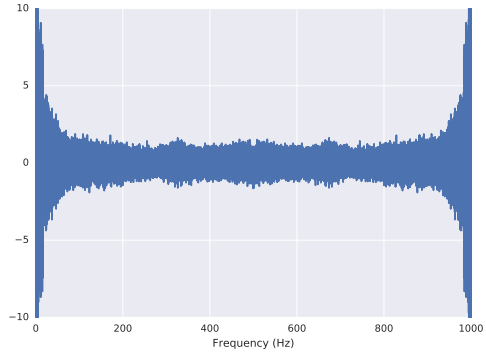

(b) A fast fourier transform with a uniform window of the signal output of the PDE electronics with a baseline signal applied, sampled at 1 kHz by an external ADC. There does not appear to be any particular noise frequencies in this plot, suggesting the power regulation has adequately removed the 60 Hz noise from mains power.

Figure 4.2: Results of the PDE detection electronics testing.

4.4.4 Discussion

The PDE circuit did not meet the requirements of the design. Firstly, the P_{min} of 2600 fW is almost two orders of magnitude off the target requirement of 56 fW detailed in Section 4.1.1, largely due to poor optimisation of the components as described below. Further, the BW of the circuit was 1.59 Hz, or only just barely enough to pass a CE signal and below the target of 5 Hz which includes a safety factor. Finally, and most importantly, the circuit exhibited high signal instability. The SRATE of 160 sps was sufficient for the application, exceeding the limit of 2 x BW. However, the uncontrolled nature of the sampling (excluding the brief frequency analysis from Figure 4.2b) was an issue as it limited the amount of data processing that could be done. In summary, of the four requirement metrics, the PDE circuit only met one and thus was not suitable for on-going use.

As discussed in Section 4.4.1 above, the gain and BW of this circuit were not well optimised. Specifically, compromises were made to the BW (setting it below the target of 5 Hz) to attempt to reduce N_T. Further analysis suggests this was a poor strategy due to the N_{TIA} being dominated by the high frequency components. For example, if the feedback capacitor was decreased from 1 nF to 300 pF the BW would increase to 5.3 Hz (based on Equation 4.2) and meet the BW requirement, but only increase the N_{TIA} by 1.5% (based on the calculations in Appendix D). Thus, this BW restriction was not very useful for noise reduction. Another optimisation that could be readily implemented would be to redistribute the circuit gain such that the TIA gain is increased and the voltage amplifier gain was decreased. As previously discussed, the voltage amplifier has a very small effect on the SNR as it amplifies both signal and noise while the gain of the TIA amplifier improves SNR proportional to $\sqrt{R_f}$. For example, if the TIA gain was increased by an order of magnitude, the voltage amplifier gain was decreased by an order of magnitude (resulting in the same overall signal gain) and the feedback capacitor were optimised to 30 pF, the N_{TIA} would decrease by a factor 6.7 for identical gain and a BW of 5.3 Hz that meets the design requirements. This illustrates the need for circuit optimisation.

Another easy to implement adjustment to the circuit was to upgrade the op-amp used. The PDE circuit used a relatively low performing op-amp with a voltage floor of 35 $_{\mathrm{nV}}/_{\sqrt{\mathrm{Hz}}}$ that couples directly into the input voltage noise. Further, the bias current of the TLV272 is 1 pA, which is orders of magnitude higher than the expected photocurrents to be measured. This high bias current was likely a contributor to the poor signal stability. While low-cost design was an objective of this research, the differing cost between the low-performance op-amp used here and more optimised solutions is low while the performance difference is substantial. Later designs explored the use of op-amps optimised for low current TIA designs.

The P_{min} could also be readily improved through a change in the microcontroller used to interface with the ADC. The ADC used can theoretically operate up to 50 ksps, but was operated at only 160 sps due to the slow software SPI of the LabJack U6. The high computational overhead of using the LabJack in a windows environment also led to a high variability in the sampling rate. As a SAR ADC, there is no noise advantage to sampling at a lower rate whereas there is a substantial advantage to sampling at a higher rate as increased data averaging can be used to remove noise (assuming that it is broadband, as confirmed in Figure 4.2b). Thus, future designs used an improved microcontroller to increase the oversampling of the signal and use that oversampling to suppress noise and improve P_{min}.

The main issue with the circuit was the signal instability. While reduction in the input bias current of the op-amp will reduce the susceptibility of the circuit to the ambient environment, the primary hypothesised source lay in the fact that

the op-amp input was not guarded against leakage currents of any sort. Leakage current couples directly into the signal and is highly humidity dependent and thus sensitive to the ambient environment. The instrument the PDE circuit was tested with was also situated directly next to an air intake vent, likely exacerbating these issues. Attention to leakage currents is a crucial aspect of sub-pA design [169,170] and a notable oversight in the assembly of the PDE circuit.

Overall, this circuit had insufficient performance due to poor optimisation and assembly methods. However, it did draw attention to a number of concerns that motivated the improvements that were implemented in subsequent designs. Further, as seen in Figure 4.2b, the power regulation used here appropriately attenuated noise coupling from mains power. This regulation circuit could be re-used, as in the DEV1 circuit discussed below.

4.5 Detection Electronics Version 1 (DEV1)

DEV1 was the first detection circuit that I became involved in with the objective of exploring easily addressed issues of the PDE design in a quick iteration that re-used as much of the previous circuit as possible. Specifically, we sought to avoid a PCB re-design and re-use the board from from PDE. This imposed substantial limitations on the changes that were possible as the new design had to fit the schematic previously used. However, within these constraints targeted improvements to the key issues of the previous design could be made with respect to assembly, op-amp selection and gain distribution. The measured P_{min} of this was 122 fW, an improvement of 21x over the previous design and 8x better than the reference model in Section 1.3.1. However, in spite of this improvement, it did not quite reach the 56 fW P_{min} required to achieve 1 nM detection with low-cost, scalable optics. Further, there were a number of issues with the circuit beyond the P_{min} including an inability to detect signals close to the ground rail and a relatively uncontrolled SRATE. Despite these limitations, the improved stability and P_{min} resulted in a useful circuit that was applied as part of the demonstration in Section 5.4 with the OPT3 optics to demonstrate the state of the art in LED-Photodiode LIF detection for CE. [89]

4.5.1 Design

The DEV1 design required the circuit match the schematic of the PDE circuit, which imposed a number of design restrictions. Firstly, this required a re-use of the voltage regulation circuit from before. Since tests of the voltage regulation showed an absence of 60 Hz noise this was not considered an issue. However, it did require that the op-amp be single-ended and capable of operating from a 15 V supply. The ADC was also re-used as this was the best performing ADC with the same pin-out and power rail (3.3 V) used on the board. The ADC was not a limiting factor in the previous design so this was also not an issue. Finally, the design had to conform to the same general design, with a TIA followed by a voltage amplifer and a resistive divider. However, in spite of these limitations there was still room for targeted improvements to the op-amp, the gain/bandwidth used and the assembly methods as discussed below.

Firstly, the op-amp was changed from the relatively low performing TLV272 to the LMC6082 (Texas Instruments). By requiring that the PCB not change, the restriction on the op-amp used was that it be fully compatible with the

previous design. The specific requirements were for the op-amp to have two on-chip circuits in the standard pin-out, be capable of rail-to-rail operation as the PDE circuit was single-ended and be compatible with a 15V rail. 17 low input bias current amplifiers were analysed with the N_{TIA} analysis in Appendix D, with the LMC6082 having best expected performance. This amplifier has a much lower input bias current (10 fA down from 1 pA), a lower noise floor (22 $^{nV}/_{\sqrt{Hz}}$ down from 35) and a lower unity-gain bandwidth (1.3 MHz down from 3 MHz). Based on the calculation in Appendix D, these factors combine to lower the N_{TIA} of the circuit by a factor of 2.4, with expected improved stability from a much lower input bias current.

In addition to changing the op-amp, the circuit resistances and capacitors were also changed. For DEV1 the TIA gain was increased from 10^8 to 10^9. This was in keeping with the observation that the SNR scales with increasing TIA gain. It should be noted that while higher resistances are available, higher through-hole format resistors that fit the lead spacing on the PCB were not available at the time. The voltage amplifier gain was also increased from 32.6 to 51, resulting in an overall circuit gain increase by a factor of 15.6. The maximum gain is set by the dynamic range of the circuit and the sum of the baseline and signal expected. Improvements to the optics that were occurring simultaneously with this circuit design reduced that baseline, enabling higher electronic gain to be implemented. Based on the calculation in Append D, the gain change (independent of the op-amp change) would result in 2.7x more N_{TIA} and 15.6x more signal and an improvement in P_{min} of 5.8. The voltage divider remained from the previous design, resulting in an overall gain of 1.172×10^{10} $^{V}/_{A}$. The feedback capacitance used was 20 pF, giving a BW of 7.96 Hz, thus exceeding the requirement of 5 Hz.

One of the most significant adjustments made with the DEV1 circuit assembly was the implementation of air-wiring to combat the leakage currents in the PDE circuit. Air-wiring consists of routing the sensitive signal (photodiode, feedback resistor, feedback capacitor and op-amp inverting input) above the PCB, using air as an insulator against any leakage. Compared to introducing a guard rail, air wiring has improved leakage current rejection at the expense of being cumbersome to assemble, fragile and more sensitive to vibrations as multiple components are suspended in the air.[170] The primary reason for implementation of air-wiring, though, was that it allowed for addressing the leakage current with no changes to the PCB. This led to improved stability and eliminated the presence of the peak-like fluctuations of the PDE circuit shown in Figure 4.2a above.

Finally, the microcontroller used to probe the ADC was changed from the LabJack U6 to a BeagleBone Black Rev. A, an open-source microcontroller. This improvement allowed for the increase in SRATE from 160 sps to 1950 sps. Furthermore, the BeagleBone Black was able to more reliably sample the ADC, reducing the variability in the SRATE substantially (though the precise SRATE remained uncontrolled between 1800 and 2100 sps). Since the timescale of the application had not changed (1 Hz), this extra over-sampling allowed for further noise removal by increasing the bin-size of the post-processing moving average.

The estimated N_{TIA} for the circuit was calculated in Appendix D to be 558 μ RMS. At a SRATE of 1950 Hz, assuming white noise only, the circuit P_{min} could reach 10 fW. Similar to the discussion of PDE, this estimate does not take into account a large number of factors that practically contribute to N_T and is thus a lower-bound on what should be expected. However, since this value is below the required P_{min} of 56 fW, with good assembly and layout this circuit might meet the requirements.

One of the primary design issues for TIA circuits is control of the high frequency input voltage noise which exceeds

the signal bandwidth. In the PDE circuit, this noise dominated the design suggesting the need for a post-TIA low pass filter. This could not be readily added to this design without PCB changes, thus the high frequency noise must be controlled by judicious op-amp selection as discussed above. Analysis of the DEV1 N_{TIA} distribution shows that the Johnson and input voltage noise being comparable in value at 11 μV RMS and 46 μV RMS respectively. Thus, the op-amp, gain and feedback capacitance of this design was relatively successful in controlling the input voltage noise component. The highly optimised nature of this circuit suggests that any improvements would require PCB adjustments.

4.5.2 Testing and Data Processing

The DEV1 circuit was attached to the OPT3 optics (Section 3.8.3) and loaded with an empty microfluidic chip. These optics consisted of two LEDs side illuminating the channel, with both LEDs run at 30 mA set by a constant current source (LT3092, Linear Technologies). The resulting baseline signal of about $^1/_3$ of the ADC dynamic range (5 V at the voltage amplifier output, 1 V at the ADC) was analysed to assess the N_T. An automated program toggled on an LED, acquired 200s of data and then turned the LED off. This program was repeated 30 times. Sampling was performed by the microcontroller which saved the time of the sample and ADC reading as fast as it could. Therefore the SRATE was not strictly controlled. Empirically, it was found that during the first 0.5-0.75s of each experiment the SRATE was between 500 and 800 sps. This was attributed to the microcontroller multitasking during startup (it was not running a real-time operating system). Following this startup phase the SRATE was found to vary between 1800sps and 2100 sps with an average of 1950 sps. The reduced SRATE variation was attributed to the Linux operating system on the BeagleBone Black microcontroller being less prone to unusual behaviour as the Windows operating system used to interface with the previously used LabJack. While not ideal, since no frequency-specific post-processing was done and the SRATE remained very high as compared to the circuit bandwidth throughout the experiment, this was not a primary issue for this preliminary demonstration.

It has been noted by ourselves and others[81] that LED output light decreases even at a stable current due to junction warming effects. This resulted in signal drift with two regimes: a non-linear regime directly at startup and a long-term near linear drift over the course of the time scale associated with a CE experiment. The non-linear regime for the OPT3 optics was under 20s. Thus, this data was discarded from noise analysis. Otherwise, the standard processing method described above was used; a linear fit was applied and subtracted from the data and a 1950 point moving average applied. A frequency analysis was not done as the power regulation circuit was assessed with the PDE circuit in Figure 4.2b above.

Testing Results

The experiment resulted in a measured N_T of 154 μV and a P_{min} of 122 fW. Furthermore, no instability or "peak-like" features were seen in any of the baseline runs outside of the 20s "warmup" period at the start of each run. This held true for practical CE experiments as well as shown in Section 5.4 where the 20s warmup was instituted as part of the running protocol. The results of the 30 sample baseline test are shown in Figure 4.3.

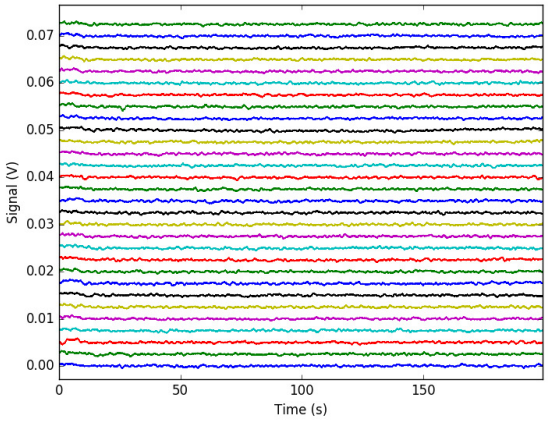

Figure 4.3: Results of the baseline test of the DEV1 circuit. The traces have been corrected for the linear drift of the LED and a 1950 point (1s) moving average applied. The average noise was 154 μV leading to a P_{min} of 122 fW for this circuit. The signal was stable for each of the baseline runs with a slight non-linear drift due to LED warm-up effects in the first 20s of each run. These first 20s are discounted during analysis, both of the noise here as well as for CE applications.

4.5.3 Discussion

The DEV1 electronics were a substantial improvement over the PDE electronics in terms of P_{min}, BW and signal stability, the three assessment metrics the previous design did not meet. For this design, the BW was increased to 7.95 Hz, thus meeting the 5 Hz requirement, the SRATE was 1950 sps, thus meeting the 2 x BW requirement and the signal was stable. However, despite these improvements, the circuit did not quite reach the 56 fW P_{min} target. Overall, this was a substantial improvement over the PDE design meeting 3/4 of the detection electronics requirements, but more design development was required. This section discusses the performance improvements while laying out strategies for future improvements.

The 122 fW P_{min} of the DEV1 design is a 21x improvement over the previous PDE circuit. This improvement was the result of both an improved circuit and higher oversampling (and thus more averaging). To separate these two improvements, a factor is needed to adjust for a uniform SRATE. Assuming normally distributed noise, the moving average suppresses noise by a factor of $\sqrt{n}$. Thus, the change of averaging from 100 samples to 1950 samples would be expected to decrease noise by a factor of 4.4. This suggests the circuit improvements account for a factor of 4.7x. As discussed above, the two main design changes to this circuit were a better op-amp and changes to the TIA gain. Calculations in Appendix D suggested these changes would improve P_{min} by factors of 2.4 and 5.8 respectively, the combination of which exceeds the measured improvement of 4.7x. This suggests that noise sources outside of the amplifier are significant on this level. These could include assembly issues (for example, the digital control lines intersected with analogue power lines on this board, possible injecting noise), power regulation noise outside of the expected 60 Hz ripple, additional resistor noise from the voltage divider and noise from the illumination. The 122 fW P_{min} is also a factor of 8x better than the reference model (1 pW), however it remains above the 56 fW required to implement 1 nM detection with optimised optical designs, suggesting the need for these improvements.

The DEV1 signal stability was greatly improved from the PDE circuit. Excluding the first 20s of the run during the LED warmup phase, each of the 30 traces in Figure 4.3 was very stable with the linear drift removal being near perfect. This is contrasted to the noisy and unstable signal in Figure 4.2a. Two strategies were implemented to improve stability: reduction in the op-amp input bias current and air-wiring to reduce leakage currents. While it is not clear how responsible these changes were to improving the signal stability, the empirical results show that they were successful. With regards to air-wiring, while it is one of the best methods of reducing leakage currents,[169] it does have a number of drawbacks. Firstly, it complicates circuit board population by forcing by-hand assembly as compared to other methods which can be assembled in a re-flow setup. This leads to higher variability in assembly as well as complicates production if a large number of boards need to be assembled. Some components, especially those that are surface mount or have tightly-spaced leads, can be difficult to robustly attach wiring to, leading to broken or poorly joined connections. Based on the results of this circuit board that was not an issue here, though it could become one going forwards, especially if this board needed to be replicated in bulk. Assembly would be further complicated if surface mount feedback resistors are required. At the time of design (and writing), the maximum through-hole resistor in stock on Digikey is 5 GΩ while surface mount components up to 50 GΩ are readily available. Air-wiring also can lead to higher sensitivity to vibrations and pick-up as the connection between components is both longer and suspended in the air. Thus, while a good strategy for quickly solving the problem on this PCB, future designs should be on a new PCB with appropriate guard traces.

The SRATE of the DEV1 circuit was vastly improved by switching to a faster microcontroller. However, this SRATE was not well controlled as it essentially consisted of "running as fast as possible" to achieve the best averaging performance. This, however, is not a very rigorous approach and, in cases where the microcontroller lags, can lead to erroneous data processing. Future designs should have a more robust sampling method to ensure that this error is not encountered.

One important deficiency in both the PDE and DEV1 circuits was their reliance on single-ended design. As the optics development proceeded, the baseline of the optical signal steadily decreased. As this baseline decreased the signal began to get closer to the negative rail. The op-amp used reports that it can swing within 20 mV of either rail, which should be sufficient for any expected signal baseline. However, this does not take into account the noise of the circuit, nor the ability of the ADC to digitise this signal or noise. This led to clipping of the optical signal, which in turn complicates data processing. Thus, in order to implement more advanced optical designs, there was a need to introduce a split power rail.

The DEV1 circuit did not quite meet the P_{min} requirement of 56 fW, but it was still a useful module for certain applications. Particularly, the OPT3 optics produced 685 fW of fluorescent signal from a 1 nM sample in 254 μm channels. Thus, the DEV1 circuit P_{min} was more than sufficient for this application. The combination of these two components for CE applications is discussed in Section 5.4 where the state of the art LOD of 150 pM for LED and photodiode based LIF detection for CE[89] is detailed.

In summary, the DEV1 circuit was a very substantial improvement over previous designs and was used in a significant application as detailed in Section 5.4. However, it did not quite reach the performance requirements for general purpose protocols. Thus, there was a number of design changes and a new revision of the circuit board. These design changes include introduction of leakage current protection at the PCB level to avoid air-wiring, implementing a robust SRATE of the circuit and moving to split-power supply rails. These were all implemented in the DEV2 design.

4.6 Detection Electronics Version 2 (DEV2)

The DEV2 circuit was a complete re-design of the detection electronics to target key improvements over DEV1 with particular attention paid to the PCB layout and assembly. This involved a new regulation circuit for split power rails, a new TIA layout to minimise leakage currents and input capacitance, a new op-amp with a lower input bias current and a new ADC for improved noise performance. The measured P_{min} of this circuit was 42 fW, the first circuit produced on this project capable of detecting 1 nM in 100 μm channels and meet the requirements of the detection circuit. This design combines with the most recent optics, the OPT4 optics in Section 3.8.4, to form the LIF detection of the next generation instrument detailed in Section 5.5.

4.6.1 Design

There were four key improvements required for the DEV2 design compared to DEV1: avoiding the air-wiring while maintaining low leakage currents and signal stability, improve the P_{min} by a factor of at least 2.2, introduce a split power supply to prevent noise clipping at low signal levels and introduce a reliable SRATE. These improvements can be categorised as either relating to the schematic or the layout.

Circuit Design

The schematic for the DEV2 circuit is simpler than the PDE/DEV1 design. Firstly, both the voltage amplifier and resistive divider from the previous design were removed such that the schematic features simply a single stage TIA and the ADC. This is shown in the schematic in Appendix D. As discussed previously, the voltage amplifier and divider were not important with regards tot he P_{min} performance as they scaled both the signal and the noise. Instead, their purpose was to match the TIA output to the ADC dynamic range. In this circuit, neither of these functions were necessary. Firstly, this design ensured that the op-amp and ADC combination used shared the same voltage rails ($\pm$2.5 V) to such that the op-amp output could not damage the ADC. This removed the need for the voltage divider. Furthermore, the new ADC selected (discussed below) contained a programmable gain amplifier (PGA) internally to ensure the input aligned suitably with its dynamic range. This removed the need for the voltage amplifier. The removal of these functions from the schematic both simplified the design while limiting the potential for noise injection from post-TIA sources. Other changes to the schematic include improvements replacement of the op-amp for improved performance, increased TIA gain and BW and implementation of a $\Delta - \Sigma$ ADC, each of which is discussed below.

One of the improvements to the DEV2 circuit was a change in op-amp. Without the power and layout constraints of the old PCB, the potential pool of op-amps available was increased. Of the op-amps on the market, the LMP 7721 (Texas Instruments) was deemed the best fit for this application for a number of reasons. Firstly, of the op-amps readily available on the market, very few have input bias currents lower than the expected signal. With a responsivity of 0.33 and a power of 56 fW the expected photocurrent is 168 fA. While there exist a number of op-amps with nominal 100 fA bias currents, the maximum specified currents for these components are typically at 1 pA or above. For example, the 10 fA LMC6082 used in the DEV1 circuit has a maximum input bias current of 4 pA. The LMP7721 has the lowest input bias current offered by TI (3 fA nominal, 20 fA maximum) and as such was selected as the working example in

a recent series of article on fA design.[170] This is expected to ensure high stability and less dependency on the ambient environment for this board.[166] The LMP7721 also had the lowest noise floor of any sub 100 fA bias current op-amp analysed at $7^{nV}/\sqrt{Hz}$. Finally, in comparison to most single circuit op-amps, the LMP7721 has a modified pinout that makes it more suitable for introducing guard traces and isolating the inputs from leakage currents. The only issue with the LMP7721 is that it has a particularly high gain-bandwidth product of 15 MHz. While potentially useful for higher frequency amplifications, for the low frequency high gain environment used here this merely gives more bandwidth for input voltage noise. This can be counteracted with a low pass filter which is explored below as well as in Appendix D.

The TIA gain was increased again in the DEV2 circuit to 10^{10}. This was enabled by the new circuit board being built to accommodate 10 GΩ surface mount resistors (HVC Series, Ohmite) which are readily available and have been applied to high gain applications in the literature.[166] This improves the SNR of the TIA by a factor of three over the 10^9 gain TIA design used previously (as SNR scales with $\sqrt{R_f}$). For this very high gain, it was decided to leave out the feedback capacitor entirely. With a feedback resistance of 10^{10} and a target BW of 5 Hz or higher, the maximum feedback capacitor that could be used is 3 pF. This feedback capacitance is in parallel with any parasitic capacitances from the board or the feedback resistor, which were not measurable at the time of design. Various references have stated typical PCBs have values between 500 fF and 2 pF with well-designed boards being on the lower end of this range,[163,164] thus the parasitic capacitance could be very close to the maximum feedback capacitor for the application. To guarantee a BW that exceeded the requirements, the feedback capacitor was omitted. Normally, a feedback capacitor is required to prevent gain-peaking. However, for this high-gain design, the minimum required feedback capacitance is 2 fF which is much smaller than any feasible PCB parasitic capacitance.[166] As a result, the BW of this design is not strictly set but is expected to be between 8 and 32 Hz. Any value in this range meets the requirements of the design.

The final schematic change was to switch from the single-ended 12-bit SAR ADC used in PDE and DEV1 to the ADS1248 (Texas Instruments) 24-bit split supply $\Delta-\Sigma$ ADC. There were three primary considerations for using this ADC. Firstly, by using an inherently split supply ADC the voltage rails of the ADC and TIA could be exactly matched ensuring that there was no change of damaging the ADC rails while maximising the dynamic range of the signal. Since the voltage rails were the same, there was no possibility of the TIA output exceeding the maximum voltage of the ADC, eliminating the need for protection diodes or voltage dividers which might introduce leakage currents, noises or offsets to the circuit. As briefly described above, the ADS1248 also has a built-in PGA which takes the place of the second stage of amplification previously used. The programmable nature of this amplifier eliminates the need for switching components when the application changes. The higher number of bits of the ADS1248 is considered a plus for improved quantisation of the noise, however, this was not a primary factor of concern due to the fact that this was not a limiting factor in the P_{min} (as the noise greatly exceeds the size of the least significant bit). In addition to these reasons, there were two other aspects of this ADC that prompted the switch: the ability to set a SRATE and high-frequency noise reduction. The ADS1248 contains an internal reference clock that can be to control the SRATE and prompt the microcontroller once a sample is ready for readout. Using this system, a robust SRATE could be set, satisfying a primary deficiency of the DEV1 design. A 1000 sps rate was selected as explained below. Noise reduction was another good reason for using a $\Delta-\Sigma$ ADC. These ADCs are inherently integrating and contain digital filters to remove high-frequency noise. This is particularly advantageous for TIA readouts which have a significant high-frequency component to N_{TIA} (due to input voltage noise) that is not associated with the signal gain or BW. At

1000 sps, the ADS1248 has a finite impulse response (FIR) low pass filter with a bandwidth of 732 Hz implemented. 732 Hz is much beyond the expected signal BW of 8-32 Hz and thus does not affect the signal digitisation, however, it is also much less than the gain-bandwidth product of the LMP7721 op-amp (15 MHz) and thus does attenuate a majority of the high-frequency input voltage noise. This is a crucial component to the design as otherwise this noise would easily overwhelm the signal.

The SRATE of the ADC was set at 1000 sps as this was empirically found to have the best performance. The SRATE set has a number of affects on the circuit performance. Firstly, a lower SRATE leads to lower ADC noise as it changes how much the $\Delta - \Sigma$ ADC can oversample the signal. However, the ADC noise is on the order of 10 μV RMS, and thus is one to two orders of magnitude lower than N_{TIA} and relatively insignificant in terms of N_T. The second effect of the SRATE is that it moves the bandwidth of the FIR filter in the ADC. Since the TIA BW is between 8 and 32 Hz, it would make sense to implement a filter with a low pass filter with a similar bandwidth to more aggressively remove the input voltage noise. This would suggest the optimum SRATE of the ADC would be either 160 sps with a FIR bandwidth of 118 Hz or 80 sps with a bandwidth of 19.8 Hz (depending on the parasitic capacitance). However, this also limits the amount of averaging the signal can undergo in post-processing. The moving average noise reduction not only attenuates the input voltage noise, but all components to N_T including the Johnson noise. This Johnson noise cannot be removed by the FIR filter as it occupies the same BW as the signal. Thus, in practice, it was found that the post-processed noise performance was best at the highest possible SRATE. This suggests use of the maximum 2000 sps SRATE the ADC can support. However, with the microcontroller used there was a very minor error rate when increasing the SRATE beyond 1000 sps corresponding to roughly one dropped reading per 100,000 samples. This loss in data integrity was not worth the expected $\sqrt{2}$ improvement in noise and thus 1000 sps was set as the ideal rate for this circuit.

The microcontroller used for this circuit was a BeagleBone Black rev C. This device is very similar to the previous rev. A used in the DEV1 design but with increased memory such that it can run the Linux distribution Debian. This did not have any noticeable effect on the circuit, which was tested with both rev. A and rev. C microcontrollers. However, it was found that the Debian OS was more stable than the Angstrom OS previously used. One complication of the design was that the HDMI output of the BeagleBone had to be disabled in order to access more digital pins. A method for doing this in the Debian environment is included in the SI.

The noise analysis of this circuit is covered in Appendix D. Without the FIR filter of the $\Delta - \Sigma$ ADC the LMP7721 on paper appears to be a slight step back as compared to the DEV1 TIA, with a predicted N_{TIA} of 32 μ and a P_{min} of 14.4 fW (slightly above the 9.71 fW predicted for the DEV1 design). However, this is due to the N_{TIA} in the DEV2 circuit being heavily dominated by the input voltage noise between the signal BW and 15 MHz, with most of it occurring between 1 and 15 MHz. This frequency regime is heavily attenuated by the FIR filter in the ADC. After taking this filter into account, the predicted N_{TIA} drops to 3.3 μV. This noise is heavily dominated by the Johnson noise which is over an order of magnitude higher than the input voltage noise. The estimated P_{min} is thus 1.48 fW. As before, this is a very optimistic estimate for the circuit performance, However, considering that a practical implementation of the DEV1 circuit was only a factor of 2.2x higher than the 56 fW target, there was good reason to believe that the DEV2 circuit would finally fulfil the detection electronics requirements.

Layout Design

In addition to the circuit changes above, a number of implementation improvements were also implemented. These include a more clear separation of the digital signals and power from the sensitive analogue ones, introduction of a guard to reduce leakage currents, implementation of a fully metallic shield around the TIA design and a low parasitic capacitance region for the TIA. This was implemented in a four-layer PCB, with CAD files available in the SI. An image of the PCB is shown in Figure 4.4. The circuit contains the TIA and ADC described above, a suite of voltage regulators and two low noise DAC controlled current sources based on the application note by analogue devices.[171] This current source design was found to be comparable to the previously used LT3092 while being DAC controllable, allowing for the user to adjust the LED current and therefore the brightness. This was considered an important feature for SIS optics where the baseline might require tuning. Testing and implementation of this circuit is detailed in a report in the SI. The board accepts a 10 V analogue voltage which is regulated to 5V and a 1.26V reference for the current sources, inverted to -5 V then regulated to -2.5 V with a linear regulator for the negative voltage rail of the TIA/ADC and regulated to 2.5 V with a linear regulator for the positive voltage rail of the TIA/ADC. Communication is done through a 3.3V SPI signal which is buffer on-board by Schmidt triggers to improve reliability.

The TIA region of the circuit was designed to minimise the parasitic capacitance and provide appropriate guarding and shielding. In the region surrounding the photodiode, feedback resistor and feedback capacitor (not populated in final designs) the soldermask of the board has been removed as well as all copper fills beyond the thin 0.203 mm thick traces. In the circuit design section above the bandwidth of the circuit is discussed. This bandwidth is set by the parasitic capacitance of the TIA section, which can vary from 0.5 to 2 pF resulting in a bandwidth between 32 Hz and 8 Hz. Based on this design decision the bandwidth is predicted to be on the upper end of this spectrum. The TIA is also shielded with a guard trace just past the edge of the solder-mask free region and connected to the guard pins of the op-amp. A second, exposed guard trace was implemented with wide (3.125 mm) traces. This is used to attach a metal shield on both sides of the PCB to isolate the TIA region as well as possible (this guard is present on the interior layers as well). This guard is held at ground as the photodiode is in photovoltaic mode and thus all pre-amplification signals will be very close to ground.

Additional design considerations include a complete separation of all analogue power and signal traces from digital lines. There are five chips that have digital signals on the board: two buffers to improve the serial communication reliability, the ADS1248 ADC and two low-noise digital-analogue converters (DAC) for setting the LED current. The connector used is a 30-pin FFC connector that is split between digital lines (left side of the connector in Figure 4.4) and analogue power lines (right side of the connector in Figure 4.4). This separation is maintained throughout the board to reduce interference from the noisy digital lines. The digital chips are all powered by the 3.3V output of the microcontroller.

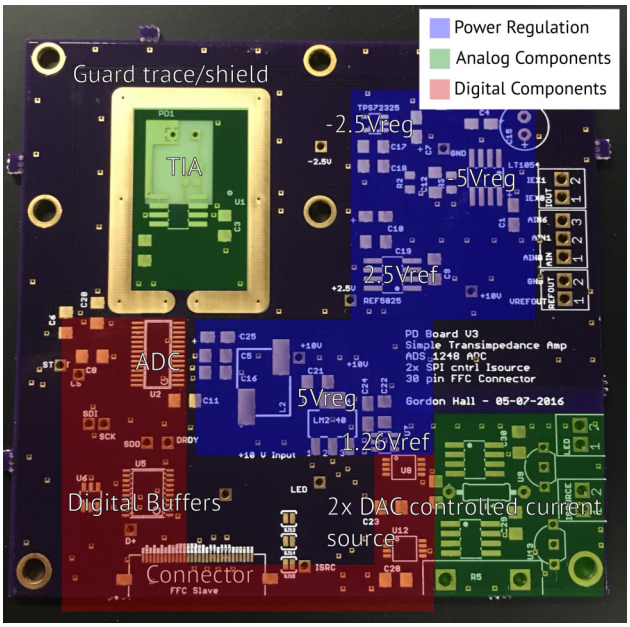

Figure 4.4: Labelled image of the DEV2 PCB. The PCB contains a TIA in the top left corner with a soldermask and copper fill free region for minimised input capacitance, a small guard trace (not visible) and a thick guard trace of exposed metal (labelled) upon which a metallic shield can be mounted to isolate the region. In the bottom left corner the PCB contains two low noise DAC controlled current sources for powering LEDs. The centre and top right board regions contain regulators to supply analogue circuit powers and references. Finally, the bottom and left hand side contain all digital electronics (digital power supply by the microcontroller off-board). There is no overlap of digital and analogue power or signal traces to minimise coupled noise.

4.6.2 Testing and Data Processing

To assess N_T and baseline of the DEV2 circuit it was combined with the OPT4 optics discussed in Section 3.8.4. This involved a single cyan LED pointed directly at the optical input with 30 mA of running current (using the on-board current source), creating a notable baseline of 1.75 V (85% of the ADC dynamic range). Practically, this is a higher baseline than expected in an application where the LED will be held slightly further from the optics and light will be lost due to reflection of the LED light from the microfluidic chip. A test procedure was developed where the system was run for 30 minutes, then left to cool down for 30 minutes before restarting. This allowed for estimation of the thermal effects on the LED. Previously, in the DEV1+OPT3 system, the LED required 20s to warm-up such that the baseline was in the linear regime rather than exponential decay regime as described above in Section 4.1.1. For this instrument that warm-up time was extended to nearly 80s due to a different thermal mass surrounding the LED. The SRATE was set to 1000 sps. This experiment was performed for 24 hours, resulting in 24 runs of the instrument under a variety of ambient conditions. For example, on-going projects by others caused the lights within the lab to be toggled on and off multiple times throughout the experiment and the lab temperature and humidity vary by a few degrees/10% typically during this period. The data was processed in the standard way with linear drift removal and a 1000 point moving average applied. The noise was assessed for 30s increments of the baseline with the average reported as N_T.

The DEV2 circuit also introduced a new power regulation design. This was assessed by taking the fast Fourier

transform with a uniform window of the baseline and analysing it for 60 Hz noise peaks. Since the SRATE of the DEV2 circuit was reproducibly 1000 sps, no change in ADC was required.

4.6.3 Testing Results

The results of the DEV2 noise assessment test give a N_T of 94 μV for a final P_{min} of 42 fW. No instability or peak-like features were observed in any of the runs, suggesting that efforts to maintain the leakage current stability were successful. Figure 4.5a showing a representative run (run 8) and Figure 4.5c showing all 24 curves from the experiment. Differing from previous designs, the testing time for this module was extended to 1800s (30 minutes) to further emphasise the stability of the baseline. Figure 4.5b shows the fast Fourier transform of the baseline signal with a uniform window. Similar to Figure 4.2b, no noise peaks are observed in this analysis, suggesting that the influence of 60 Hz noise from mains power are being appropriately attenuated by the voltage regulation used.

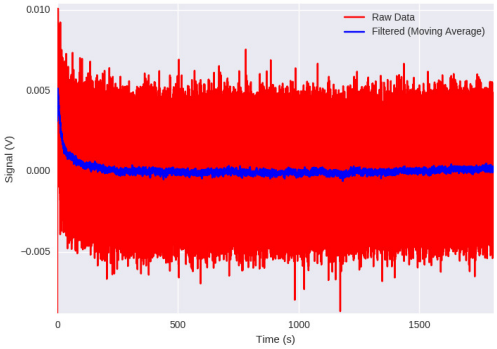

(a) A representative trace of the electronics performance of the v3 optics over 30 minutes with the raw-signal in red and the processed signal in blue. The signal is highly stable after an initial warmup period where the LED output is decreased due to thermal effects,[81,147] and the signal is effectively de-noised with a 1000 point (1s) moving average applied.

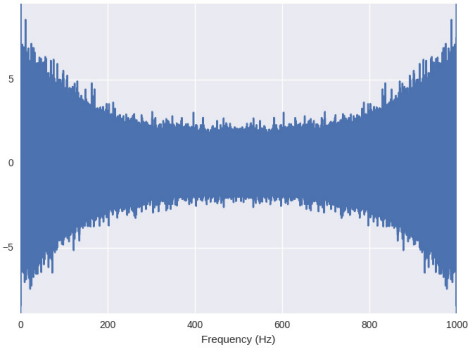

(b) The results of a fast fourier transform with a uniform window of a baseline signal from the DEV2 circuit. No frequency peaks can be seen suggesting a good attenuation of 60 Hz noise by the circuit

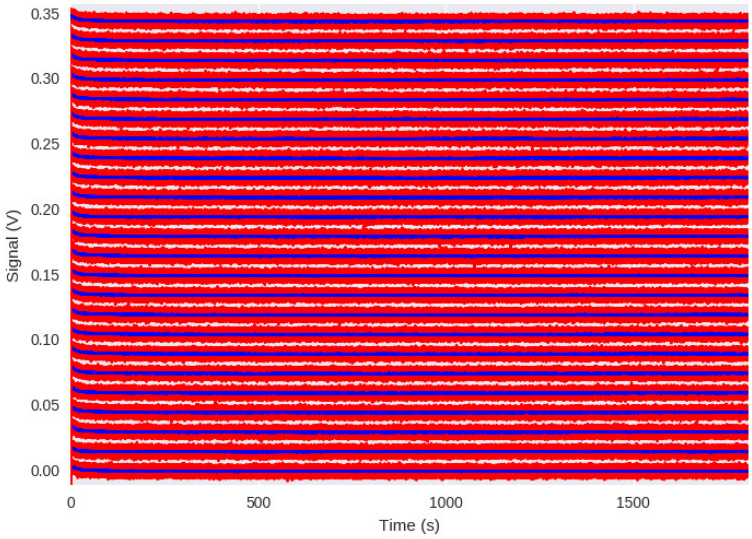

(c) The results of 24 warmup runs where the LED was turned on and the baseline measured over 30 minutes, and the instrument was left to rest for 30 minutes. Similar to Figure 4.5a, the raw data is shown in red and the processed signal in blue. Each run is highly consistent, indicating the high reliability and stability of the electronics. The average N_T within a 30s period after a 1s moving average was applied was 94 μV, which corresponds to a P_{min} of 42 fW of fluorescent light. This meets the requirement of 1 nM detection as detailed in Section 3.8.4.

Figure 4.5: Results of the DEV2 detection electronics testing.

4.6.4 Discussion

The DEV2 electronics satisfy the detection requirements of this module with a P_{min} of 42 fW (below the 56 fW requirement), a BW between 8 Hz and 32 Hz (which meets the 5 Hz requirement), a SRATE of 1000 sps (which meets the 2 x BW requirement) and a high degree of stability over the course of half an hour. As a result, this is the first detection electronics iteration that meets all design requirements to implement a CE application with 1 nM detection in 100 μm channel with LED illumination as per the predicted performance of the most recent OPT4 optics in Section 3.8.4.

As discussed in the design discussion in Section 4.6.1, the DEV2 circuit was expected to have an P_{min} 6.7x higher than DEV1. However, in a practical implementation, this difference was only about three. This suggests that other factors beyond the N_{TIA} are becoming significant components of N_T at this scale. Further analysis should be done to determine if these originate in the power supply, the assembly or in the TIA design. The data sheet for an Analog Devices op-amp similar to the LMP7721 discusses a circuit with 10^{10} gain that exhibits slightly increased noise due to the amplifier not being quite fully compensated. This is unlikely to be the issue here as that circuit has a much lower gain-bandwidth product as compared to the LMP7721 (and thus is more likely to require loop compensation). However, future work could verified this with a spectrum analysis of the amplifier response.

The SRATE limit imposed by the ADC clock worked well with no observed dropped measurements over the course of the 40+ million samples shown in Figure 4.5c, nor over any other preliminary tests done. As detailed above, the ADC used is technically capable of a SRATE of 2000 sps, though the microcontroller used cannot reliably address the ADC at that rate. Therefore, a future design might use a microcontroller with less overhead than the Linux-based BeagleBone Black to reach a higher SRATE. However, in an ideal scenario where the noise is normally distributed, the improvement in noise reduction is proportional to $\sqrt{n}$. For 2000 sps, this is only a factor of 1.4. Therefore, microcontroller changes for higher SRATEs would only introduce very minor improvements to the P_{min}. Thus, future work on increasing SRATE would not likely be worth the design effort.

In terms of design, this circuit is approaching the practical limit of TIA design. As discussed in Section 4.6.1, after the 732 Hz filter is applied the N_{TIA} is heavily dominated by the Johnson noise of the feedback resistor as the FIR filter removes the majority of the high frequency input voltage noise. This leaves a "base" Johnson noise that is independent of the rest of the design with the same bandwidth as the signal. In the Johnson dominated regime, the SNR can only be improved with decreasing bandwidth and/or increasing gain. Currently, the bandwidth is set with parasitic capacitances and is estimated between 8 and 32 Hz. Thus, with improved testing equipment it is feasible to verify the parasitic capacitance and introduce more gain. For example, if we could guarantee a parasitic capacitance of 100 fF or lower the gain could be set to 2×10^{11} Ω with a bandwidth of 8 Hz. However, this would only improve the Johnson noise by a factor of 3 (SNR scales with $\sqrt{R_f}$). Switching PCB substrates from the standard FR4 used to a material with improved dielectric relaxation such as Rogers 4350B is also recommended,[166] which can further reduce parasitic capacitances and enable higher gain. However, the improvements here are minimal, suggesting the current design is near the limit of a simple TIA. One approach to improve SNR would be to implement frequency specific gain in the form of a lock-in amplifier. This is the approach taken by the Manz group[172] with great success. Some preliminary attempts at a lock-in were done in 2012 by other students, however, these did not yield usable designs. Future work might explore this concept further for improved performance.

4.7 Circuit Performance Comparison and Summary

Table 4.1 summarises the detection electronics presented here, along with the reference circuit from Section 1.3.1. As stated previously, the reference design is a circuit previously used by the Backhouse group as part of its own publication[85] and as part of one of the PCR-CE demonstrations discussed in the literature review in Section 1.2.3. This is a single-stage TIA with a gain of 10^9 $^{\mathrm{V}}/_{\mathrm{A}}$ and 114 μV of noise after a wavelet processing technique to give a P_{min} of 1 pW. For more information, the circuit design is discussed in the application note it was based on,[83] the data processing in the thesis of Sheng Choi[173] and the detection results in the thesis of Allison Bidulock.[84]

	Reference Model	CMOS Electronics	PDE	DEV1	DEV2
Data Processing Method	Wavelet analysis[173]	30 point moving average	100 pnt moving average	1950 point moving average	1000 point moving average
Gain ($^{\mathrm{V}}/_{\mathrm{A}}$)	10^9	†	7.27×10^8	1.17×10^{10}	2×10^{10}
N_T (μV)	114[84]	2.4 counts	210	154	94
SRATE (sps)	1000	38	≈ 160	≈ 1950	1000
BW	30 Hz$\star$	43 Hz	1.59 Hz	7.95 Hz	8-32 Hz
P_{min} (fW)	1000	$\approx$ 900 fW ‡	2600	122	42

Table 4.1: A summary of the various detection electronics performances with the performance of a previously demonstrated circuit by the Backhouse group. Of these designs, only the DEV2 circuit meets requirements of a P_{min} below 56 fW as specified in Section 4.1.1 above.
$\star$: Bandwidth assumed to be the same as in the source application note the circuit was based on.[83]
†: The circuit gain and responsivity were not available for this design.
‡: Estimated value based on the measured LOD and estimated optical power from Section 3.8.1.

In Section 1.3.1 the reference optical design and reference circuit were presented for a combined LOD of 100 nM, two orders of magnitude above the requirement for PCR-CE. Chapter 3 then presented a more refined model for the signal that optimised the design around the constraints of scalable, low-cost optics resulting in only a factor of 5.6x improvement in signal from the reference model and a power of 56 fW. This showed that the reference circuit as previously implemented by the Backhouse group was insufficient for reaching the detection goal and more design iterations were required. These first began with a multifunctional prototype CMOS microelectronic chip which had very comparable performance to the reference circuit. Due to the difficulty in making design adjustments to the prototype CMOS and the short chip lifetime, this was not a platform for future iterations. Thus, attention towards discrete component implementations was required. The first pass, PDE designed by another student, was actually a step backwards with worse P_{min} and poor stability. Adjustments of this design as part of DEV1 substantially improved the performance over both the PDE and reference designs, but still proved insufficient. This prompted me to re-design the circuit and PCB to implement DEV2. This was the first circuit to meet all detection electronics requirements.

Based on Table 4.1 it is clear the DEV2 circuit is a notable improvement over the reference design, having a P_{min} over 20x improved while maintaining a BW above 5 Hz (and, depending on parasitics, possibly the exact same BW as the reference circuit). However, there are two complications that make a direct comparison difficult. Firstly, the

measured noises presented here factor in the illumination noise as well. In the discussion of the detection electronic iterations presented in this chapter this has generally been considered a negligible noise source because LED signal stability, provided thermal effects have been taken into account, tracks the stability of the provided current.[81,147] This stability is on the order of 100 nA in all LED circuits tested here, or 0.001%. Thus, illumination noise is expected to be on the order of 10^{-5}V, which is much less than any of the raw noises observed. In comparison, a number of laser-referred fluctuations were noted in the thesis of Allison Bidulock, some on the order of 20-30 mV[84] though these large fluctuations were excluded from the noise analysis. Despite the exclusion of the large fluctuations, any lower-level changes would couple straight into the reported noise value. A second issue lies in the data processing. In the iterations presented in this thesis only a simple moving average was applied. This ensured signal integrity. In comparison, the noise value for the reference circuit was reported after wavelet analysis. This is a more complicated signal processing method that can yield much higher noise suppression, though one challenge is that inappropriate parameters can cause significant artefacts in the signal.[174] Thus, it is likely that if the same processing algorithm were applied to this work even lower P_{min} values might be obtained. However, use of wavelet analysis was avoided here to ensure a higher degree of transparency with respect to the noises present and to ensure no artefacts (for example, phantom signals) were introduced into the data. Overall, while a direct comparison is difficult, it is clear the new DEV2 design is a notable improvement from the reference circuit, and a necessary improvement for implementing PCR-CE detection with optimised low-cost optics. The DEV2 electronics were bundled with the OPT4 optics in the next generation instrument detailed in Section 5.5.

In summary, there was a need for detection electronics with a P_{min} below 56 fW, a BW above 5 Hz and high signal stability to enable the optical detection of 1 nM of fluorophore in a 100 μm channel as outlined by the most recent OPT4 optics design in Section 3.8.4. This need was unfulfilled by the prototype CMOS microelectronics from our collaboration with the University of Alberta, necessitating the in-house development of discrete detection electronics. A TIA approach was selected, though previous designs were highly insufficient for use in DNA analysis. Through targeted design improvements, the DEV1 circuit was created which had improved and nearly sufficient P_{min}. This circuit was combined into an instrument and demonstrated state-of-art LIF detection for low-cost CE, though in slightly larger channels than required for general purpose instruments. A new circuit, DEV2, was developed to improve on those electronics and reached a P_{min} of 42 fW with a 8-32 Hz BW with high signal stability. Thus, the design objectives were met.

Chapter 5

Instrument Development

5.1 Introduction

This chapter details the testing of a series of instruments designed and built over the course of this project. These instruments integrate various iterations of the rapid-prototyped microfluidics from Chapter 2, the optics from Chapter 3 and detection electronics from Chapter 4 with technical instrumentation from Appendix A to implement various CE demonstrations. This chapter focuses solely on the CE aspect of PCR-CE as this is the location of the fluorescence detection point and therefore the primary point of development on this project. Furthermore, CE is also more sensitive towards the microfluidic fabrication than PCR due to the need for smaller features and surface sensitivity. Thus, this focus allows for the validation of multiple design parameters while simplifying the experiment by excluding PCR. The primary objectives of these demonstrations were to measure and assess the LOD, which provides validation of the signal model from Chapter 3, and demonstrate interim utility of the various designs developed.

This chapter briefly details three key CE instrument demonstrations with the materials and methods for each described in Appendix E. Section 5.2 presents what we have dubbed the intelligently packaged CMOS (IP-CMOS) system, a first pass at scalable optical detection with a CMOS microelectronic chip and micromilled fluidics. This combined the generation 1 milled fluidics (Section 2.2.2), the OPT1 optics (Section 3.8.1 and the prototype CMOS microelectronics from the University of Alberta collaboration (Section 4.2 to perform a CE separation of end-labelled DNA. The IP-CMOS demonstrated nM LOD, albeit in large 381 μm channels with low-resolution agarose. The second instrument tested, named CE Instrument 1 (CEI1), integrated the generation 2 milled fluidics (Section 2.2.3), the OPT2 optics (Section 3.8.2) and the PDE detection electronics (Section 4.4) with HV and valving technical functions to perform enzymatic analysis of a DNA analyte. This instrument demonstrated integrated functionality with moderate success, however the poor LOD of roughly 2 nM in still too-large channels meant it fell short of the research objectives. This illustrated the need for more robust optical and detection electronics design. The final CE demonstration, CEI2, combined the generation 2.5 milled fluidics (Section 2.2.3), the OPT2 optics (Section 3.8.3) and the PDE detection electronics (Section 4.5) to implement a CE separation of both end-labelled DNA products as well as a serial dilution of fluorophores for a robust LOD analysis. The measured LOD of 0.15 nM[89] was over two orders of magnitude better

than the previous best LED and photodiode based CE detection module,[88] and the first under the 1 nM threshold for reliable DNA analysis. Thus, this was an important milestone in the field of cost accessible molecular biology instrumentation.

The final topic of this chapter briefly describes a next-generation instrument that this project culminated in. This instrument combines not only the best optical design with a SIS arrangement (OPT4, Section 3.8.4) and the best detection electronics (DEV2, Section 4.6) for improved LIF performance, but also contains a series of updated technical modules that are described in Appendix A. The result is a low-cost, flexible μTAS instrument that supports a wide range of DNA diagnostic applications with a predicted LOD of 0.75 nM from 1 nL samples, thus satisfying the detection objectives for this project. Furthermore, by adhering to the scalable optical detection outlined in Section 3.1.3, this inexpensive μTAS serves as a testbed for future monolithic LOC device that can feasibly be made in a CMOS process. Therefore, this instrument presents a path through the manufacturability roadblock that has impeded the development of a true, single-chip instrument.

5.2 IP-CMOS- First Tests of Scalable Optical Detection

The IP-CMOS instrument was the first designed to implement scalable light collection optics in the form of a GRIN relay to interface a prototype multifunctional CMOS microelectronic chip developed by the Elliott VLSI design group at the University of Alberta with micromilled polymer fluidics. This minimised the NRE development costs by allowing the Elliott group to focus on developing the electronic-only aspects of LOC instrumentation on CMOS while the microfluidic and optical aspects could be iterated separately. As described in Sections 3.1.3 and 3.6.2, this was done with short-working distance GRIN lenses which imitated as close as possible the optical design of the monolithic LOC device, but with physical separation of the optics and fluidics. This was particularly required for this version of the prototype CMOS as it protected the bond wires used to connect the CMOS to the external DIP packaging. This was the first instrument that implemented the GRIN design.

The IP-CMOS detection module was composed of the OPT1 optics (Section 3.8.1) and the multi-functional CMOS chip for photodiode detection (Section 4.2) with 381 μm wide and deep PMMA microfluidics and an agarose sieving matrix. The LOD was assessed with a CE separation and found to be 0.9 nM, a value sufficient for DNA analysis. However, the resolution was estimated to be comparable to previous work using this sieving matrix at 50 bp, well above the 10 bp requirement for standard applications. The same microfluidics and DNA product were also assessed with a commercial confocal instrument, the Micralyne Microfluidic Toolkit (μTK). This yielded improved LOD (due to the the higher performance, higher cost optics), though with comparable resolution. This suggested protocol limitations were the primary issue regarding the resolution and the need for a different sieving matrix. However, as mentioned previously, using a different matrix would require substantially reduced channel dimensions which not only would require better fabrication techniques than were available at the time, but also would push the LOD well above the 1 nM target. Therefore, more LIF detection instrumentation development was required. Overall, this was a successful first-pass demonstration of the optics and the feasibility of its scaling though with a number of issues that required improvement. This work was presented at the 20th International Symposium on Electro- and Liquid Phase Separation Techniques in Tenerife, Spain and subsequently published.[48]

5.2.1 Brief Demonstration Description

The specifics for this demonstration are described in Appendix E and the publication.[48] Briefly, PMMA microfluidics made using the generation 1 milled channel parameters described in Section 2.2.2 (381 μm wide and deep) were capped with PCR-tape (as discussed in Section 2.3.1) to form microfluidic chips. The IP-CMOS instrument was composed of the OPT1 optics and the 11th generation of the CMOS microelectronics produced by the Elliott group at the University of Alberta. The functionality of this chip is described in associated publications.[49,115,160] The optics were implemented primarily in polyvinyl chloride (PVC) due to the ease of machining this polymer. The PVC jig was attached to the CMOS microelectronic chip by a machined PMMA alignment jig that press-fit to the DIP package that contained the CMOS. Microfluidics were slotted into the PVC optics jig via a press-fit recess, thus aligning the channel, optics and photodiode. In this work, the CMOS microelectronics were not used for HV generation. Instead, the HV output from the μTK were used. This allowed for a de-coupling of the optical assessment from the HV module. An image of the PMMA-PVC alignment jig is shown in Figure 5.1 which depicts the PCB that contains the CMOS-DIP package with PMMA alignment layer, the PVC holder with the alignment pins and a PMMA microfluidic chip. The side-illuminating blue LEDs are turned on. Not pictured is the top manifold, also PVC, which holds four platinum electrodes for CE and the third LED for baseline offset as described previously in Figure 3.14a.

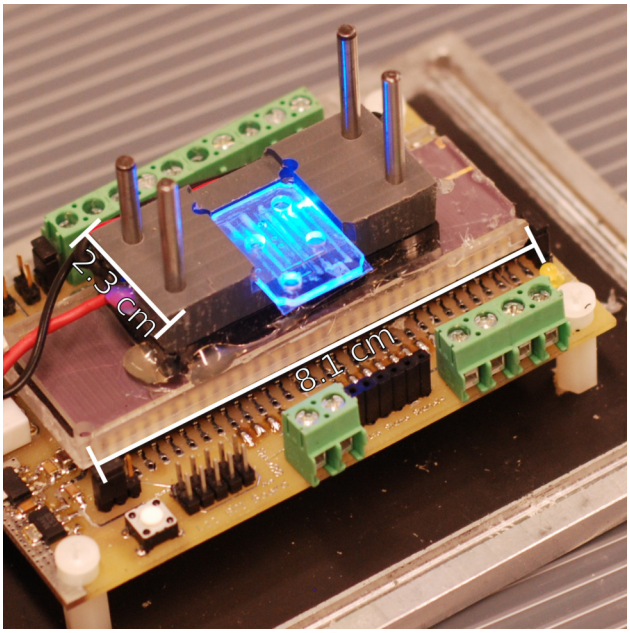

Figure 5.1: A picture of the assembled CMOS-PMMA optics with the LEDs turned on. The 23.5 mm x 16 mm fluidic chip loaded in the system is of the same format as previously used,[56] though with wider, micromilled channels (381 μm x 381 μm cross-section). Channels were capped with tape. Not pictured is a top layer containing a third LED (to offset the baseline into the ADC working range) and electrodes for CE. Image taken from[48]

The testing procedure involved a series of inject-separate (as described in Section 1.2.2) processes of a DNA product (β2M, 236 bp) from its primer. Three separations were performed on this instrument. After these separations, the microfluidics were carefully unloaded and placed into the μTK where a fourth separation using the confocal optics

was performed. Since the analyte contained only a single DNA product, the resolution for the separation could not be directly assessed. However, by performing a separation using the same protocol, matrix, microfluidic chip and analyte in the manner described on both the low-cost instrument and the μTK, the relative resolution of the instrument could be assessed. Furthermore, by performing the experiment on both systems the detection performance could be compared to a typical instrument representative of the current state of the field. Data acquired by the CMOS microelectronics was logged at 38 sps using a C# program while data from the μTK was logged at 200 sps using its own software.

The data was processed by first correcting the time-scale of the separations such that the primer peak arrival time was set to 0 seconds. This was done to account for the variable time delay between initiating the data acquisition and the HV program, functions performed using two different instruments on two different PCs. A linear baseline was assessed based on the data up to 20 s before and 100 s after the primer peak (i.e. before and after any peaks). The baseline and any linear drift was then removed. A 30 point moving average was applied. The LOD was assessed by first estimating the primer-product conversion ratio based on the area under the primer and product curves. This allowed for the estimation of the DNA product concentration. This concentration was then adjusted for dilution effects in the well (the sample was diluted 1:10 for this application) as well as injection effects. Briefly, by adjusting the ionic concentration in the well, the analyte mobility in the well can be made much higher than in well and than in the channel. This is referred to as stacking and concentrates the sample as described in more detail in various references such as Landers[54] and Breadmore et al..[175] In this work, the concentration was by a factor of five. It should be noted that these concentration adjustments were not made in Hall et al.[48] such that the reported LOD in that work was 2x higher than discussed here. However, this change was made in this theses to make it consistent with other works in the field and later discussions. Finally, the detector noise was assessed by taking the standard deviation of the baseline regions as described above (20s before and 100s the primer peak). This gives an LOD value representative of the minimum fluorescent signal the instrument could detect. The results are shown in Table 5.1.

5.2.2 Results

The separation results are shown below. Figure 5.2a shows the data collected from the above experiment, while Figure 5.2b compares directly the IP-CMOS instrument and commercial instrument. Table 5.1 shows the results of the data processing. The average LOD of the injections shown was 0.9 nM in the 381 μm channels. The FWHM of the DNA product in the IP-CMOS detection is highly comparable to the μTK. Therefore, the two instruments have the same resolution. In a previous publication, 50 bp resolution was obtained using the μTK and comparable PMMA microfluidics with agarose sieving matrix. Thus, the IP-CMOS resolution can similarly be estimated to be 50 bp.

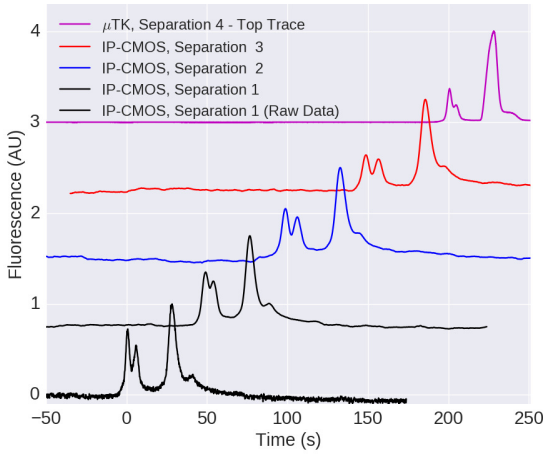

(a) Results of four consecutive separations of the 236 bp β2m PCR product on the IP-CMOS system and on a commercial confocal optics system. The bottom trace (raw data) from the first IP-CMOS separation shows noise levels 3x higher than the processed trace above it. Traces from successive separations are shown above. The topmost trace is of the same chip and sample run immediately after the last IP-CMOS separation. The IP-CMOS system can easily detect this sample representative of a POC diagnostic and has an LOD of approximately 0.9 nM (summarised in Table 5.1) [48]

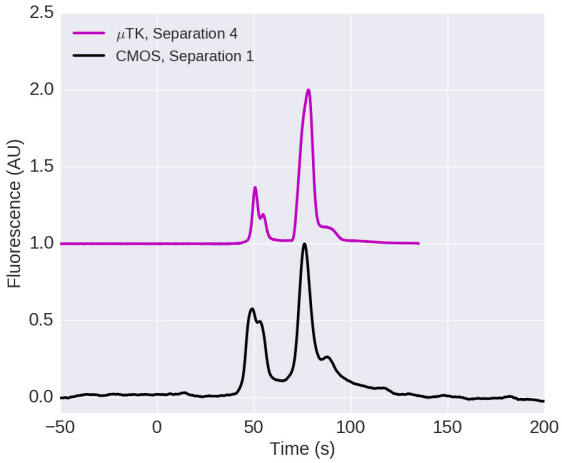

(b) A direct comparison of the IP-CMOS and commercial confocal instrument results. The IP-CMOS has notably higher noise, though the resolutions for the two systems is roughly equivalent (about 50 bp as per [96])

Figure 5.2: Results of the IP-CMOS instrument for electrophoresis

	Injection1	Injection 2	Injection 3	Injection 4
System	OPT1+CMOS	OPT1+CMOS	OPT1+CMOS	Commercial confocal instrument
Signal	398 counts	409 counts	382 counts	1.97 V
Noise	2.3 counts	3.0 counts	1.8 counts	63.5 μV
SNR	170	135	210	3104
LOD	0.90 nM	1.1 nM	0.65 nM	0.05 nM
FWHM	6.6 s	7.7 s	7.6 s	7.3 s

Table 5.1: Table of metrics obtained from Figure 5.2a. The average LOD of the injections was 0.9 nM.

5.2.3 Discussion

The measured LOD for the system was 0.9 nM as shown in Table 5.1. Thus, this instrument could be used with the protocol and microfluidics above to perform analysis on end-labelled DNA products, an important application milestone for LED-photodiode based LIF detection. Comparing the LOD with the confocal module, the commercial instrument clearly has a substantial advantage. This advantage is actually understated in this comparison as the μTK LOD could be improved by increasing the voltage across its PMT. However, for this application (sizing PCR products), both systems can comfortable detect not only the main product peak, but also non-specific features such as the slight shoulder to the right of the product, or the presence of primer-dimers. Therefore, for this agarose separation the confocal is ”over-designed” with the excess LOD not contributing meaningfully to the practical implementation of the

instrument. This presents the opportunity for a low-cost alternative, such as this instrument, that can perform the same application with a performance that does not impact the results and a very substantial drop in cost. The IP-CMOS system consisted of a packaged a 5 mm x 5 mm CMOS die, some polymer alignment jigs and $80 of GRIN lenses, at least two orders of magnitude lower component cost than the commercial system.

Although resolution was a secondary issue in this work, it was still estimated to be comparable between the IP-CMOS and the μTK at about 50 bp. Firstly, the fact that the IP-CMOS and μTK have nearly identical FWHM (and thus resolution) shows that the OPT1 optics do not affect the separation resolution for these microfluidics. As discussed in Chapter 3, the optics should not have an effect on the resolution if the spot-size is less than the channel width. For this instrument, the spot-size can be estimated to be the same size as the CMOS photodiode, which was 150 μm x 150 μm. This is much less than the 381 μm channel width and therefore consistent with this hypothesis. The 50 bp resolution was much larger than the 10 bp requirement for DNA analysis specified by Ugaz et al.[59] and thus this instrument did not meet the requirements for robust CE analysis. However, the agarose separations in Ugaz et al.[59] reported 100 bp resolution, suggesting that this demonstration was in fact a good result considering the sieving matrix used. Therefore, improvements to the resolution to the 10 bp required a sieving matrix change, which in turn requires smaller channel dimensions.

When considering shrinking the channels, three considerations needed to be made. Firstly, at the time of demonstration the fabrication techniques for micromilled fluidics were still being developed. Shrinking the channel below 381 μm would require improved fabrication techniques and a new source of tooling. Secondly, the signal will decrease as the channel is scaled. Analysis in Section 3.8.1 suggested a 100 μm x 100 μm channel would be expected to decrease the signal by a factor of 55x, resulting in a LOD of 50 nM based on the results in Figure 5.2a. This clearly does not meet the 1 nM LOD requirement. The second parameter relates to the baseline. As discussed in Section 3.8.2, the baseline for orthogonal illuminated LIF detectors such as this design is related to the spot-size and channel width; when the spot-size is smaller than the channel the collection of scattered excitation light (and baseline) is lower. Since the photodiode width of this instrument was 150 μm, this microelectronic chip would likely see baseline issues with 100 μm channels. Overall, this instrument met neither the LOD nor the resolution research objectives, necessitating development on the microfluidic, optics and electronic fronts.

The OPT1 optics used in this instrument were relatively simple and did not contain an excitation filter. As demonstrated in Section 3.4.1, an excitation filter can be used to improve the SBR at the expense of signal. Typically, this is advantageous as it enables increased gain in the detection circuit that more than compensates for the signal losses. However, in this instrument the integrator on the CMOS microelectronics was run at its maximum integration time. Therefore, there was no possibility of addition signal gain and SBR improvement would not benefit the LOD, meaning there were limited amounts of optical improvements that could be made with these electronic limitations. Another issue was that following this demonstration, experiments were performed on the HV charge-pump that was included on-board the CMOS microelectronic chip. However, due to an error in the power-up procedure, the charge-pump activation resulted in degradation of the a number of sub-systems including the optical signal stability, ultimately leading to the destruction of the microelectronic chip. The use of the on-board charge pump with optical detection is discussed elsewhere in a series of IEEE presentations.[49,115,160] Based on the performance limitations and premature demise of the CMOS microelectronics, there was a pressing need for in-house developed detection electronics. These would enable the introduction of optical improvements such as excitation filtering. The first such demonstration is

detailed in Section 5.3 below.

5.3 CEI1- Automated Enzymatic Digests with a Discrete CE Instrument and On-Chip Valving

The first demonstration of a scalable but fully discrete CE instrument, CEI1, integrated the LIF detection design with HV generation and pneumatic valves. As described above, the prototype CMOS microelectronic chip that the IP-CMOS was based on lacked stability and ultimately had a very short operational lifetime. There was therefore an impetus to develop discrete electronic infrastructure with the same functionality as the CMOS, but with discrete components on circuit boards, specifically the PDE detection electronics design described in Section 4.4. Instruments could then be made and tested in a low-development cost environment with more rapid iterations that later would guide the CMOS design. The new detection circuit also enabled optics with excitation filters for improved detection performance in the form of the OPT2 optics from Section 3.8.2. In addition to the electrical and optical changes, this instrument featured improved microfluidics, featuring smaller channels (254 μm) and the introduction of an integrated pneumatic valve. This demonstration used the valve to automate fluidic mixing, specifically to implement a restriction fragment length polymorphism (RFLP) experiment. This experiment estimated the LOD, the resolution and demonstrated the added utility enabled through functionality integration. Ultimately, the performance of this instrument proved insufficient towards meeting the research objectives. However, analysis of the results was important in identifying key avenues of improvement for future designs.

CE can not only be a useful method for verifying PCR product sizes, it can also be used as a diagnostic tool unto itself with methods like RFLP analysis. In an RFLP an enzyme is used to selectively cleave the analyte DNA strand upon recognition of a certain genetic pattern. The experiment is designed such that this cut-site is specific to a mutation of a particular nucleotide and thus can be used to detect single nucleotide sequence polymorphisms (SNPs). RFLP analysis has been shown to have very high sensitivity[176] and LOC implementations have previously been demonstrated by the Backhouse group to be effective in reducing cost and experiment time.[3] However, these demonstrations required substantial user interaction with the sample and a large, expensive instrument (specifically, the μTK used above). Thus, while useful, the protocols could not be implemented in a portable manner. This demonstration sought to improve upon that work by implementing this standard technique with an automated system of valves. The target application was to detect mutations in the *HFE* gene linked to hereditary haemochromatosis. While many mutations can be detected with an RFLP diagnostic, perhaps none would have the immediate social impact as *HFE* gene analysis. Approximately 30% of Caucasians are carriers for one of the two major point mutations in the *HFE* gene, C282Y, a 845G¿A transition, and H63D, a 187C¿G transversion.[177] Early diagnosis of hereditary haemochromatosis and treatment by venesection effectively reduces the risk of complications in affected individuals.[178] The combination of clearly identified genetic testing along with low-impact treatment methods and widespread mutations makes HFE diagnostics uniquely important, and it is the most requested genetic diagnostic prescribed to Molecular Diagnostics Laboratory, Alberta Health Services. This application tested both of the key mutations, enabling the early detection of between 68% and 99% of all hereditary haemochromatosis patients.[179]

The LOD for this instrument was measured to be 2 nM with a resolution between 60 and 110 bp. Clearly, these

metrics do not meet the research objectives, even with larger than expected channels. As discussed below and in previous sections, the results from this system identified key development issues for the microfluidics, optics and detection electronics going forwards.

5.3.1 Brief Demonstration Description

The specifics for this experiment are outlined in Appendix E and described briefly here. The microfluidics used were made in PMMA in two parts. First, the CE microchannels were made using the generation 2 micromilling parameters described in Section 2.2.3, resulting in 254 μm x 254 μm channels with relatively high surface roughness. Next, a pneumatic valving section was patterned with laser ablation. The valve design is discussed in Appendix A.2.2. Both the CE channels and pneumatics section were capped with PCR-tape as discussed in Section 2.3.1 to form the microfluidic chips.

The optics used were the OPT2 design from Section 3.8.2 which contained an excitation filter. Based on the model from Chapter 3, these optics were expected to produce a signal of 380 fW for each nM of fluorophore with a spot-size of 323 μm. The detection electronics were the PDE design produced by Victor Shadbolt with a P_{min} of 2600 fW. Combining these factors, the LOD for this instrument was expected to be 6.8 nM and therefore this design should not have been expected to meet the detection requirements. However, this was a readily implemented design with easily available components. Therefore, testing was performed such that this could form a reference point for future work. Similar to the instrument in Section 5.2, the optics were designed in two parts with one side containing the LEDs, collection lens and a recess for alignment to the microfluidics and the other containing the second lens, emission filter and alignment to the detection electronics. In an improvement from the previous design, the top layer of the optics were fabricated in aluminum. Since the LEDs were embedded in the optics jig the use of aluminum effectively performed the function of a heat sink. As mentioned in Section 3.3, the thermal stability of the LED is an important factor in the stability of the baseline, suggesting a heat sinking material would improve the excitation stability. Aluminum is also more sturdy than PVC and therefore this design should be able to maintain alignment over a larger number of tests than previously. In addition to the optics, an external box containing air pumps and regulators was made to make the instrument field deployable. Figure 5.3a shows the optics module and manifold while Figure 5.3b shows everything required to implement this instrument.

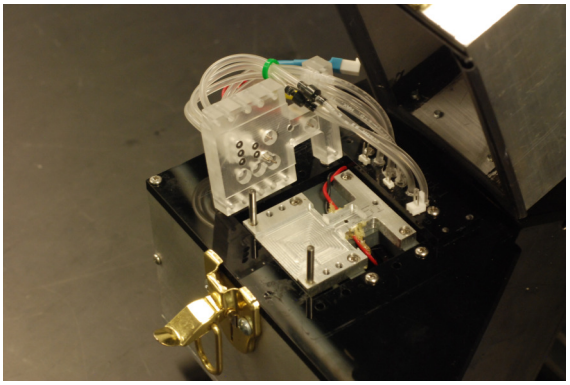

(a) A picture of the instruments LOC section. The chip is press fit into a recess in the aluminum jig, which also contains two $^1/_8$" alignment dowels and two LEDs (fixed with gorilla glue). The PMMA manifold can be seen with five o-rings for valves and four nickel electrodes for applying high voltage. Pneumatic lines and HV are connected to the manifold from tubes and electrical connectors on the instrument top. This whole section is closed with an aluminum lid seen in the top right of the image

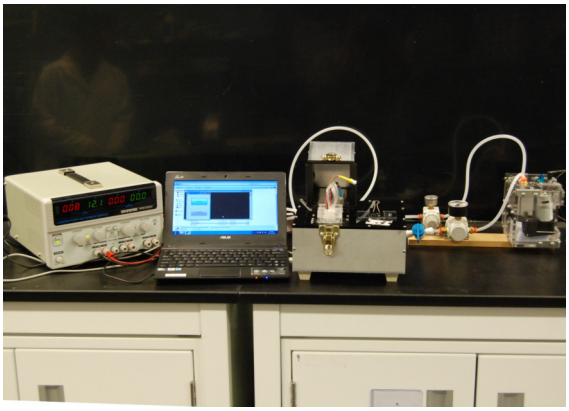

(b) A picture of all of the instrumentation required to implement this analysis. From right to left: a power supply at 12 V, a laptop, the instrument with manifold, fluidic chip and membrane and a rudimentary unit to provide the pneumatic pressures. This instrument could be substantialyl miniaturised as most of its internal space was left empty for future considerations. The external box was later re-used for subsequent instruments

Figure 5.3: A discrete instrument for RFLP analysis

The testing involved four different DNA products with two inject-separate processes per sample. The DNA products tested were wild-type and heterozygous mutations of exons 2 and 4 of the *HFE* gene. For each experiment, the sample was first loaded into the CE well and the instrument valves were used to mix it with the appropriate buffers. An inject-separate process was done to assess the state of the sample prior to enzymatic activity. Next, the instrument valves were used to mix in the relevant enzyme for the exon product being tested. A second inject-separate process was done to assess whether or not the enzyme acted. This is discussed in more detail in Appendix E. For all samples, the pre-digestion electropherogram should have two peaks, primer and product (234 bp for exon 2, 436 bp for exon 4). After digestion for both exons the wild-type sample should show two peaks while the mutated sample should show three peaks. The three peaks correspond to the primers, the digested product (72 bp for exon 2, 158 bp for exon 4) and an undigested DNA peak (the heterozygous mutation means that some DNA strands will not be digested). Data was collected at approximately 160 sps as discussed in Section 4.4.

Data processing consisted of a linear removal of the baseline based on the data collected prior to the primer peak arrival and a 100 point moving average with no time-domain adjustments. To assess the LOD, the pre-digestion electropherograms are used as these traces have fewer contaminants (the post-digestion sample contains by-products and the enzyme) and are therefore more representative. Following digestion, the FWHM of the digested and undigested products in the mutated sample can be used to roughly assess resolution according to Equation 5.1 below.

$$Resolution = \frac{w_1 + w_2}{2 \times \Delta t} \times (s_1 - s_2) \tag{5.1}$$

Where w_x refers to the FWHM of peak x, s_x refers to the size of the DNA at peak x (in bp) and Δt is the difference in

time between the two peaks. However, with only two peaks present this is only a rough estimate of the resolution.

5.3.2 Results

The results of the exon 4 and exon 2 tests are shown in Figures 5.4b and 5.4a respectively. The detection results are shown in Table 5.2. The most representative LOD values are those from the pre-digestion electropherograms which suggest a LOD of 2 nM.

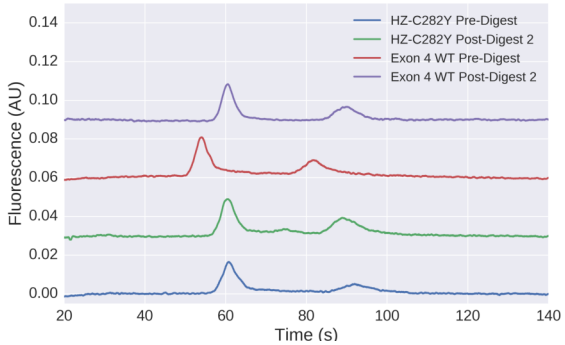

(a) Results of the automated analysis of exon 4 of the HFE gene. Red and Blue traces indicate pre-digestion separations for the wildtype (WT) and heterozygous C282Y mutatated samples (HZ-C282Y) respectively. For the WT the restriction enzyme has no effect as expected as the *Sna*BI enzyme only acts on C282Y homoduplexes. The for the HZ-C282Y a third peak appears roughly equidistant between the primer and product. This barely detected peak indicates enzymatic activity.

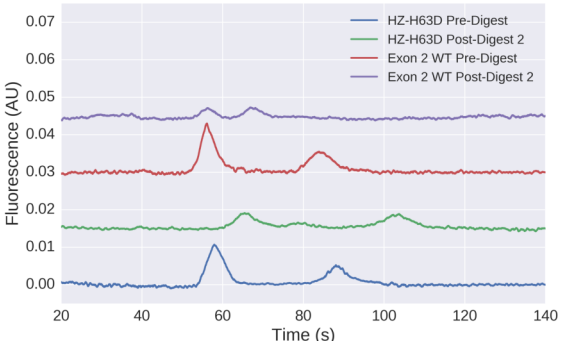

(b) Results of the automated analysis of exon 2 of the HFE gene. Red and Blue traces indicate pre-digestion separations for the wildtype (WT) and heterozygous H63D mutatated samples (HZ-H63D) respectively. After digestion, the WT sample has only two peaks that are close together (purple trace), indicating complete digestion as expected. The HZ-H63D sample exhibits three peaks after digestion, indicating incomplete digestion due to the BClI enzyme being unable to cleave H63D homo or heteroduplexes

Figure 5.4: The results of the discrete electrophoretic instrument for RFLP analysis

Sample	Raw Noise (mV)	Noise after Averaging (μV)	Primer Peak Height (mV)	Main Product Peak height (mV)	Digested Product Peak Height (mV)
HZ-C282Y, pre-digestion	1.88	190	16.5	3.9	
HZ-C272Y, post-digestion	1.69	228	19.0	7.9	2
Exon 4 WT, pre-digestion	1.48	247	20.7	6.9	
Exon 4 WT, post-digestion	1.49	212	18.8	6.7	
HZ-H63D, pre-digestion	1.11	141	11.2	4.6	
HZ-H63D, post-digestion	1.29	234	4.0	1.3	3.5
Exon 2 WT, pre-digestion	1.68	160	13.2	5.2	
Exon 2 WT, post-digestion	1.65	228	3.0	2.4	
Average	1.53	205			

Table 5.2: Table of results from the discrete system test for heterozygous C282Y mutations in exon 4 and heterozygous H63D mutation in exon 2 of the *HFE* gene.

Sample	Total Signal (mV)	Concentration in well (nM)	Signal per nM (mV)	Signal per nM (pW)	LOD (nM)
HZ-C282Y, pre-digestion	20.4	71	0.289	1.19	2.6
HZ-C272Y, post-digestion	28.9	63	0.458	1.89	1.6
Exon 4 WT, pre-digestion	27.6	71	0.391	1.61	1.9
Exon 4 WT, post-digestion	25.5	63	0.404	1.67	1.7
HZ-H63D, pre-digestion	15.8	44	0.356	1.47	2.0
HZ-H63D, post-digestion	8.8	40	0.220	0.91	3.2
Exon 2 WT, pre-digestion	18.4	44	0.414	1.71	1.7
Exon 2 WT, post-digestion	5.4	40	0.135	0.56	5.1
Average, pre-digestion	20.6	58	0.362	1.5	2.0

Table 5.3: Table of processed results that follow from the measurements in Table 5.2. The average LOD was estimated from the pre-digestion electropherograms in an attempt to reduce the potential for electrophoretic artefacts and was found to be 2 nM. This is 3.5x improved over what was estimated

5.3.3 Discussion

The results of this experiment show that the automated system was capable of automating enzymatic digestion with each experiment producing the expected result. However, there were a number of issues with this preliminary demonstration which led to this work remaining unpublished.

Firstly, the LOD for the system was measured to be 2 nM for pre-digestion separations, a value above the 1 nM research objective despite the use of larger microchannels in this demonstration. For this application, the primer and undigested products were easily visualised, however the low-level digested peaks were difficult to see. If we take the concentration of PCR primers used to generate the test samples, assume a 50% PCR conversion ratio, compensate for the dilution of the product with the buffers and assume that $^1/_4$ of the PCR product is digested, we can estimate the concentration of the low-level peaks to be 5 nM for the HZ-H63D sample and 8 nM for the HZ-C282Y sample. These values are very close to the the LOD and thus the detection was quite marginal. This LOD also benefited from larger microchannels. As discussed in Section 3.8.2, miniaturising the channel to 100 μm is expected to reduce the signal by a factor of 16.5, resulting in a LOD for this instrument that was an order of magnitude off the research objective. Thus, improvements to the detection were the primary objective for the next iteration.

Since this instrument was tested with discrete electronics with known responsivity and gain, the signal power per nM could be assessed and compared with the model. Based on the results in Table 5.3 and the transfer function of the PDE electronics from Section 4.4 the measured signal per nM can be estimated to be 1.5 pW. This is about 4x higher than the 380 fW estimated by the model in Chapter 3. This discrepancy was considered within the limits of the model considering the assumptions made that were not factored into the analysis. Firstly, the model estimated the excitation power by assuming the LED was illuminating the sample in free-space. In the orthogonal arrangement this was not the case as the excitation light passes through the PMMA microfluidic chip on its way to the detection point. Since PMMA has a refractive index (≈ 1.49) higher than air (1), the excitation light would be somewhat waveguided through the chip and less light would be lost. Therefore, the excitation power should be higher than estimated. Another factor to

consider was that the optical module was machined from aluminum, a highly reflective material which would further confine the excitation light. The GRIN lenses were also encased in aluminum, thus any rays that might ”escape” the lens system have the potential to be reflected back in and collected by the optics. Therefore, the efficiencies of both coupling in the LED light and coupling out the emission light are likely underestimated. Finally, this experiment was potentially subject to protocol issues as discussed below that would impact the accuracy of the LOD assessment. Considering these effects, the measured results are considered consistent with the signal estimation model.

One substantial issue with this experiment was that it was highly prone to injection artefacts due to the complex contents in the injection well. Unlike the previous demonstration in Section 5.2 or the subsequent demonstration in Section 5.4 where the sample well contained only the running buffer and sample, the injection well in this experiment also contained the buffer required for enzymatic action and the enzyme itself for post-digestion separations. Therefore, the ionic composition of the sample well was very different than the microchannels which could have an unknown effect on the injection of sample into the intersection, and thus potentially cloud the analysis. This highlights the need for improved experimental design for future instruments.

In addition to the generally marginal LOD, there was a lot of uncorrelated signal variation observed in the form of drift and bumps with periods on the order of multiple seconds as discussed previously in Section 4.4. One such bump can be seen in the first 40s of the post-digest run for exon 2 (Figure 5.4b purple trace). These bumps were particularly problematic given the marginal LOD as they can easily be interpreted as false peaks. In sample-less runs the occurrence of these stability issues seemed to correlate somewhat with the laboratory HVAC schedule in that runs during the night exhibited substantially higher stability. This was likely due to the susceptibility of this instrument to leakage currents (due to no precautions being undertaken at the time to limit them) and the placement of the instrument directly next to an air vent was poorly advised. This was not conclusively proven, though it was clear an iteration on the electronics to improve stability was required.

The signal to baseline ratio here was quite poor, with mV level signals against a 1.7 V baseline. As discussed previously in Section 3.8.2, this was surprising as it was roughly the same as the OPT1 optics on the CMOS platform despite the introduction of an excitation filter for improved baseline suppression. The hypothesis for this discrepancy was attributed to the instrument having a spot-size larger than the CE channel. This contrasts to the IP-CMOS design which had a smaller spot-size than the test channel. Another effect was that the generation 2 milled fluidics exhibited very high surface roughness as described in Section 2.2.3 which was expected to increase the amount of excitation light scattered into the detector and therefore increase the baseline. While improving the LOD was the primary objective for the next iteration, improvements to LOD would require more signal gain. This signal gain would exceed the dynamic range of the electronics without a reduction in baseline. Therefore, SBR improvements were also required at this stage, prompting development on the microfluidic fabrication, optical filters and spot-size.

The resolution of this system was also poor. Equation 5.1 was used to estimate the resolution for the post-digested heterozygous samples, though this provides only an estimate due to the difficulty in determining the FWHM for peaks with poor SNR. For exon 2, the peaks have sizes of 72 bp and 234 bp, with FWHM values of 6.8s and 9.5s respectively. The separation of the peaks was 23.2s, giving an estimated resolution of 57 bp. For exon 4, the resolution was worse. The 158 bp peak had a FWHM of 4.8s and the 436 bp peak a FWHM of 9.5s. The separation of these peaks was 14s, giving a resolution of 110 bp. Of these two resolutions (57 bp, 110 bp) the latter should be considered more representative as the exon 2 digested product is very small (only about 2x the size of a primer), likely leading to different

separation physics for this gel. Therefore, the resolution for the CEI1 system was considered to be 110 bp, however due to the limited number of tests and the low SNR this should be considered a rough estimate. Since resolution was not a primary concern, further testing on the matter was not a priority. 110 bp resolution is consistent with the 100 bp resolution separations in Agarose cited by Ugaz et al.[59] in their review of microfabricated electrophoresis systems, though it is a factor of two worse than previous work with a confocal module by Ma et al..[96] Since the spot-size for the optics in this instrument (323 μm) were larger than the channel width (254 μm) it was expected that the optics would have a negative effect on the resolution. This further emphasised the need for a reduction in spot-size in future instruments.

In summary, this application demonstrated the fabrication techniques for combined milled/laser patterned fluidics, the use of excitation filters, the use of discrete electronics and completed previous RFLP work to demonstrate the potential for CE diagnostics. The LOD and resolution were assessed to be roughly 2 nM and 110 bp respectively. This marginal optical performance and a host of technical challenges prevented this work from reaching its potential. Thus, the primary attention remained on development of the LIF module for CE, specifically reduction in the spot-size.

5.4 CEI2- State of Art LED-Photodiode CE Optical Detection

The final instrument demonstration as part of this thesis, CEI2, implemented a number of key changes identified in the previous iteration to implement a new state of the art in LED-photodiode LIF detection for CE applications. The instrument was composed of the OPT3 optics designs (Section 3.8.3), the DEV1 detection electronics (Section 4.5) and with the 254 μm wide and deep generation 2.5 micromilled fluidics (Section 2.2.3). This amounted to improvements to the microfluidic fabrication (smoother channels to scatter less light), optics (improved excitation filters and a pinhole for spot-size reduction and better baseline) and detection electronics (improved stability and P_{min}). Two experiments were performed on this platform. First, to test the LOD in a more robust manner end-labelled PCR primers were injected and separated. These primers were diluted down to 0.4 nM, thus testing the LOD across a broad range of values. Next, a practical separation was done with a mix of two different PCR products. This allowed for a rough estimation of the system resolution as well as a demonstration of a typical usage of the system. The combination of the fabrication, optical and electrical improvements resulted in the first demonstration of sub-nM LOD for instruments of this type at 0.15 nM, making it the first such cost-accessible instrument with detection capabilities sufficient for DNA analysis with CE. However, due to the larger channels and need to use an agarose sieving matrix, the resolution remained poor at 43 bp. Therefore, while a very notable milestone, achieving the research objectives required additional development.

5.4.1 Brief Demonstration Description

The specifics for this experiment are outlined in Appendix E and described briefly here. The microfluidics were made in PMMA with the 254 μm x 254 μm channels being micromilled with the generation 2.5 parameters described in Section 2.2.3. In comparison to the channels used to demonstrate the enzymatic digests in Section 5.3, these channels exhibited much lower surface roughness which should translate into improved optical coupling of the excitation light

into the channel and reduced scatter of the excitation light into the detector, providing a slight boost to signal and a reduction in baseline. The channels were capped with PCR-tape as previously discussed in Section 2.3.1.

The optics used were the OPT3 design from Section 3.8.3 which consisted of an improved excitation filter and the introduction of a pinhole. The pinhole reduced the spot-size of the instrument to a predicted 152 μm. This was a crucial development as the spot-size was then less than the channel width, ensuring that the separation resolution was no longer affected by the optics and was instead dominated by the protocol. The combination of the improved filter and spot-size both improved the baseline, the primary issue with the previous CEI1 design. The baseline improvements also enabled more signal amplification and therefore better detection electronics. The electronics used here were the DEV1 design from Section 4.5. Through improvements to the components and assembly techniques, stable baseline was achieved and the P_{min} was improved to 122 fW. Section 3.8.3 and Table 3.11 estimated the fluorescence signal from a 1 nM sample with these channels to be 250 fW. Therefore, this instrument was expected to have a LOD of 0.5 nM albeit with larger channels. The practical implementation of the optics used the same instrument box as the previous instrument in Section 5.3 with the optics being implemented in aluminum as before.

Two experiments were performed. In the first, end-labelled primers of known concentration were used as the test analyte. These primers were diluted 1:10 in the sample well and an inject-separate procedure was executed. The concentrations tested were 40 nM, 4 nM and 0.4 nM, thus spanning the 1 nM target. Next, a mixture of two end-labelled PCR products was separated. These were both diluted 1:10 and had sizes of 234 bp and 436 bp, allowing for an estimation of the resolution. Agarose was again used as the sieving matrix due to the channels being still larger than 100 μm. In contrast to the previous demonstrations, these experiments used the same buffer concentration in each well, therefore avoiding any stacking effects and minimizing injection artefacts. Sampling was performed at 1950 sps as per Section 4.5, though this sampling rate varied slightly as it was not strictly controlled. Data was processed by first fitting a linear baseline to the first 80s of the trace (i.e. approximately up to 40 s before the primer arrival time) and removing this linear baseline from the signal. Next, a 1950 (1 s) moving average was applied. LOD was assessed based on the 0.4 nM primer separation (the closest concentration to the LOD) and the resolution was estimated based on Equation 5.1. Results are shown in Figure 5.5.

5.4.2 Results

Representative electropherograms for both the LOD determination and DNA PCR product analysis are shown in Figure 5.5. For the LOD test, the primer peak heights were 1.2, 8.1 and 103.5 mV for the PCR primer at concentrations of 0.4, 4 and 40 nM respectively. For the two weakest peaks (i.e. for 0.4 and 4 nM), the LOD was 0.15 and 0.16 nM respectively. The resolution could be estimated based on the separation of the DNA products and Equation 5.1. The FWHM for the 436 bp and 234 bp products were 3.1s and 2.7s respectfully and the peaks were separated by 13.7s. This gives a resolution estimation of 43 bp, comparable to previous work with agarose sieving matrix and a confocal optics module Ma et al..[96]

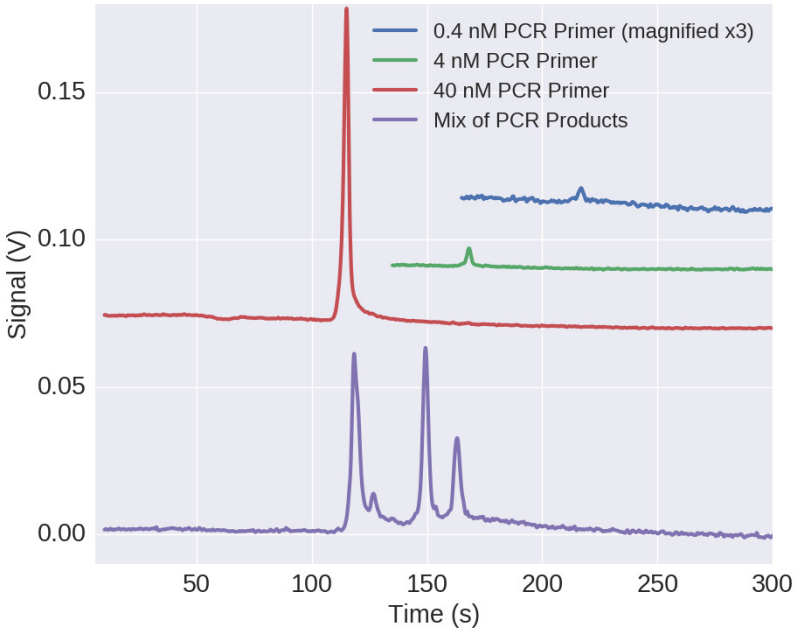

Figure 5.5: Representative electropherograms from the system. The bottom trace is a separation of two PCR products from primers and, as a series dilution, the higher traces are separation of the unamplified PCR primers at concentrations of 0.4, 4 and 40 nM with signals of 1.2, 8.1 and 103.5 mV respectively. The corresponding signal to noise levels (with noise standard deviations calculated as described above) were 8, 74 and 345 respectively. For ease of display, the 40nM primer trace was offset vertically by 80 mV with the traces from lower concentrations successively offset vertically by 20mV each and horizontally by 60 and 90 s. In the bottom trace, the peak identities for the product mixture (from left to right) are primer, primer-dimer from the exon 4 reaction, HFE exon 2 PCR product (234 bp) and HFE exon 4 product (436 bp).

5.4.3 Discussion

The measured LOD was 0.15 nM of fluorophore, a factor of 3.33x higher than the model estimated value from Chapter 3. This factor was comparable to the factor of four found from the CEI1 instrument and can be explained by the same model deficiencies discussed in Section 5.3.3, notably the uncompensated waveguiding of the excitation light through the polymer microfluidic chip to the sample. The consistency of the discrepancy between the model and the measured LODs and the relatively small magnitude of the factor suggests that the developed model tracks the measured performance well enough to function as a good design tool. However, due to the small sample size of only two instruments and the large number of factors that go into the model calculation, further conclusions (for example, estimating the magnitude of the waveguiding factor) would be premature.

The LOD of this instrument represents a substantial improvement over the previous iterations discussed in this chapter. In comparison to the IP-CMOS instrument in Section 5.2, the LOD at first appears to be only a modest improvement (0.9 nM to 0.15 nM). However, the channels in Section 5.2 were much larger than those used here (381 μm a side vs. 254 μm) with 3.4x more fluorescent material. Therefore, this instrument represents over an order of magnitude

(x20) improved detection after factoring in the sample volume difference. In a comparison of the normalised signal from Table 3.12, the optics in this instrument actually collect less signal than the those in Section 5.2 (x0.8 less) after accounting for differing sample sizes due in part to the attenuation of excitation light by the excitation filter. However, this loss was made up for with improved optical filtering that analysis in Table 3.6 showed would improve SBR by an order of magnitude. Therefore, while the OPT3 design used in this system collected less signal, the lowered baseline enabled the use of higher gain detection electronics to improve the LOD. As described previously in Section 4.2, the detection electronics in the IP-CMOS instrument were run at their integration time (i.e. highest signal gain). Therefore, in order to benefit from the improved SBR of this optical implementation the use of a discrete detection electronics design was required.

The LOD was was also over an order of magnitude improved over the CEI1 discrete instrument in Section 5.3 (2 nM to 0.15 nM). Since these two works utilised the same separation channel dimensions, their LODs can be directly compared. This improvement can be separated into optical and detection electronic improvements, as discussed in more detail in previous chapters. Optically, as shown previously in Table 3.11, the changes introduced improved the SBR by a factor of 26x at the expense of a slight factor of 0.7x decrease in signal, mostly due to the pinhole reducing the collection efficiency of fluorescent light imposed by the pinhole. However, similar to the discussion above, the signal decrease was more than compensated by the detection electronics advancements enabled by the SBR improvement; the change from the PDE circuit to the DEV1 circuit represented a factor of 20 improvement in the P_{min}. Therefore, the design changes for SBR and LOD improvements instituted for this module were had their designed effect.

In this work, the key optical advancement was implementation of a pinhole for spot-size control. In comparison to the CEI1 instrument from Section 5.3, this pinhole reduced the 323 μm spot-size to 152 μm, smaller than the channel width of 254 μm. As explored in Chapter 3, orthogonal optics arrangements benefit in two ways from having a spot-size less than the channel width. Firstly, this results in the collection of less scattered light, reducing the baseline. As discussed above and in Section 3.8.3, this instrument exhibited substantially improved SBR as compared to the CEI1. Secondly, if the spot-size is less than the channel width it should not affect the separation resolution. The estimated resolution for the CEI2 was 43 bp. This was a substantial improvement over the 110 bp estimated for the CEI1 instrument in Section 5.3 and quite consistent with the 50 bp resolution achieved with a 10 μm spot-size confocal module used previously.[96] Overall, both in terms of SBR and resolution, the introduction of the pinhole should be considered a great success.

The 0.15 nM LOD represents not only an improvement over the previous instruments in this thesis, but also over those in the literature making it the best reported LOD for LED+photodiode based CE instruments. Comparing LODs is difficult due to the vastly differing performance of various fluorophores, therefore a series of adjustments have been made to account for fluorophore-specific effects. Firstly, this involved adjusting for the fluorophore quantum yield and coefficient of absorption (i.e. adjusting for how the fluorophore is excited and how well this excitation converts to emitted light). This was done for three relevant fluorophores in Table 5.4. Works that utilised intercalating dyes must also be adjusted for as each DNA molecule in these works would have multiple fluorophores bound. For example, Namasivayam et al.[69] utilised the dye YOYO-1 which they previously reported bound to DNA every five base pairs for their applications.[68] Such works typically express their LOD as a mass concentration of DNA, requiring a conversion factor to a DNA size in bp as well as a conversion factor for the binding frequency of fluorophore to a given DNA size. In this comparison, a 300 bp (i.e. the average of the two DNA products used in Figure 5.5) and mass

conversions from the ThermoFisher website will be used.[180] Using these adjustments, I have compared the LOD for this instrument with the two best known reports in the literature for LED + photodiode based LIF detection by Yang et al.[88] and Namasivayam et al.[69] which were highlighted by reviews by Castro and Manz,[26] Macka et al.[81] and/or Xiao et al..[86] Based on this analysis, it is clear that this instrument represents a substantial detection improvement over previously published results, having a LOD that is multiple of orders of magnitude better than the two state of the art works presented here. Furthermore, at time of writing this was the only instrument that clears the 1 nM threshold for end-labelled DNA analysis, meaning this improvement has direct application ramifications.

Fluorophore	Quantum Yield	Extinction ε Coeff. ($M^{-1}cm^{-1}$)	Scaling Factor
AF532	0.61[154]	81,000[181]	1
Fluorescein	0.93[182]	76,900[182]	1.45
Yoyo-1	0.52[183]	98,900[183]	1.04

Table 5.4: Fluorophore scaling factors used for LOD comparisons. The scaling factor is the product of the extinction coefficient and the quantum yield, normalised to AF532, a representative end-label for DNA applications. The scaling factor allows for the comparison of different systems as shown in Table 5.5. (In the basic borate buffer used in Yang et al.,[88] the fluorescein dianion dominates the observed fluorescence.[184] As such, we have used the properties of the dianion for the scaling factor.)

Work	Cited LOD (nM)	Fluorophore	Fluorophores per DNA molecule	Effective LOD for AF532 (nM)
This work	0.15	AF532	1	0.15
Yang et al.[88]	100	Sodium Fluorescein	1	145
Namasivayam et al.[69]	0.9 $^{ng}/_{\mu L}$	YOYO-1	1 per 5 bp (x60 for 300 bp product)	341

Table 5.5: Comparison of the LOD for this system with other LED + photodiode detector based CE instruments. The effective LOD is calculated by correcting for the fluorophore as described for Table 5.4 and accounting for the multiple-labelling of intercalators.

Namasivayam et al.[69] is a continuation of the project that included previously discussed works by Webster et al.[68] (discussed in Section 3.8.5) and Burns et al.[67] (discussed in Section 1.2.3 as a PCR-CE instrument example) where the microfluidics were brought into close proximity with a photodiode to form a miniaturised device. The instrument was demonstrated with a number of CE separations of intercalated DNA. In contrast to the relatively monolithic instrument by Webster et al.[68], Namasivayam et al.[69] split their device into two parts that were later glued together, a fluidic aspect in glass and an electronic aspect in silicon with an interference-based optical filter. This was likely done to simplify the fabrication process as compared to Webster et al..[68] In their work, Namasivayam et al.[69] cited an order of magnitude improvement in LOD over Webster et al.[68] to 0.9 $^{ng}/_{\mu L}$. Similar to this work, resolution was not a primary concern and was not explicitly assessed. However, it can be estimated from their data output to be between 50 bp and 100 bp using a cross-linked polyacrylamide gel and can therefore be considered comparable to this work. This is expected as the gel and separation length are relatively similar and the spot-size of their instrument was smaller than their channel width (a 10 μm x 500 μm photodiode to pair with the 500 μm wide channels). However,

the poor LOD (341 nM after conversion) precludes further advancement to end-labelled separations and is multiple orders of magnitude off the LOD reported here. Furthermore, Namasivayam et al.[69] relied on an external high-performance lock-in amplifier and interference filters to perform their analysis and therefore their implementations can be considered neither low-cost nor scalable. The work by Namasivayam et al.[69] also highlights the practical development challenges of these projects. Starting with the PCR-CE demonstration by Burns et al.[67] to the CE chip by Webster et al.[68] to the split solution by Namasivayam et al.,[69] each iteration on their project reduced the integrated functionality to reduce fabrication complexity and cost. In contrast, this project was designed to target scalable solutions that were low-cost to develop and could be readily iterated and improved.

The work by Yang et al.[88] has been cited as the state of the art in LED and photodiode based CE[26,81] with an adjusted LOD of 145 nM. This work was discussed previously in Section 3.1.1. This is the most relevant work in the literature to this project, implementing a low-cost LIF module that featured a LED, pinhole, a single interference filter and photodiode. In terms of cost and complexity, the lack of lenses as compared to this thesis is offset by the use of an interference filter. Overall, based on commercial interference filter costs, the instrument in this thesis is about a factor of three to four less expensive. Furthermore, the LOD in Figure 5.5 was nearly three orders of magnitude improved. While Yang et al.[88] did not assess their resolution (as they did not implement a DNA application), if they did it would likely be very poor. Yang et al.[88] limited the spot-size of their instrument with a pinhole on the LED illumination, however this pinhole was 1.1 mm in diameter and held about 1.1 mm from the detection point. The resultant spot-size was not assessed in their work, but would be expected to be very large and much larger than any microchannel. Overall, the CEI2 instrument was less expensive, ≈x1000 improved LOD and had a vastly reduced spot-size, leading to substantially better CE performance.

In summary, the CEI2 instrument was a landmark demonstration both in terms of this projects progression as well as in the literature. The 0.15 nM LOD easily cleared the 1 nM threshold for robust end-labelled DNA analysis. However, the 43 bp resolution did not meet the 10 bp requirement set out by Ugaz et al..[59] The consistency with which ≈50 bp resolution was measured across multiple different channel geometries and optics modules suggests that the agarose sieving matrix was the main limiting factor and attention should be turned to higher performance matrices and smaller channel dimensions. Another issue was the channel composition used, which for this work was three sides of PMMA and one side of tape. This created uneven zeta potentials for the channel which would be expected to have a more pronounced effect with higher performance applications. Therefore, there were two fabrication improvements that needed to be made following on this demonstration; channel size reduction and implementation of a homogeneous channel. These improvements were achieved through the next-generation microfluidic fabrication detailed in Section 2.4 and Appendix C. However, in the process of shrinking the channel, the signal strength would be decreased. As discussed previously in Section 3.8.3, shrinking the channel to 100 μm would decrease the signal by a factor of x16.5 for this design. Therefore, based on the measurement in Figure 5.5, the LOD would be expected to be about 2.5 nM. Thus, it would not meet the 1 nM objective. Furthermore, this change would decrease the channel width to less than the spot-size, leading to resolution and baseline issues. Therefore, more development was required to meet the research objectives.

5.5 Next Generation Instrument

The next-generation instrument was the culmination of this project, bringing together all of the best designs presented in this thesis to form a comprehensive LOC instrumentation platform capable of implementing PCR-CE. This includes the new OPT4 optics from Section 3.8.4, the DEV2 detection electronics from Section 4.6 and the technical functions detailed in Appendix A which include HV generation and switching, pneumatic valving and thermal instrumentation for PCR. This section provides a design overview, system specification and preliminary testing details. A usage guide for this instrument is presented in Appendix F while the SI contains a tool that facilitates the design of microfluidics. Combining this tool with the broad functionality and flexible alignment structures, this instrument is readily re-configurable to a broad spectrum of applications. Finally, this instrument carries a total prototype cost of roughly $1000, a price below the cost of just the optical components of a typical industrial or academic PCR-CE implementation and over two orders of magnitude lower than the only commercially available PCR-CE instrument[66].

5.5.1 Design Overview

The next-generation instrument includes the best designs developed as part of the microfluidic infrastructure detailed in Appendix A. For fluidic actuation, the updated high voltage electronics from Section A.1.2 were used. These allow for high voltage control from 50 to 300 V at up to 0.5 mA, with current monitoring between 0.5 and 118 μA. For the short channel CE applications targeted by this project, the fields generated were more than sufficient for standard separations with a variety of sieving matrices. The fluidic control module also includes pneumatic valving with 24 toggle-able pneumatic lines. The number of lines required varies depending on the application and fluidic architecture used. So far, a number of various concepts have been developed such as bead-based DNA sample preparation (15 valves), sample preparation with PCR (17 valves), sample preparation with PCR and CE (17 valves) and sample preparation with PCR and a RFLP analysis (22 valves). These valve numbers were estimates based on worst-case scenarios and can be readily reduced by, for example, connecting multiple valves to a single pneumatic line, or optimising path lengths to reduce the number of valves needed. However, in order to ensure the instrument supports the ambitious application roadmap, 24 valves were selected. These were implemented with three 8-position mini-style pneumatics blocks as detailed in Section A.2.4. A single PCB that implements both these fluidic actuation functions is detailed in F, Section F.2.3.

In terms of thermal design, the instrument contains electronics to support a resistive heater, a thermocouple for temperature measurement and a second, dedicated microcontroller for thermal control similar to the PCR demonstration in Appendix A.3.8. However, for this iteration an updated controller was used as discussed in Appendix A.3.7. The instrument currently does not have a heater, as the thermal design and technology has as yet not been developed and is outside the scope of this thesis. However, the thermal drive circuit can set currents up to 1 A, 12 V and the voltage can be readily increased by connecting an external power supply.

The instrument includes a single optical detection point based on the most recent OPT4 optics design and DEV2 detection electronics. These were discussed in Sections 3.8.4 and 4.6 respectively. In short, this features a cyan LED, optimised pinhole GRIN lens collection optics and improved optical filters in a staring-into-the-sun arrangement with a high gain transimpedance amplifier. This optics arrangement not only allows for simplified scaling towards more

miniaturised systems as discussed in Section 3.1.3, but also is easier to implement in designs. Previously, Section 3.8.4 estimated a signal of 56 fW for a 1 nM sample in a 100 μm x 100 μm channel and the OPT4 optics. Since the DEV2 detection electronics can detect a signal of 42 fW (as described in Section 4.6), the LOD for this instrument is predicted to be 0.75 nM of AF532. Thus, this instrument exceeds the LOD required for implementing PCR-CE outlined in Section 1.2.2 in channels compatible with high resolution separation matrices. Future work can readily demonstrate a sub-nM, sub-10 bp CE separation on this platform making it the first low-cost LIF detection instrument capable of standard CE. Subsequent demonstrations that leverage the valving and thermal capabilities could then be shown, implementing PCR-CE. Finally, due to the scalability of the optics used, these demonstrations would provide design metrics and optimisations to justify and guide the on-going development of a monolithic CMOS-based single chip LOC device.

5.5.2 Specifications

The input specifications for the next-generation system are presented in Table 5.6. The performance specifications are presented in Table 5.7.

Parameter	Nominal Value	Maximum Value	Interface	Notes
Digital Input	-	-	USB-B Female	Connects directly to BeagleBone Black
Input Voltage	+12 V	+13 V	Wall wart	+12 V feeds directly to HV relays and HV supply
Input Current	2 A	-		
Input Pressure	138 kPa	206 kPa	$^1/_8$ OD shark-bite	Pressure - vac not to exceed 206 kPa
Input Vacuum	-60 kPa	-206 kPa	$^1/_8$ OD shark-bite	
Heater Voltage	+12 V	40 V	Banana Plug	Voltage limited by transistor used (TIP29)

Table 5.6: Input specifications for the next-generation system

Module	Parameter	Nominal	Notes
Valves	Number of Valves	24	$^1/_{16}$ barbed fitting. $^1/_{16}$ ID tubing
	Simultaneous Valves Open	0 - 10	10 Valves = 1.5 A, maximum supported by cabling
	Actuation rate	10 Hz	300 Hz is valve maximum.
High Voltage	Output Voltage	50 V - 300 V	Operating below 50 V can result in less accurate voltage setting
	Voltage Set Accuracy	2%	
	Minimum Current Measurement	0.5 μA	
	Maximum Current Measurement	118 μA	
	Current Measurement Noise	152 nA	
	Current Measurement Rate	500 Hz	
Thermal	Thermal Measurement Accuracy	2.2^o	Thermocouple accuracy with no calibration.
	Temperature Reading Increment	0.25^oC	
	Heater Current	3 mA - 1000 mA	3 mA off-current can be avoided by cutting power to heater
	Controller Update rate	1 kHz	
Optics	LED supply 1	0 - 56.6 mA	Typ. LED = 30 mA
	LED supply 2	0 - 126 mA	Can be used as a heater as well.
	Sampling rate	5sps - 2000 sps	Typically 1000 sps
	Transimpedance Gain	$2-128\times10^{10}\frac{\text{V}}{\text{A}}$	Set with ADS1248 PGA. Typically 2
	Bandwidth	8-32 Hz	Calculated in Section 4.6
	P_{min}	42 fW	Calculated in Section 4.6
	LOD (estimated)	0.75 nM	Calculated in Section 3.8.4
	Spot Size (estimated)	134 μm	Calculated in Section 3.6.3

Table 5.7: Table of performance specifications for the next-generation LOC system.

5.5.3 Construction and Design

The instrument is a rectangular aluminum structure that is 12" wide, 6" deep and 6" high. It was made from 6"x6" aluminum square tubing with $^1/_4$" walls for rapid construction and easy sealing against ambient light. Thus, the width of the instrument was split into two connected sub-boxes, with the leftmost sub-box housing electronics and pneumatics, while the rightmost sub-box contains the fluidics and detection electronics. Figure 5.6 shows the front of the instrument. The left-hand side contains ports in three rows. The top row relates to the thermal subsystem. Since the thermal design was not known, there are ports to provide an external voltage to drive the heater circuit. A switch is included to toggle the heater drive power from this external voltage and the internal +12 V supply. The middle row contains a USB port. This is a USB-2 type B female port and it is internally connected to the BeagleBone Black microcontroller, which supplies all internal digital communication functions. Also included is a power jack to connect a 12 V wall wart to (standard 2mm ID, 5.5 mm OD mating diameter) and a switch to toggle on and off the power. Finally, along the bottom are two ports for introducing vacuum and pressure to the pneumatics blocks. These accept

$^1/_4$” OD tubes and it is heavily recommended that stiff polyethylene tubing be used.

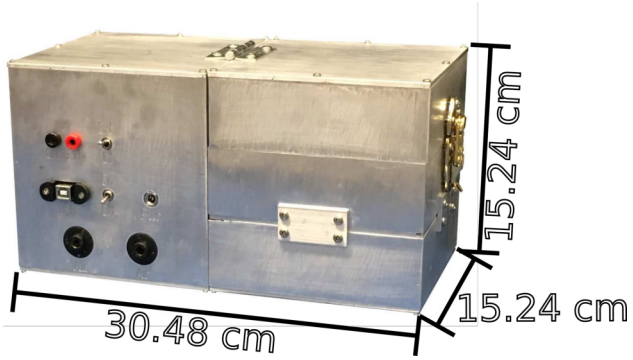

Figure 5.6: Picture of the front of the instrument. The instrument has two sections. The left-hand section is a singular piece of aluminum tubing that contains the bulk of the electronics (BeagleBone Black, interface board, heater board, fluidics board) and all the pneumatics modules. This section also has all of the interfacing ports.
Top row: external heater power supply ground (left), external heater power supply positive voltage, heater power supply toggle (up for external, down for internal 12 V supply)
Middle row: USB-2 type B connector for microcontroller (left), power on toggle, input power (+12 V from wall wart)
Bottom row: Vacuum supply (left, -60 kPa), Pressurised air supply (+138 kPa)

The rightmost section contains three levels: the detection electronics in the lower layer, the microfluidics section which forms a base and a lid to seal the microfluidics from ambient light. The microfluidics layer (pictured in Figure 5.7) was designed to accommodate a variety of microfluidic chips with flexible alignment options. Firstly, many microfluidic options, both in industry[51] and in the Backhouse laboratory, are based on a microscope slide sized substrate (3” x 1.5” or 7.62cm x 3.81cm). Two methods were designed to accommodate chips of this dimension: one based on alignment pins and pone based on a spring-fit system. The alignment pins are $^1/_8$” dowels embedded in the base that chips can be made to fit over to align to the detection point. A design tool is included in the SI to ensure pin-based designs conform to the dowel placement and a sample CE chip using this arrangement is shown in Appendix F.3. However, this method requires the machining of holes clean through the microfluidic chip, which is not always feasible for all substrate materials. The spring-fit system was implemented for such applications. This includes a hard stop that is attached to the base on one side of the chip and spring-loaded arm on the other. The spring pushes and holds a 1” wide strip with its centre over the detection spot. In Figure 5.7 the red zone indicates the region designed for microscope slide sized chips. This region is sufficiently long that the alignment pins do not interfere with the spring-fit system. The spring-fit system can also be removed from the base to enable the Large Format Chip, shown in blue in Figure 5.7. This is a 3” x 3” recess with a series of mounting holes arranged in a grid. The design tool in the SI also includes guides for facilitating the design process of these chips and Appendix F.3 includes a sample output from this tool. Currently, there is no design for a fully-function microfluidic chip that can implement sample preparation, PCR, enzymatic digestion and CE all at the same time and such a device is beyond the scope of this work. The Large Format provides ample space and mounting options to accommodate future designs.

Due to the lack of a thermal design, a heater zone was made. This heater zone contains two holes for wires/thermocouple access and is 1” x 1” in side and 2 mm deep. This dimension was used as most of the heaters that are commercially available in Canada use imperial units. The heater zone is indicated in Figure 5.7 in cyan. Surrounding

the heater zone, extra alignment screw holes were included such that previously used pneumatic manifolds (described in Appendix A.2.3) can be used. This gives the instrument a degree of backwards compatibility.

There are a large number of ports made available to the user inside the middle section of the box. On the wall are 24 valves (split amongst the three pneumatics modules as labelled), two HV lines in the form of 3.5 mm audio jacks and two banana plug adapters for heaters. 3.5 mm audio jacks have been used for HV lines because their design ensures that the ground pin contacts the board prior to any live pin to limit electrostatic discharge. For both connectors the tip of the jack is ground, the first connector band is toggled between floating and HV, the second conductor band is toggled between float and ground and the base is grounded as well. This is described in the schematic for the fluidics circuit that is included in the SI. On the microfluidic mounting base there are two additional 3.5 mm audio jacks labelled LED and ISRC. These correspond to two current sources with the former being controlled up to 56.6 mA and the latter up to 126 mA. For these connectors, the first connector band is the high side, the second band is the low side and the tip and base are grounded as before.

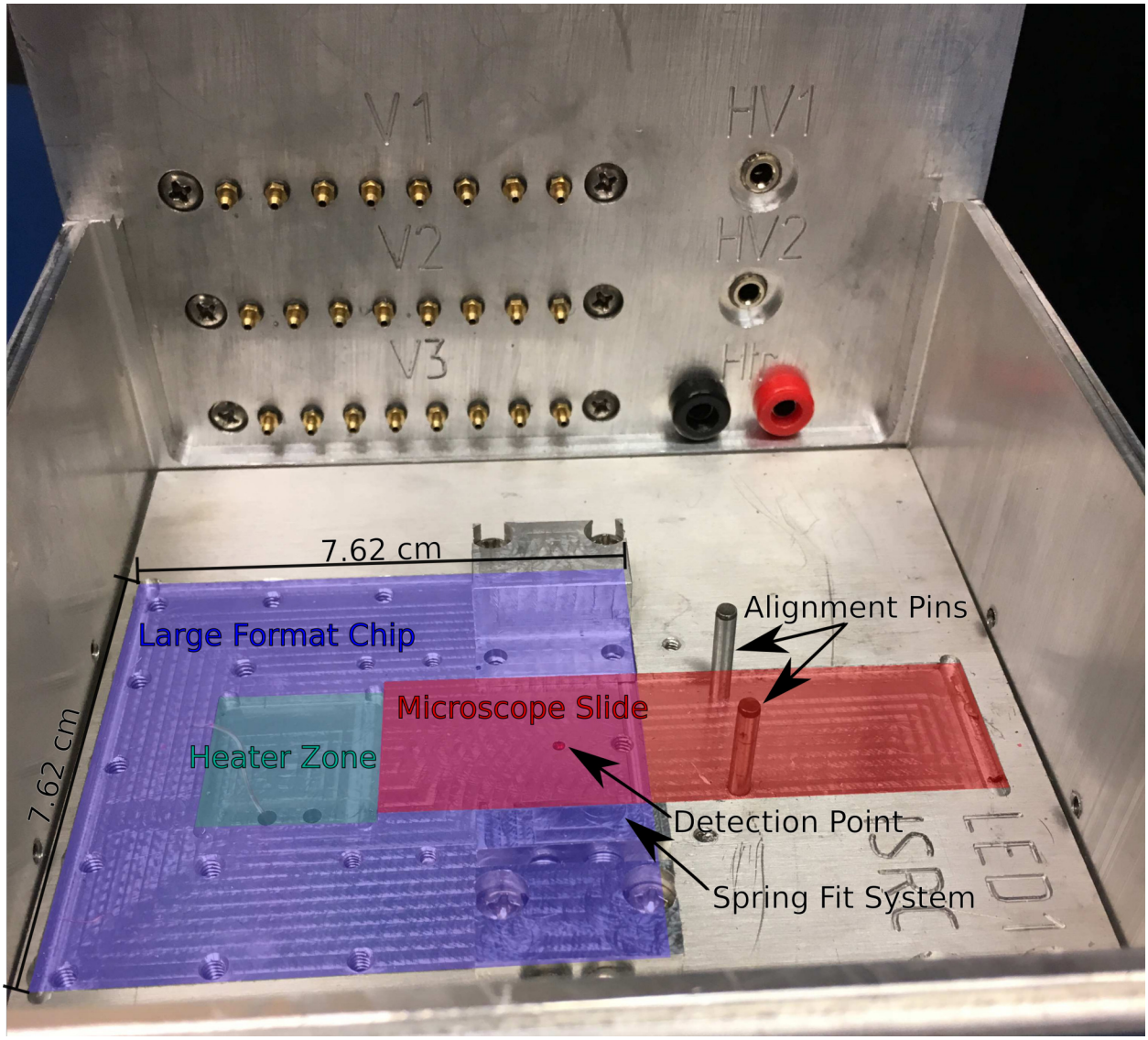

Figure 5.7: Picture of the inside of the microfluidics section. The wall contains ports to access electronics encased in the leftmost section of Figure 5.6 such as the 24 pneumatic lines, two high voltage lines with accompanying ground lines and the heater. The base contains alignment structures for a wide variety of chips. Microscope slide sized chips with a channel in the centre can be readily aligned to the detection point either with the alignment pin system ($^1/_8$" dowels) or using the spring fit system which pushes the chip against a hard-stop to align the optics 0.5" from the hard stop edge. If larger sized chips are required, a 3" x 3" area can be had by removing the spring fit system. This area has a variety of mounting holes, including legacy holes for previously designed pneumatic manifolds enabling backwards compatibility with previous fluidic designs. A heater zone was made to accommodate future thermal designs. Finally, two ports (at the bottom of the image, not visible) can be used to access the LED and 0-126 mA current sources.

An Asymptote file which generates the CAD designs for every aspect of the instrument is available in the SI along with all of the tool path files used to fabricate this instrument.

5.5.4 Testing

One of the primary concerns with instruments of this type is reproducibility and robustness. Biological protocol optimisation is a lengthy process with a very large number of potential variables to tune and any instrumentation errors compound these issues substantially. To demonstrate robust operation, a testing procedure was developed where the instrument executes the following functions:

1. Cycle each pneumatic valve one at a time. This ensures the valve modules are appropriately connected and facilitates troubleshooting of this module
2. Execute a pump cycle with the first three valves of each module for 10 cycles with a 0.2 s delay. This demonstrates the that the instrument can simultaneously toggle multiple lines (six open at once) with reliable timing
3. Execute a pump cycle where the middle three lines on the second module (valves 12, 13 and 14) are held open while the last three lines on modules one and three are pumped. This demonstrates the instrument can have seven lines simultaneously toggled (1.05 A current draw).
4. Turns on the HV module to 50 V, 100 V, 200 V and 300 V. For each voltage it first does an injection, then a separation, holding each stage for 1s (i.e. 50 V injection, 50 V separation, 100 V injection, etc.). The current is measured for at each level and displays mean, maximum, minimum and noise of the current measurement
5. Turns on the current source through the resistive heater. Sets current to off, 100 mA, 250 mA, 500 mA, 750 mA and 1 A. Each level is held for 1 s
6. Measures the temperature 10 times at 1 Hz using the thermocouple, displaying the value on screen
7. Measures the optical signal for 3 seconds at 10 Hz, displaying the value on-screen. This is done with the LED off, then set to 10 mA, 20 mA and 30 mA.

Thus, the 90 s test executes each instrument function, ensuring reliable communication between the various modules. Prior to executing the test, the user should make the following connections:

- Connect an ammeter to the heater current
- Connect a 2+ MΩ resistor to both the injection and separation HV connections
- Supply pressurised air (+15 psi) to the vacuum line. Leave the pressurised line at atmospheric pressure
- Attach a LED and manifold to the instrument for staring-into-the-sun analysis and close the instrument lid

These connections allow the user to monitor the current source, monitor the stability and current reading capability of the HV circuit, easily observe which valves have been toggled (as they switch from ambient to pressurised lines) and ensures the optical signal is measured. The heater current should be within 5%, with a 3 mA offset when off, the HV current noise should be much less than 200 nA, with an accuracy within 3%, the pneumatics testing should have no errors and the photodiode signal should be consistent.

Overall, this test was run without error 120 times consecutively on three separate days (360 total iterations). This testing was supplemental to the module testing detailed in Appendix A.1.2 for the HV module and Section 4.6.3 for the optics module which were also performed within this instrument. Thus, this demonstrates reliable operation, leaving the instrument ripe for future application development.

5.5.5 Comparison to Literature and Industry

Table 5.8 compares the functionality of this next-generation instrument with the instruments demonstrated in the literature in Section 1.2.3 of the Introduction. This is discussed in more detail below. In comparison to the literature, this instrument is one of the most functional as it contains all of the key functionality. Furthermore, it is the only instrument that can be considered cost-accessible.

In terms of valving, the 24 valves in this instrument compare very favourably to the other works in the literature; many (Liu et al.[39], Shaw et al.[77], Pan et al.,[76] Koh et al.[42]) have neglected active valves altogether while Le Roux et al.[40] and Kaigala et al.[80] have a very limited number of available lines. This is important as many of the more complicated standard protocols that this instrument aspires to implement require up to 22 valves, thus only the work by Scherer et al.[41] would be capable of implementing this level of complexity.

HV instrumentation is an aspect that has been optimised in this instrument for lower cost. Compared to the rest of the literature, the HV here has both the fewest outputs and the lowest voltage. This was an intentional design choice (discussed in Appendix A.1). Firstly, for CE the key issue is not the absolute voltage, but the field applied to the sample. Since the channel lengths targeted ($\approx$ 1 cm separation distance) by this work are shorter than typical in the field, the channel lengths are also shorter leading to typically lower running voltages. Ugaz et al.[59] cites a number of optimised CE separations with high-performance sieving matrices with typical fields around 100 $^{V}/_{cm}$. Thus, for 300 V the separation channel must therefore be shorter than 30 mm, a constraint every demonstration above has met. Furthermore, 300 V is the maximum voltage achieved by the charge-pump on prototype CMOS microelectronic chips as part of this project as discussed by Sloan et al..[160] Maintaining the HV limit to 300 V therefore ensures scalability of the protocols to future monolithic designs.

For thermal instrumentation, this work implements a resistive heater and thermocouple readings. This is a lower-cost option as compared to the peltier modules used by Liu et al.[39] and Shaw et al.[77] or the IR-laser used by Le Roux et al.,[40] though not a unique identifier for this instrument as compared to the literature.

The use of rapid-prototyping of polymer fluidics is an important aspect of this work as established in Chapter 2. Firstly, many of the literature PCR-CE instruments focus on the use of glass microfabrication, a method that inherently carries high material and development costs.[18] These instruments are therefore not suitable for resource-poor applications. Liu et al.,[39] Le Roux et al.[40] and Koh et al.[42] all utilise polymer fluidics that are either injection moulded or hot embossed. These are excellent technologies for high manufacturing volume, and in the future microfluidics for this project should leverage these techniques as well. However, in the development stage both injection moulding and hot embossing carry significant costs as each design change required new moulds.[24] This project used rapid-prototyping such that design changes could be readily implemented in-lab within an hour. Thus, while these other works have similar material costs and have microfluidics that can be mass produced, this approach enables faster iterations and

lower development costs.

The primary differentiator between this work and the literature is the LIF detection (as detailed in Chapters 3 and 4). Firstly, to the best of my knowledge this is the only PCR-CE instrument that uses LED excitation or absorption filters. Furthermore, most of the modules demonstrated use a confocal arrangement. As discussed in Section 1.3 and 3.1.1, the confocal module is both expensive and bulky. As such, one would expect the majority of the literature PCR-CE instruments to be comparable in cost to that of the Integen RapidHIT[65] in the $\$10^5$-$\$10^6$ range. There are three non-confocal designs presented. Shaw et al.[77] presents an instrument which uses a bifurcated optic fibre to both transmit the excitation light to the sample and collect the fluorescent light. This design would not be expected to have sufficient performance with poor collection efficiency of emission light (leading to poor expected LOD) and no limitation on spot-size (leading to poor expected resolution). It is telling that no detection assessment was performed in either of the groups published works on this subject.[77,78] Pan et al.[76] does not use a confocal design, but does use all the same high-end optical components to perform their detection. Thus, while possibly less expensive than other works this is still a decidedly high-cost optical solution. Finally, there is the previous work by the Backhouse group by Kaigala et al..[80] This design, described and pictured previously in Section 3.1.1 and Figure 3.1b, features a side-illuminating laser, a single interference filter and a GRIN lens for the lowest component count and detection cost of the cited literature works. However, in comparison the design presented in Chapter 3 is substantially lower cost with a total optical component cost (≈$87: $42/GRIN lens, $0.02/filter, $1.4/photodiode, $1.13/LED) less than either the filter or the laser used in Kaigala et al..[80] Furthermore, the use of a SIS LED as per Section 3.8.4 makes this instrument scalable to future designs while previous work was not.

		This work	Liu et al.[39] and Kagebayashi et al.[43]	Le Roux et al.[40]	Shaw et al.[77] and Docker et al.[78]	Scherer et al.[41]	Pan et al.[76]	Kaigala et al.[80]	Koh et al.[42]
Fluid Handling	Valve	Yes	No	No	No	Yes	No	Yes	Passive(gel)
	# Valves	24	N/A	7 pump channels	N/A	32	N/A	7	N/A
	Pumping	Peristalsis	None/manual	Syringe pump	None/manual	Peristalsis	None/manual	Peristalsis	None/manual
	HV	1 x 300 V supply, 2 channels	2+ x >2.2 kV	1 x 500 V, 1 x 3 kV	3 x 10 kV	3 x 1 kVsupply, 1 x 3 kV	6 x HV supply, 12 channels	1 x 6kV, 2 channels	1 x 2kV, 1 x 1kV
PCR	Heater	Resistive	Peltier	IR laser	Peltier	Resistive	Resistive	Resistive	Resistive
	Temp. Read	Thermocouple		IR thermometer	Thermocouple	Resistive	Resistive	Resistive	Thermocouple
Chip	Material	PMMA	Polycarbonate	COC	Glass	Glass	Glass	Glass	COC
	Method	Rapid prototyping	Injection moulded	Injection moulding	Photolith.	Photolith.	Photolith.	Photolith.	Hot embossed
Detection	Excitation	LED (500 nm, 1 mW)	Laser (532 nm)	Laser (200 mW)	Laser (488 nm, 25 mW)	Laser (488 nm, 75 mW)	Laser (473 nm, 20 mW)	Laser (635 nm, 5 mW)	Laser (288 nm)
	Detection	Photodiode	Photodiode	CCD	CCD	PMT	CCD	Photodiode	PMT
	Filtering	Absorption filters	Interference filters	Transmission Grating	Schott glass	Interference filters	Interference filters	Interference Filters	Interference filters
	Style	Staring-into-sun	Confocal	Fiber-optic coupled confocal optics	Bifurcated optic fibre	Confocal	Angular	Angular	Confocal
	LOD	750 pM (Section 3.8.4)	1.4 pM	-	-	30 pM	-	700 pM	-

Table 5.8: Comparison of this instrument with leading devices in the literature. The instrument presented here is the only instrument that combines LED illumination, photodiode detection and absorption filters for low-cost, scalable optics. Furthermore, this instrument has a full breadth of line of functionality including a valves, pumping, HV and thermal control. Thus, this instrument is unique in the field as the first low-cost testbed capable of performing the gold-standard PCR-CE methods

Chapter 6

Conclusion

6.1 Thesis Summary

This thesis describes the solution to key problems towards the implementation of a cost-accessible PCR-CE instrument, both in the short term development environment as well as future, integrated designs. The core issue in the development of PCR-CE instruments lies in the LIF detection, as current methods either are too expensive for cost-accessible instrumentation or do not meet the performance metrics required for reliable operation. The approach here was to develop the microfluidic technology (Chapter 2), optics (Chapter 3) and detection electronics (Chapter 4) such that each component that contributes to the fluorescent signal is low-cost and optimised for the application. These aspects were integrated with technical instrumentation (Appendix A) to form a series of instruments that were demonstrated with molecular biology applications in Chapter 5 culminating in the development of a next-generation instrument that contains all the functionality for PCR-CE at a prototype cost orders of magnitude lower than commercially available equipment. This instrument serves as a viable platform upon which future students can demonstrate the crucially important diagnostic protocols the world requires.

First, the development of rapid-prototyping methods for polymer microfluidic fabrication was described in Chapter 2, aiming at developing channels that are compatible with both high-performance CE sieving matrices and the short-working distance optics. Previous LOC instruments from the Backhouse group (for example the work by Kaigala et al.[80]) implemented their microfluidics with costly and time-consuming photolithography in glass. These designs, while having good performance, carried too high a material cost for resource-poor applications[18] and their high developmental cost led to long iteration times on the order of weeks preventing design optimisation. In comparison, the methods presented in this thesis can be completed within a couple hours and the material cost of the microfluidic chips is negligible. Attention to polymer fluidics also enables future use of high-throughput manufacturing (like injection moulding) after designs are optimised, potentially enabling commercial application of this technology in a manner that glass fabrication cannot achieve.[12] Two aspects were detailed in this chapter. Firstly, through successive improvements to technique and equipment a series of fabrication protocols for micromilled fluidics were developed, starting with large 381 μm channels and iterating down to 127 μm. These channels, while not quite meeting the 100 μm target

dimension, exhibited low surface roughness and high reproducibility and can be considered at or near the state of the art in the field of micromilled microfluidics. This technology was readily combined with agarose sieving matrices and was a workhorse for the Glerum molecular biology lab and the CE applications in Chapter 5. The fabrication also included a discussion of bonding techniques including a quick, but low-performance tape application and a solvent bonding technique. The solvent bonding had sufficient strength that it enabled the development of a next-generation fabrication technique for polymer fluidics. These new fluidics have laser ablated channels that are capped with solvent bonded PMMA which is then milled down by the CNC mill to enable compatibility with the optics. The result is a microfluidic chip with a dimension of 75 μm deep, 180 μm wide for a 0.8 nL sample and a capping layer of 85 μm, though there remains room for optimisation. To the best of my knowledge, these are the only microfluidic chips developed in polymer that can implement high-performance CE sieving matrices while having a thin-enough capping layer to be used with the low-cost optics in this thesis.

The bulk of this thesis concerns the development of low-cost, scalable LIF detection. This was accomplished by adhering to only scalable, low-cost optical components (LED, absorption filters, photodiode detection) and with substantial optimisation. Section 1.3.1 presented a reference model with a back of the envelope calculation suggesting that a LIF module based these design parameters would be expected to have detection performance nearly two orders of magnitude worse than required for PCR-CE applications. In response to this, Chapter 3 details the factors that go into low-cost optics design, refining the model and establishing the performance impact low-cost options have. This model enabled a number of optimisations and the development of the OPT4 design, featuring a cyan LED in a SIS arrangement with polymer absorption filters, GRIN lens light collection and an optimised pinhole. The result is a predicted signal of 56 fW from 100 μm channels and a spot-size of 134 μm. This is a factor of 5.6x improvement over the reference model in terms of signal, though the spot-size remains slightly above the 100 μm objective due to fabrication constraints at the time. More importantly, by adhering to scalable components and implementing SIS illumination this optics module can be directly scaled to more miniaturised designs. Thus, this model and optics design can be extended to devices that cannot be readily prototyped due to high NRE costs.

The optimised low-cost optics from Chapter 3 resulted in signals that were too faint to be detected with the reference detection electronics previously used by the Backhouse group.[84,85] Chapter 4 discusses aspects of circuit design for reading and amplifying signals. The DEV2 circuit presented improves upon the reference design by a factor of 24x through gain and BW optimisation, introduction of a Δ-Σ ADC for high-frequency noise attenuation, significant oversampling of the signal to perform time-domain noise reduction with a moving average filter and better assembly techniques. The circuit exhibited a stable baseline and was capable of detecting 42 fW of optical power, a value sufficient for sub-nM detection when combined with the optimised OPT4 optics from Chapter 3.

Chapter 5 details the integration of the various components to this project into a series of instruments that were demonstrated with CE applications. These applications targeted primarily LOD assessment and utilised robust, but lower-performance agarose as a sieving matrix. This allowed for the use of larger microchannels. This was important for the demonstration of the microfluidic iterations as techniques were refined and developed as well as boosting the signal for the early LIF module iterations that did not have as high performance. Notable works include the integration of low-cost LIF detection and valving to perform automated enzymatic digests and integration of a prototyping CMOS microelectronic chip with polymer fluidics. One of the most important demonstrations was the combination of the OPT3 optics and DEV1 detection electronics with the generation 2.5 microfluidics to demonstrate a 0.15 nM LOD

in 254 μm x 254 μm channels. As detailed in Section 5.4, this was demonstrated as the state of the art in low-cost LIF detection for CE and the first application of a LED and photodiode based optics module towards end-labelled DNA analysis. However, the resolution was expectedly poor due to the use of agarose. Scaling the channel to the required 100 μm to enable higher performance sieving matrices would reduce the signal and push the LOD above the 1 nM requirement, meaning that it does not meet the research objectives (though it would remain the state of the art published to date by a significant margin). This led to the development of the next-generation instrument, which integrates all of the best designs from this thesis for an estimated 0.75 nM LOD from 100 μm channels. Table 6.1 compares this LIF modules with previous designs demonstrated in the literature.

	OPT4+DEV2	Yang et al.[88]	Kaigala et al.[80]	Scherer et al.[41]
Excitation Source	LED, 1mW	LED, 1 W	Laser, 5 mW	Laser, 75 mW
Excitation Wavelength	500 nm	470 nm	635 nm	488 nm
Excitation Filter	Absorption	None	None	Interference
Emission Filter	Absorption	Interference	Interference	Interference
Optical Arrangement	Staring-into-the-sun (SIS)	Axial	Orthogonal	Confocal
LOD	0.75 nM	100 nM	0.7 nM	0.03 nM

Table 6.1: Comparison of the LIF module in this work with those in the industry. This design is substantially higher performance than the previous state of the art in low cost detection by Yang et al.,[88] while being much lower cost than the confocal optics like those in Scherer et al..[41] Comparing this module to previous designs by the Backhouse group, this work has a similar LOD at a lower cost. Furthermore, this module is fully scalable to a more miniaturised device as per Section 3.1.3, thus providing a testbed for future monolithic single-chip LOC instruments.

Comparing these works, it is clear the designs in this thesis are substantially lower cost. The GRIN lens used here retails for $42 /unit, while the filter material used costs about $0.02, the photodiode $1.4 and the LED $1.13 for a total optics prototype cost of about $87. This is much less than even a single interference filter (Chroma filters are priced at $325[152]), making it lower cost than any of the other works cited (all of which use at least one of these filters). In terms of performance, this module clearly bests the previously cited state of the art low-cost LIF detection for CE by Yang et al.[88] by two orders of magnitude. This LOD improvement is crucial as it pushes the instrument below the 1 nM threshold required for robust analysis of end-labelled DNA. Thus, while the LOD does not meet the performance of a conventional confocal like Scherer et al.,[41] it still has adequate detection for PCR-CE applications. Comparing this work with Kaigala et al.,[80] this design is more scalable (due to the LED, absorption filters and SIS arrangement) and lower-cost while maintaining nearly the same LOD. Therefore, not only does the LIF design enable cost-accessible instrumentation, but also solves a core issue towards the long-term objective of the Backhouse research group; by exceeding the LOD requirement with strictly scalable designs this instrument is a proof of concept that a monolithic, single-chip LOC design as per Figure 1.4b in the Introduction is feasible. Thus, future work can therefore be justified towards implementing these designs.

In addition to the improved LIF detection, this instrument also integrated all of the other technical instrumentation required for PCR-CE including HV generation and switching, thermal control and pneumatic valving. The instrument was also designed to be flexible, capable of accommodating a wide variety of fluidic and instrumentation functions.

Therefore, it provides a flexible based upon which future work can demonstrate a number of different applications. Compared to the other PCR-CE instruments in the literature and industry, this instrument is one of the most fully-featured available. More importantly, to the best of my knowledge it is the only device in the literature that contains low-cost optics, making it the first PCR-CE instrument that can be considered cost-accessible. Finally, adherence to scalable principles lends any application demonstrations additional commercial relevance. In the short term, development costs are minimised based on the low-cost instrument and the rapid-prototyped microfluidics from Chapter 2. As designs are finalised, the use of polymers ensures material compatibility with high-volume manufacturing processes such as injection moulding and hot embossing, fabrication methods that only become inexpensive when in bulk production. Finally, the use of fully scalable optics means that this instrument essentially operates as a testbed for future fully-monolithic LOC devices that can be made in a CMOS process. This instrument can therefore be considered the first step on a roadmap towards a truly paradigm shifting technology with controlled developmental costs, providing a path through the lab-on-chip manufacturing roadblock.

6.2 Contributions

The contributions of this thesis to the field can be summarised as follows:

- Developed a series of micromilling methods for direct-write patterning of microfluidic channels between 127 μm and 381 μm. These channels were reliably fabricated, had very short design to fabrication turnaround times and were applied to a number of applications both within this thesis and in the Glerum molecular biology group. Compared to the literature, this approach is at or near the state of the art and more completely described in Appendix B than even a recently published tutorial review.[24] However, the minimum channel dimension was limited by available tooling and machine parameters and did not quite meet the research objective of 100 μm.

- Developed a new fabrication method that combines laser ablation, solvent bonding and CNC milling to form 180 μm x 75 μm channels (0.8 nL CE samples) with a capping layer of 85 μm. These microfluidics are compatible with both high resolution CE sieving matrices and short working distance optics, satisfying the fabrication research objective for microfluidic fabrication. To the best of my knowledge, this process is unique to this work.

- Developed a refined model to estimate the fluorescence signal from the optical designs contained within this thesis. This model enables the tracking of performance trade-offs, optimisation of the design and extrapolation of the design to more miniaturised and integrated devices.

- Designed, built and tested a CE instrument that combined older optics and electronics with 254 μm rapid-prototyped fluidics to demonstrate a measured LOD of 0.15 nM of end-labelled DNA. This represents multiple orders of magnitude improved LOD over the previously cited state of the art in LIF detection for CE by Yang et al.[88] and the first demonstration in the literature of a LED and photodiode based optical design capable of standard DNA analysis with CE. However, due to the larger channels, agarose was required as the sieving matrix and the resolution of 43 bp did not meet the performance metric. Shrinking the channels for high-performance sieving matrices would result in a LOD above 1 nM, hence this demonstration did not quite meet the research objective.

- Developed and built a LIF detection module that is low-cost and meets all scalability constraints with a LOD of 0.75 nM, a spot-size of 134 μm and a bandwidth of 8-32 Hz (based on estimated parasitic capacitance). This meets almost all of the research objectives with the exception of spot-size, which is 34 μm too large. Nevertheless, this is, to the best of my knowledge, the only LIF detection module in the literature that adheres to the scalability constraints applied to CE, the best LIF detection performance achieved in the literature for CE samples with LED excitation and photodiode detection and the lowest cost LIF module capable of standard DNA analysis with CE.

- Designed and built a next-generation instrument in Section 5.5 featuring all of the required instrumentation for PCR-CE including: 24 pneumatic lines for implementing sufficient valves for extensive PCR-CE experiments and pumping, a thermal controller for a resistive heater and thermocouple compatible with the PCR demonstration in Section A.3, HV generation and switching with current measurement for CE and the aforementioned best LIF detection module (OPT4 optics + DEV2 electronics for 0.75 nM LOD in 100 μm channels). This satisfies the final research objective

In summary, this thesis satisfies nearly all of the research objectives from Section 1.4 with the exception of the spot-size, which requires improved fabrication methods to shrink slightly. As detailed in the body, due to the SIS arrangement of the optics the effect of the spot-size being larger than the channels is minimised and, depending on the separation protocol, might not even affect the instrument performance.

6.3 Future Work

There remains some future work that could be done to extend and complete this research project. These are separated according to the various chapters of this thesis:

For fabrication:

- Validate and refine the next-generation fabrication protocol detailed in Appendix C. Aspects that are not optimised are highlighted in this appendix.
- Apply this protocol to produce a series of PCR-CE devices. Suggested designs are in Appendix F and a design tool to simplify microfluidic design is included in the SI.

For optical design

- Refine the fabrication of the optics module such that the pinhole can be shrunk from 300 μm diameter to 224 μm. This would require a finer drill that was unavailable at the time of fabrication.

For detection electronics

- Measure the typical parasitic capacitance for the DEV2 design, increase gain to optimise on a 5 Hz BW for improved detection. This is only expected to introduce minor improvements to the detection.

- Introduce a discrete low-pass filter before the ADC to further attenuate high frequency noise components.
- Increase the oversampling of the signal to allow further noise suppression with post-processing. This is only expected to introduce minor improvements to the detection.
- Implement a lock-in amplifier design to enable gain that does not amplify all the Johnson noise.

Significant effort is also required to demonstrate applications of the next-generation instrument presented in this thesis. These demonstrations require molecular biology and thermal design expertise beyond the scope of this thesis and should include:

- Demonstrate the optical detection of PCR-primers using the same sample concentrations used previously[89] to validate the optical detection capabilities. This demonstration should be in miniaturised 100 μm x 100 μm channels.
- Develop CE protocols using high-performance sieving matrices based on this platform. Demonstrate for the first time sub-nM, sub-10bp CE separations with polymer fluidics and low-cost optics. This demonstration would be readily publishable due to the performance of the optics (as an extension of the state of the art designs from previous work[89]), implications of SIS optical design and novelty in the microfluidic fabrication.
- Develop an improved thermal design that fits within the specifications of the next generation instrument.
- Demonstrate a simple experiment that involves fluidic mixing and PCR. This would likely be publishable due to the use of the advanced valve (detailed in Appendix A) and rapid-prototyped fluidic processing methods.
- Demonstrate an integration of PCR and CE. This would be readily published as by far the lowest-instrumentation cost PCR-CE demonstration.
- Demonstrate an integration of PCR and CE with enzymatic digestion as per the applications in Chapter 5. This would be readily published and possibly a commercially relevant instrument.

Finally, this research was executed as part of a larger research project to develop a single-chip, monolithic LOC device where all of the instrumentation and fluidics are fabricated in the same CMOS process on the same substrate. Towards this goal, LIF detection was a particular problem as it essentially required completion of the entire device to test. Due to the developmental expense of doing so, this problem had not been solved. The OPT4 optics module developed in this thesis is fully scalable with comparable performance and component selection as a potential future device. Thus, following the demonstration of this optics module and validation of the LOD, the model developed here suggests that a CMOS design per Section 3.8.5 is entirely feasible. However, to implement this design a number of CMOS improvements are required, these include improved detection electronics (a factor of 20x improved over the prototype CMOS detailed in Section 4.2), an improved ADC (need over 14 effective bits of dynamic range for this application) and a number of fabrication challenges (particularly, how to deposit filter material). Nevertheless, this thesis provides a crucial proof of concept in terms of how such optical systems could be designed and built without paying the costly NRE price of CMOS development.

Bibliography

[1] World Health Organization, "WHO information for the molecular detection of influenza viruses," 2017. [Online]. Available: http://www.who.int/influenza/gisrs_laboratory/WHO_information_for_the_molecular_detection_of_influenza_viruses_20171023_Final.pdf

[2] J. M. Simpson, J. W. Santo Domingo, and D. J. Reasoner, "Microbial Source Tracking: State of the Science," *Environmental Science & Technology*, vol. 36, no. 24, pp. 5279–5288, dec 2002. [Online]. Available: http://pubs.acs.org/doi/abs/10.1021/es026000b

[3] T. Footz, M. J. Somerville, R. Tomaszewski, B. Elyas, and C. J. Backhouse, "Integration of combined heteroduplex/restriction fragment length polymorphism analysis on an electrophoresis microchip for the detection of hereditary haemochromatosis." *The Analyst*, vol. 129, no. 1, pp. 25–31, jan 2004. [Online]. Available: http://www.ncbi.nlm.nih.gov/pubmed/14737579

[4] D. Voet and J. G. Voet, *Biochemistry*, 3rd ed., H. David and F. Patrick, Eds. Hoboken: John Wiley & Sons Inc., 2004.

[5] S. A. Bustin, V. Benes, J. A. Garson, J. Hellemans, J. Huggett, M. Kubista, R. Mueller, T. Nolan, M. W. Pfaffl, G. L. Shipley, J. Vandesompele, and C. T. Wittwer, "The MIQE guidelines: minimum information for publication of quantitative real-time PCR experiments." *Clinical chemistry*, vol. 55, no. 4, pp. 611–22, apr 2009. [Online]. Available: http://www.ncbi.nlm.nih.gov/pubmed/19246619

[6] R. A. King, D. S. Read, M. Traugott, and W. O. C. Symondson, "Molecular analysis of predation: A review of best practice for DNA-based approaches," *Molecular Ecology*, vol. 17, no. 4, pp. 947–963, 2008.

[7] IBISWorld, "62151 - Diagnostic & Medical Laboratories in the US," 2016. [Online]. Available: www.ibisworld.ca

[8] I. M. Longini, "Containing Pandemic Influenza at the Source," *Science*, vol. 309, no. 5737, pp. 1083–1087, aug 2005. [Online]. Available: http://www.sciencemag.org/cgi/doi/10.1126/science.1115717

[9] P. Yager, T. Edwards, E. Fu, K. Helton, K. Nelson, M. R. Tam, and B. H. Weigl, "Microfluidic diagnostic technologies for global public health," *Nature*, vol. 442, no. 7101, pp. 412–418, jul 2006. [Online]. Available: http://www.nature.com/doifinder/10.1038/nature05064

[10] T. Maxson and D. A. Mitchell, "Targeted treatment for bacterial infections: prospects for pathogen-specific antibiotics coupled with rapid diagnostics," *Tetrahedron*, vol. 72, no. 25, pp. 3609–3624, jun 2016.

[11] R. Laxminarayan, A. J. Mills, J. G. Breman, A. R. Measham, G. Alleyne, M. Claeson, P. Jha, P. Musgrove, J. Chow, S. Shahid-Salles, and D. T. Jamison, "Advancement of global health: key messages from the Disease Control Priorities Project," *The Lancet*, vol. 367, no. 9517, pp. 1193–1208, apr 2006. [Online]. Available: http://linkinghub.elsevier.com/retrieve/pii/S0140673606684407

[12] C. D. Chin, V. Linder, and S. K. Sia, "Commercialization of microfluidic point-of-care diagnostic devices," *Lab on a Chip*, vol. 12, no. 12, p. 2118, jun 2012. [Online]. Available: http://xlink.rsc.org/?DOI=c2lc21204h

[13] P. Yager, G. J. Domingo, and J. Gerdes, "Point-of-care diagnostics for global health." *Annual review of biomedical engineering*, vol. 10, no. 1, pp. 107–44, aug 2008. [Online]. Available: http://www.ncbi.nlm.nih.gov/pubmed/18358075

[14] K. Yamada, H. Shibata, K. Suzuki, and D. Citterio, "Toward practical application of paper-based microfluidics for medical diagnostics: state-of-the-art and challenges," *Lab on a Chip*, vol. 17, no. 7, pp. 1206–1249, 2017. [Online]. Available: http://xlink.rsc.org/?DOI=C6LC01577H

[15] Y. Wang, L. Ge, P. Wang, M. Yan, S. Ge, N. Li, J. Yu, and J. Huang, "Photoelectrochemical lab-on-paper device equipped with a porous Au-paper electrode and fluidic delay-switch for sensitive detection of DNA hybridization," *Lab on a Chip*, vol. 13, no. 19, p. 3945, 2013. [Online]. Available: http://xlink.rsc.org/?DOI=c3lc50430a

[16] G. G. Morbioli, T. Mazzu-Nascimento, A. M. Stockton, and E. Carrilho, "Technical aspects and challenges of colorimetric detection with microfluidic paper-based analytical devices (μPADs) - A review," *Analytica Chimica Acta*, vol. 970, pp. 1–22, jun 2017. [Online]. Available: http://dx.doi.org/10.1016/j.aca.2017.03.037

[17] A. Manz, N. Graber, and H. Widmer, "Miniaturized total chemical analysis systems: A novel concept for chemical sensing," *Sensors and Actuators B: Chemical*, vol. 1, no. 1-6, pp. 244–248, jan 1990.

[18] H. Becker and C. Gärtner, "Polymer microfabrication technologies for microfluidic systems," *Analytical and Bioanalytical Chemistry*, vol. 390, no. 1, pp. 89–111, jan 2008. [Online]. Available: http://link.springer.com/10.1007/s00216-007-1692-2

[19] H. Becker and L. E. Locascio, "Polymer microfluidic devices," *Talanta*, vol. 56, no. 2, pp. 267–287, feb 2002. [Online]. Available: http://linkinghub.elsevier.com/retrieve/pii/S003991400100594X

[20] D. Lipomi, R. Martinez, L. Cademartiri, and G. Whitesides, "Soft Lithographic Approaches to Nanofabrication," in *Polymer Science: A Comprehensive Reference*. Elsevier, 2012, vol. 7, pp. 211–231. [Online]. Available: http://dx.doi.org/10.1016/B978-0-444-53349-4.00180-1

[21] J. C. McDonald, D. C. Duffy, J. R. Anderson, D. T. Chiu, H. Wu, O. J. A. Schueller, and G. M. Whitesides, "Fabrication of microfluidic systems in poly(dimethylsiloxane)," *Electrophoresis*, vol. 21, no. 1, pp. 27–40, jan 2000.

[22] N. Bhattacharjee, A. Urrios, S. Kang, and A. Folch, "The upcoming 3D-printing revolution in microfluidics," *Lab Chip*, vol. 16, no. 10, pp. 1720–1742, 2016. [Online]. Available: http://xlink.rsc.org/?DOI=C6LC00163G

[23] Microfluidic ChipShop GmbH, "Microfluidic ChipShop," 2017. [Online]. Available: http://www.microfluidic-chipshop.com/index.php

[24] D. J. Guckenberger, T. E. de Groot, A. M.-D. D. Wan, D. J. Beebe, and E. W. K. Young, "Micromilling: a method for ultra-rapid prototyping of plastic microfluidic devices," *Lab on a Chip*, vol. 15, no. 11, pp. 2364–2378, 2015. [Online]. Available: http://xlink.rsc.org/?DOI=C5LC00234F

[25] R. C. McGlennen, "Miniaturization technologies for molecular diagnostics," *Clinical Chemistry*, vol. 47, no. 3, pp. 393–402, 2001.

[26] E. R. Castro and A. Manz, "Present state of microchip electrophoresis: State of the art and routine applications," *Journal of Chromatography A*, vol. 1382, pp. 66–85, feb 2015. [Online]. Available: http://dx.doi.org/10.1016/j.chroma.2014.11.034

[27] L. García-Carmona, A. Martín, T. Sierra, M. C. González, and A. Escarpa, "Electrochemical detectors based on carbon and metallic nanostructures in capillary and microchip electrophoresis," *Electrophoresis*, vol. 38, no. 1, pp. 80–94, jan 2017. [Online]. Available: http://doi.wiley.com/10.1002/elps.201600232

[28] P. Kubá and P. C. Hauser, "Contactless conductivity detection for analytical techniques- Developments from 2014 to 2016," *Electrophoresis*, vol. 38, no. 1, pp. 95–114, jan 2017. [Online]. Available: http://doi.wiley.com/10.1002/elps.201600280

[29] L. Hernandez and J. Escalona, "Laser-induced fluorescence and fluorescence microscopy for capillary electrophoresis zone detection," *Journal of Chromatography*, vol. 559, pp. 183–196, 1991. [Online]. Available: http://www.sciencedirect.com/science/article/pii/002196739180069S

[30] T. Hirschfeld, "Optical microscopic observation of single small molecules," *Applied Optics*, vol. 15, no. 12, pp. 2965–2966, dec 1976. [Online]. Available: http://www.ncbi.nlm.nih.gov/pubmed/20168369

[31] Life Technologies, "DNA Fragment Analysis by Capillary Electrophoresis," 2014. [Online]. Available: http://tools.thermofisher.com/content/sfs/manuals/4474504.pdf

[32] Cepheid, "GeneXpert® Omni," 2017. [Online]. Available: http://www.cepheid.com/administrator/components/com_productcatalog/library-files/582440bdfd052a99174a022a7c1af8d8-GeneXpert-Omni-PreRelease-US-0518-02.pdf

[33] BioFire Diagnostics, "FilmArray," 2017. [Online]. Available: http://www.biofiredx.com/products/filmarray/

[34] Roche Diagnostics USA, "cobas Liat PCR System," 2015. [Online]. Available: https://usdiagnostics.roche.com/en/instrument/cobas-liat.html#overview

[35] BioCartis, "BioCartis," 2017. [Online]. Available: https://biocartis.com/

[36] Becton Dickinson and Company, "BD MAX System," 2017. [Online]. Available: http://moleculardiagnostics.bd.com/product/max/

[37] Verdus Laboratories, "Verdus Laboratories," 2017. [Online]. Available: http://vereduslabs.com/

[38] GenePOC, "GenePOC," 2017. [Online]. Available: http://www.genepoc-diagnostics.com/about/

[39] Y. Liu, C. Li, Z. Li, S. D. Chan, D. Eto, W. Wu, J. P. Zhang, R.-L. Chien, H. G. Wada, M. Greenstein, and S. Satomura, "On-chip quantitative PCR using integrated real-time detection by

capillary electrophoresis," *ELECTROPHORESIS*, vol. 37, no. 3, pp. 545–552, feb 2016. [Online]. Available: http://doi.wiley.com/10.1002/elps.201500298

[40] D. Le Roux, B. E. Root, J. A. Hickey, O. N. Scott, A. Tsuei, J. Li, D. J. Saul, L. Chassagne, J. P. Landers, and P. de Mazancourt, "An integrated sample-in-answer-out microfluidic chip for rapid human identification by STR analysis," *Lab Chip*, vol. 14, no. 22, pp. 4415–4425, sep 2014. [Online]. Available: http://xlink.rsc.org/?DOI=C4LC00685B

[41] J. R. Scherer, P. Liu, and R. A. Mathies, "Design and operation of a portable scanner for high performance microchip capillary array electrophoresis," *Review of Scientific Instruments*, vol. 81, no. 11, p. 113105, nov 2010. [Online]. Available: http://aip.scitation.org/doi/10.1063/1.3502457

[42] C. G. Koh, W. Tan, M.-q. Zhao, A. J. Ricco, and Z. H. Fan, "Integrating Polymerase Chain Reaction, Valving, and Electrophoresis in a Plastic Device for Bacterial Detection," *Analytical Chemistry*, vol. 75, no. 17, pp. 4591–4598, sep 2003. [Online]. Available: http://pubs.acs.org/doi/abs/10.1021/ac0343836

[43] C. Kagebayashi, I. Yamaguchi, A. Akinaga, H. Kitano, K. Yokoyama, M. Satomura, T. Kurosawa, M. Watanabe, T. Kawabata, W. Chang, C. Li, L. Bousse, H. G. Wada, and S. Satomura, "Automated immunoassay system for AFPL3% using on-chip electrokinetic reaction and separation by affinity electrophoresis," *Analytical Biochemistry*, vol. 388, no. 2, pp. 306–311, may 2009. [Online]. Available: http://dx.doi.org/10.1016/j.ab.2009.02.030

[44] M. Dandin, P. Abshire, and E. Smela, "Optical filtering technologies for integrated fluorescence sensors," *Lab on a Chip*, vol. 7, no. 8, p. 955, aug 2007. [Online]. Available: http://xlink.rsc.org/?DOI=b704008c

[45] S. Nayak, N. R. Blumenfeld, T. Laksanasopin, and S. K. Sia, "Point-of-Care Diagnostics: Recent Developments in a Connected Age," *Analytical Chemistry*, vol. 89, no. 1, pp. 102–123, jan 2017. [Online]. Available: http://pubs.acs.org/doi/abs/10.1021/acs.analchem.6b04630

[46] M. Behnam, G. V. Kaigala, M. Khorasani, P. Marshall, C. J. Backhouse, and D. G. Elliott, "An integrated CMOS high voltage supply for lab-on-a-chip systems." *Lab on a chip*, vol. 8, no. 9, pp. 1524–9, sep 2008. [Online]. Available: http://www.ncbi.nlm.nih.gov/pubmed/18818808

[47] M. Behnam, G. Kaigala, M. Khorasani, S. Martel, D. Elliott, and C. Backhouse, "Integrated circuit-based instrumentation for microchip capillary electrophoresis," *IET Nanobiotechnology*, vol. 4, no. 3, p. 91, sep 2010. [Online]. Available: http://www.ncbi.nlm.nih.gov/pubmed/20726675

[48] G. H. Hall, D. L. Sloan, T. Ma, M. H. Couse, S. Martel, D. G. Elliott, D. M. Glerum, and C. J. Backhouse, "An optical relay approach to very low cost hybrid polymer-complementary metal-oxide semiconductor electrophoresis instrumentation," *Journal of Chromatography A*, vol. 1349, pp. 122–128, jul 2014. [Online]. Available: http://www.ncbi.nlm.nih.gov/pubmed/24856905

[49] D. L. Sloan, G. H. Hall, C. J. Backhouse, and D. G. Elliott, "300 V integrated charge pump for lab on chip applications," in *14th IEEE International Conference on Nanotechnology*. IEEE, aug 2014, pp. 939–942. [Online]. Available: http://ieeexplore.ieee.org/lpdocs/epic03/wrapper.htm?arnumber=6968182

[50] L. Gutierrez-Rivera, J. Martinez-Quijada, R. Johnstone, D. Elliott, C. Backhouse, and D. Sameoto, "Multilayer bonding using a conformal adsorbate film (CAF) for the fabrication of 3D monolithic

microfluidic devices in photopolymer," *Journal of Micromechanics and Microengineering*, vol. 22, no. 8, p. 85018, aug 2012. [Online]. Available: http://stacks.iop.org/0960-1317/22/i=8/a=085018?key=crossref.997f2953f4cfbb1e2a945e564aec9ffa

[51] H. Becker, "One size fits all?" *Lab on a Chip*, vol. 10, no. 15, p. 1894, 2010. [Online]. Available: http://xlink.rsc.org/?DOI=c005380p

[52] J. F. Huggett, S. Cowen, and C. A. Foy, "Considerations for Digital PCR as an Accurate Molecular Diagnostic Tool," *Clinical Chemistry*, vol. 61, no. 1, pp. 79–88, jan 2015. [Online]. Available: http://www.clinchem.org/cgi/doi/10.1373/clinchem.2014.221366

[53] J. Martinez-Quijada, T. Ma, G. H. Hall, M. Reynolds, D. Sloan, S. Caverhill-Godkewitsch, D. M. Glerum, D. Sameoto, D. G. Elliott, and C. J. Backhouse, "Robust thermal control for CMOS-based lab-on-chip systems," *Journal of Micromechanics and Microengineering*, vol. 25, no. 7, p. 075005, jul 2015. [Online]. Available: http://stacks.iop.org/0960-1317/25/i=7/a=075005?key=crossref.0c704a48ed6fe9720f303b4f01ee0b93

[54] J. P. Landers, Ed., *Capillary and Microchip Electrophoresis and Associated Microtechniques*, 3rd ed. Boca Raton: Taylor & Francis Group, LLC, 1997.

[55] Thermo Fisher Scientific Inc., "Applied Biosystems SeqStudio Genetic Analyzer," 2017. [Online]. Available: https://www.thermofisher.com/ca/en/home/life-science/sequencing/sanger-sequencing/sanger-sequencing-technology-accessories/seqstudio-genetic-analyzer.html

[56] D. P. Manage, D. G. Elliott, and C. J. Backhouse, "Millimeter scale separation of DNA with a replaceable polymer matrix." *Electrophoresis*, vol. 33, no. 21, pp. 3213–3221, nov 2012. [Online]. Available: http://www.ncbi.nlm.nih.gov/pubmed/23027089

[57] New England BioLabs Inc, "PCR Protocol for Taq DNA Polymerase with Standard Taq Buffer (M0273)," 2017. [Online]. Available: https://www.neb.com/protocols/1/01/01/taq-dna-polymerase-with-standard-taq-buffer-m0273

[58] J. Hadfield, "Index mis-assignment between samples on HiSeq 4000 and X-Ten," 2016. [Online]. Available: http://enseqlopedia.com/2016/12/index-mis-assignment-between-samples-on-hiseq-4000-and-x-ten/

[59] V. M. Ugaz, R. D. Elms, R. C. Lo, F. a. Shaikh, and M. a. Burns, "Microfabricated electrophoresis systems for DNA sequencing and genotyping applications: current technology and future directions." *Philosophical transactions. Series A, Mathematical, physical, and engineering sciences*, vol. 362, no. 1818, pp. 1105–1129, 2004.

[60] V. M. Ugaz, R. Lin, N. Srivastava, D. T. Burke, and M. a. Burns, "A versatile microfabricated platform for electrophoresis of double- and single-stranded DNA." *Electrophoresis*, vol. 24, no. 1-2, pp. 151–7, 2003. [Online]. Available: http://www.ncbi.nlm.nih.gov/pubmed/12652585

[61] Alere, "Alere i Influenza A & B," 2016. [Online]. Available: http://www.alere.com/en/home/product-details/alere-i-influenza-ab.html

[62] F. S. Nolte, L. Gauld, and S. B. Barrett, "Direct Comparison of Alere i and cobas Liat Influenza A and B

Tests for Rapid Detection of Influenza Virus Infection," *Journal of Clinical Microbiology*, vol. 54, no. 11, pp. 2763–2766, nov 2016. [Online]. Available: http://jcm.asm.org/lookup/doi/10.1128/JCM.01586-16

[63] K. C. Chapin and E. J. Flores-Cortez, "Performance of the Molecular Alere i Influenza A & B Test Compared to That of the Xpert Flu A/B Assay," *Journal of Clinical Microbiology*, vol. 53, no. 2, pp. 706–709, feb 2015. [Online]. Available: http://jcm.asm.org/lookup/doi/10.1128/JCM.02783-14

[64] U.S. Food and Drug Administration, "Class 2 Device Recall Alere i Influenza A & B," 2015. [Online]. Available: https://www.accessdata.fda.gov/scripts/cdrh/cfdocs/cfres/res.cfm?id=135960

[65] IntegenX, "RapidHIT System," 2017. [Online]. Available: https://integenx.com/rapidhit-system/

[66] V. Figarelli, "The Arizona DPS Rapid DNA Program," 2014. [Online]. Available: https://integenx.com/wp-content/uploads/2014/08/Figarelli-ASCLD-Rapid-DNA_2014.pdf

[67] M. A. Burns, B. N. Johnson, S. N. Brahmasandra, K. Handique, J. R. Webster, M. Krishnan, T. S. Sammarco, P. M. Man, D. Jones, D. Heldsinger, C. H. Mastrangelo, and D. T. Burke, "An integrated nanoliter DNA analysis device." *Science (New York, N.Y.)*, vol. 282, no. October, pp. 484–487, 1998.

[68] J. R. Webster, M. A. Burns, D. T. Burke, and C. H. Mastrangelo, "Monolithic Capillary Electrophoresis Device with Integrated Fluorescence Detector," *Analytical Chemistry*, vol. 73, no. 7, pp. 1622–1626, apr 2001. [Online]. Available: http://pubs.acs.org/doi/abs/10.1021/ac0004512

[69] V. Namasivayam, R. Lin, B. Johnson, S. Brahmasandra, Z. Razzacki, D. T. Burke, and M. A. Burns, "Advances in on-chip photodetection for applications in miniaturized genetic analysis systems," *Journal of Micromechanics and Microengineering*, vol. 14, no. 1, pp. 81–90, jan 2004. [Online]. Available: http://stacks.iop.org/0960-1317/14/i=1/a=311?key=crossref.2eb189169fd75905fb4e167871a17e36

[70] E. T. Lagally, P. C. Simpson, and R. A. Mathies, "Monolithic integrated microfluidic DNA amplification and capillary electrophoresis analysis system," *Sensors and Actuators, B: Chemical*, vol. 63, no. 3, pp. 138–146, may 2000. [Online]. Available: http://linkinghub.elsevier.com/retrieve/pii/S0925400500003506

[71] E. T. Lagally, I. Medintz, and R. A. Mathies, "Single-Molecule DNA Amplification and Analysis in an Integrated Microfluidic Device," *Analytical Chemistry*, vol. 73, no. 3, pp. 565–570, feb 2001. [Online]. Available: http://pubs.acs.org/doi/abs/10.1021/ac001026b

[72] E. T. Lagally, C. A. Emrich, and R. A. Mathies, "Fully integrated PCR-capillary electrophoresis microsystem for DNA analysis," *Lab on a Chip*, vol. 1, no. 2, p. 102, 2001. [Online]. Available: http://xlink.rsc.org/?DOI=b109031n

[73] W. H. Grover, A. M. Skelley, C. N. Liu, E. T. Lagally, and R. A. Mathies, "Monolithic membrane valves and diaphragm pumps for practical large-scale integration into glass microfluidic devices," *Sensors and Actuators B: Chemical*, vol. 89, no. 3, pp. 315–323, apr 2003. [Online]. Available: http://linkinghub.elsevier.com/retrieve/pii/S0925400502004689

[74] P. Liu, X. Li, S. a. Greenspoon, J. R. Scherer, and R. A. Mathies, "Integrated DNA purification, PCR, sample cleanup, and capillary electrophoresis microchip for forensic human identification," *Lab on a Chip*, vol. 11, no. 6, p. 1041, 2011. [Online]. Available: http://xlink.rsc.org/?DOI=c0lc00533a

[75] R. A. Mathies, J. Bada, and F. Grunthaner, "Microfabricated Organic Analyzer (MOA) for in situ Exploration of Mars and other Solar Bodies." [Online]. Available: http://astrobiology.berkeley.edu/PDFs_present/RMBoulder.pdf

[76] X. Pan, L. Jiang, K. Liu, B. Lin Bingcheng, and J. Qin Jianhua, "A microfluidic device integrated with multichamber polymerase chain reaction and multichannel separation for genetic analysis," *Analytica Chimica Acta*, vol. 674, no. 1, pp. 110–115, 2010. [Online]. Available: http://dx.doi.org/10.1016/j.aca.2010.06.005

[77] K. J. Shaw, D. A. Joyce, P. T. Docker, C. E. Dyer, G. M. Greenway, J. Greenman, and S. J. Haswell, "Development of a real-world direct interface for integrated DNA extraction and amplification in a microfluidic device," *Lab Chip*, vol. 11, no. 3, pp. 443–448, 2011. [Online]. Available: http://xlink.rsc.org/?DOI=C0LC00346H

[78] P. T. Docker, J. Baker, and S. J. Haswell, "Fast Track DNA Analysis Suite for human identification," *PeerJ PrePrints*, vol. 1, no. e6v1, 2013.

[79] A. K. Au, H. Lai, B. R. Utela, and A. Folch, "Microvalves and Micropumps for BioMEMS," *Micromachines*, vol. 2, no. 4, pp. 179–220, may 2011. [Online]. Available: http://www.mdpi.com/2072-666X/2/2/179/

[80] G. V. Kaigala, M. Behnam, A. C. E. Bidulock, C. Bargen, R. W. Johnstone, D. G. Elliott, and C. J. Backhouse, "A scalable and modular lab-on-a-chip genetic analysis instrument," *The Analyst*, vol. 135, no. 7, p. 1606, jul 2010. [Online]. Available: http://xlink.rsc.org/?DOI=b925111a

[81] M. Macka, T. Piasecki, and P. K. Dasgupta, "Light-Emitting Diodes for Analytical Chemistry," *Annual Review of Analytical Chemistry*, vol. 7, no. 1, pp. 183–207, jun 2014. [Online]. Available: http://www.annualreviews.org/doi/abs/10.1146/annurev-anchem-071213-020059

[82] T. Datta-Chaudhuri, E. Smela, and P. A. Abshire, "System-on-Chip Considerations for Heterogeneous Integration of CMOS and Fluidic Bio-Interfaces," *IEEE Transactions on Biomedical Circuits and Systems*, vol. 10, no. 6, pp. 1129–1142, dec 2016. [Online]. Available: http://ieeexplore.ieee.org/document/7456210/

[83] Burr-Brown, "Designing Photodiode Amplifier Circuits with OPA128," 1994. [Online]. Available: http://www.ti.com/lit/an/sboa061/sboa061.pdf

[84] A. C. E. Bidulock, "Scalable, Modular, Integrated Genetic Analysis Systems," MSc, University of Alberta, 2011.

[85] G. Kaigala, M. Behnam, C. Bliss, M. Khorasani, S. Ho, J. McMullin, D. Elliott, and C. Backhouse, "Inexpensive, universal serial bus-powered and fully portable lab-on-a-chip-based capillary electrophoresis instrument," *IET Nanobiotechnology*, vol. 3, no. 1, p. 1, 2009. [Online]. Available: http://ieeexplore.ieee.org/Xplore/login.jsp?url=/iel5/4123961/4531111/04531112.pdf?arnumber=4531112

[86] D. Xiao, L. Yan, H. Yuan, S. Zhao, X. Yang, and M. M. F. Choi, "CE with LED-based detection: An update," *Electrophoresis*, vol. 30, no. 1, pp. 189–202, jan 2009. [Online]. Available: http://doi.wiley.com/10.1002/elps.200800415

[87] S. Götz and U. Karst, "Recent developments in optical detection methods for microchip separations,"

Analytical and Bioanalytical Chemistry, vol. 387, no. 1, pp. 183–192, dec 2006. [Online]. Available: http://link.springer.com/10.1007/s00216-006-0820-8

[88] F. Yang, X.-C. Li, W. Zhang, J.-B. Pan, and Z.-G. Chen, "A facile light-emitting-diode induced fluorescence detector coupled to an integrated microfluidic device for microchip electrophoresis," *Talanta*, vol. 84, no. 4, pp. 1099–1106, may 2011. [Online]. Available: http://dx.doi.org/10.1016/j.talanta.2011.03.020

[89] G. H. Hall, D. M. Glerum, and C. J. Backhouse, "Light emitting diode, photodiode-based fluorescence detection system for DNA analysis with microchip electrophoresis," *Electrophoresis*, vol. 37, no. 3, pp. 406–413, feb 2016. [Online]. Available: http://doi.wiley.com/10.1002/elps.201500355

[90] H. Becker and C. Gärtner, "Polymer microfabrication methods for microfluidic analytical applications." *Electrophoresis*, vol. 21, no. 1, pp. 12–26, jan 2000. [Online]. Available: http://www.ncbi.nlm.nih.gov/pubmed/10634467

[91] D. Le Roux, B. E. Root, J. A. Hickey, O. N. Scott, A. Tsuei, J. Li, D. J. Saul, L. Chassagne, J. P. Landers, and P. de Mazancourt, "An integrated sample-in-answer-out microfluidic chip for rapid human identification by STR analysis," *Lab Chip*, vol. 14, no. 22, pp. 4415–4425, sep 2014. [Online]. Available: http://xlink.rsc.org/?DOI=C4LC00685B

[92] P. N. Nge, C. I. Rogers, and A. T. Woolley, "Advances in microfluidic materials, functions, integration, and applications," *Chemical Reviews*, vol. 113, no. 4, pp. 2550–2583, apr 2013. [Online]. Available: http://pubs.acs.org/doi/abs/10.1021/cr300337x

[93] B. Lu, S. Zheng, B. Q. Quach, and Y.-C. Tai, "A study of the autofluorescence of parylene materials for uTAS applications," *Lab on a Chip*, vol. 10, no. 14, p. 1826, 2010. [Online]. Available: http://xlink.rsc.org/?DOI=b924855b

[94] T. F. Hong, W. J. Ju, M. C. Wu, C. H. Tai, C. H. Tsai, and L. M. Fu, "Rapid prototyping of PMMA microfluidic chips utilizing a CO2 laser," *Microfluidics and Nanofluidics*, vol. 9, no. 6, pp. 1125–1133, 2010.

[95] J. a. Lounsbury, B. L. Poe, M. Do, and J. P. Landers, "Laser-ablated poly(methyl methacrylate) microdevices for sub-microliter DNA amplification suitable for micro-total analysis systems," *Journal of Micromechanics and Microengineering*, vol. 22, no. 8, p. 085006, aug 2012. [Online]. Available: http://stacks.iop.org/0960-1317/22/i=8/a=085006?key=crossref.ffcd6d3b8cd3163136a1f9882844dac2

[96] T. Ma, V. Northrup, A. O. Fung, D. M. Glerum, and C. J. Backhouse, "Polymeric rapid prototyping for inexpensive and portable medical diagnostics," in *Proc. SPIE*, J.-C. Kieffer, Ed., vol. 8412, no. 519, oct 2012, p. 84120B. [Online]. Available: http://proceedings.spiedigitallibrary.org/proceeding.aspx?articleid=1387270

[97] A. Manz, J. Fettinger, E. Verpoorte, H. Lüdi, H. Widmer, and D. Harrison, "Micromachining of monocrystalline silicon and glass for chemical analysis systems A look into next century's technology or just a fashionable craze?" *TrAC Trends in Analytical Chemistry*, vol. 10, no. 5, pp. 144–149, may 1991. [Online]. Available: http://linkinghub.elsevier.com/retrieve/pii/0165993691851169

[98] Bio-Rad Laboratories Inc., "Experion Automated Electrophoresis System," 2018. [Online]. Available: http://www.bio-rad.com/webroot/web/pdf/lsr/literature/Bulletin_3140.pdf

[99] Medimate, "uChip CE," 2013. [Online]. Available: https://www.medimate.com/en/μchip-ce

[100] Perkin Elmer, "LabChip Microfluidics Product Note," 2015. [Online]. Available: http://www.perkinelmer.ca/en-ca/CMSResources/Images/44-161587PRD_LabChip-GX-Touch-DNA-Assays.pdf

[101] M. L. Kovarik, P. C. Gach, D. M. Ornoff, Y. Wang, J. Balowski, L. Farrag, and N. L. Allbritton, "Micro Total Analysis Systems for Cell Biology and Biochemical Assays," *Analytical Chemistry*, vol. 84, no. 2, pp. 516–540, jan 2012. [Online]. Available: http://pubs.acs.org/doi/abs/10.1021/ac202611x

[102] I. R. G. Ogilvie, V. J. Sieben, B. Cortese, M. C. Mowlem, and H. Morgan, "Chemically resistant microfluidic valves from Viton®membranes bonded to COC and PMMA." *Lab on a chip*, vol. 11, no. 14, pp. 2455–2459, 2011. [Online]. Available: http://www.ncbi.nlm.nih.gov/pubmed/21617822

[103] T. D. Boone, Z. H. Fan, H. H. Hooper, A. J. Ricco, H. Tan, and S. J. Williams, "Plastic advances microfluidic devices." *Analytical chemistry*, vol. 74, no. 3, pp. 78A–86A, 2002.

[104] A. Waldbaur, H. Rapp, K. Länge, and B. E. Rapp, "Let there be chiptowards rapid prototyping of microfluidic devices: one-step manufacturing processes," *Analytical Methods*, vol. 3, no. 12, p. 2681, 2011. [Online]. Available: http://xlink.rsc.org/?DOI=c1ay05253e

[105] A. K. Au, W. Huynh, L. F. Horowitz, and A. Folch, "3D-Printed Microfluidics," *Angewandte Chemie - International Edition*, vol. 55, no. 12, pp. 3862–3881, 2016.

[106] H. Gong, M. Beauchamp, S. Perry, A. T. Woolley, and G. P. Nordin, "Optical approach to resin formulation for 3D printed microfluidics," *RSC Adv.*, vol. 5, no. 129, pp. 106 621–106 632, 2015. [Online]. Available: http://xlink.rsc.org/?DOI=C5RA23855B

[107] D. K. Walburger, I. A. Afonina, and R. Wydro, "An improved real time PCR method for simultaneous detection of C282Y and H63D mutations in the HFE gene associated with hereditary hemochromatosis." *Mutation research*, vol. 432, no. 3-4, pp. 69–78, jan 2001. [Online]. Available: http://www.ncbi.nlm.nih.gov/pubmed/11465544

[108] C. F. Chen, J. Liu, L. P. Hromada, C. W. Tsao, C. C. Chang, and D. L. DeVoe, "High-pressure needle interface for thermoplastic microfluidics." *Lab on a chip*, vol. 9, no. 1, pp. 50–5, 2009. [Online]. Available: http://www.ncbi.nlm.nih.gov/pubmed/19209335

[109] O. D. Rahmanian and D. L. DeVoe, "Single-use thermoplastic microfluidic burst valves enabling on-chip reagent storage," *Microfluidics and Nanofluidics*, vol. 18, no. 5-6, pp. 1045–1053, may 2015. [Online]. Available: http://dx.doi.org/10.1007/s10404-014-1494-8

[110] D. Chen, M. Mauk, X. Qiu, C. Liu, J. Kim, S. Ramprasad, S. Ongagna, W. R. Abrams, D. Malamud, P. L. A. M. Corstjens, and H. H. Bau, "An integrated, self-contained microfluidic cassette for isolation, amplification, and detection of nucleic acids," *Biomedical Microdevices*, vol. 12, no. 4, pp. 705–719, aug 2010. [Online]. Available: http://link.springer.com/10.1007/s10544-010-9423-4

[111] J. C. Bowman and A. Hammerlindl, "Asymptote: The Vector Graphics Language," *TUGboat*, vol. 29, no. 2, pp. 288–294, 2008. [Online]. Available: http://www.tug.org/TUGboat/tb29-2/tb92bowman.pdf

[112] R. Grzesek, "How to Choose a Stepover," 2017. [Online]. Available: http://www.grzsoftware.com/blog/how-to/choose-stepover/

[113] Microscopy U, "Depth of Field and Depth of Focus," 2017. [Online]. Available: https://www.microscopyu.com/microscopy-basics/depth-of-field-and-depth-of-focus

[114] B. Warfield, "Enjoy CNC Micromachining & Micro-Cutter Success: Easy Guide," 2017. [Online]. Available: http://s3.cnccookbook.com/CCCNCMillFeedsSpeedsMicroMachining.htm

[115] G. H. Hall, T. Ma, M. H. Couse, S. Hume, D. L. Sloan, D. G. Elliott, D. M. Glerum, and C. J. Backhouse, "An automated hand-held CMOS-based instrument for hand-held mutation detection via electrophoresis," in *14th IEEE International Conference on Nanotechnology*. IEEE, aug 2014, pp. 8–12. [Online]. Available: http://ieeexplore.ieee.org/lpdocs/epic03/wrapper.htm?arnumber=6968061

[116] C. W. Tsao and D. L. DeVoe, "Bonding of thermoplastic polymer microfluidics," *Microfluidics and Nanofluidics*, vol. 6, no. 1, pp. 1–16, 2009.

[117] I. R. G. Ogilvie, V. J. Sieben, C. F. a. Floquet, R. Zmijan, M. C. Mowlem, and H. Morgan, "Reduction of surface roughness for optical quality microfluidic devices in PMMA and COC," *Journal of Micromechanics and Microengineering*, vol. 20, no. 6, p. 65016, jun 2010. [Online]. Available: http://stacks.iop.org/0960-1317/20/i=6/a=065016?key=crossref.e2fbcc86fc1545219235e745b992ee14

[118] J. Ma, X. Yuan, B. Küçüköz, S. Li, C. Zhang, P. Majumdar, A. Karatay, X. Li, H. Gul Yaglioglu, A. Elmali, J. Zhao, and M. Hayvali, "Resonance energy transfer-enhanced rhodaminestyryl Bodipy dyad triplet photosensitizers," *Journal of Materials Chemistry C*, vol. 2, no. 20, p. 3900, 2014. [Online]. Available: http://xlink.rsc.org/?DOI=c3tc32456g

[119] L. A. L. A. Herzenberg, D. Parks, B. Sahaf, O. Perez, M. Roederer, and L. A. L. A. Herzenberg, "The history and future of the fluorescence activated cell sorter and flow cytometry: a view from Stanford." *Clinical chemistry*, vol. 48, no. 10, pp. 1819–27, oct 2002. [Online]. Available: http://www.ncbi.nlm.nih.gov/pubmed/12324512

[120] Bio-Rad Laboratories Inc., "CFX Connect Real-Time PCR Detection System Specifications Sheet," 2016. [Online]. Available: http://www.bio-rad.com/webroot/web/pdf/lsr/literature/Bulletin_6102.pdf

[121] Illumina Inc., "HiSeq 3000 / HiSeq 4000 Sequencing Systems," 2015. [Online]. Available: http://www.illumina.com/content/dam/illumina-marketing/documents/products/datasheets/hiseq-3000-4000-specification-sheet-770-2014-057.pdf

[122] M. E. Johnson and J. P. Landers, "Fundamentals and practice for ultrasensitive laser-induced fluorescence detection in microanalytical systems," *Electrophoresis*, vol. 25, pp. 3513–3527, 2004.

[123] Micralyne Inc., "Microfluidic Products from Micralyne." [Online]. Available: https://www.scribd.com/document/2909561/Standard-Microfluidic-Chips

[124] C. D. Ahrberg, B. R. Ilic, A. Manz, and P. Neužil, "Handheld real-time PCR device," *Lab Chip*, vol. 16, no. 3, pp. 586–592, 2016. [Online]. Available: http://xlink.rsc.org/?DOI=C5LC01415H

[125] Roche Molecular Systems Inc., "LightCycler® 480 Instrument II," 2016. [Online]. Available: https://shop.roche.com/shop/products/lightcycler14301-480-instrument-ii

[126] P. Diao, H. Yuan, F. Huo, L. Chen, D. Xiao, M. C. Paau, and M. M. F. Choi, "A simple and sensitive CE method for the simultaneous determination of catecholamines in urine with in-column optical fiber light-emitting diode-induced fluorescence detection," *Talanta*, vol. 85, no. 3, pp. 1279–1284, 2011.

[127] K. Miyaki, Y. Guo, T. Shimosaka, T. Nakagama, H. Nakajima, and K. Uchiyama, "Fabrication of an integrated PDMS microchip incorporating an LED-induced fluorescence device," *Analytical and Bioanalytical Chemistry*, vol. 382, no. 3, pp. 810–816, jun 2005. [Online]. Available: http://link.springer.com/10.1007/s00216-004-3015-1

[128] M. L. Chabinyc, D. T. Chiu, J. C. McDonald, A. D. Stroock, J. F. Christian, A. M. Karger, and G. M. Whitesides, "An integrated fluorescence detection system in poly(dimethylsiloxane) for microfluidic applications," *Analytical Chemistry*, vol. 73, no. 18, pp. 4491–4498, 2001.

[129] B. Yao, G. Luo, L. Wang, Y. Gao, G. Lei, K. Ren, L. Chen, Y. Wang, Y. Hu, and Y. Qiu, "A microfluidic device using a green organic light emitting diode as an integrated excitation source." *Lab on a chip*, vol. 5, pp. 1041–1047, 2005.

[130] H. Nakajima, Y. Okuma, K. Morioka, M. Miyake, A. Hemmi, T. Tobita, M. Yahiro, D. Yokoyama, C. Adachi, N. Soh, K. Nakano, S. Xue, H. Zeng, K. Uchiyama, and T. Imato, "An integrated enzyme-linked immunosorbent assay system with an organic light-emitting diode and a charge-coupled device for fluorescence detection," *Journal of Separation Science*, vol. 34, no. 20, pp. 2906–2912, 2011.

[131] S. Wang, X. Li, J. Yang, X. Yang, F. Hou, and Z. Chen, "Rapid determination of creatinine in human urine by microchip electrophoresis with LED induced fluorescence detection," *Chromatographia*, vol. 75, pp. 1287–1293, 2012.

[132] G. Cosa, K. S. Focsaneanu, J. R. McLean, J. P. McNamee, and J. C. Scaiano, "Photophysical properties of fluorescent DNA-dyes bound to single- and double-stranded DNA in aqueous buffered solution." *Photochemistry and photobiology*, vol. 73, no. 6, pp. 585–599, 2001.

[133] M. J. Waring, "Complex formation between ethidium bromide and nucleic acids," *Journal of Molecular Biology*, vol. 13, no. 1, pp. 269–282, aug 1965. [Online]. Available: http://dx.doi.org/10.1016/S0022-2836(65)80096-1

[134] A. E. Barron and H. W. Blanch, "DNA Separations by Slab Gel, and Capillary Electrophoresis: Theory and Practice," *Separation and Purification Methods*, vol. 24, no. 1, pp. 1–118, jan 1995. [Online]. Available: http://www.tandfonline.com/doi/abs/10.1080/03602549508014343

[135] T. Datta-Chaudhuri, P. Abshire, and E. Smela, "Packaging commercial CMOS chips for lab on a chip integration," *Lab on a Chip*, vol. 14, no. 10, p. 1753, may 2014. [Online]. Available: http://xlink.rsc.org/?DOI=c4lc00135d

[136] J. P. Devadhasan, I. S. Yoo, and S. Kim, "Overview of CMOS image sensor use in molecular diagnostics," *Current Applied Physics*, vol. 15, no. 3, pp. 402–411, mar 2015. [Online]. Available: http://dx.doi.org/10.1016/j.cap.2015.01.009

[137] T. Luo, H. Wang, H. Song, and J. B. Christen, "CMOS-based on-chip electrochemical sensor," in *2014 IEEE Biomedical Circuits and Systems Conference (BioCAS) Proceedings*. IEEE, oct 2014, pp. 336–339. [Online]. Available: http://ieeexplore.ieee.org/document/6981731/

[138] M. Khorasani, M. Behnam, L. van den Berg, C. J. Backhouse, and D. G. Elliott, "High-Voltage CMOS Controller for Microfluidics." *IEEE Transactions on Biomedical Circuits and Systems*, vol. 3, no. 2, pp. 89–96, apr 2009. [Online]. Available: http://www.ncbi.nlm.nih.gov/pubmed/23853200

[139] Y. Temiz, R. D. Lovchik, G. V. Kaigala, and E. Delamarche, "Lab-on-a-chip devices: How to close and plug the lab?" *Microelectronic Engineering*, vol. 132, pp. 156–175, jan 2015. [Online]. Available: http://www.sciencedirect.com/science/article/pii/S0167931714004456

[140] G. Patounakis, K. Shepard, and R. Levicky, "Active CMOS Array Sensor for Time-Resolved Fluorescence Detection," *IEEE Journal of Solid-State Circuits*, vol. 41, no. 11, pp. 2521–2530, nov 2006. [Online]. Available: http://ieeexplore.ieee.org/document/1717675/

[141] H. Norian, R. M. Field, I. Kymissis, and K. L. Shepard, "An integrated CMOS quantitative-polymerase-chain-reaction lab-on-chip for point-of-care diagnostics," *Lab Chip*, vol. 14, no. 20, pp. 4076–4084, aug 2014. [Online]. Available: http://xlink.rsc.org/?DOI=C4LC00443D

[142] M. Herper, "Illumina Unveils $20,000 Desktop Sequencer Aimed At Sequencing Germs," 2018. [Online]. Available: https://www.forbes.com/sites/matthewherper/2018/01/08/illumina-unveils-20000-desktop-sequencer-aimed-at-sequencing-germs/#3ea602f81000

[143] M. Heger, "At AGBT, Illumina Provides Additional Details on Project Firefly," 2016. [Online]. Available: https://www.genomeweb.com/sequencing-technology/agbt-illumina-provides-additional-details-project-firefly

[144] Illumina Inc., "iSeq100 Sequencing System," 2018. [Online]. Available: https://support.illumina.com/content/dam/illumina-marketing/documents/products/datasheets/iseq100-sequencing-system-spec-sheet-770-2017-020.pdf

[145] Edmund Optics, "Premier Laser Diode Modules," 2016. [Online]. Available: http://www.edmundoptics.com/lasers/laser-diode-modules/premier-laser-diode-modules/2472/

[146] Illumina Inc., "MiniSeq System," 2016. [Online]. Available: http://www.illumina.com/content/dam/illumina-marketing/documents/products/datasheets/miniseq-system-specification-sheet-770-2015-039.pdf

[147] Labsphere, "The Radiometry of Light Emitting Diodes," pp. 1–15, 2008. [Online]. Available: https://www.labsphere.com/site/assets/files/2570/the-radiometry-of-light-emitting-diodes-leds.pdf

[148] Commission Internationale de L'Eclairage, "Selected Colorimetric Tables," 2016. [Online]. Available: http://www.cie.co.at/publications/cie-colorimetry-part-1-standard-colorimetric-observers

[149] A. Khadjavi, "Calculation of Solid Angle Subtended by Rectangular Apertures," *Journal of the Optical Society of America*, vol. 58, no. October, p. 1417, 1968.

[150] U.S. Lasers, "US-Lasers: 635nm-5mW - Red Laser Diode and Red Diode Laser Module," 2017. [Online]. Available: http://www.us-lasers.com/n635nm5m.htm

[151] Life Technologies, "Fluorescence SpectraViewer," 2016. [Online]. Available: https://www.thermofisher.com/ca/en/home/life-science/cell-analysis/labeling-chemistry/fluorescence-spectraviewer.html

[152] Chroma Technology Corporation, "Complete Filter Sets," 2016. [Online]. Available: https://www.chroma.com/products/complete-filter-sets

[153] C. F. Floquet, V. J. Sieben, A. Milani, E. P. Joly, I. R. Ogilvie, H. Morgan, and M. C. Mowlem, "Nanomolar detection with high sensitivity microfluidic absorption cells manufactured in tinted PMMA for chemical analysis," *Talanta*, vol. 84, no. 1, pp. 235–239, mar 2011. [Online]. Available: http://www.ncbi.nlm.nih.gov/pubmed/21315925

[154] Life Technologies, "Fluorescence quantum yields (QY) and lifetimes (τ) for Alexa Fluor dyesTable 1.5." [Online]. Available: https://www.lifetechnologies.com/ca/en/home/references/molecular-probes-the-handbook/tables/fluorescence-quantum-yields-and-lifetimes-for-alexa-fluor-dyes.html

[155] F. Lopez Arbeloa, T. Lopez Arbeloa, M. J. Tapia Estevez, and I. Lopez Arbeloa, "Photophysics of rhodamines: molecular structure and solvent effects," *The Journal of Physical Chemistry*, vol. 95, no. 6, pp. 2203–2208, mar 1991. [Online]. Available: http://pubs.acs.org/doi/abs/10.1021/j100159a022

[156] N. Kaplinsky, "Scavenging parts from the GAIIx vs the HiSeq," 2014. [Online]. Available: http://blogs.swarthmore.edu/Illumina+GAIIx+Teardown/?p=125#comments

[157] Nikon Instruments Inc., "Objective Selector," 2017. [Online]. Available: https://www.nikoninstruments.com/Product-Selectors/Objective-Selector

[158] A. Yariv and P. Yeh, *Photonics: Optical Electronics in Modern Communications*, 6th ed. Oxford: Oxford University Press, 2007.

[159] A. E. Nkodo, J. M. Garnier, B. Tinland, H. Ren, C. Desruisseaux, L. C. McCormick, G. Drouin, G. W. Slater, and I. C. Sadron, "Diffusion coefficient of DNA molecules during free solution electrophoresis," *Electrophoresis*, vol. 22, no. 12, pp. 2424–2432, 2001.

[160] D. L. Sloan, B. Martin, G. Hall, A. Hakman, P. Marshall, S. Martel, C. Backhouse, V. Gaudet, and D. G. Elliott, "HV-CMOS single-chip electronics platform for lab-on-chip DNA analysis," in *2016 IEEE International Symposium on Circuits and Systems (ISCAS)*, vol. 2016-July, no. Ic. IEEE, may 2016, pp. 2427–2430. [Online]. Available: http://ieeexplore.ieee.org/lpdocs/epic03/wrapper.htm?arnumber=7539082

[161] V. G. Shadbolt, "Development of a Flame Atomic Emission Spectrometer for Lab on Chip Applications," MASc, University of Waterloo, 2015.

[162] P. Horowitz and W. Hill, *The Art of Electronics*, 3rd ed. New York: Cambridge University Press, 2015.

[163] J. Graeme, *Photodiode Amplifiers*. New York: McGraw-Hill, 1996.

[164] Burr-Brown, "Noise Analysis of FET Transimpedance Amplifiers," 1994. [Online]. Available: http://www.ti.com/lit/an/sboa060/sboa060.pdf

[165] T. Wang and B. Erhman, "Compensate Transimpedance Amplifiers Intuitively," 2005. [Online]. Available: http://www.ti.com/lit/an/sboa055a/sboa055a.pdf

[166] Analog Devices, "ADA4530-1 Data Sheet," 2017. [Online]. Available: http://www.analog.com/media/en/technical-documentation/data-sheets/ADA4530-1.pdf

[167] B. Baker, "Transimpedance-amplifier-noise issues," 2008. [Online]. Available: https://www.edn.com/electronics-blogs/bakers-best/4326137/Transimpedance-amplifier-noise-issues

[168] Texas Instruments, "Noise Calculator, Generator and Examples," 2017. [Online]. Available: https://www.ti.com/tool/opamp-noisecalc

[169] P. Grohe, "Design femtoampere circuits with low leakage, part one," 2011. [Online]. Available: http://www.edn.com/design/analog/4368681/Design-femtoampere-circuits-with-low-leakage-part-one

[170] P. Grohe, "Design femtoampere circuits with low leakage - Part 3: Low-current design techniques," 2012. [Online]. Available: http://www.edn.com/design/analog/4395651/Design-femtoampere-circuits-with-low-leakage---Part-3--Low-current-design-techniques

[171] Analog Devices, "Single Supply Low Noise LED Current Source Driver Using a Current Output DAC in the Reverse Mode AN-1212 Rev. A," 2012. [Online]. Available: http://www.analog.com/media/en/technical-documentation/application-notes/AN-1212.pdf

[172] L. Novak, P. Neuzil, J. Pipper, Y. Zhang, and S. Lee, "An integrated fluorescence detection system for lab-on-a-chip applications." *Lab on a chip*, vol. 7, pp. 27–29, 2007.

[173] S. H. Choi, "Signal processing and amplifier design for inexpensive genetic analysis instruments," MSc, University of Alberta, 2011.

[174] C. Perrin, B. Walczak, and D. L. Massart, "The Use of Wavelets for Signal Denoising in Capillary Electrophoresis," *Analytical Chemistry*, vol. 73, no. 20, pp. 4903–4917, oct 2001. [Online]. Available: http://pubs.acs.org/doi/abs/10.1021/ac010416a

[175] M. C. Breadmore, A. I. Shallan, H. R. Rabanes, D. Gstoettenmayr, A. S. Abdul Keyon, A. Gaspar, M. Dawod, and J. P. Quirino, "Recent advances in enhancing the sensitivity of electrophoresis and electrochromatography in capillaries and microchips (2010-2012)." *Electrophoresis*, vol. 34, no. 1, pp. 29–54, jan 2013. [Online]. Available: http://www.ncbi.nlm.nih.gov/pubmed/23161056

[176] A. Koeken, C. Cobbaert, W. Quint, and L.-J. van Doorn, "Genotyping of hemochromatosis-associated mutations in the HFE gene by PCR-RFLP and a novel reverse hybridization method." *Clinical chemistry and laboratory medicine : CCLM / FESCC*, vol. 40, no. 2, pp. 122–125, feb 2002. [Online]. Available: http://www.ncbi.nlm.nih.gov/pubmed/11939483

[177] E. Beutler, T. H. Bothwell, R. W. Charlton, and A. G. Motulsky, "Hereditary Hemochromatosis. IN: Valle D, Beaudet AL, Vogelstein B, Kinzler KW, et al, eds. Scriver's Online Metabolic and Molecular Bases of Inherited Disease." 2006.

[178] P. Clark, L. J. Britton, and L. W. Powell, "The diagnosis and management of hereditary haemochromatosis." *The Clinical biochemist. Reviews / Australian Association of Clinical Biochemists*, vol. 31, no. 1, pp. 3–8, mar 2010.

[179] R. Seckingrton and L. Powell, *HFE-Associated Hereditary Hemochromatosis In: Pagon RA, Adam MP, Ardinger HH, et al., editors*. Seattle: University of Washington, 2000. [Online]. Available: http://www.ncbi.nlm.nih.gov/books/NBK1440/

[180] Life Technologies, "DNA and RNA Molecular Weights and Conversions."

[Online]. Available: https://www.lifetechnologies.com/ca/en/home/references/ambion-tech-support/rna-tools-and-calculators/dna-and-rna-molecular-weights-and-conversions.html

[181] Life Technologies, "The Alexa Fluor Dye SeriesNote 1.1." [Online]. Available: https://www.lifetechnologies.com/ca/en/home/references/molecular-probes-the-handbook/technical-notes-and-product-highlights/the-alexa-fluor-dye-series.html

[182] R. Sjöback, J. Nygren, and M. Kubista, "Absorption and fluorescence properties of fluorescein," *Spectrochimica Acta Part A: Molecular and Biomolecular Spectroscopy*, vol. 51, no. 6, pp. L7—-L21, jun 1995. [Online]. Available: http://linkinghub.elsevier.com/retrieve/pii/058485399501421P

[183] A. L. Benvin, Y. Creeger, G. W. Fisher, B. Ballou, A. S. Waggoner, and B. A. Armitage, "Fluorescent DNA nanotags: Supramolecular fluorescent labels based on intercalating dye arrays assembled on nanostructured DNA templates," *Journal of the American Chemical Society*, vol. 129, no. 7, pp. 2025–2034, 2007.

[184] M. M. Martin and L. Lindqvist, "The pH dependence of fluorescein fluorescence," *Journal of Luminescence*, vol. 10, no. 6, pp. 381–390, jul 1975. [Online]. Available: http://linkinghub.elsevier.com/retrieve/pii/0022231375900034

[185] Occupational Safety and Health Administration, "Controlling Electrical Hazards," 2002. [Online]. Available: https://www.osha.gov/Publications/osha3075.pdf

[186] W. Kok, *Capillary Electrophoresis: Instrumentation and Operation*, ser. Chromatographia CE-Series. Wiesbaden: Vieweg+Teubner Verlag, 2000, vol. 4. [Online]. Available: http://link.springer.com/10.1007/978-3-322-83133-0

[187] S. Huang, Q. He, X. Hu, and H. Chen, "Fabrication of micro pneumatic valves with double-layer elastic poly(dimethylsiloxane) membranes in rigid poly(methyl methacrylate) microfluidic chips," *Journal of Micromechanics and Microengineering*, vol. 22, no. 8, p. 085008, aug 2012. [Online]. Available: http://stacks.iop.org/0960-1317/22/i=8/a=085008?key=crossref.f1344436e283163ff7d5277989d9c977

[188] K. W. Oh and C. H. Ahn, "A review of microvalves," *Journal of Micromechanics and Microengineering*, vol. 16, no. 5, pp. R13–R39, may 2006. [Online]. Available: http://stacks.iop.org/0960-1317/16/i=5/a=R01?key=crossref.c5cf9020613ed3137ffb01175e1871b7

[189] K. Hosokawa and R. Maeda, "A pneumatically-actuated three-way microvalve fabricated with polydimethylsiloxane using the membrane transfer technique," *Journal of Micromechanics and Microengineering*, vol. 10, no. 3, pp. 415–420, sep 2000. [Online]. Available: http://stacks.iop.org/0960-1317/10/i=3/a=317?key=crossref.c00cd0bc796b383e05a7d6e10cba683a

[190] D. Irimia and M. Toner, "Cell handling using microstructured membranes." *Lab on a chip*, vol. 6, no. 3, pp. 345–352, 2006. [Online]. Available: http://xlink.rsc.org/?DOI=b515983k

[191] J. Kim, A. M. Stockton, E. C. Jensen, and R. A. Mathies, "Pneumatically actuated microvalve circuits for programmable automation of chemical and biochemical analysis," *Lab Chip*, no. 510, 2016. [Online]. Available: http://xlink.rsc.org/?DOI=C5LC01397F

[192] P. Zhou and L. C. Young, "Microfluidic systems," U.S. Patent 9 151 701, 2015.

[193] G. V. Kaigala, R. D. Lovchik, U. Drechsler, and E. Delamarche, "A Vertical Microfluidic Probe," *Langmuir*, vol. 27, no. 9, pp. 5686–5693, may 2011. [Online]. Available: http://pubs.acs.org/doi/abs/10.1021/la2003639

[194] J. Kim, E. C. Jensen, A. M. Stockton, and R. A. Mathies, "Universal Microfluidic Automaton for Autonomous Sample Processing: Application to the Mars Organic Analyzer," *Analytical Chemistry*, vol. 85, no. 16, pp. 7682–7688, 2013. [Online]. Available: http://pubs.acs.org/doi/abs/10.1021/ac303767m

[195] M. A. Unger, H. P. Chou, T. Thorsen, A. Scherer, and S. R. Quake, "Monolithic microfabricated valves and pumps by multilayer soft lithography." *Science (New York, N.Y.)*, vol. 288, no. 5463, pp. 113–6, apr 2000. [Online]. Available: http://www.sciencemag.org/cgi/doi/10.1126/science.288.5463.113

[196] G. V. Kaigala, V. N. Hoang, and C. J. Backhouse, "Electrically controlled microvalves to integrate microchip polymerase chain reaction and capillary electrophoresis." *Lab on a chip*, vol. 8, no. 7, pp. 1071–8, jul 2008. [Online]. Available: http://www.ncbi.nlm.nih.gov/pubmed/18584081

[197] X. Yu, Y. Wang, Y. Liu, T. Li, H. Zhou, X. Gao, F. Feng, T. Roinila, and Y. Wang, "CMOS MEMS-based thermoelectric generator with an efficient heat dissipation path," *Journal of Micromechanics and Microengineering*, vol. 22, no. 10, p. 105011, 2012. [Online]. Available: http://stacks.iop.org/0960-1317/22/i=10/a=105011?key=crossref.876f308bb03a5c770bac6c32dbc5ff3d

[198] B. Beauregard, "Improving the Beginner's PID," 2011. [Online]. Available: http://brettbeauregard.com/blog/2011/04/improving-the-beginners-pid-introduction/

Appendix A

Technical Instrumentation

This appendix details work towards implementing the auxiliary instrumentation functions required for PCR-CE. This includes development of high voltage (HV) instrumentation for electrophoretic separations, microfluidic valving for fluidic actuation and mixing and thermal instrumentation for PCR. For each of these functions I detail the module requirements for implementing the standard protocols, design efforts to meet these requirements and preliminary validation of the module. Various aspects of this technical infrastructure were used in the instruments detailed in Chapter 5.

A.1 High Voltage Instrumentation

HV generation and switching is a core function to implement electrophoresis, with the generation required to provide the separation field and the switching required to implement the inject-separate technique from Figure 1.3. Another important aspect is the need to monitor the current drawn from the HV source, which is an important data point when troubleshooting protocols.[54] The primary assessment parameters are the voltage applied, the stability of the voltage, the accuracy of the current measurement and the ”off” resistance of the HV switching. Two HV electronics designs were used in this thesis. The first was an initial design that unfortunately lacked current monitoring and therefore did not meet the required functionality. This early design was used for the demonstrations in Sections 5.3 and 5.4. Section A.1.2 details briefly the implementation and testing of the current monitoring and some digital communications improvements that were introduced for inclusion within the next-generation instrument in Section 5.5.

A.1.1 Requirements

The requirements for the HV module are that it conforms to the performance metrics required to implement a general purpose CE protocol and have high reproducibility and stability. In terms of the HV supply, the instrument must be capable 100 $^{V}/_{cm}$ to ensure compatibility with the protocols outlined in the review by Ugaz et al..[59] However, the field

is both a function of the channel length and the voltage supplied. In previous designs within the lab we have targeted 11-13 mm separations.[96] The separation channel length, however, is defined as the length of channel between the intersection as outlined in Figure 1.3 and the detection point. This is a subset of the length the high voltage is applied over, which is typically about 20 mm. Thus, a 100 $^{V}/_{cm}$ field corresponds to an applied voltage requirement of 200 V or greater. The current required from the chip depends very heavily on the channel dimensions and buffer being used (i.e. it is protocol dependent). Very high current can cause Joule heating, and thus is generally avoided.[54] Further, the combination of HV and current presents an electrical hazard that is largely unnecessary. Thus, in order to ensure that the user is safe, the current available to the supply should not exceed 1 mA.[185] The current output must, however, also be sufficient to drive a variety of channel dimensions. The commercial CE device in the lab has a maximum current of 100 μA, and this seems to be a very reasonable target. Thus a 300 V supply with between 100 μA and 1 mA of current output is required.

Voltage stability is a difficult parameter to set specifications for as its effect on the separation resolution is not very clear. Stability can be separated into three different parameters: ripple (i.e. AC variation about the DC set value), drift and run-to-run variation. Of these parameters, ripple on the supply is the least important as all components of the sample will feel the same field changes and, due to the plug-flow nature of electrophoretic motion, the sample resolution should not be notably affected.[186] Further, typical DC-DC supplies have relatively low ripple (10 mV peak to peak for the supply used in this work). Thus, dielectrophoretic motion is not considered to be an issue due to the multiple orders of magnitude difference in the ripple RMS voltage and the DC set voltage of a typical supply. Drift refers to the set voltage changing with time without user interaction. This can cause unpredictable changes to resolution, lead to unreliable instrument readings and cause run-to-run variation. Run-to-run variation refers to the difference in performance of two otherwise identical experiments run on the instrument. It differs from drift in that drift refers to an in-experiment variation whereas run-to-run refers to between experiments. As previously stated, reproducibility is a core requirement of the module, especially for implementing sizing experiments. The combination of drift and run-to-run variation must be under 5% to ensure that the sizing accuracy is less than 10 bp for products greater than 50 bp in size.

In order to perform an inject-separate experiment, the HV subsystem must be capable of both changing HV on the fly as well as switching HV with extremely high off-impedances. The current flowing through a channel is a function of the ionic concentration in the channel. Due to the difference in composition of the channels (injection is sample + buffer, separation is just buffer), the current at a given voltage in the injection channel is typically much higher. This high current causes Joule heating of the matrix, a very negative effect.[54] Thus, the field for injection is typically less than separation. Further, depending on the design the injection and separation channels might not be the same length. These two factors mean that the user must be capable of adjusting the voltage between injection and separation. The principle of the inject-separate technique is to create a defined sample plug in the intersection. This relies on ensuring that during injection, there is no electrophoretic flow down the separation channel and vice versa. During an inject or separate step, the unused wells are left floating such that there is no current (i.e. analyte movement) through the unused channel. In order for this to be true, the impedance between the floating wells and ground must be much higher than the channel analyte is flowing through. Since the typical impedance for CE work ranges in the 5-10 MΩ range, a GΩ or higher switching impedance is needed. Inject-separate also requires at least two full HV lines (i.e. two HV outputs, two ground outputs).

Finally, it is very important that the user be able to read the current flowing through the electrophoretic channel for troubleshooting and consistency checking purposes. A change in current can mean a number of things including contamination, buffer depletion, disconnected electrodes, leakage currents, etc. Further, by monitoring the current the user can calculate the amount of Joule heating occurring in the channel. Joule heating causes substantial problems for CE as it not only affects mobility (2%-3% per ^{o}C), but also can cause structural changes within the gel itself which can cause unknown effects. Thus, the user must be able to monitor the current such that the heating can be calculated and controlled. The current must be read to within 1 μA in order to be reliable for troubleshooting purposes.

In summary, the HV module must supply a programmable HV at 300 V, 100 μA - 1 mA, contain two HV lines and two ground lines with 10GΩ or higher off-impedance and be capable of reading currents at 1 μA. With all aspects, high reproducibility within 5% is required.

A.1.2 High voltage generation and switching electronics

Previous Designs

Initial designs for a HV module were executed by other students, Victor Shadbolt and Sibi Sutty. This design did not include current monitoring and was controlled with external analogue signals which complicated its integration with other instrumentation functions. However, despite these limitations it was sufficient for the applications tested and they formed the based upon which the new module was based on. The previous design was based around a Matsusada TS-0.3P DC/DC miniature DC-DC converter to provide the HV generation. This chipset was designed for biassing avalanche photodiodes and features a 15-300 V programmable output with a 500 μA maximum output and low ripple ($<$ 10 mV peak to peak). Therefore, this meets the HV generation requirements. The HV switching was provided with a HV relay controlled by a MOSFET driver. This provided two HV outputs and two ground lines with $> 10^{10}\Omega$ off-impedance which is also in accordance with the HV requirements. Thus, many of the core requirements of the design were satisfied by the board. However, there were three primary issues that required modification. Firstly, the inputs to the board were 12 V power, ground, an analog line that must be controlled between 0 and 10 V, which maps to the DC-DC output, and digital outputs which toggle each of the MOSFET drivers/relays and thus the board requires a dedicated connector. This complicated inclusion of the board in multi-functional systems. A substantial improvement would be to make the whole board controllable over a standard digital communication protocol, such as serial protocol interface (SPI). More importantly, the board did not feature any current monitoring. Thus, some modifications were required. While the lack of current monitoring complicates troubleshooting and likely prevents the development of high-performance protocols, it does not in theory affect the separation conditions of a known and stable protocols. Therefore, this design (with some additional components to provide the connector) was used in the the CE instruments described in Section 5.3 and 5.4. Detailed discussion of the board construction and design can be found in Chapter 4.3 and Appendix F of Victor Shadbolt's thesis.[161]

Design improvements

There were two primary changes that were implemented to the HV module: implementing current monitoring and changing the board to adhere to a standard SPI communication. Thus, the DC-DC converter and relay design were kept as these met the module requirements and were conveniently available in the lab. Further, more attention and verification was done to ensure that the module meets the required specifications.

The DC power supply used remained the Matsusada TS-0.3P due to the convenience as well as familiarity with the product in previous work. The supply provides the appropriate voltages and currents for the application and has proved to be very steady with excellent ripple and stability. However, one big problem is that the voltage output from the supply varies with the load applied. This can be a substantial problem in CE as the resistance of the channel during a run can change by a notable amount. The datasheet for the part specifies a load regulation of within 6 V for load changes of 10%, which at face value is fairly problematic. However, the supply becomes much more steady at higher loads. These high loads are more indicative of the practical performance of the module as CE channels typically feature 5 MΩ or higher impedances. Investigating the true accuracy of the supply at these voltages was one of the key verification experiments performed in below in Section A.1.2. Another component used from the previous circuit board was the HV reed relay. These relays had proven to be reliable across a large number of actuations, well shielded, and well suited for CE work with a minimum off impedance of $10^{11}\Omega$.

Low-side current monitoring was added to both of two switchable ground lines as shown in Figure A.1. This was done by sinking the HV current through a 1 kΩ resistor to ground and monitoring the voltage drop with a non-inverting amplifier circuit (OPA2302) and a total gain of 27.8. The rail voltage was 3.3 V, thus this corresponds to a maximum current measurement of 118 μA. Low-side monitoring was picked over high-side due to the simplicity of implementation and to avoid the high common mode voltage that a high-side solution would need to deal with. The 1kΩ shunt resistor is under 0.1% of the estimated load resistance of a channel, thus it can be considered negligible for this application.

One of the major changes to the HV switching circuit was to introduce on-board digital logic, making the circuit controlled with a standard SPI signal and more readily integrated into a wider infrastructure. This involved adding a 12-bit DAC (MCP 4922, Microchip Technology) to control the HV supply, a 12-bit ADC (MCP 3202, Microchip Technology) to monitor the current and digital power logic (TPIC6C596, Texas Instruments) to switch the relays. The power logic chip accepts SPI and can toggle up to eight transistors from an off state to an on state where they can sink up to 150 mA continuously, which is more than sufficient for the 24 mA relays. Previously, the instrument used a digital line to switch a MOSFET driver, which then switched the relay as the digital outputs could not source or sink the required current. This solution simplifies the circuit from a minimum of five chips to a single IC.

A high-level diagram of how the HV module operates is shown in Figure A.1. This design was implemented as part of a fluidics control PCB as detailed briefly in Section F.2.3, and EAGLE CAD schematics are available in the SI.

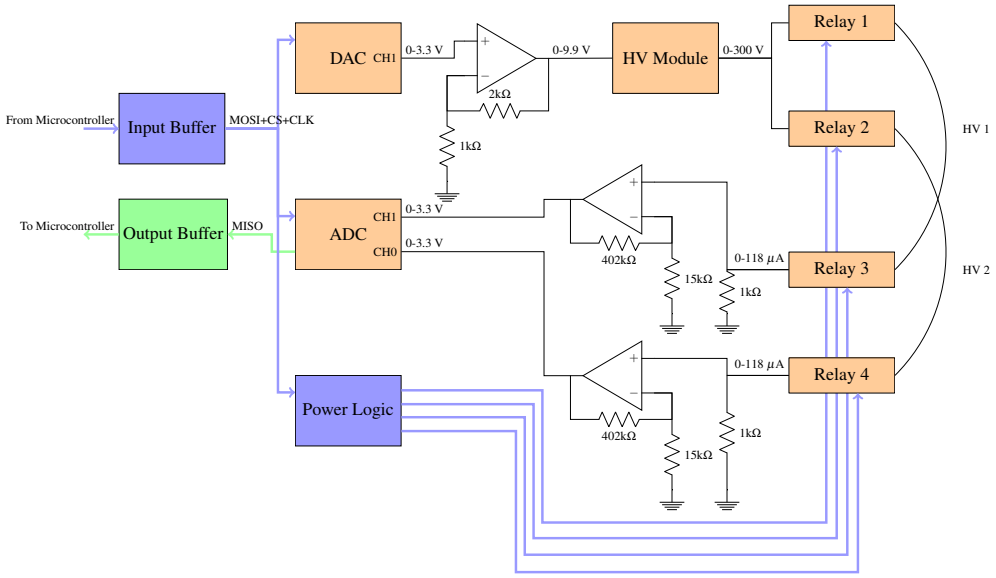

Figure A.1: A diagram of the HV board signals and voltages. The HV subsystem is controlled with SPI with both board inputs and outputs buffered for improved signal reliability. The DAC provides a controlled voltage between 0 and 3.3 V that, when amplified by 3, provides the 0-10V control for HV supply up to 300 V. The power logic is used to toggle on/off the four relays. Relays 1 and 3 are connected to the HV supply, while relays 2 and 4 are connected to a 1 kΩ shunt resistor and to ground. The voltage drop across the shunt resistor is measured by an op amp circuit with 27.8x gain and digitised by an ADC.This allows for the measurement of currents up to 118 μA.

Design Verification

A number of key experiments were done to verify the robust operation of the HV module: calibrating the DAC to HV output transfer function, assessing the voltage set error across various load impedances, quantifying the current measurement accuracy and noise, and assessing the communication reliability. To both calibrate the DAC as well as assess the voltage set error the DAC voltage was scaled from 512 to 4095 (12-bit) in increments of 256. The DAC reference voltage was 3.3 V with the output amplified by a factor of three by a non-inverting amplifier circuit as shown in Figure A.1. Thus, this corresponds to scaling the HV control line from 1.238 V to 9.9 V in increments of 0.619 V. The output of the HV supply was passed through resistances between 1 MΩ (a lower resistance than will be present in most CE applications) and 20 MΩ (representative of small channel separations) and the voltage drop across this resistor was measured with a multi-meter (Fluke 189) connected to a HV probe (PR 28A-ND, BK Precision). The probe was necessary as it increased the measurement input impedance from the 10 MΩ DMM input (which is similar in magnitude to the channel) to the 1 GΩ of the probe. The experiment was repeated in duplicate. A plot of the output voltage vs. DAC set value for the various impedances is shown in Figure A.2a. Below a DAC set value of 1000 (2.418 V) the transfer function was substantially non-linear. This was not quite expected behaviour as the datasheet implies a linear correlation above an input voltage of 1.2 V. However, this was not considered a significant issue as the HV output at the onset of linear behaviour was 50 V, which is much lower than common CE voltages. Furthermore, the response was consistent both between the two runs presented as well as during preliminary testing not shown, and thus it could conceivably be calibrated for with a second linear trend if sub-50 V separations were needed. To calculate the

transfer function a linear trend with a least squares fit was performed on the data points in Figure A.2a. The 1 MΩ and 20 Ω traces were excluded to improve the fit accuracy as these resistances fall outside the typical channel load in this lab's work. The transfer function is presented in Equation A.1. Note that this transfer function deviates slightly from the one provided in the component data sheet (which is specified for 600 kΩ loads). For CE applications, Equation A.1 should be considered more accurate.

$$\begin{aligned} \mathrm{HV} &= 0.08117 \times \mathrm{DAC} - 24.272 \\ \mathrm{DAC} &= 12.32 \times (\mathrm{HV} + 24.272) \end{aligned} \tag{A.1}$$

Figure A.2b shows the error between the calculated transfer function and the measured voltage at the various set points. The error between the estimated set voltage and measured voltage was typically within 2% except for 20 MΩ, 60 V (2.1% deviation) and 2 MΩ, 305 V (2.1% deviation). These data points were outliers as the former is a voltage below typical CE levels while the latter is an impedance lower than typical CE channels. The datasheet specifies load regulation within 2% for changes up to 10%, thus these results suggest that with the higher impedances of CE channels the load regulation was actually substantially better than specified. Ripple was not assessed as it is four orders of magnitude less than the voltage output according to the datasheet and thus not relevant to the module performance. The 2% variation across voltages between 60 V and 305 V and 2Ω to 20 Ω covers a wider range than the expected running voltages and impedances for typical CE runs. Further, the impedances tested span much more than the expected variation within a CE run which is typically a factor of 2 or less (compared to the order of magnitude tested here). No drift was observed during any of the experiments. Overall, this experiment showed that this module meets the stability and run-to-run requirements with a voltage set accuracy and load regulation within 2% across the expected range of CE voltages and impedances, less than the 5% requirement detailed above.

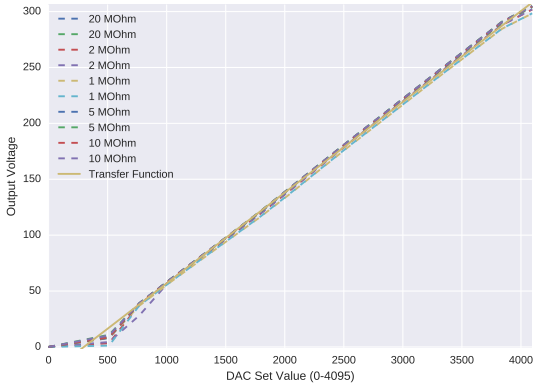

(a) Plot of the HV output vs. DAC set value for various load resistors used to calibrate the DAC-HV transfer function. At very low output voltages the trend is no longer linear, these voltages have been excluded from the fit. The 2 MΩ to 15 Ω resistors were used for calibration as these resistances are more representative of the typical loads of a CE microchannel.

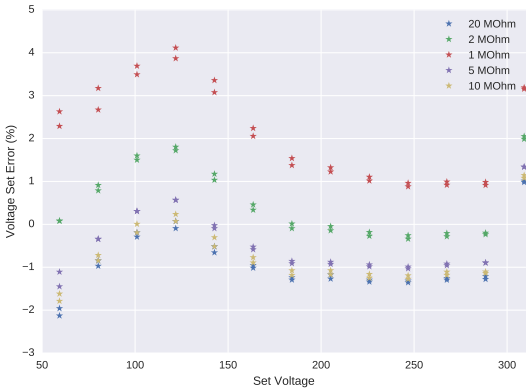

(b) Plot of the difference between the measured voltage and the voltage as predicted by the DAC-HV transfer function. For load impedances of 2 MΩ and above the voltage is set within ≈2%.

Figure A.2: Results of the current generation HV electronics instrumentation

The second key test was to determine the accuracy and limits of the current measurement. For this experiment, a series of voltages were applied to a 5 MΩ and a 10 Ω load representative of a CE channel and the current was measured for 1000 data points ($\approx$ 2 seconds as the highest sampling rate for this chip is about 500 Hz). The resistance of the load and noise on the current measurement were recorded. This experiment was repeated in triplicate. The HV probe was not used in this experiment. Instead, the voltage was assumed to be consistent with Equation A.1.

Figure A.3 shows the error in the resistance estimation for the various voltages and the two load impedances. The estimated resistance measurement was between 0.5 % and 3.8% and within 4 % throughout the whole range. This error was comparable to the HV set error ($\approx$ 2%), and well within the resistor tolerance (5% for both resistors). Further, the triplicate runs were found to vary by less than 1%, indicating high run-to-run reproducibility. The maximum noise on the current measurement was 152 nA at the 500 Hz sampling rate, and the average noise of the runs was 121 nA. Taking the maximum noise, the limit of detection (SNR=3) would be 0.5 μA, which is less than the 1 μA requirement. If further current measurement accuracy was needed, this could be improved by oversampling and averaging the result in a manner similar to the optical signals detailed in Chapter 4. However, without averaging the current reading meets the requirements.

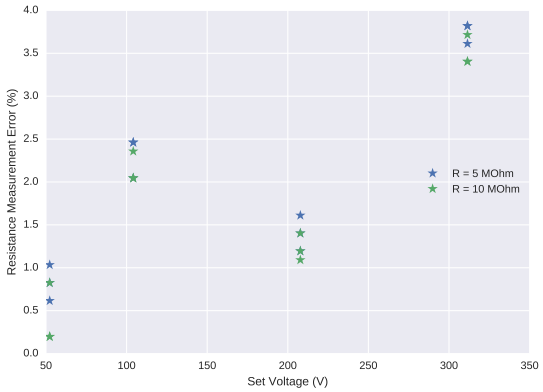

Figure A.3: Plot of the error in measured resistance for 5 MΩ and 10 MΩ resistors at a variety of voltages. The trend in resistance measurement error is consistent with the HV set error in Figure A.2b, implying that much of the error originates in the HV module rather than current measurement. Overall error is within 4%.

Table A.1 details the requirements of the module and measured instrument performance. The module meets or exceeds the design specifications. This module is incorporated within the next generation instrument detailed in Section 5.5.

Parameter	Requirement	Instrument
Maximum voltage	$>$ 300 V	300 V
Rated current at Vmax	$>$100 μA	500 μA (118 μA maximum read)
Maximum current	$<$ 1 mA	500 μA
Voltage stability	Combine to $<$ 5%	2.1 %
Voltage accuracy		
HV switching	Available, 2 or more outputs	Available, 2 HV, 2 GND
HV switch off impedance	$> 10^9\Omega$	$> 10^{11}\Omega$
Current reading	$<$ 1 μA	0.5 μA, averaging can reduce
Current read rate	$>$ 1 Hz	500 Hz

Table A.1: Table of requirements and results for the HV module

A.1.3 Future Work

The current HV module meets the specifications, but some minor adjustments could be made to improve its performance. The primary source of error in this module came from the relatively poor load regulation of the Matsusada HV supply. Thus, a move to a difference HV supply would improve performance. Most works in the literature use EMCO power supplies[40,41,80] which have sub-1% load regulation from short circuit to full-load. These supplies, however, typically target kV level applications which are outside the voltage range of the short-distance separations targeted in this work. Another source of HV supplies is Ultravolt, who market a wide variety of miniature HV supplies within the target range. Specifically, the 0.5US5-P0.1-WS would extend the HV output to 500 V, provide a HV out monitoring lead, vastly superior regulation (0.01% load, 0.01% line) and reduce the power consumption to 5 V, 50 mA at the expense of output current, which would be reduced to 200 μA. This output current still remains in the acceptable range for this module. Thus, future students are highly recommended to pursue this option.

A.2 Lab-on-chip Valve and Pneumatic Instrumentation Development

The LOC field not only carries the promise of lower cost and faster diagnostics, but also implies a substantial amount of process automation. This automation is crucial for integrating multiple functions on chip (such as PCR and CE), and a lack of advanced fluid handling is a notable limitation of the currently available commercial products. It is with this goal in mind that work was done on implementing a scalable and flexible LOC valve compatible with the rapid-prototyping methods outlined in Chapter 2. A well executed LOC valve not only provides the ability to selectively seal and unseal fluidic channels, but multiple valves in series can be used to move fluid using peristalsis.[79] Thus, a well-executed valve can provide multiple LOC functions and is crucial for automating fluidic functionality. LOC valves can be categorised based upon their initial state in the absence of actuation (normally open or normally closed) as well as their actuation method (pneumatic, electrostatic, passive). Over the past few years the Backhouse research group has been developing a normally closed pneumatic valve in the via-doormat style first proposed by Grover et al.[73] in glass and PDMS. The advantage to the via-doormat valve style is that it is readily sealed to prevent fluid leaks, which is very important to ensure robust operation. Pneumatic actuation is the most common valve actuation method as it is robust and has well-described physics,[187] and was used here for the same reasons. The valving project has been

a collaborative effort between myself and two other students (Tianchi Ma, with the early valve development being contained in his thesis,[118] and Robert Bennett). This section focuses on my contributions to the project, though a brief overview of the valve operation is included in Figure A.4 as this valve was implemented as part of the automated enzymatic digest instrument described in Section 5.3.

Implementing a microvalve in the lab required both the valve itself, as well as the pneumatic instrumentation to run it. In terms of the valve itself, there are three key components. First, there is the valve structure itself described in Section A.2.2. This valve structure, in turn, can be considered in two parts: the substrate layer containing fluidics and vias and the active membrane layer that opens and closes the valve. The former was designed and developed by by Tianchi Ma and more detail can be found in his thesis,[118] while the latter was a collaborative effort and is discussed in Section A.2.2. Above the membrane is a pressurised chamber that controls the valve state. This chamber is defined by a manifold structure which is described in Section A.2.3. Finally, there is the pneumatic instrumentation that is used to toggle a pressure line in order to actuate the valve. Towards this goal I have developed two styles of pneumatics modules described in Section A.2.4, one for benchtop prototyping and one for integrated instruments, as well as the electronic instrumentation to run them, described in Section A.2.5. There are a number of requirements for the valving infrastructure as well as some stretch goals for future designs. These are summarised and justified below.

A.2.1 Requirements

The overall requirements for the LOC valve were that it operates reliably, can implement peristaltic pumping, is PCR compatible, can be scaled to enough valves to implement the complexity of a PCR-CE and be consistent with the rapid-prototyping fabrication processes in Chapter 2.

The most important requirement for the LOC valve was that it operates reliably; meaning that when closed, the valve will seal a microchannel, and when opened the flow resistance of fluid through the valve is consistent. This reliability pertains to both the instrumentation as well as the valve itself and is assessed in a number of different ways. In order to ensure that the valve closes properly the structure must be verified to be both fluid and air tight up to a pressure of 70 kPa. This ensures that the valve can resist the pressure created by a heated reaction chamber during a PCR. To assess flow resistance, the most representative application is to measure the volume moved per peristaltic pump stroke. In order to be considered reliable, the target metric set was that the volume should be consistent within 20%. In addition to the valve operation, the rest of the pneumatic instrumentation must also be reliable. This means that the control software and electronics must operate error-free. Finally, there must be no cross-talk between the pressurised lines, meaning that toggling one pressure line from pressure to vacuum does not change the state or operation of other pressure lines. This ensures that the user can implement their desired protocol without undesired leakages.

In order to implement a variety of peristaltic pumping protocols, the valve should be capable of implementing a peristaltic pump operation with a stroke volume between 1 nL and 100 nL, a pump rate of 10 Hz or higher and be capable of self-priming. The stroke volume should be significant enough such that protocols do not take very much time, but also small enough such that metering reagents is possible. The maximum pump rate is related to the maximum rate of actuation of the valves and can be limited by a number of different parameters. First, the pneumatics instrumentation must be capable of robust operation at this rate. However, this is not typically the limiting factor.

Instead, the limit is imposed by the pressure lines themselves. There are two primary factors to consider: the volume of air being switched between pressure and vacuum and the flow rate of the supply pressure/vacuum into this volume. In the case where the volume is high and/or the supply flow rate is low the time taken to make the pressure switch is higher and the maximum actuation rate is reduced. Another result is that when a line is switched, the "dump" of pressure/vacuum through the system can cause cross-talk with neighbouring pressure lines. These effects can be countered by reducing the switched air volume of the pneumatic line, adding a pressurised chamber to supply the pneumatic line to act as a "capacitor" and increasing the supply flow rate to the lines. In order to be useful for peristaltic pumping operations, the pressurised lines must be controllable at 10 Hz or faster without cross-talk. Finally, the valve must be capable of self-priming. Without self-priming the user would either have to manually prime the pump, or the chip would need to be stored "wet". Both of these alternatives are not consistent with reliable pumping operation.

To be useful for PCR applications there are three requirements. The first, as already stated, is that the valve must remain sealed and resistant to 70 kPa of pressure. Further, the valve must remain sealed at elevated temperatures up to 95 ^{o}C. Finally, the valve material must be PCR compatible. PCRs can be readily contaminated by a large number of materials, decreasing the reaction efficiency, sometimes drastically. If the valve is to be used to seal a reaction chamber for PCR, it is thus necessary for the valve material to not negatively impact the reaction.

The number of available valves is an important parameter as it dictates the fluidic complexity that is possible with the system. In order to implement the variety of protocols that have been discussed internally within the lab, the instrument must support at least 22 valves. Having more than the minimum requirement would be advantageous as it relaxes the design constraints for future work.

Finally, it is crucial that the valve fabrication procedure is as simple as possible, consistent with high volume manufacturing and easily rapid-prototyped. The fabrication details are discussed later in Chapter 2, though in general this requirement forces the use of polymers over glass as a chip material.

Category	**Parameter**	**Requirement**
Valve Structure	Fluid Seal	Remain sealed against pressurised fluid up to 70 kPa for 1 minute
Valve Structure	Air seal	Remain sealed against pressurised air up to 70 kPa for 1 minute
Valve Structure	Elevated temperature seal	Remained sealed with heated fluid at 95 ^{o}C for 1 hr
Valve Structure	Pump stroke volume	Between 10 and 100 nL. Consistent within 20%
Valve Structure	PCR compatibility	Does not substantially affect PCR efficiency
Valve Structure	Pump Priming	Capable of self-priming
System	Total number of valves	$>$22
System	Cross-talk	No observed cross talk between valves at 10 Hz
System	Pump rate	Capable of operation up to 10 Hz
Pneumatic Instrumentation	Reliability	Error-free operation

Table A.2: Table of requirements for the LOC valve and associated instrumentation

In addition to the requirements, there are a number of stretch goals for future work. One of the key issues with the use of peristaltic pumps is their choppy, uneven flow performance due to their "two steps forwards, one step back" nature.

This motion is sufficient for many applications, like the automated fluid mixing required for a LOC PCR or enzymatic digest. However, some LOC applications such as emulsion droplet formation require stable flow rates and pressure which cannot be readily supplied by raw peristaltic motion. A solution to this problem would enable the system to perform other experiments and tasks not previously designed for.

Another stretch goal is to use the system to meter precise volumes of fluid from larger reservoirs. This can be very advantageous towards reducing fluidic complexity and can be useful for parametrised experiments. For example, if metering was available a LOC device could feature a single, large, centralised reservoir of buffer to be used for dilution at multiple stages of a protocol. If metering were not available, each usage of buffer would require a dedicated well and valve, increasing the device complexity. Another example would be use of a large sample and buffer well that can be mixed to make serial dilutions. This can be used to rapidly optimise processes. In order for metering to be considered a capability of the device the pump stroke volume must be 10 nL or less with a 5% variability or better.

Finally, for future system development, it would be very advantageous for the instrumentation to be readily miniaturised and consistent with a USB-power budget. This would allow for the development of a fully portable instrument, expanding the marketability of the device.

A.2.2 Microvalve Development

Microvalves can be categorised in a number of ways. Firstly one must differentiate between active and passive valves, where the former involves moving parts and the latter does not. Passive valves cannot be actuated to form pumps, and typically do not seal and thus cannot meet the valve requirements.[188] Active valves can be separated into normally open and normally closed categories, referring to the state of the valve without actuation. We have focused on normally-closed valves as they can be more readily adapted to different channel geometries and, most importantly, are easier to seal.[79] Normally-closed valves typically take either the "doormat" design of those proposed by Hosokawa and Maeda[189] in PDMS and Lagally et al.[70] in Latex and glass, or the "curtain" style developed by Irimia and Toner.[190] In the "doormat" valve design, two channels are brought into close proximity with a membrane sealing the space between and closing the valve. Upon deflection of the membrane, the two channels can communicate. The "curtain" style of normally-closed valve is similar to the "doormat" except that the feature that separates the channels is patterned into the membrane rather than the channel. In a lithography based fabrication process this can reduce the number of required layers,[191] however it does require patterning of the membrane and precise alignment of the patterned membrane to the fluidic chip, complicating fabrication. Grover et al.[73] presents two methods of implementing the "doormat" microvalve. In one implementation the membrane material is the capping layer that seals the microchannels. This approach has the advantage of using fewer photopatterned layers in a lithography microfabrication setup and having lower dead volume.[191] However, unless the device is entirely made from elastomer (as in the all-PDMS device by Hosokawa and Maeda[189]), this will result in inhomogenous channels that complicate operation. Another design uses two closely spaced vias to bring the channels into a valving layer which is then sealed with the membrane.[73] There are several advantages to this, notably that the channel materials are now predominantly homogenous (excluding the valved region), interactions of the reagents with the membrane are minimised and the requirements for sealing the membrane to the microfluidic chip are substantially relaxed.

We have opted to develop around a via-style "doormat" valve illustrated in Figure A.4. In this structure two channels are terminated in vias that are disconnected from one another. A membrane is placed over the region between the vias. In the off state (Figure A.4B), or when a positive pressure P_{+ve} is applied, the membrane seals the vias and they cannot communicate. When a negative pressure P_{-ve} is applied the membrane deflects upwards (Figure A.4C), connecting the two vias and thus allowing the two channels to fluidically communicate. The majority of the valve structure development was done by Tianchi Ma and is described in his thesis.[118]

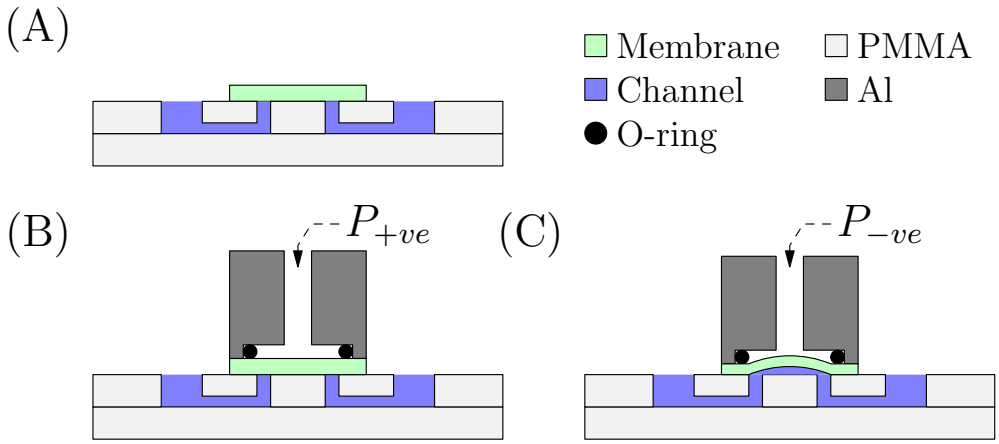

Figure A.4: (A) The valve structure is patterned into a two layer PMMA fluidic chip with a layer of elastomer placed on top. The structure consists of two channels that terminate in vias. These vias are spaced apart and covered with the elastomer.
(B) The valve structure is assembled with an aluminum manifold that typically contains viton o-rings that isolate the valve region on the elastomer membrane. This chamber is initially pressurised with a positive P_{in} which holds the valve closed.
(C) When a negative pressure is applied to P_{in} the elastomeric membrane deflects upwards. This connects the two vias, thus the two channels.

The via-style doormat microvalve structure was first demonstrated in glass by Grover et al..[73] In contrast to this work, our valve structure can be easily rapid-prototyped and assembled. Our valve structure consists of a microfluidic chip that contains three layers: a layer of unpatterned PMMA, a layer of patterned PMMA and a membrane layer. In order to simplify fabrication and ensure alignment, all fluidic features are patterned at the same time with laser ablation (channels are engraved and the vias are through-cut). Thus, this is consistent with the fabrication methods of Chapter 2 which also include a fluidic layer pattered from on side (the fluidic layer) and an unpatterned layer (the cap) with the only difference being the introduction of a membrane on-top of the chip.

Membrane Considerations

The membrane is the most important variable in this valve system in terms of the valve performance. One of my contributions to the valving project was to move from rigid, low stroke volume membranes that could not meet the requirements in Table A.2 to a more flexible nitrile membrane with improved performance. However, while improved, this nitrile membrane also did not meet all of the valve requirements. The project was then transferred back to other

students (Tianchi Ma, Robert Bennett) while my role focused on developing an improved fabrication rocedure to improve membrane reproducibility. This section presents an overview of these developments.

For a pneumatic valve, the deflection of a circularly clamped membrane can be estimated with Equation A.2.

$$w(r) = \frac{3P(r_0)^4(1-\nu^2)}{16Y_M t^3}\left(1-\left(\frac{r}{r_0}\right)^2\right)^2 \tag{A.2}$$

Where $w(r)$ is the membrane deflection at a distance r from the centre, P is the applied pressure, r_0 is the radius of the membrane, ν is the Poisson ratio, Y_M is the Young's modulus of the membrane material and t is the membrane thickness. For a given valve structure, the radius is clamped which leaves only the pressure and membrane related properties to tune the valve performance. Of these parameters, the deflection pressure is limited by the logistics of the lab (our house air and vacuum ranges within the lab are +138 kPa and -70 kPa respectively) and the tear strength of the membrane. Thus, tuning valve performance typically comes down to the membrane properties.

Polydimethyl Siloxane (PDMS) is a very common material used in the literature for valve membranes due to its high Young's modulus and ability to be easily patterned within the lab with soft lithography. However, PDMS is not readily manufactured in high throughput processes[9] due to long cycle times.[?] Thus it is inherently unsuitable for scaled up manufacturing, which is orthogonal to the objectives of this research project. Furthermore, it is hydrophobic, and typically requires transient hydrophilic treatments to get adequate performance.[92] Most importantly, PDMS is gas permeable which leads to the potential for air bubbles entering the fluidics, cross-contamination concerns and fluid loss.[92,102] A valve based heavily on PDMS is thus very unlikely to satisfy the valve module requirements. Relatively little work has been done that integrates non-PDMS membranes with rapid-prototyped fluidics. Much of the development motivation for the LOC valve was to develop methods of integrating different membranes with our rapid-prototyped fluidics.

The first membrane material used in the lab was polypropylene (PP), and was pioneered by Tianchi Ma. Specifically, a 40 μm thick sheet protector (10524, Staples Canada). This material was very rigid (Y_M=2 GPa), leading to very little deflection. However, this was offset by it being very thin and readily purchased at low cost. Polypropylene is also PCR compatible and fairly inert. The membrane was functional due to the manifold structure used and was used for fluid pumping in an application that was published.[115] However, there were a number of issues with the material that prevented a valve using the PP membrane from achieving the requirements in Table A.2. Firstly, the actual pump stroke volume was approximately 4x higher than expected, suggesting that the material properties of the film were not well understood. Further, it was found that the pump did not reliably self-prime. It was thus possible to perform a demonstration with the membrane under controlled conditions, but use as part of a wider infrastructure would have been ill advised. Finally, while no leaking of fluid through the valve was ever observed, the valve was not air-tight at either room temperature or elevated temperatures. The high Y_M means the membrane was not conformal enough to effectively seal the via structures, likely due to the "lipping" caused by the laser ablation step. This refers to the tendency of materials to protrude upwards out in the vicinity of an ablation point and this lip would prevent the PP from sealing. While many techniques have been developed to reduce the effect of lipping, this issue highlights the difficulties in using a non-conformal membrane in that the material must be extremely flat to make air-tight seals and it was not apparent that such a flat surface was achievable given the source materials and fabrication equipment

available. The lack of an air-tight seal prevented PCR applications (where the lack of seal would allow evaporation of the analyte through the valve structure), despite the chemical compatibility of its surface. Thus there was a need for a conformal membrane material.

The second membrane material tested was nitrile rubber. The hypothesis was that a reduced Y_M of roughly 2 MPa (three orders of magnitude lower than PP) would enable higher pump stroke volumes, self-priming of the pump and improved sealing due to being more conformal. However, sourcing a thin nitrile was difficult. Two main thickness were tested, a 794μm thick sheet purchased directly (86715K269, McMaster-Carr) and a 60μm thick nitrile glove. The thick sheet was capable of air-tight seals, however, was too thick to behave reproducibly; the thick material compressed when the manifold was lowered leading to uneven valve performance. This compression meant the valve performance was a strong function of the amount of force used to hold down the membrane and made practical implementation of a reliable valve impossible. Further, being an order of magnitude thicker than the PP membrane, it had a low pump stroke volume and could not self-prime. The nitrile glove was found to be surprising good fit with improved pump stroke volumes, capable of self-priming and potential for retaining fluids at elevated temperatures as evidenced by retaining a 2 μL water sample for over 30 minutes at 95 ^{o}C. Based on these parameters it was used in an application detailed in Section 5.3. However, the membrane material still had a number of deficiencies that led to the development of other membrane materials. Firstly, the pump stroke volume was found to be too high for many applications, and varied fairly substantially ($\approx$ 30%), leading to uneven performance. The hypothesis for this error was the high potential for thickness variations in the glove material, though this was not assessed at the time. Further, while preliminary tests showed a good seal was possible, this seal was highly operator specific and thus was not reproducible. Thus, while it had successfully held fluids at elevated temperatures, it also leaked during some tests. This was attributed to the fact that the nitrile gloves were intentionally textured to assist the user's grip. This is a desirable trait for a laboratory glove, however this likely interfered with the material's suitability as a valving membrane. For these reasons, work was discontinued on the nitrile gloves.

Currently, the laboratory is using a thermoplastic elastomer Enflex (S4055A CL NAT, Enplast Americas). This material has a Y_M comparable to nitrile at 1.5 MPa and is easily thermoformed. This allows for tuning of the membrane thickness and is a notable improvement over the nitrile membranes. The initial fabrication protocol was developed by Tianchi Ma, and was a two step process. First, a 1 mm thick sheet of elastomer is made by heating pellet material at 200 ^{o}C for 1 hr sandwiched between tempered glass plates pressed together with binder clips. This 1 mm sheet is diced into $\approx$ 60 mm x 4 mm strips that are then recompressed to a final thickness of 200 μm. This second level of compression was done by sandwiching the material between glass microscope slides with a 200 μm spacer, applying pressure with binder clips, and placing the assembly in the oven at 200 ^{o}C for half an hour. This fabrication procedure was an excellent start and produced membranes that met most of the target requirements such as reliable sealing, ability to seal against elevated temperatures, pump stroke volume of 0.31 μL with a reproducibility of 6.5%. These properties were tested in an unpublished manuscript that is available in the SI. However, the fabrication process was quite sensitive, and was not well reproduced by other students. This led to a substantial increase in the standard deviation of pump stroke volume to nearly 40%, which does not meet the requirements of the module. Furthermore, the fabrication resulted in a fairly low yield as many membranes became spoiled due to broken glass slides. To address this issue, a milled aluminum jig was developed for reliable membrane fabrication. The jig contains two chambers that were 25.4 mm x 76.2 mm x 0.2 mm in size with pressure release holes at either end. The jig was made with sub 10 μm roughness and accurate to $\approx$ 2 μm thickness. Size 6 screws are used to attach a similarly built top plate

that compresses the strip. This jig yielded a more reproducible thickness and had a much higher yield. Testing of the jig was done by Rob Bennett, and the resulting membrane thickness was found to have a standard deviation of 5.2%, an improvement from the roughly 36% variation seen with the old protocol. Equation A.2 shows a the pump stroke volume relates to the third power of the membrane thickness. Thus, this improvement was crucially important for controlling this parameter. Further, the yield of membranes has approached unity, which was very advantageous for future valve development.

Table A.3 summarises the properties of the membranes used. As the only membrane capable of meeting the valving requirements, Enflex is recommended for future use.

Material	Y_M (Mpa)	t (μm)	Estimated Stroke Volume (nL)	Measured Stroke Volume (nL)	Sealing		
					Fluid	Air	Heat
Polypropylene (10524, Staples Canada)	2000	40	163.8	394 [118]	Yes	No	No
Nitrile Glove (KC300, Kimberly Clark)	2	50	6290.3	Unmeasured	Yes	Transient	Transient
Nitrile Sheet (86715K269, McMaster Carr)	2	800	98.3	Unstable	Yes	Yes	Yes
Enflex (Enplast, S4085 CL NAT)	1.5	$271 \pm 5.2\%$	67.1	145	Yes	Yes	Yes

Table A.3: Table summarising the various membrane materials used in the valve testing. The only material capable of satisfying the requirements of the valving module is Enflex.

A.2.3 Manifold fabrication and testing

One of my contributions to the microvalve project was the design and fabrication method development for the manifold. The manifold is the re-usable piece that interfaces the microfluidic valve with the pneumatic actuation lines by creating a sealed pressurised chamber above the membrane as shown in Figure A.4B and C. There were two key connections that needed to be made: a connection between the actuation lines and the chamber, and a method of sealing the chamber against the valve membrane. For all of the iterations described below, a force was required to hold the manifold down onto the membrane. This force was applied through four screws as shown in Figure A.5. I have developed two methods for handling each interface, briefly described below. The current manifold design enables reproducible behaviour on Enflex membranes while being very convenient to connect and disconnect from the system.

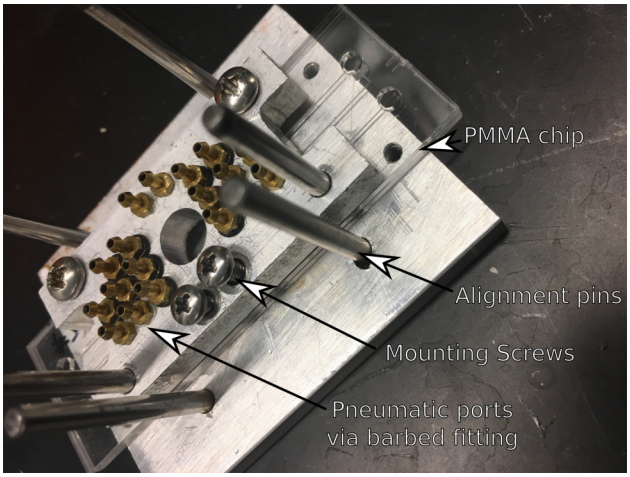

Figure A.5: Picture of the aluminum manifold that forms the pneumatic interface with the fluidic chip. Pictured are the alignment pins and screws that are used to align the pressure chambers to the valve structures. The brass barbs allow easy connection of $^1/_{16}$" ID tygon tubing for connecting actuation line. These barbs connect to an air chamber that is above the membrane (not visible). The pins and screws in the base align the manifold to the chip/membrane, enabling easy connection and disconnection of the system.

Early manifold designs were built through CNC machining of PMMA or PVC. This was largely due to the limitations of my milling technique at the time as both PMMA and PVC are soft materials that are easy to machine. For these manifolds, the connection between the pneumatic actuation line and the manifold was accomplished through the use of a low-viscosity acrylic glue. $^1/_8$" OD, $^1/_{16}$" ID tygon tubing was coated with glue (1668383, LePage) around its circumference about 3 mm from the end and gently pressed into a hole that was 3.20 mm (0.126") in diameter. This resulted in an air-tight seal with the slight gap between the tube end and where the glue was placed ensuring that the glue did not seal the chamber. While a viable fabrication method, this approach had a number of drawbacks. Most significantly, the combination of a relatively rigid glue with compliant tygon tubing made the interface very fragile. This was later alleviated by inserting 5-10 mm of $^1/_{16}$" OD steel tubing into the tygon before gluing (thus making the tubing that is glued rigid), but it was never robust enough for very extended use. Further, in the case of the glue seal breaking, it was difficult to assess and repair the piece. Finally, the glue style connection relied on the manifold being made from a polymer. This became problematic over time as the pressure used to hold the manifold down onto the membrane began introducing creep into the manifold material, leading to short instrument lifetimes. Thus, this approach interfered with the requirement of reliable, error-free operation and was discontinued. Manifolds with glued connectors were used in application detailed in Sections 5.3.

As fabrication processes became more refined, the manifold reliability was addressed through the move to CNC machined aluminum. This necessitated a new style of pneumatic attachment to replace the previous "glue" method (which was not compatible with metal manifolds). The approach used was to take miniature barbed fittings (5454K74, McMaster Carr), place a small o-ring (9263K545, McMaster Carr) over the threads and screw the assembly down into size 3-56 tapped hole. This proved to not only be a more robust connection, but also allowed for the tubing to be easily connected/disconnected from the manifold. The one disadvantage was a very slight increase in the minimum spacing between pneumatic lines by 400 μm to the current pitch limit of 4.2 mm. The manifolds currently in use utilise this

design, including the next generation instrument in Section 5.5.

There were two methods used for the manifold-membrane interface. The first, and most generally useful method, was to place small o-rings (9263K545, McMaster Carr) into a recess milled into the bottom of the manifold. The manifold was then firmly tightened until the manifold surface was flat against the membrane and the o-ring was compressed to make a seal. These particular o-rings had a thickness of 1 mm, and we found empirically that sinking them 864 μm into the manifold was ideal for this application. The main advantage to this method was that the seal could be readily made with a wide variety of membranes, including rigid, non-conformal materials like polypropylene. We note the work on rigid membrane materials for LOC applications recently patented by the company Rheonix [192] that also uses a manifold style attachment. The o-ring style manifold was implemented in both polymer and aluminum manifolds and used in the application detailed in Section 5.3. However, recent measurements suggested that for certain membranes the o-ring style connection can lead to lower reliability, specifically thicker, compliant membranes such as the 250 μm elastomeric membranes used recently. The Young's modulus of enflex and viton are very similar. Thus, when pressure is applied by the user to secure the manifold not only does the o-ring compress, but so too does the membrane itself. To relieve the compression of the membrane, the membrane expands into the most readily available relief region, the pressure chamber. Thus, this causes the valve to unseal slightly and changes the performance of the valve. This leads to the structure being sensitive to how much force is being applied to the manifold, and a lack of reproducibility, a behaviour that was noted for the very thick nitrile membrane material (794 μm thick) to a much greater extent.

To address this issue the o-ring was removed in favour of milling a micrometer scale barb into the manifold bottom. The rationale was that the issue with the o-ring style was that the membrane was too conformal, suggesting that the membrane itself could function as the conformal component to seal pressurised chamber. Initially, the o-ring was simply removed, however this led to the need for very low surface roughness on the microfluidic chips and very high force applied to the manifold to get reliable seals. This high force again caused local deflection of the membrane and uneven valve performance. Therefore, a 10 μm high, 248 μm wide barb was carefully milled locally around each pressure port. The manifold was then tightened to the membrane until a sudden increase in resistance was felt when tightening the screws. This resistance increase was attributed to the vast increase in surface area compressing the membrane as the 10 μm barbs would be fully embedded, and thus sealing the chamber. Using this piece, the standard deviation of the pump stroke volume was decreased to $\approx 10\%$, which meets the requirements in Table A.2. Details of this work will be reported elsewhere.

A.2.4 Pneumatic Instrumentation

The use of pressures and vacuums to actuate fluid movement in LOC systems is very common, having been used to directly manipulate flows [193] as well as to actuate valves that interact with the fluid. [194,195] Specifically, the Backhouse group has been using pneumatically actuated valves for some time [80] due to their ability to be rapidly actuated and the simplified physics of operation as compared to other actuation methods such as phase change [196] or electrostatic. However, in order to use pneumatic valves the user must be able to program the system to toggle various lines with either pressure or vacuum. The pneumatic module designed to perform these toggles is described here. The electronics used to drive this pneumatics module is described briefly below in Section A.2.5.

The pneumatics modules have been designed around a miniature solenoid valve (LHDA0523112H, Lee Company) which provides the pressure switching function. In order to have multiple pneumatic lines, a series of pneumatics modules have been developed that connect the solenoid valves in parallel. There are two primary variables that need to be considered when designing these modules: the pneumatic volume being switched and the airflow rate into that volume. The switched volume here refers to all space after the solenoid valve, which essentially is composed of the air chamber above the membrane and the volume of the tubing that connects this chamber to the solenoid. The airflow rate into this volume is limited by the narrow solenoid port and the diameter of the feed-tubing into the module. This can be offset by designing an air chamber the solenoid can draw from, which essentially acts as a buffer. In the case where the volume being switched is high compared to how fast the volume can be filled, the act of switching a pressure line will cause a perturbation on other pneumatic lines. This leads to crosstalk and unreliable operation.

Previous work by Kaigala et al.[80] used a similar miniature solenoid valve, however it used "barbed" style valve. This eliminated the need for a pneumatics module as the solenoids could be connected with small diameter tubing. However, while convenient and easy to implement, this eliminated the possibility of a buffering air chamber and constricted the airflow into the pneumatics system. Thus, this approach was highly susceptible to valve crosstalk. The work described here uses a "panel mount" style miniature solenoid, thus enabling the mounting of the solenoid directly to the module.Two styles of pneumatics module were developed: a block-style module which was optimised for robustness, but was large and therefore best suited for bench-top prototyping described in Section A.2.4 and a mini-style module which was optimised for size to be integrated into systems described in Section A.2.4. Both of these designs present improvements over past systems in that they can accommodate 18+ valves and are capable of valving reliably at 10 Hz with no crosstalk in accordance with the requirements outlined in Table A.2.

Block-style pneumatics module

The block-style pneumatics module was optimised for high reliability for bench-top prototyping of microfluidic systems. Since the target application was on a bench-top, there was requirement for the module size. However, one constraint was that the tubing used to connect the module to the chip needed to be much longer in a bench-top usage scenario, leading to very high switching volumes. To address this issue, a large pressurised chamber to supply the solenoids was implemented to create as big a buffer as possible. Further, the tubing connecting the blocks to the house air/vacuum had an inner diameter of $^1/_8$". This ensured a high airflow rate into the blocks. These valve modules combine with work done by another student, Tianchi Ma, to form a microfluidics testing station. Implementation details for the operation of the station are available in the SI.

The block-style pneumatics module comes in two parts: the base and the lid. The base was made from 1.9 cm thick aluminum and had two deep trenches milled into it. These trenches connected to $^1/_4$" NPT threaded fittings with shark bite style connectors to attach tubing providing air/vacuum. A nitrile gasket was placed over the base and the lid was attached with size 6 screws to form an air-tight container. The lid contained holes for mounting the panel mount solenoid valves as well as the valve outputs. The outputs pass through both the lid and base to the other side where miniature barbed fittings were placed to allow easy attachment of $^1/_{16}$" ID tygon tubing. This design was technically scalable to any number of solenoid valves per module, though modules currently in use have only six valves present due to limitations on the previous pneumatics actuation electronics. A CAD drawing of the block style module is

shown in Figure A.6a and a picture of the module is shown in Figure A.6b. CAD files for this module are available in the SI.

This block style was tested up to 10 Hz with tubing up to 30 cm in length with no observed crosstalk in a variety of fluidic configurations showing no erratic performance, uncontrolled valve toggling or fluid leakage. The module has since been used in on-going experiments for upwards of two years as a standard instrument for valve development in the Backhouse group. Thus, this design meets the requirements of the pneumatics module.

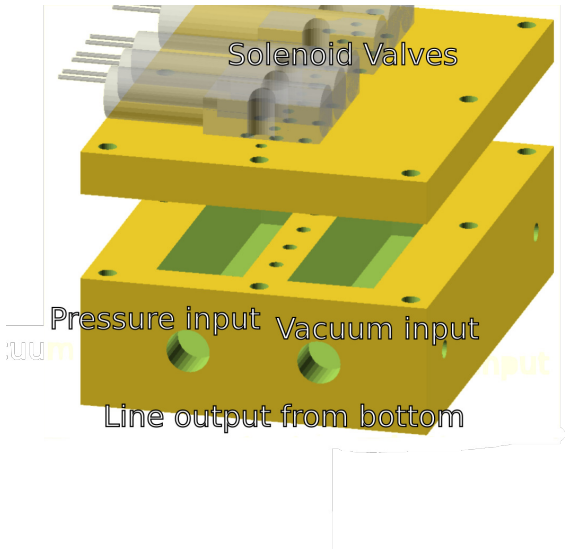

(a) A model of the block style pneumatics. The module comes in two parts. The base contains two deep trenches and ports for attaching air/vacuum. The lid mounts the solenoid valves. The two parts attach together with size 6 screws around the outside. A nitrile gasket (not pictured) sits between the layers to ensure an air-tight seal

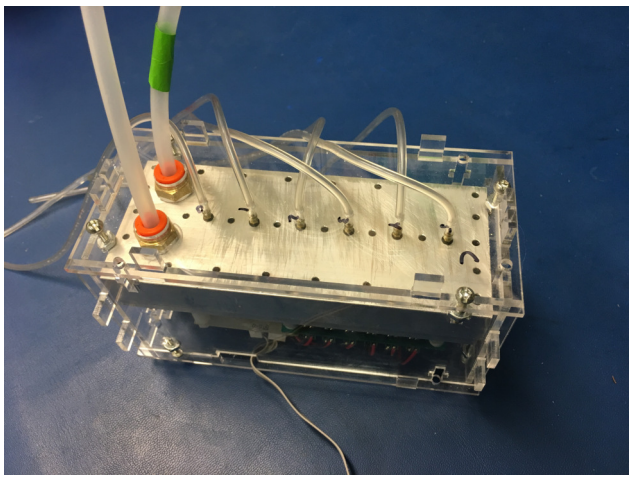

(b) A picture of the block style pneumatics module with tubing connected. Due to its larger size, it is much easier to interface with on a benchtop and well suited for valve prototyping

Figure A.6: The block-style pneumatics module

Mini-style pneumatics module

The mini-style pneumatics module was optimised for integration into instruments. In contrast to bench-top applications, the size of the module was now very important. Thus, the mini-style module had to be much smaller than the block-style module. Another difference in the design was that within instruments the volume of tubing used is typically much less. For example, the most recent instrument has ≈10 cm tubing, 3x less than the benchtop instrument. This allows for size savings from reducing the air chamber volume used to buffer the pneumatic lines. Two iterations on the mini-style pneumatics were done, with one in PMMA used in the instrument from Section 5.3 and the newer version in aluminum used in the Next generation instrument in Section 5.5. The newer version addressed the issues of the early iterations with more robust construction, eight solenoids per block and are capable of effectively switching at 10 Hz with no crosstalk.

The principle of the mini-style module was to put the valve, input and output on different faces of a rectangle such that the input and output holes can be offset from one another vertically. The result was a small part that could be readily mounted inside of an instrument and manufactured from a single block of material. Figure A.7a is a picture from the bottom of an early mini-style module built in PMMA, with all of the access ports clearly visible. Air and vacuum lines come in from the left and are connected to each solenoid. The solenoid output was routed towards the page, over the input lines, then to the top, terminating in recessed o-rings. Two 6-32 screws on either side of the block could then be used to screw it to a panel, compressing the o-rings and making a seal to that surface. This early version was functional, however there were a number of issues that needed to be addressed. Firstly, the glued connections for the air-input led to a very low input air flow rate. This, combined with the limited diameter of the air chambers, led to crosstalk. The crosstalk was exacerbated as more modules were added in parallel, thus precluding larger integrations. Further, the glued connections were very fragile and prone to leaks, which reduced reliability and made troubleshooting difficult. Fabrication methods at the time limited the number of valves per module to five (Figure A.7a has only four). Thus, in order to get 22 valves the user would need five parallel modules, a poor strategy given the cross-talk issues observed. This mini-style module therefore did not meet the design requirements. However, they were usable for relatively simple applications where only five valves or less were required, such as the application demonstration in Section 5.3.

The upgrade to a larger CNC machine and improved fabrication processes enabled a next generation block with more capabilities. Specifically, the block material was changed to aluminum, a much sturdier material. This enabled improved alignment, as well as more robust connections. A larger diameter drill (4.04 mm up from 3.125 mm previously) increases the air-chamber volume while also improving the air flow into the module, thus addressing the crosstalk issue previously encountered. Finally, each block can now accommodate eight valves. This was convenient as the electronics used also toggle eight valves per IC. Figure A.7b shows a CAD model of this block and Figure A.7c shows a picture of the module mounted inside of an instrument. The CAD and tool path designs for the CNC are available in the SI. The 3x8 position aluminum style blocks are used in the current instrument described in Section 5.5, giving a total of 24 valves. This exceeds the requirement detailed in Table A.2.

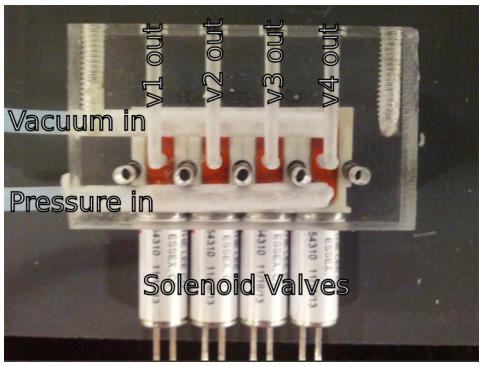

(a) The bottom view of a PMMA mini-style pneumatics module. Air and vacuum is brought into the module via tubing from the left of the image. These lines are shared with all of the solenoids. The output is routed first towards the page, over the input lines, and out to the top. Each output is terminated in a recessed o-ring for panel mount applications.

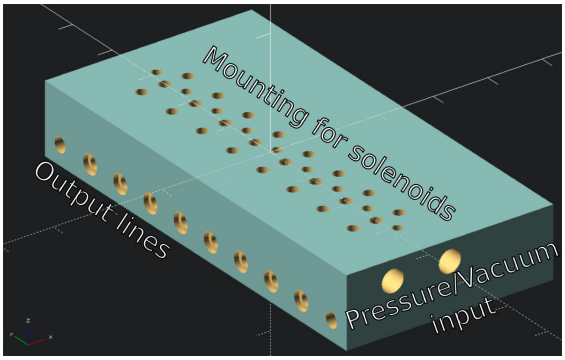

(b) A CAD image of the larger mini-style module with eight valves available. The input holes have also been widened to increase chamber volume and accommodate a barbed fitting. The output style is generally the same as A.7a.

(c) A picture of an aluminum module mounted within a system. The input tubing is now much larger (1/8" ID tygon tubing) and more easily connected.

Figure A.7: The mini-style pneumatics module

A.2.5 Control Electronics

The solenoid valves used in these modules require a 5 V, 150 mA source applied across their leads in order for the valve to switch. Initial designs used digital outputs to toggle a MOSFET driver (MIC 4422), which in turn switched a 5 V supply, similar to the method initially used for HV control above in Section A.1.2. This worked well initially when only five valves were needed. However, as the number of valves increased this became very cumbersome to deal with both in terms of the number of digital control lines, but also in terms of the number of components (one IC and two capacitors per valve). To address this issue, as well as make the instrument more compatible with the standard SPI used in the rest of the infrastructure, a power logic circuit based around the TPIC6A595 was implemented. The TPIC6A595 operates similarly to a standard 595 logic chip in that it accepts a serial signal and converts it to a parallel out. However, unlike standard chipsets, this IC can sink up to 350 mA per output, and is thus compatible with the Lee company valves. In order to provide 24 valves, three power logic chips were daisy chained such that they share common clock and latch pins with the serial communication being chained using the SEROUT pin. Figure A.8 shows the communication flow. This circuit was implemented on the same PCB as the HV electronics as described briefly

in Section F.2.3, with design files available in the SI. Both the old and new styles of control electronics meet the minimum requirements of the module (reliability and switching speed at 10 Hz or better), though neither are USB power compatible due to the high current drain from the solenoid valves.

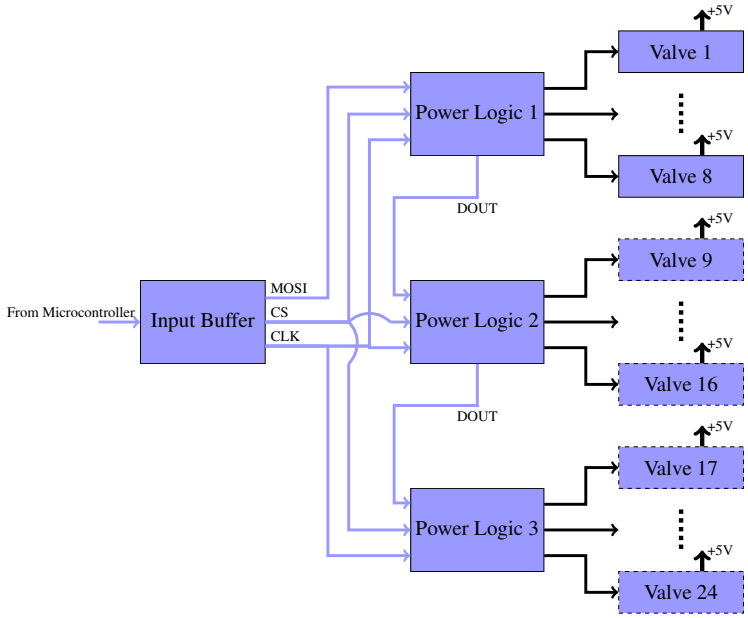

Figure A.8: A diagram of the pneumatics instrumentation signals and voltages. The circuit uses SPI, that is first passed through a buffer for improved signal reliability, to control 3 chained power logic chips. The power logic toggles outputs between a float and a ground thus enabling current through the solenoids and opening of the valve. Each power logic chip is connected to eight solenoids, giving 24 total valves.

A.2.6 Future Work

In terms of construction purposes, the final version of the two valve module designs were reasonably well optimised and proven to work well for these applications. However, one issue was their reliance on the Lee company solenoid valves which draw a substantial amount of current (150 mA each) to actuate. Many of the protocols that we have run in the past have required four to five valves to be opened simultaneously, a total draw of 600-750 mA. This is beyond a USB power budget, meaning that this approach will always require an external supply. The Lee company also market a three way latching valve where the valve is toggled between states with a brief (10 ms) pulse. This would drop the power consumption of the board by nearly an order of magnitude. However, this would require a change in electronics and software.

A.3 Thermal Instrumentation

There are three components to a successful PCR: instrumentation, thermal design and biochemistry. This thesis deals solely with the first of those. The main figures of merit when considering a PCR system are the thermal uniformity

and the time constant for heating/cooling. Uniformity is a central issue as PCR is very temperature sensitive with the annealing step typically requiring the entire reaction volume to be held to a certain temperature within 1 ^{o}C.[53] The binding of the primers to the DNA is a strictly thermodynamic argument, and if the temperature drops below the target level this will allow non-specific primer binding, and thus non-specific amplification and corruption of the experiment. On the other hand, annealing at too high a temperature leads to low binding efficiency of the primers to the target DNA and thus low amplification efficiency. The time constant for heating and cooling is also important as the less time is wasted cycling between temperature steps, the faster the reaction can proceed. This is important as an excessive time at high temperature can spoil the polymerase and reduce the amount of amplification obtained. Ultimately, both the uniformity and the time constant are predominantly functions of the thermal design, which is beyond the scope of this work. However, what is required is flexible thermal instrumentation that can accommodated a wide variety of thermal designs such that future work can use it as a base to implement optimised designs.

There are three primary subsystems to the thermal instrumentation: heater driving, temperature reading, and a controller implementation. The vast majority of commercial benchtop PCR devices use a thermoelectric module to control the temperature as it can provide both heating and cooling. These devices work by utilising the Seebeck effect to generate heat, and the Peltier effect to actively cool down the surface. This active cooling can be used to speed up the rate the system can thermally cycle. While CMOS built thermoelectric modules are being developed in the literature, these modules do not have the ability to source and sink temperature effectively over the PCR range with USB-compatible power requirements.[197] Thus, to maintain scalability for future systems, the Backhouse group has focused on designs that use resistive heating and passive cooling,[53,80] thus giving up active cooling. The approach taken by Martinez-Quijada et al.[53] was to place the heater in intimate contact with both the reaction chamber and a heat sink, encouraging as much passive cooling as possible. This has allowed for the development of systems that are much lower power, lower cost and lower complexity than Peltier based systems. It is expected that future designs will similarly follow a resistive heating/passive cooling mode of operation, so it is important that any instrumentation be capable of driving a broad range of heaters. To this end, the instrumentation must be capable of at least 400 mA output to be compatible with previous systems,[53] and ideally should be capable up to 1A. The overall power is expected to be on the order of 1 W, though the voltage driving the circuit must be flexible to include a variety of potential resistances. The driving circuit is discussed in Section A.3.3. Temperature reading for LOC systems is challenging as it is difficult to ensure that the mechanism of measurement is intimate enough to be indicative of the temperature of the reaction volume, while being sufficiently separated to ensure that it does not perturb the thermal uniformity of the system. The approach taken in this work is to embed a very small thermocouple in a thermally conductive plate, which is in intimate contact with both the heater and the PCR reaction chamber. A thermal controller is then used to control the temperature of this plate to a a given temperature. This controller must update faster than 10 Hz in order to reliably control the temperature on a time scale on the order of seconds or better. The plate approach gives the thermal simulations a standard boundary condition to operate with, and simplifies the instrumentation design. Implementing the measurement is discussed briefly in Section A.3.2, while the thermal controller is discussed in Section A.3.5.

A.3.1 Requirements

The requirements for a general purpose thermal instrumentation module are that it can implement a variety of thermal designs. This involves planning for a range of resistive heaters (and a wide operating voltage and current range) and

time constants. In terms of heaters, a number of different resistances and power densities have been investigated, some built from the ground up in the lab and some purchased off of the shelf. The heater drive circuit must be capable of taking inputs at 5 V (USB-power), 12 V (standard wall wart supply) and ideally 35 V (maximum output from a lab bench supply), and controlling current up to at least 0.5 A (ideally 1 A). This corresponds to 5-17.5 W of power, which is considered very high for a LOC application, though these values are for prototyping only and future miniaturisations will reduce them. Depending on the thermal controller implementation, precise current control is not necessary as the controller can theoretically compensate. Thus, current setting must be done within 10%. However, what is needed is a reliable and consistent response to the thermal controller output (i.e. a call to increase temperature always results in an increase in current). This means that current stability and drift are important and must be kept under 1% over a time period of 1 minute (typical time periods for PCR are sub-minute). Temperature measurement must be reproducible within 1 ^{o}C for the sub-1 ^{o}C temperature control required for PCR. In an ideal world the time constant for the thermal design is very low and the time taken for each temperature step is about 20s or less. Thus the thermal controller must have an update rate much faster than this, and a requirement of 10 Hz or faster has been set. The combination of the controller, measurement and heater drive all must ensure that the instrumentation does not limit the thermal system time constants (i.e. the system can heat and cool at its maximum rate based on the thermal design). Finally, the controller must be optimised to ensure that the controlled volume temperature does not "overshoot" the set points. Specifically, it is crucial that the temperature does not dip below the set annealing temperature (as this would result in non-specific binding and corruption of the PCR) and does not exceed 100 ^{o}C (as this would cause a drastic increase in pressure as the sample boils). Finally, the controller must be capable of reporting the temperature with respect to time and reporting this data in a manner consistent with the rest of the system infrastructure. These requirements are summarised in Table A.4

Parameter	**Requirement**
Maximum Heater Voltage	$>$ 12 V, ideally $>$35 V
Maximum Heater Current	$>$ 500 mA
Current set accuracy	Within 10%
Current stability	Within 1% per minute
Temperature reading reproducibility	0.5 ^{o}C
Controller update rate	$>$ 10 Hz
System capable of	Rapid heating
	Rapid cooling
	No chamber overshoot
	Communication with system infrastructure

Table A.4: Table of requirements for the thermal subsystem

A.3.2 Thermal measurement instrumentation

Thermal measurement was done with a standard thermocouple, where the Seebeck effect causes a voltage difference across a metal-metal junction that correlates to the temperature. However, this generated voltage is relative, thus there is a need for temperature compensation (termed cold-junction compensation). For this function the MAX31855K chipset was implemented, a single chip ADC that operates from a single-ended power supply and converts a thermocouple reading to a 12-bit digital output with cold junction compensation and an SPI interface as shown at the

bottom of Figure A.9. The advantages of this method was the simplicity of implementation and the use of standard thermocouples with known accuracy and stability. The design provides temperature readings reproducible to 0.25 ^{o}C and can be readily probed at higher than 10 Hz, thus meeting the temperature reading requirements. However, the main disadvantage was that even micro thermocouples are quite large in comparison to LOC dimensions and thus will have an effect on the thermal performance of the system. Therefore, this required the system to be designed around the thermocouple. The approach to thermocouple integration (as detailed below in Figure A.11) was to embed a small thermocouple in a thin layer of metal which has a thermal conductivity about three orders of magnitude higher than the polymer fluidic chip. This resulted in a "pad" of known temperature. Provided that the separation of the chamber from this pad was small, this allowed for the control of the reaction chamber. Thermal simulations of comparable structures had been done by the Backhouse group to verify this assumption.[53,118] Thin metallic disks were readily produced through CNC machining brass or copper shim stock that was readily available at the engineering machine shop.

A.3.3 Heater drive instrumentation

The heater driver used was based on a floating load op amp current source circuit shown in Figure A.9. The op amp controls the voltage drop across the output resistor to be the same as the analogue voltage applied to the op amp - terminal. This voltage drop sets a current that flows through the npn transistor and thus the heater. This circuit was tested to up to 1 A with an error of about 5% and an off current of 3 mA. This offset was reproducible and appeared to originate due to a voltage offset and nominal ground resistance between the heater circuit and microcontroller within the box. This could likely be rectified with a robust PCB design (as the prototype circuit was implemented with low-performance protoboard). Ultimately, the absolute accuracy of the heater drive current was not relevant provided the error was reproducible as the temperature controller can fully compensate for consistent offsets. The circuit required a set voltage (0-1 V mapped to 0-1 A) and operated from split $\pm$5 V rails for the op amp and a V+ rail that supplies the heater (voltage requirement depends on the heater resistance, for an early iteration this was +30 V). The set voltage was supplied by a DAC.

A.3.4 Overall thermal instrumentation

Figure A.9 shows the implementation of the thermal instrumentation. The instrument was based around a thermal controller which provided a serial protocol interface (SPI) to both a DAC and an ADC, with the DAC controlling the current source and the ADC providing the cold-junction compensated temperature reading. The thermal controller accepted the temperature reading and set the current based on the specific controller algorithm implemented as described below. A master microcontroller which controls the thermal instrumentation as well as other functions of the instrument (i.e. HV, valving, detection) communicates with the thermal controller. This communication involved passing a set temperature to the thermal controller and the controller passing back the measured temperature. Two iterations on this design were implemented as described below. The first was a design with a controller heavily optimised for a specific thermal system (and thus was not transferable to other thermal designs) that was constrained by a limited master microcontroller. This was later improved in the second design which implemented a standard interface of commands

that could be readily re-programmed on the fly.

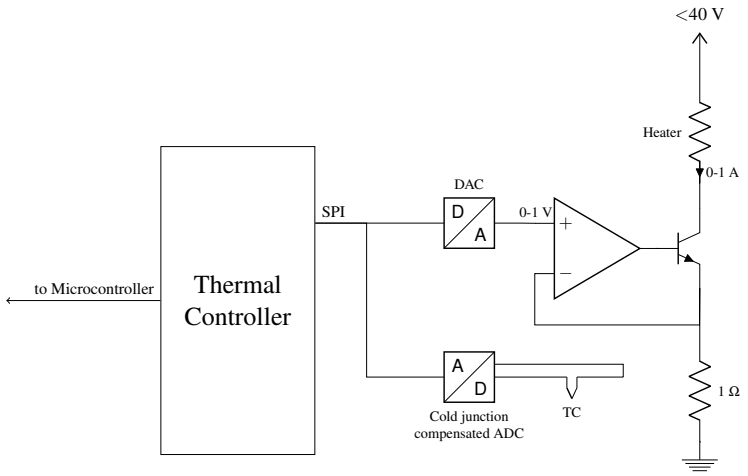

Figure A.9: A rough schematic of the thermal instrumentation. A thermal controller (Arduino or Teensy microcontroller) provides SPI communication to both a DAC and ADC. The ADC is the MAX31855K which digitises the thermocouple reading and provides cold-junction compensation. The DAC drives a floating load current source circuit that can provide up to 1 A of current. The applied voltage is flexible and can be up to 40 V (limited by the transistor used). The thermal controller communicates with the rest of the system either using analog signals as in the V1 design or UART as in the V2 design.

A.3.5 Thermal Instrumentation v1

The first iteration of the thermal instrumentation was designed with an Arduino (ATmega328, Atmel Corp) as the thermal controller and was designed to fit a system that had a well defined thermal design and a LabJack U6 master microcontroller. The LabJack presented a design challenge as its digital communication protocols were very poorly documented at the time of design. This forced a creative solution where the communication between the master microcontroller and the thermal controller was done with analog signals. Specifically, a temperature reading was developed where temperatures from 0 to 100 ^{o}C were mapped to 0 to 10 V. An extra DAC and ADC were added to the thermal controller to send the current temperature and receive set-temperature information from the LabJack. Offsets and noise in the analog signals led to a temperature set/read accuracy of 0.5 ^{o}C, which is more than the 0.25 ^{o}C that the MAX31855K ADC is capable of. However, this error was still within the requirements for PCR instrumentation.

The first iteration was based around a thermal design that is detailed in the thesis of Tianchi Ma [118] and discussed briefly in Section A.3.8. This allowed for an aggressive controller algorithm to be implemented for optimised performance. Specifically, a PID algorithm was adapted to include special provisions on heat-up and cool-down operations (i.e. if a new set temperature was above or below the current read temperature). On heat up, the controller runs at maximum current until within 10 degrees of the set point at which stage the PID controller becomes active. This minimized the heat up time of the heater with only an overshoot of the setpoint on the first melting step as discussed below. On cool down, the controller runs at 0 current until close to the set point (defined by the equation $\frac{T_{set,old}-T_{set,new}}{T_{set,new}}$, where $T_{set,old}$ is the previous step's set temperature and $T_{set,new}$ is the current step's set temperature). This maximized the cool down rate of the system with minimal to no overshoot. The controller first calculated a series of errors as in Equations A.3.

It then used the errors to determine the appropriate set current for the heater in Equation A.4. After calculating the set current, the controller ensured the current did not exceed 400 mA (the maximum for the heater used) or go below 0 mA (which is non-physical). Finally, the PID modifications were introduced and the current was sent to the current control circuit. The PID algorithm is available in the SI.

$$\begin{aligned} e_{new} &= T_{set} - T \\ e_{diff} &= e_{new} - e_{old} \\ e_{sum} &= s_{sum} + e_{new} \\ e_{old} &= e_{new} \end{aligned} \tag{A.3a}$$

$$i = kI \times e_{sum} + kP \times e_{new} + kD \times e_{diff} \tag{A.4}$$

where T_{set} is the set temperature, T is the temperature read from the thermocouple, e_{new} is the error, e_{old} is the error from the previous step, e_{diff} is the change in error, e_{sum} is the sum of the error, i is the set current, $kI = 0.0005$, $kP = 0.0391$, $kD = 0.1$. These values were determined empirically for this thermal design using after manual PID tuning. Briefly, this involved first setting kI and kD to 0 and increasing kP until oscillations occurred for a step response, then setting kP to half the value that caused the onset of oscillation. Next, kI was increased until the set-point offset from a pure kP controller was removed. Finally kD was increased to reduce offset and improve settling time. PID tuning, in general, is highly specific to the system being designed for and thus these parameters are useful only to this thermal design. Further, the modifications to the PID controller were also well tuned to this design. Thus, for other thermal systems a new algorithm would have to be made and uploaded to the thermal controller.

There are three main requirements of the controller algorithm: rapid heating, rapid cooling and no chamber overshoot. The rate at which a PID controller reaches setpoint can be further optimised from equation A.4 given appropriate knowledge of the system's time constant for response. The rate of heating and cooling are limited by the range of supply currents (400 mA and 0 mA) that the heater can take. In terms of heating rate, there was not much that can be done beyond the 400 mA supply. However, the cooling rate could be somewhat optimised. Specifically, a provision was programmed into the controller where on a cooling step the heater was forced off until the temperature cooled to 75% below the previous set point. At this stage the e_{sum} value was pre-initialised to a value of $6.63*T_{set}$. While non-standard, it was empirically found that these values reliably allowed the instrument to cool down as fast as possible across a range of relevant temperatures. The chamber overshoot was a key issue, especially with regards to the cooling step. Overshoot can be caused by the e_{sum} becoming too large. To prevent over-shoot for heating phases, the e_{sum} was capped at 0 until within 10 ^{o}C of the target. The e_{sum} for the cooling step was taken care of with the pre-initialised value. This damped the cool-down phase, but also ensured that there was no overshoot. This method held valid for cool downs from 95 ^{o}C-45 ^{o}C, 95 ^{o}C-50 ^{o}C, 95 ^{o}C-70 ^{o}C and 70 ^{o}C-45 ^{o}C for this specific system, thus covering the range of expected transitions. The thermal design is briefly described in Section A.3.8.

A.3.6 Thermal subsystem results

The heater instrumentation was tested extensively by performing a number of thermal cycles. Specifically, a 40 cycle mock PCR with set temperatures of 94 ^{o}C, 65 ^{o}C and 72 ^{o}C was done 11 times without incident. A representative plot of the first two cycles (note that the first 95 ^{o}C step is longer to guarantee DNA has been fully melted) is shown in Figure A.10a while a representative 40 cycle run is shown in Figure A.10b.

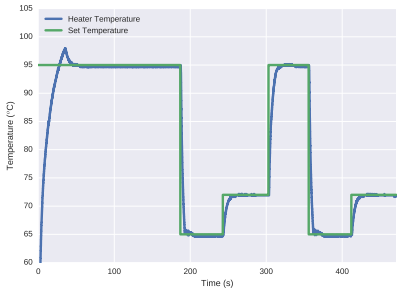

(a) Measured temperature and set temperature for the first two PCR cycles. There is a very brief overshoot on the very first heat cycle that is not considered an issue as it is still less than 100 ^{o}C and has a time constant much less than the fluid being heated. The cooling period shows no overshoot, which allows for control of non-specific binding

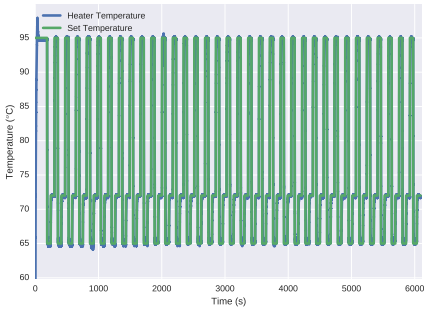

(b) A representative 40 step PCR cycle. Excluding the slight overshoot in cycle one described above, there is no overshoot greater than 0.5 ^{o}C on heating or cooling steps for all 40 cycles. The total experiment time was just over 1hr 40 minutes.

Figure A.10: Results of the v1 thermal instrumentation

In the very first melting step the temperature goes from 24 ^{o}C to 94 ^{o}C, though there was a notable overshoot. This overshoot was 3 ^{o}C in magnitude (maximum temp, 97 ^{o}C) and lasted 20 seconds. Though not ideal, this did not affect the instrument performance as the time constant for the PCR chamber was estimated to be between 20 and 30s. Thus, this 3 ^{o}C overshoot would practically be much less for the actual reaction chamber. Furthermore, the overshoot was not considered an issue as it did not exceed 100 ^{o}C (thus, no boiling occurs) and the requirements of the temperature for the melting step are much more relaxed than other temperature steps; the only requirement is that all the DNA fully separates, and higher than expected temperatures do not affect this mechanism (however, it could lead to faster polymerase degradation). Finally, this overshoot occured only on the first step, as seen by analysis of the remaining 39 cycles. The hypothesis was that when transitioning from room temperature to 95 ^{o}C the system in general heated slower, such that the error sum accumulated more than when heating from $\approx$70 ^{o}C to 95 ^{o}C. Other experiments cycling from 45 ^{o}C to 95 ^{o}C did not have this overshoot. Therefore, this issue was considered confined to only the first cycle. Future designs might impose a special first cycle to account for this.

The most important analysis concerns the minimum temperature of the reaction chamber upon cool down. As seen in Figure A.10a, there was typically no overshoot at all for the annealing step, an important conclusion. Analysis of subsequent steps showed that on cycle five there was an uncharacteristic dip. However, this dip was only 0.5 ^{o}C which was within the error of the system. Further, in a similar manner as the above discussion of the first cycle overshoot, this dip was well within the time constant of the reaction chamber and thus would have a much lesser impact on the reaction

chamber temperature than indicated in Figure A.10b. Thus, this design met the thermal requirements. However, one issue was that even with the aggressive optimisation the total time for a PCR experiment was still over 1hr 40 minutes. This was comparable to a conventional PCR and considered very long by LOC standards. The long cycle time was due to the need to extend each temperature step to accommodate the high thermal time constant imposed by the thermal design. Thus, while the instrumentation did meet specifications, the thermal design did not, and, since the controller was heavily optimised for this specific use-case scenario, use of this instrumentation for ongoing projects was not pursued. Thus, there was a need to redesign the instrumentation for more general purpose implementations.

A.3.7 Heater Instrumentation v2

The second generation of thermal instrumentation implemented a number of changes to allow for integration into a wide variety of thermal designs. These changes included replacement of the analog communication of the v1 design with a standard UART communication line and implementation of a more standard PID control algorithm that could be re-programmed over the UART interface on the fly. In this design the Arduino was replaced with a Teensy 3.2 microcontroller that included a low-noise DAC, reducing the component requirement. Furthermore, the Teensy had a number of minor advantages that, while not necessarily impacting the performance, were nevertheless attractive including being less expensive, occupying a smaller footprint and having a faster processor. The master microcontroller (external to the thermal instrumentation) used in the lab was changed from the LabJack to a BeagleBone Black as discussed in Chapter 4. This enabled the writing of a UART interface for the Teensy which in turn allowed for more robust communication. Furthermore, the thermal instrumentation could then report back more information including the current and controller time as well as the temperature, a significant improvement over the v1 design. This added information was important for comparing the thermal results to a simulation model, a function that previously could not be performed. Overall, the new interface improved both the reliability and amount of information available from the system.

Changes were also made to the controller algorithm itself. One of the key assumptions made was that the e_{sum} term directly tracks the integral of the error. This holds true if the sampling rate is constant, where the sampling time can be folded into the proportionality constant. However, in the iteration described above the sampling rate was uncontrolled. Due to the limited complexity of the program, this likely was not a substantial issue, and the reproducible behaviour of the system confirms that. However, this lack of control was not good design and was therefore rectified. This was done by implementing a timer and interrupt to set a 1 kHz update rate. The previous controller was well optimised for the specific thermal system used previously, however due to high power consumption and a high thermal time constant the thermal design had to be changed. Thus, the optimizations used previously no longer applied. However, the issue of overshoot remained a concern. To reduce overshoot, a maximum e_{num} was implemented such that the integration error does not run away to very high values. This is a more general solution to the problem, though once a thermal system is decided upon a more optimisation can be developed similar to the previous controller. These improvements, along with most of those detailed in the Arduino PID library,[198] were implemented in this design.

The instrument was entirely controlled and set through a UART serial interface with a baudrate of 9600. Commands were sent with a newline command (”\n”) and typically are of the form ”Command, Value” with a comma separating the two. A list of commands is shown in Table A.5. When the PID controller is running it reports back the time for the

step in seconds, the temperature in degrees, the set current in mA and the set temperature in degree in tab separated columns.

Command	Function	Notes
? \n	Displays help, lists commands and current values	Writes 21 lines
TEMP, ** \n	Starts the PID controller with a set temperature of **	Microcontroller will being outputing data
SETkp, ** \n	Sets the k_p constant to **	
SETki, ** \n	Sets the k_i constant to **	
SETkd, ** \n	Sets the k_d constant to **	
SETerrmax, ** \n	Sets the maximum e_{sum} to **	
SETimax, ** \n	Sets the maximum current to **	
ISET, ** \n	Outputs a current of **	Note: ensure PID is disabled before using this mode

Table A.5: List of serial commands for the new heater controller

The code for the updated PID is available in the SI. The version 2 thermal controller is included in the next generation instrument detailed in Section 5.5 and is capable of temperature measurements to 0.25 ^{o}C, resistive heater driving at up to 40 V, 1 A and on-the-fly reprogramming without re-flashing the Teensy. This enables the same design to be used for a broad spectrum of thermal designs in future work.

A.3.8 Preliminary PCR demonstration

This section briefly describes a PCR demonstration based on the Thermal Instrumentation v1 controller and rapid-prototyped PMMA microfluidics. The thermal design was developed by another student, Tianchi Ma, and is described in more detail his thesis.[118] Even though the Backhouse group has previously developed LOC PCR reactors (for example, [80]), these demonstrations were built on a glass fabrication technology that was not suitable for rapid prototyping, nor low-cost development. Thus there was a need to develop a PCR technology that was broadly compatible with other fabrication technologies being developed. This section details such a development with the testing of the thermal design with a PCR amplification and verification of the PCR with a commercial CE instrument. In this application I provided the thermal instrumentation, thermal controller code and troubleshooting while another student, Madeline Couse, performed the molecular biology.

The results of this experiment were mostly positive. Firstly, the thermal instrumentation proved robust and operated exactly as expected. Further, the reaction showed ample conversion. However, some non-specific amplification was present. The primary hypothesis of this was that it is composed of primer-dimer formations that were due to the relatively slow start-up and could be avoided in the future with improved molecular biology protocols. Further PCR developments were not done as this was sufficient to demonstrate the utility of the instrumentation that I designed and the project focused shifted towards CE as the central challenge. Furthermore, the thermal design was inefficient and the valving subsection at the time was not capable of PCR. Nevertheless, this was an important confirmation of the instrumentation functionality.

Materials and Methods

Reagents Genomic DNA was isolated from lymphocytes of individuals (obtained with informed consent) using a QIAamp DNA Blood Maxi Kit (QIAGEN, Canada), and solubilised in low Tris-EDTA (TE) buffer (pH 8.0). PCR buffers, $MgCl_2$ and polymerase were from Invitrogen Canada. Primers were from Eurofins MWG Operon, USA. Bovine Serum Albumin (BSA) was from New England Biolabs. Agarose III™ was from Amresco® Canada. 10X Tris-Borate (TB) buffer was prepared from Tris (tris (hydroxymethyl) aminomethane) (BioShop, Canada) and boric acid (EMD Chemicals, Canada), and was diluted to 1X and 0.1X with Milli-Q water.

Polymerase Chain Reaction Mixture The PCR was done both on-chip and using a conventional PCR machine. The primer pair used was designed to flank exon 2 of the HFE gene associated with hereditary haemochromatosis. The forward primer is unlabelled (5'-CAT ACC CTT GCT GTG GTT GTG ATT-3') and the reverse primer is labelled with AF532 (5'-AminoC6 + Alexa 532 TCA GAG CAG GAC CTT GGT CTT TCC-3') for subsequent analysis. The resultant product is 234 bp. 20 μL of PCR brew was made with the reagents in Table A.6 and used for the PCR procedures.

Component	Volume	Final Concentration
Sterile Milli-Q H_2O	13.2	-
10x PCR buffer (with $MgCl_2$)	2	1X
$MgCl_2$ - 50mM	0.8	2mM
dNTPs- 10mM	0.4	200 μM
BSA- 10μg/mL	0.4	0.2 μg/μL
Forward Primer	0.4	400 nM
Reverse Primer	0.4	400 nM
Recombinant Taq- 5U/μL	0.8	0.2 U/μL
gDNA (15 ng/μL	1.6	1.2 ng/μL

Table A.6: Components for PCR brew

PCR Thermal Cycle Protocol A PCR was performed using a conventional PCR machine using the 20 μL brew described in Table A.6. The thermal cycling protocol is listed in Table A.7. To perform the on-chip PCR first the chip described above was cleaned with Milli-Q water. A 4 μL of the PCR brew in Table A.6 was added to the PCR well and sealed with PCR tape. The chip was then pushed into contact with the brass spreading layer described in Figure A.11.The thermal cycling protocol in Table A.7 was input into the temperature controller described in Section A.3. Comparing the conventional and on-chip PCR thermal cycling protocols, an extra 30 seconds was added to each step to account for a time constant difference between the heater layer that was being temperature controlled and the PCR reactor.

Step	Temperature	Step time for conventional PCR (seconds)	Step time for on-chip PCR
1	95 ^{o}C	120	120
2	95 ^{o}C	10	40
3	65 ^{o}C	20	50
4	72 ^{o}C	20	50
5	GO TO 2 X 35	-	

Table A.7: Thermal Cycling Protocol for Conventional and On-Chip PCR. The step time is defined differently for the conventional and on-chip PCR. For the conventional time, each well was held at the step time described above. For the on-chip PCR, the step time is defined as the time the brass pad is held at the defined temperature. Due to the thermal heat capacity of water, the chamber temperature lags the heater temperature by roughly 20s. Thus, longer step times are implemented.

Thermal Design The on-chip PCR reactor was designed in two parts: the PCR chip and the heater system, both of which are shown in Figure A.11. The chip was designed to be fabricated out of 1.5 mm PMMA (Acrylite-FF, Evonik) and polypropylene PCR tape (AB1170, Fisher) to allow for rapid-prototyping fabrication. The chip was fabricated using CNC milling to create a 500μm deep and 1.6 mm in radius well in the PMMA (layer CP2 in Figure A.11). The well was loaded with PCR brew described in Table A.6 and capped with a 100 μm layer of PCR tape (layer CP1 in Figure A.11). Using this method, a batch of 6 PCR reactors could be built in less than five minutes. The thermal design was performed by Tianchi Ma, with the design details and thermal performance estimation being described in his thesis.[118]

The chip interfaced with a heater system built primarily out of PCR tape and centred on a commercially available heater (KHLV0502, Omega) and thermocouple (Type K, Omega). An aluminum base was first machined with alignment pins to ensure alignment of the chip and the heater. Several layers of PCR tape were then used as well defined thickness insulator layers (layers PP1, PP2 and PP3 in Figure A.11) to separate the heater from the heat sink. Atop the PCR tape lies the heater as well which was nearly the same thickness as the PCR tape (layer PP4/Heater in Figure A.11). A thin brass shim layer (layers PP5/Brass/Thermocouple, PP6/Brass and PP7/Brass in Figure A.11) was used to spread the heat from the heater; the heater has mm scale traces that would produce local temperature variations that need to be smoothed by a ”spreader” layer. The thermocouple was also embedded in this brass layer to provide a more representative reading of the heater temperature. A 0.5” manifold was added to the system for future fluidic integrations. The manifold was spaced from the chamber to prevent it from interacting meaningfully with the PCR reactor. Figure A.11 describes the entire system.

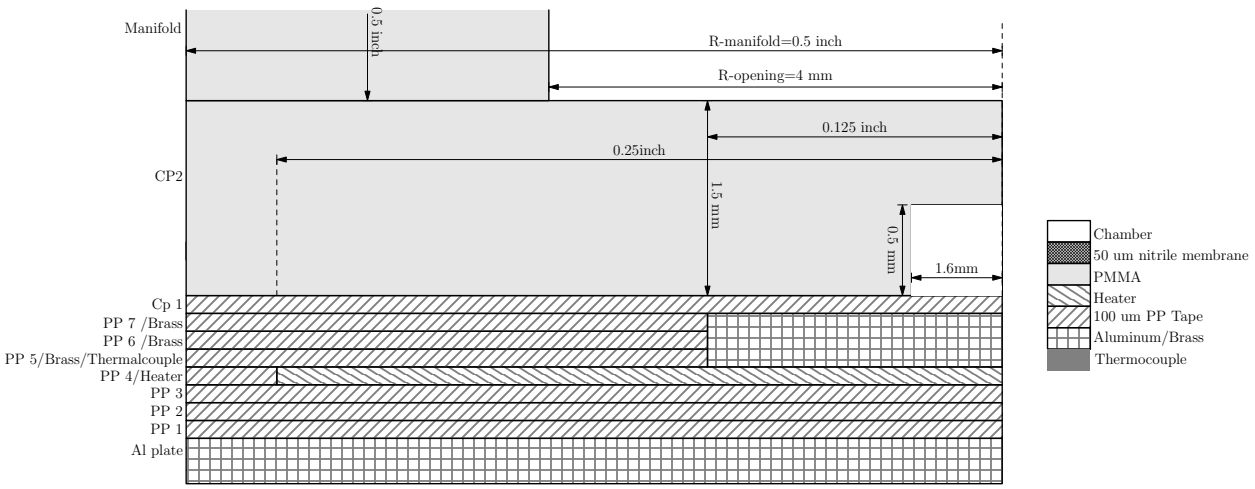

Figure A.11: Cross-section of on-chip PCR system and chip. The design relies on the very short distance between the chamber (white) and the brass pad (squares). This thickness is set by the layer CP1, which is 100 μm. Thus the chamber and brass are in tight thermal contact, the thermocouple is embedded in the brass, and thus the thermocouple tracks the chamber temperature. Image from the thesis of Tianchi Ma [118]

Reaction Validation Procedure Following the PCR reaction the resultant product was tested using microchip electrophoresis using a commercial CE instrument with confocal optics (Microfluidic Toolkit, Micralyne). The channels used were the generation 2 micromilled fluidics in PMMA described in Section 2.2.3 which were 254 μm x 254 μm. The sieving matrix used was 2.5% agarose in 1X TB buffer and the sample was diluted 1:10 with 0.1X TB for 10x sample stacking. A sample protocol for use of this matrix is available in the SI. Data was collected using the commercial instrument at 200 Hz. The experiment followed an inject-separate procedure as previously detailed in Section A.1 with an injection field of 88.5 $^{\mathrm{V}}/_{\mathrm{cm}}$ and a separation field of 98.5 $^{\mathrm{V}}/_{\mathrm{cm}}$. The detection distance was 11 mm.

Results

Figure A.12 shows two electropherograms that shows the sized products of the on-chip PCR and a conventional PCR as described above. The Microfluidic Toolkit data contains many non-physical values of 0 due to serial communication issues, thus the data processing for this figure consisted of first removing these false ”0” readings. Next, a 10 point moving average was applied (0.05s of data). The maximum peak heights were normalised to a height of 1, and the on-chip curve was offset for display purposes. The thermal cycling results were shown previously in Figure A.10.

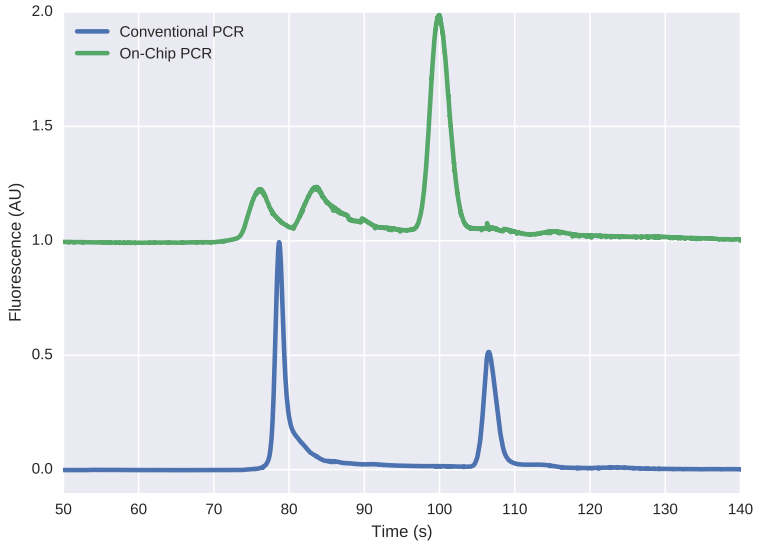

Figure A.12: Electropherograms for the separation of end-labelled DNA produced with a conventional PCR instrument (blue) and using the LOC instrument (green). The on-chip PCR exhibited very strong product conversion, though there exists some primer-dimer contamination. The arrival time differences are well within the instrument error. Separation was performed at 98.5 $^{V}/_{cm}$ in 254 μm x 254 μm milled PMMA channels with 2.5 % agarose sieving matrix and a separation distance of 11 mm on a confocal CE instrument (Microfluidic Toolkit, Micralyne)

Both the on-chip and conventional PCRs converted product at roughly the same size. There was a slight difference in arrival times with the primer peak (left most peak) of the on-chip PCR arriving 2 s earlier than the conventional product, and the main product peak (right most peak) arriving 3.7 s earlier. This was a 2-4% variation in arrival time, which was well within the generally experienced variation for this protocol which has variation introduced from differences in micromilled chips, matrix filling variation and placement errors (the optics for this instrument were manually aligned). This shows that the on-chip PCR successfully amplified the product.

Discussion

Figure A.12 shows that the on-chip PCR amplified a product that predominantly was the same size as that produced by a conventional instrument. The conversion ratio estimated by the ratio of the area under the main product peak to the area under all the peaks was 60%. This was very high, and more than adequate for most applications. In fact, this exceeds the 39% conversion ratio of the conventional PCR. Thus, the amplification was successful. Analysis of Figure A.10b showed that the temperature cycling was performed as expected. Thus, this was overall a successful first attempt at on-chip PCR demonstrating amplification, the thermal instrumentation and the compatibility of the materials and fabrication. However, there were many issues present which are discussed below.

First and foremost, there was a third peak in the on-chip electropherogram between the primer and the main product peak. The presence of this peak was particularly problematic for the application being targeted by the PCR, which

was ultimately to perform RFLP analysis as in the application described in Section 5.3. In the RFLP, the initial DNA strand is cleaved into smaller products. Since there already exists a smaller product in the electropherogram, this would obscures the presence of the enzymatic digestion, complicating analysis. It is therefore crucial to identify and rectify the source of the primer-dimer peak. This primer-dimer peak likely arose from the amplification of non-specific primer interaction, though sample contamination can also be a source of non-specific amplification. The principle of PCR is that the anneal temperature is such that it is only thermodynamically favourable for the primers to bind to the specific DNA sites of interest. However, if the temperature drops below this temperature then the primers can bind in other, non-specific locations, causing the production of DNA that does not match the primers. There were two steps in the procedure where the primers see low temperature: the annealing steps and the start-up phase.

As detailed previously, it is very important that the anneal temperature is very well controlled with no overshoot of the heating curve. The temperature cycling shows that the thermally controlled brass pad never dipped more than 0.5 ^{o}C below the set anneal temperature of 65 ^{o}C. A gradient PCR was done by Madeline Couse and found no notable primer-dimer content at anneal temperatures down to 60 ^{o}C, thus the error in the thermal instrumentation is not expected to be a source of error. There is also the possibility that the chamber temperature did not track the thermal instrumentation temperature closely. Simulations of the system suggest that this would have the opposite effect, however, in that since the chamber spends most of its time at temperatures above 65 ^{o}C the chamber temperature tends to be above that measured by the thermocouple. Therefore, deviations of the system from the model would suggest lower amounts of conversion and less non-specific amplification, the opposite issue facing this preliminary demonstration. In the startup phase, prior to beginning the thermal cycling, the reaction mixture is at room temperature. In this procedure, the brew was quickly mixed into the well, capped and loaded into the instrument for cycling. However, due to the cumbersome nature of the capping and loading, this took a few minutes. Therefore, the reaction mixture was at a low, uncontrolled temperature for some time, giving many opportunities for non-specific binding. Since the annealing temperature was well controlled, it was hypothesised that the non-specific amplification was due to this startup time. This error can be controlled in two main ways. The first is to introduce on-chip sample preparation such that the time between mixing the brew and beginning the amplification is substantially reduced. Secondly, the use of a "hot-start" Taq could be used. These special Taq's are inactive until they reach a high temperature. Thus, during the sample preparation stage there would be no amplification, as amplification would only become viable after the sample was melted. The second step where the sample sees a lower temperature is during the anneal step. Therefore, the reaction mixture would not be in an uncontrolled state until after all cycling has been finished.

In addition to the primer-dimer issue above, it should be noted from Figure A.10b that the entire PCR run took 100 minutes to run, which is very long, and comparable to a conventional system. This was particularly problematic as one of the primary motivations for miniaturising PCR is to reduce the thermal mass of fluid that needs to be thermally cycled. The on-chip PCR volume of 4 μL is 20% of a standard 20μL PCR, thus one would expect the system to be able to cycle faster. However, this system operated with passive cooling, avoiding the use of a Peltier module that is common in nearly all commercially available units. Thus, the cooling rate was slower. Passive cooling rate is a function of the temperature difference between the region being cooled and the heat sink. Unfortunately, in this instrument the heat sink gradually heated up during the course of the PCR cycle, ultimately reaching temperatures of around 40 ^{o}C. This effect should have been expected as the heater at maximum power drew 10 W of power, which is clearly far too much for a 4 μL volume. The reason for this high power was the poor optimisation of the heater size. We used a commercially available Omega KHLV0502 polyimide heater. Since it could be purchased directly, this was

a good option with a low-lead time that we could rapidly iterate with. However, the heater dimensions were 2" (50.8 mm) by 0.5" (12.7 mm). We used a brass shim as a spreader layer to create a thermally uniform pad. This brass region was $^1/_4$" (6.35 mm) in diameter to be optimised to the well geometry. Thus, only 5% of the heater area was actually being used effectively by the thermal system, and the rest used to essentially heat the heat-sink. One of the primary sources for improvement would be to reduce the heater size to a 5 mm x 5 mm sized dimension or smaller such that it matches the true temperature control region. It should be noted that against this fluctuating thermal environment, the thermal controller managed to hold to specifications, demonstrating the robustness of the instrumentation.

Finally, in terms of project logistics, this demonstration was performed prior to the development of air-tight valving membranes (discussed in Section A.2.2 above). Attempting to perform PCR without an air-tight valve would be ill-advised as the escape of water vapour (especially over the course of the 100 minute experiment described here) would cause substantial sample loss. Thus, PCR-CE could not be attempted as there was no valve technology available at the time that could perform the interface between the two methods.

In summary, a preliminary PCR was demonstrated with a high conversion ratio and robust thermal cycling instrumentation. However, the presence of non-specific primer-dimer amplification and long-cycling times suggest further iterations are needed prior to integration of the module with other instrument components. The future adjustments recommended include biochemical, simulation and thermal design changes. In terms of biochemistry it is highly recommended to use a hot-start Taq to reduce non-specific amplification that occurs prior to thermal cycling. Based on the recent development of an air-tight valve membrane that can perform PCR described in Section A.2.2 and the readiness with which hot-start Taq can be integrated into the protocol it is recommended that future work re-visit on-chip PCRs. However, prior to a second attempt, the thermal design should be completely overhauled to remove the over-sized heater and replace it with a part optimised for this solution. The company Minco provides such options, as well as options with embedded thermal read-out that would address this issue and reduce the cycle times. Since the thermal design is currently undecided, provisions were made in both the new thermal controller (Section A.3.7) and the next-generation instrument (Section 5.5) to accommodate a variety of design dimensions and heater properties.

Appendix B

MicroMilled Chip Protocol for Generation 2.5 Microfluidics

This is a fabrication protocol for the 3rd generation of micromilled fluidic chips. The resulting channels are 254 μm wide and 254 μm deep with a high aspect ratio square geometry. The channel composition is milled polymethyl methacrylate (PMMA) on three walls and PCR tape (AB1170, Thermo Scientific) on the fourth. These fluidic chips are designed to be used with an agarose sieving matrix for CE. This protocol was designed to be used with the old CNC mill (MicroMill). The general procedure is very comparable if the newer Tormach mill is used, though cutting parameters can be found in Section 2.2.

The channels produced here are likely representative of the state of the art for micromilled fluidics, though a lack of appropriate reporting makes this difficult to assess. The surface roughness has been optimised here to be as good as possible given the equipment but has not been assessed. The channels are sealed with PCR tape. This method is easy to implement, fast and does not require additional annealing steps. Further, the tape is readily removed for easy re-use of fluidic chips. However, due to the heterogeneous nature of the channels, for electrophoretic separations this fabrication method forces the use of agarose or other similar high viscosity sieving matrices. These are generally lower performance gels that are useful for prototyping. Previous work has suggested that the surface roughness of micromilled channels is sufficient to prevent agarose ”noodling”. However, future work must verify this is the case. Strategies for reducing/eliminating noodling have been pursued by other researchers in the AML lab and are available elsewhere.

Higher performance gels can be used with the next generation chips that have a smaller, homogeneous channel. These are found in Appendix C

B.1 Chip Specifications

B.2 Required Equipment, Materials and Tools

- MicroMill DSLS 3000 CNC Mill (MicroProto Systems)
- Convection Oven @ 80 ^{o}C (Fisher Sci. model # 6916)
- 0.25”, 4 flute carbide endmill (102-840, Sowa Tool)
- 0.010”, 2 flute carbide endmill (1610-0100.030, Kyocera Tool)
- 0.125” HSS drill (118-005, Sowa Tool)
- 0.125”, 2 flute carbide endmill (102-836, Sowa Tool)
- 2.25”x6”x0.5” PVC coupon
- 1.5 mm PMMA stock (Acrylite-FF, Evonik Industries)
- Plastic cutter
- 3M double sided tape (410m, 3M)
- PCR tape (AB1170, Thermo Scientific)
- Scalpel
- Cutting mat
- Tweezers
- Plastic ruler or wooden spatula
- Upright microscope with 4x and 10x objective lenses.

B.3 Chip Milling

B.3.1 Mill Maintenance

The mill should be re-oiled every week or every time it is used, whichever is less frequent. This maintenance will improve the longevity of the CNC mill. The mill should also be trammed (i.e. ensuring the z-axis and xy plane are perpendicular). This is done by attaching a dial gauge to the CNC mill head and scanning the mill table to determine

the height of the table relative to the mill head. Ideally, the gauge should measure the entire table to be the same height, though it frequently is not due to tilting of the z-axis. The user should loosen the nut on the back of the z-axis and adjust the z-axis angle such that the entire mill table is the same height accurate to 0.001" or better. This should be checked prior to any microfluidic fabrication.

Note that this maintenance is not necessary on the new Tormach mill due to an automatic oiler and a robust z-axis that does not require re-tramming.

B.3.2 Workholding

The first step is to set the piece up for milling. This process produces a 2.25" x 6" coupon that can be used 3 times. The total milled dimensions are 2.25" x 1.8" per set of 3 chips (i.e. it can be used to mill 9 chips). I am not happy with the current workholding arrangement and would like to make adjustments in the future.

1. Cut 2.25" x 6" x 1.5 mm PMMA strip. The strip MUST be less than 2.25" wide or the clamping will not work well.
2. Add 2 strips of 3M double sided tape to the 2.25"x6"x0.5" PVC coupon. The thick PVC is used to reduce the flexing of the support material for smoother surface flattening.
3. Tape the PMMA strip to the PVC strip, ensuring that all of the PMMA is within the PVC. Any overhang will need to be filed off as it will prevent clamping.
4. Remove the top surface blue covering from the PMMA
5. Place the taped coupon into the CNC mill vice.
6. Clamp the coupon in the vice as flat as possible.

B.3.3 Chip Milling

After loading the PMMA into the mill, the chips can be cut. These steps are all done with toolpaths made in the CAM software. Each milling step is detailed in a small table.

1. Set the x-y coordinates such that the entirety of the process fits within the coupon clamped and uses the PMMA efficiently.
2. Place a $\frac{1}{8}$" HSS drill into a $\frac{1}{8}$" collet and load this tool into the mill
3. Zero this tool to the surface of the PMMA at its lowest point
4. Drill the wells using the cutting parameters below

Operation	Drill Wells
Tool	0.125” drill, 118^o point, carbide
Plunge Feed	40”min^{-1}
Feed	N/A
Speed	4300 RPM
Cut Depth per pass	0.0625” per peck
Stepover	N/A
Total cut depth	0.078”
Path Type	Peck Cycle
Z-zero position	Zero the z-axis on the surface of the PMMA

5. Execute a safe tool change to remove the drill and load a $\frac{1}{4}$” 4 Flute carbide endmill in a $\frac{1}{4}$” collet into the mill

6. Zero the z-axis by probing each corner of the mill area and zeroing the z-axis to the minimum point. This process removes only 0.001”, so this is crucial to ensure that the cutter removes material from the entire piece

7. Flatten the piece to minimize surface roughness and perfect tramming of the mill to the chip with the cutting parameters below.

Operation	Flatten Piece
Tool	0.25” endmill, 4 flutes, carbide
Plunge Feed	10”min^{-1}
Feed	60” min^{-1}
Speed	4300 RPM
Cut Depth per pass	0.001”
Stepover	20%
Total Cut Depth	0.001”
Path Type	Pocket, zig-zag pattern, 0^o lace angle
Z-zero position	Zero the z-axis on the surface of the PMMA at its lowest point

8. Execute a safe tool change to remove the $\frac{1}{4}$” endmill and load a 0.010” 2 Flute carbide endmill in a $\frac{1}{8}$” collet into the mill

9. Zero the z-axis by very carefully stepping the mill z-axis down onto a region flattened in the previous process but not crucial to the final chip (i.e. near the edges).

10. Cut the channels using the parameters below. Ensure the injection channel is cut prior to the separation channel. Note: a very high plunge rate can be used as the tool plunges into a pre-drilled well.

Operation	Mill Channels
Tool	0.01” Kyocera endmill, 2 flutes, carbide
Plunge Feed	30”min^{-1}
Feed	5” min^{-1}
Speed	10500 RPM
Cut Depth per pass	0.001”
Stepover	N/A
Total Cut Depth	0.010”
Path Type	Profile cut, zero offsets
Z-zero position	Zero the z-axis on the flattened PMMA surface

11. Execute a safe tool change to remove the 0.010” endmill and load a $\frac{1}{8}$” 2 Flute carbide endmill in a $\frac{1}{8}$” collet into the mill

12. Zero the z-axis to the original PMMA surface (i.e. un-flattened region)

13. Cut out the chips from the stock and profile the inside corners (to ensure chips will push into place appropriately).

Operation	Cut out Chips
Tool	0.125” endmill, 2 flutes, carbide
Plunge Feed	30”min^{-1}
Feed	60” min^{-1}
Speed	4300 RPM
Cut Depth per pass	0.026”
Stepover	N/A
Total Cut Depth	0.078”
Path Type	Profile cut, offset to right (for BobCAD/CAM)
Z-zero position	Zero the z-axis on the original PMMA surface

14. Safely remove the tool from the mill.

15. Remove the chips from the tape gently. Twisting the chip is often helpful

16. Remove the blue tape from the chip

17. Inspect the channels under the microscope. Image the bottom of the channel to ensure that it matches Figure B.1a below.

18. Anneal chips in the convection oven set at 80C for 2+ hours

B.4 Channel Sealing

After the chips have been milled the channels need to be sealed with AB1170 PCR tape.

1. Cut the PCR tape to a size slightly larger than a chip. Do not peel off the adhesive protection layer yet.
2. Using a $\frac{1}{8}$" drill, clean out the wells of the chip. Often tape and blue cover material can adhere to the well edge
3. Using ethanol, clean off the work area to reduce particulates
4. Using a soap squirt bottle rinse the channels and chip surface thoroughly.
5. Using a DI water squirt bottle with the nozzle as close to the channel as possible, rinse the channels thoroughly. Each channel should be rinsed at least 2 times clean out debris
6. Dry the chip thoroughly with filtered clean dry air from the laboratory supply.
7. Gently remove the PCR tape from its backing and place the tape over the chip channels. This step should be completed quickly and smoothly to reduce chances of dust getting under the tape.
8. Using a clear plastic ruler or wooden spatula, firmly smooth out the tape. It is helpful to start at the bottom and slowly work up. Ensure there are no wrinkles or air pockets trapped under the tape. The slightly frosted surface of the chip will go clear when the tape is in good contact.
9. Gently flip the chip over and cut away excess tape

B.5 Adjustments for the Newer Tormach Mill

The newer Tormach mill has a few notable improvements over the MicroMill that can be used to improve the quality of the chip and the throughput of the protocol, specifically higher horsepower, higher feeds, improved alignment and flood coolant. The above protocol is still usable, though the user should use the flood coolant for every milling step. Further, a few changes should be made to the milling parameters to reflect the improved machine capabilities and tools available. Specifically:

The Tormach does not need to have its z-axis realigned with each toolchange. Instead, the user must ensure the tool table in PathPilot reflects the tools being used, and use the touch tool to align the z-axis to the minimum height on the PMMA chip area. All other z-axis alignments are done in software.

Step 7 should reflect the following changes. These changes reflect a lower feed, and much higher speed which would catastrophically melt the PMMA chip material were flood cooling not available. However, in the presence of flood cooling, this produces improved surface finish:

Operation	Flatten Piece
Tool	0.25” endmill, 4 flutes, carbide
Plunge Feed	15” min^{-1}
Feed	30” min^{-1}
Speed	10000 RPM
Cut Depth per pass	0.001”
Stepover	20%
Total Cut Depth	0.001”
Path Type	Pocket, zig-zag pattern, 0^o lace angle
Z-zero position	Zero the z-axis on the surface of the PMMA at its lowest point

Step 10 should reflect the following changes. The higher depth per pass is possible with the improved chip removal of the flood coolant, which results in less chipload and thus less tool deflection. This halves the milling time, resulting in higher throughput.

Operation	Mill Channels
Tool	0.010” Kyocera endmill, 2 flutes, carbide
Plunge Feed	100” min^{-1}
Feed	5” min^{-1}
Speed	10000 RPM
Cut Depth per pass	0.002”
Stepover	N/A
Total Cut Depth	0.010”
Path Type	Profile cut, zero offsets
Z-zero position	Zero the z-axis on the flattened PMMA surface

It should be noted that the well drilling and chip cutout procedures can also see improved throughput, though this is not crucial, does not affect the chip performance and results in only modest time savings so is not discussed here. Note also that due to the improved z-axis alignment in the Tormach, aluminum support material can be used instead of PVC. This support material can be readily re-used, reducing lab waste.

B.6 Sample Pictures

The following images were obtained with the microscope. Figure B.1a is an image of the channel bottom showing the marks from the mill at a zoom of x10. Circular patterns are seen, though they are not very high and can be readily imaged with the depth of focus of the x10 lens. If the marks appear to be substantially more pronounced, such as in Figure B.1b, this implies that either the endmill used is becoming very worn and needs to be replaced, or more likely that the mill was not properly trammed before cutting. The user should double check the tram of the mill. If the mill is not in tram, it should be adjusted and a new batch of chips remade. On the other hand, if it is well trammed then the

culprit is the endmill, which should be replaced.

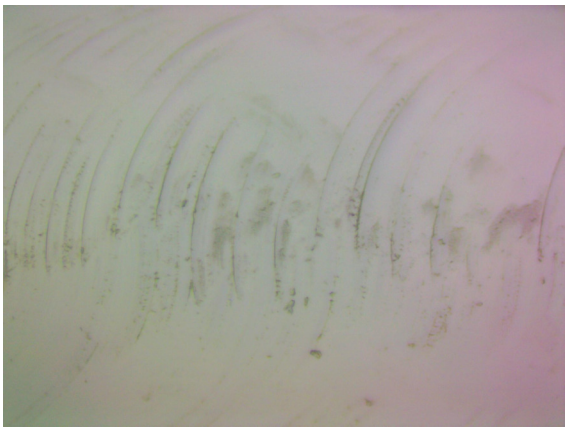

(a) Microscope image of the a good channel bottom using the 10x lens. Milling marks can be seen along the bottom, though they are not so pronounced due to use of a sharp endmill and a well trammed CNC milling machine. Channels produced with this protocol should look like this image

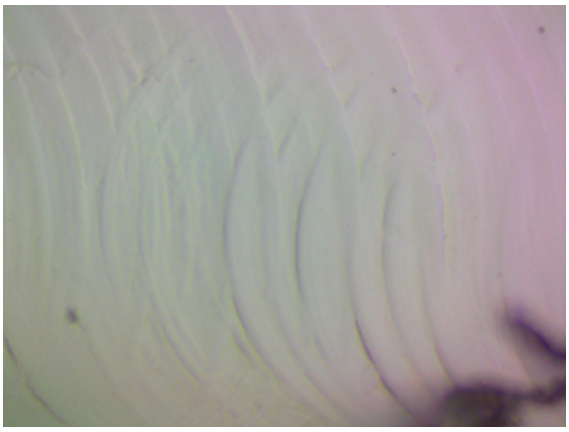

(b) Microscope image of a relatively poor channel bottom using the 10x lens. Milling marks are much more pronounced along the bottom, which implies a higher channel roughness. This particular image is due to poor tram as it was obtained prior to implementing the best practices outlined here

Figure B.1: Images of a good and bad channel finish

Figure B.2 shows an image of the channel from the side after it has been snapped in half along the channel using the 4x lens. The user should be looking to ensure the high aspect ratio of the cut, and that the channel matches the desired dimensions. A snap test is not strictly required as a consistency check as the channel bottom finish in Figure B.1 is a much more sensitive variable indicative of the channel performance.

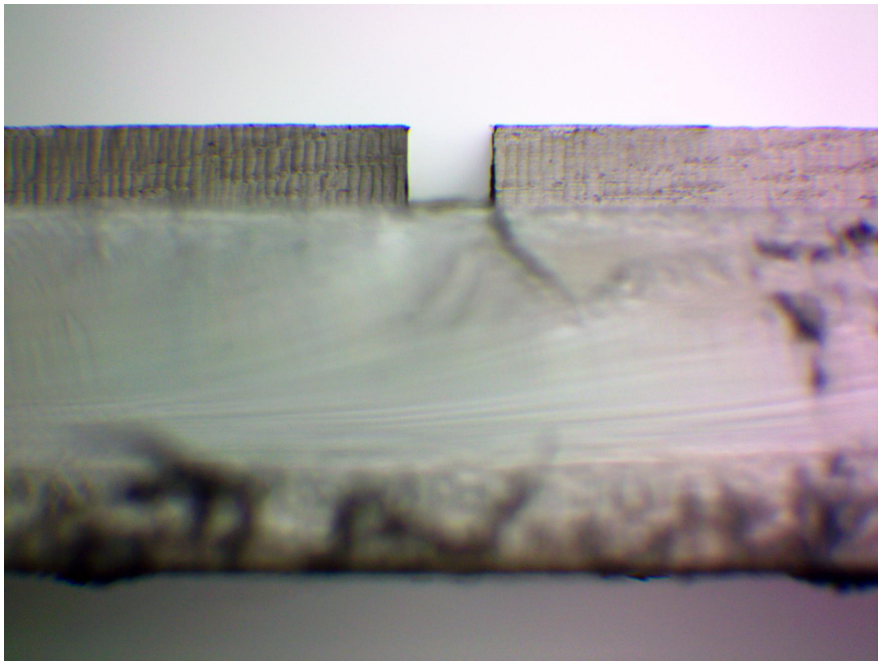

Figure B.2: Image along a milled channel after snapping the chip along the channel. The image was obtained using a 4x lens.

Appendix C

Next Generation Fluidic Chip Fabrication Preliminary Protocol

C.1 Introduction

This report details a preliminary fabrication protocol to produce thinned, bonded PMMA chips for next generation testing. This procedure has required a few additional design requirements detailed in Section C.3. The fabrication is split into three key steps: Patterning using the CO_2 laser(Section C.4), Bonding using chloroform vapour exposure (Section C.5) and Thinning using the CNC mill (Section C.6). This is the first fluidic technology in PMMA by the AML lab that can be readily used with a variety of sieving matrices as well as the short-working distance optical instruments (not demonstrated here). In addition, it allows for the controlled manufacture of precisely located microchannels and optical systems with rapid-prototyping equipment and at room temperature.

The bonding protocol is based on work by Ogilvie et al..[117] However, there were a number of changes to that protocol in order to ensure reliable bonding without channel erasing and to avoid the use of equipment that we do not have (notably a hot press). Briefly, an annealing step before bonding was introduced as the laser ablated channels have higher thermal stresses than micromilled channels, the exposure time was reduced, the exposure is set with a custom build jig in Polytetrafluoroethylene (PTFE) as compared to glass, bonding is now done at room temperature, bonding time has been reduced and the bonding pressure has been reduced. As far as I am aware, this is the only reported fabrication of laser ablated PMMA with solvent bonding. Further, as far as I am aware this is the only work that then thins the capping layer for improved optical detection.

This report is missing validation, and has not been used to replicate the process by others. Further, many steps (identified with a **) have not been optimised yet. However, this procedure has been used to make 4 chips of the structure shown in Figure C.1 where the capping layer is 90 μm (0.0035”), the channel depth is 75 μm, the channel width at its widest point is 180 μm and the top layer is 1.524 mm (0.06”) thick. Chips are made from PMMA and are 1 inch by 3 inches in size.

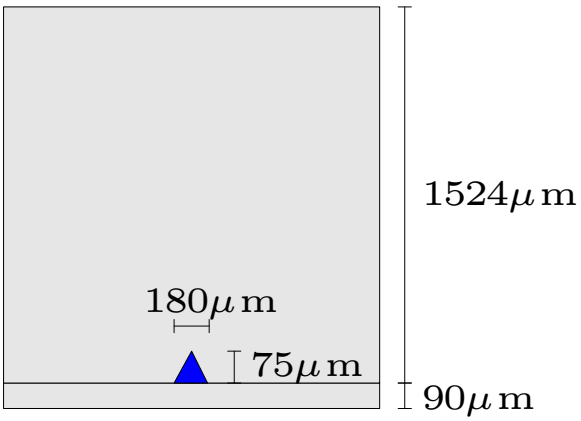

Figure C.1: Dimensions of the chip produced from this fabrication process. A 75 μm x 180 μm channel is sealed with 90 μm of PMMA for use with short working distance GRIN lenses

C.2 List of Equipment and Chemicals

- CO_2 Laser (Model # VLS 2.3 with 30 W laser tube)
- CNC Mill (Tormach PCNC770)
- Forced air convection oven (Fisher Sci. model # 6916)
- Chloroform bath
- Chloroform chip holder and cap
- Bonding jig
- 2 x 1.4" x 3.4" x $\frac{1}{32}$" Nitrile sheet
- 2 x doubled glass slide
- 6 x 1" binder clips (Staples, part #671985)
- Vacuum table for "bigchips" (contains 1.5" x 3.5" vacuum pocket)
- $\frac{3}{8}$" 6 flute carbide endmill
- $\frac{1}{8}$" 2 flute downcut endmill
- Isopropyl Alcohol (IPA) in spray bottle
- Ethanol

- RO spray bottle (from RO tap)
- $\approx$ 30 mL of Chloroform
- Clean dry air (CDA)

C.3 Design

The current infrastructure is designed to accommodate a 1 inch by 3 inch chip (i.e. microscope slide sized). However, in order to avoid edge effects both in the bonding as well as the chip thinning a larger 1.5 inch by 3.5 inch chip was designed, with the outer quarter inch (6.25 mm) left as sacrificial material.

As in previous work, a single chip is made in two layers with a patterned fluidic layer and a relatively blank capping layer. One other design change required in this process is to introduce a hole in the capping layer, preferably near the middle of the chip, that does not overlap any fluidic structures. This hole is used in the chip thinning process to appropriately zero the mill.

C.4 Chip Patterning

Chips are patterned using laser ablation with the CO_2 laser. The parameters are the same used by Rob in his report titled "Optimized Aspect Ratio/Undulations Writeup" on September 20, 2016. The procedure is as follows:

1. Cut a strip of PMMA that is roughly 3.75" width and 12" long from stock PMMA. This strip is cut from the stock in a landscape orientation
2. Peel the top layer of blue tape off the strip and load it into the CO_2 laser
3. Load the appropriate design into Corel Draw X5 and print using the windows driver for the Universal Control Panel (VLS 2.3)
4. Pattern first the wells and vias using the parameters in Table C.1. Both a fluidic layer and a capping layer should be patterned
5. Use the "Home-Z" function to ensure the laser table is appropriately aligned in the x-axis
6. Pattern the channels using the parameters in Table C.1.
7. Unload the strip of PMMA and break off the patterned fluidic and capping layers without disturbing the blue tape on the back
8. Reload the rest of the strip into the CO_2 laser. Repeat steps 4 to 7 until the strip is depleted. This should yield 3 fluidic and 3 capping layers per strip.

9. Put chips into the oven at 80 ^{o}C for at least 2 hours to overnight to anneal. This is crucial as chloroform exposure will result in immediate crazing without this step.**

** Note: the time for annealing has not been well developed. Other students have observed that a 30 minute anneal is sufficient to prevent crazing. Thus, this time can be reduced

Feature	Power	Speed	PPI	Z-Focus	Passes
Throughcuts	20	5	1000	1.5	1
Vias	18	25	1000	0.7	10
Channels	3.3	1	1000	2	1

Table C.1: Laser parameters for patterning fluidic chips and capping layers

C.5 Chip Bonding

Chips are bonded using a chloroform vapour exposure in a manner similar to Ogilvie et al..[117] However, the parameters reported in that work would not work for our applications (specifically, I have eliminated the thermal exposure, reduced the pressure by an order of magnitude, reduced the exposure time by 25% and allowed the chips to vent excess vapour before bonding) in order to avoid paving over channels. The procedure followed is:

1. Using a Kimwipe that has been folded in half twice and sprayed wet with ethanol, firmly wipe down both sides of the capping layer. This step was done to remove monomer/snow on the chip surface.

2. Spray both sides of the capping layer with a jet of RO water from a nearly full squirt bottle (note: RO water from the tap).

3. Rinse both sides of the capping layer with IPA

4. Blow dry the capping layer with CDA and place the chip with the ablated side facing down into the chloroform chip holder

5. Repeat steps 1 to 4, except when spraying the chip with RO water ensure that each channel is thoroughly rinsed twice to ensure no debris from the kimwipe is left in the channel

6. Place the cap on the chloroform chip holder

7. Place a layer of nitrile into the chip bonding jig

8. Fill the chloroform bath such that the meniscus is just below the top of the bath surface ($\approx$ 30 mL). Note: It is very important that the meniscus is close (to control the distance separation of the chips from the fluid) but also that the meniscus does not exceed the top of the bath. If it does, chloroform will wick along the aluminum and directly wet the PMMA, ruining the chips.

9. Expose the chips in the chloroform chip holder to the vapour for 3 minutes. **Timing here is crucial**

10. After exposure carefully remove the chloroform chip holder and flip it upside down. Cover the chloroform bath with the chloroform chip holder cap.

11. Leave the chips face up and untouched for 1 minute and 15 seconds (this is not a controlled time step, but the timing on step 14 must be followed)

12. Carefully remove the capping layer and fluid layer from the chloroform chip holder by using a flat screwdriver to push out the corners

13. Load the fluid layer into the bottom of the chip bonding jig

14. At exactly 2 minutes after the chips were removed from the vapour exposure press the capping layer onto the fluid layer. Alignment is taken care of by the bonding jig. Push firmly onto the assembled chip **Timing here is crucial**

15. Place a second layer of nitrile on top of the chip

16. Assemble the top layer of the chip bonding jig and tighten the socket head screws. The screws should be very tight such that both aluminum layers of the jig are in contact (squishing the nitrile). The pressure applied to the chip is controlled by the compression of the nitrile

17. Leave the chip in the bonding jig at room temperature for 30 minutes **

18. Remove the bonded chip from the jig and inspect for channel closures and voids.

** The time left under pressure has not been tested. I think that a reduction in this time could be done. I have made 2 bonding jigs (no difference in bond quality so far), and it takes 10-12 minutes to clean slides, expose them, vent them and assemble the bonding jig. A reduction in bond time from 30 minutes to 15 or 20 minutes would vastly improve the process flow

C.6 Chip Thinning

Chip thinning is done on the CNC milling machine using the g-code entitled "chipflattening_newtop_bigchips_v3_edited.TAP". The procedure is as follows:

1. Clean the vacuum table and chip thoroughly with IPA and a paper towel

2. Load the chip into the vacuum table with the wells face down and the capping layer face up

3. Apply a vacuum and push firmly on the chip all over its surface. Listen very carefully for any leaks

4. Zero the touch tool to 5.5"

5. Zero the mill using the touch tool within the hole in the capping layer detailed in Section C.3 (i.e. z=0 is the top

of the fluid layer or bottom of the capping layer). Zeroing should be done by bringing the touch tool such that it reads 0.0000", then using 0.0001" steps lower it until it only JUST displaces +0.0005", then stepping the tool up by 11 steps (note: it will still read +0.0005", but actually will be at z=0).

6. Zero the mill x and y axes by aligning to the top-left corner of the vacuum table with a "wobbler". In this corner, there is a cutout of 0.1" off both the top and left side of the table, or half the diameter of the wobbler. Thus, utilise best standard practices to perform alignment and carefully step the wobbler into the cutout in 0.0001" increments until it loses concentricity. With a 0.2" diameter wobbler, this point will be x/y = 0 . Repeat for the other axis.

7. Load a $\frac{1}{8}$" 2 flute down-cut endmill into the mill

8. Cut the top of the chip to down to 0.01". The optimized code will have passes at 0.045", 0.03", 0.02" and 0.01". A roughly 3 mm strip along the left and right of the chip will not be milled. All mill plunges are done off the chip to minimize the impact on the capping layer. To minimize the risk of coolant being sucked into the vacuum system, a constant blast of CDA from the air gun should be blown at the mill. The mill moves at 50 IPM to minimize the thermal impact of the mill on the surface such that flood coolant is not required.

9. Load a $\frac{3}{8}$" 6 flute finishing endmill into the mill

10. Cut the top of the chip down to 0.004". This code will climb mill the surface at a slow rate. Here flood coolant is required. Monitor the vacuum system for sucking up coolant. The flask can accommodate a fair amount of fluid being sucked in, but only if it is at a fairly low rate.

11. After milling quickly switch the vacuum for positive pressure to push out any coolant sucked into the system and release the chip.

12. Inspect the chip with a micrometer. The capping layer should be intact edge to edge and be 0.004" thick and within 0.001" across the chip.

13. Dry the chip with paper towel

14. Load the chip into the CO_2 laser in the new jig to the left of the usual jig with the milled surface facing up. The chip should slide in firmly.

15. Cutout the centre 1 inch x 3 inch chip using the parameters in Table C.1

16. Anneal the resulting chip at 80C for 2 hours to overnight**

** I am considering replacing this step with 30 minutes at 115C and 1 hr at 80C. This has in the past proven to substantially reduce the milling marks.

C.7 Assessment

Figure C.2a shows a representative image of microchannel intersection after snapping the chip along a channel. The walls of the channel are very smooth, and no undulations along the channel bottom can be seen. This is due to the highly defocused laser pulse above. Note: due to the shallow channel it can be difficult to snap the chip. Photo credit to Rob Bennett. Figure C.2b shows a representative image of a completed chip using the protocol above and snapped perpendicular to the channel. This shows a slight change to the aspect ratio as compared to Figure C.2a, and is representative of the final product. The thickness of the capping layer can be assessed with a set of calipers. Using this method, the thickness of the capping layer should be 90 μm with a standard deviation of 15 μm. Improvements to this accuracy are a source for improvement.

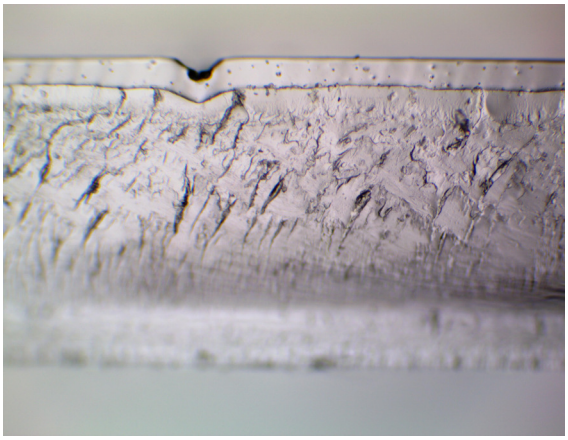

(a) Microscope image of the microchannel patterned by laser ablation prior to any solvent exposure using an x4 objective. The channel surface is very smooth, and no evidence of laser pulses is seen. Photo credit to Rob Bennett.

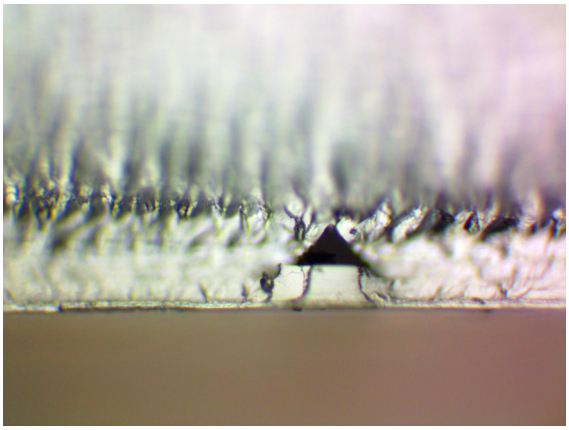

(b) Microscope image of the microchannel after bonding and cap thinning. The channel aspect ratio has changed to be higher, though in general the channel dimensions have shrunk notably. This is likely due to reflow of the PMMA from the choroform vapour exposure. The channel dimensions are measured to be 180 μm at its widest point, 76 μm deep with a 85 μm thick cap.

Figure C.2: Image of a laser patterned microchannel before and after solvent bonding

C.8 Note: Bond Forces

The bond force is set by the compression of the two $\frac{1}{32}$" shore 40A nitrile sheets in the chip bonding jig. According to engineersedge.com the maximum torque that can be applied to a 8-32 screw in aluminum is about 10 inch lbs or 1.13 Nm. This corresponds to a maximum force of 444 N. In practice, such torques will bend the $\frac{1}{2}$" aluminum in the bonding jig. Thus, a reduced force is required.

The bonding jig is designed with a 0.18" deep chamber. This chamber accommodates 2 x 0.06" PMMA plates and 2 x $\frac{1}{32}$" nitrile sheets. When screwed shut, this results in a compression of 0.0025", or a strain of 0.04. The young's modulus of shore 40A nitrile is estimated to be 1.3 MPa, thus the applied pressure is 52 kPa, or 176 N across the 1.5 inch x 3.5 inch slide ($\approx$ 40% of the maximum force possible in aluminum)

Appendix D

Detection Circuit Assessment

This appendix supports the material in the Detection Electronics chapter (Chapter 4) with schematics and transimpedance amplifier (TIA) noise estimation. In this appendix, the term noise refers to RMS voltage noises (referred to as n_{TIA} in Chapter 4). The method used to estimate the noises was the well-reviewed book on photodiode amplifiers by Graeme,[163] though the equations are also available online in an article by Bonnie Baker.[167]

D.1 Circuit Schematics

Figure D.1 shows the circuit schematics for the PDE, DEV1 and DEV2 designs. These are all very similar in their implementation, with PDE and DEV1 actually having an identical design/layout with changed component values.

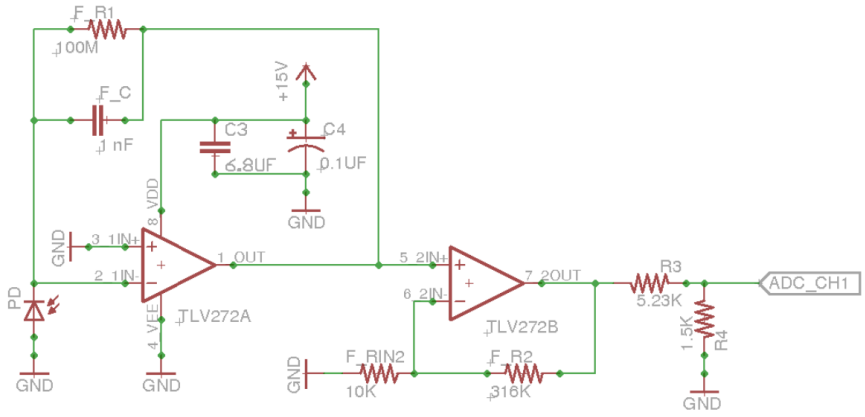

(a) The TIA design for the PDE circuit. It contains a TIA with a gain of 10^8 followed by a voltage amplifier with a gain of 32.6 and a resistive divider with to reduce the output voltage by a factor of 0.223. The overall transfer function was 7.27×10^8 $^{V}/_{A}$.

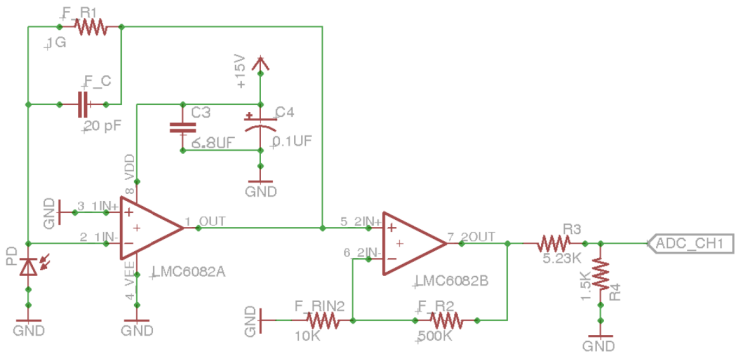

(b) The TIA design for the DEV1 circuit, which was based on the PDE PCB. It contains a TIA with a gain of 10^9 followed by a voltage amplifier with a gain of 51 and a reistive divider with to reduce the output voltage by a factor of 0.223. The overall transfer function was 1.17×10^9 $^{V}/_{A}$.

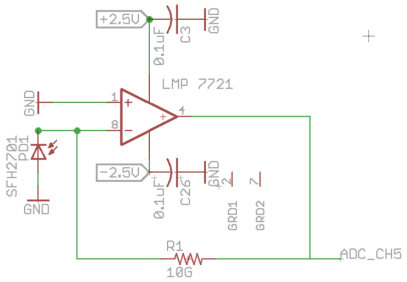

(c) The TIA design for the DEV2 circuit. IT consists only of a TIA with 10^{10} gain as voltage amplification was done by the amplifier within the ADC.

Figure D.1: Schematics for the TIA circuits discussed in Chapter 4

D.2 TIA Calculations

D.2.1 Compensating the TIA Design

TIA circuits must be compensated to avoid gain-peaking which results in an increase in high-frequency noise. This is done by ensuring there is sufficient feedback capacitance. The minimum capacitor required can be estimated based on Equation D.1 from a commonly cited application note.[165]

$$C_{F,min} = \frac{1}{4\pi R_f \text{GBW}} \left[1 + \sqrt{1 + 8\pi R_F C_D \text{GBW}}\right] \tag{D.1}$$

Where R_f is the feedback resistance, GBW is the gain bandwidth product of the op-amp used and C_D is the photodiode capacitance (3 pF for the SFH2701 photodiode used in each of the circuits here). For the DEV1 circuit (Rf=10^9, GBW=1.3 MHz, C_D=3pF) this is 19 fF and for the DEV2 circuit (Rf=10^{10}, GBW=15 MHz, C_D=3pF) this is 1.8 fF.

D.2.2 Estimating Transimpedance Noise

The approach followed for the TIA noise estimation was that by Graeme in his book on photodiode amplifiers.[163] The RMS voltage noise from the transimpedance amplifier circuit can be split into three different sections: Johnson noise from the feedback resistor (e_{noR}), noise due to the amplifier's input current noise (e_{noi}) and the noise due to the amplifier's input voltage noise (e_{noe}). The circuit total noise (n_{TIA}) is the root mean square summation of all these noise values.

$$n_{TIA} = \sqrt{e_{noR}^2 + e_{noi}^2 + e_{noe}^2} \tag{D.2}$$

The resistor and current noises are comparatively simple to calculate and can each be encompassed in one single equation. However, the amplifier's input voltage noise is highly frequency dependent and much more involved. Graeme splits the input voltage noise calculation into 5 regions to simplify the calculation. Single stage and two stage amplifier circuits have slightly different noises and are discussed separately.

Noise Due to Feedback Resistor and Amplifier's Input Current Noise

The noises due to the feedback resistor and amplifier's input current noise are both constant with frequency until a bandwidth limit truncates their effect. This bandwidth limit is the same bandwidth as the circuit (BW from Chapter 4, Equation D.5). The feedback resistor noise density is given by Equation D.3 and the amplifier's input current density by Equation D.4.

$$e_{noR} = \sqrt{2KTR_f \pi \mathrm{BW}} \tag{D.3}$$

Where K is Boltzman's constant ($1.38 \times 10^{-23} \frac{J}{^oK}$), T is the temperature in Kelvin, R_f is the feedback resistance (shown in Figure 4.1) and BW is the bandwidth.

$$e_{noi} = R_f \sqrt{qI_B \pi \mathrm{BW}} \tag{D.4}$$

Where q is the charge of an electron ($1.6 \times 10^{-19} C$) and I_B is input bias current. Typically the e_{noi} is very low as the

op-amps for these applications have pA or less input bias current.

$$BW_t = \frac{1}{2\pi R_f C_s} \tag{D.5}$$

Where C_s is the stray capacitance (or $C_s = C_f + C_{stray}$ if feedback capacitance exists)

Noise Due to Amplifier's Input Voltage Noise

The noise due to the amplifier's input voltage noise is amplified by the various capacitances of the system and is therefore highly frequency dependent. This is addressed by separating the frequency space between DC and the op-amp unity gain crossover frequency into five distinct regions based on the capacitances involved. Each region has a starting and ending frequency shown in Figure D.2. The total e_{noe} is the root mean square summation of these regions.

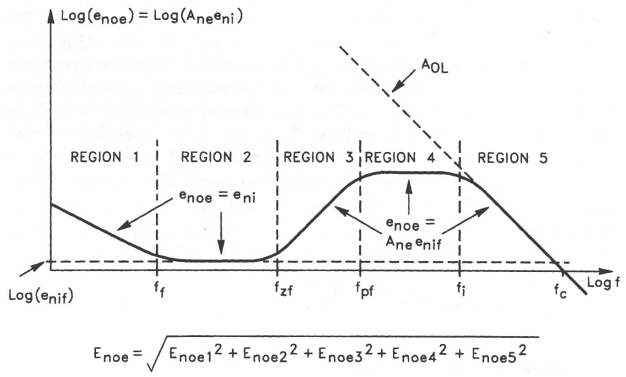

Figure D.2: The five sections of the noise due to the amplifier's input voltage noise. The regions are defined by their frequencies calculated in Equation D.6. Image taken from Graeme[163]

The frequencies are defined by the $^1/_f$ corner frequency f_f, f_{zf}, f_{pf}, f_i and the op-amp crossover frequency f_c. The first step is to calculate these frequencies as if they overlap the calculation needs to be amended. In cases where $f_{zf} < f_f$ or $f_i < f_{pf}$ then the summation must be changed as described below. f_f and f_c are properties of the op-amp being used and can be found in the data sheet. The other frequencies are calculated with Equations D.6.

$$\begin{aligned} f_{zf} &= \frac{1}{2\pi R_f (C_i + C_s)} \\ f_{pf} &= \frac{1}{2\pi R_f (C_s)} \\ f_i &= \frac{f_c C_s}{(C_i + C_s)} \end{aligned} \tag{D.6}$$

$$C_i = C_D + C_{id} + C_{icm} \tag{D.7}$$

Where R_f is the feedback resistance (shown in Figure 4.1), C_s is the stray capacitance (or $C_s = C_f + C_{stray}$ if feedback capacitance exists), C_i is the overall input capacitance, C_D is the photodiode capacitance, C_{id} is the differential input capacitance between the amplifier inputs, C_{icm} is the common-mode input capacitance for the inverting amplifier input to ground and f_c is the op-amp crossover frequency.

The equations for the various regions of e_{noe} are shown below in Equations D.8.

$$
\begin{aligned}
e_{noe1} &= e_{nif}\sqrt{f_f \ln\frac{f_f}{f_1}} \\
e_{noe2} &= e_{nif}\sqrt{f_{zf} - f_f} \\
e_{noe3} &= \frac{e_{nif}}{f_{zf}}\sqrt{\frac{(f_{pf})^3 - (f_{zf})^3}{3}} \\
e_{noe4} &= \left(1 + \frac{C_i}{C_s}\right) e_{nif}\sqrt{f_i - f_{pf}} \\
e_{noe5} &= \left(1 + \frac{C_i}{C_s}\right) e_{nif}\sqrt{\frac{\pi}{2}(f_c - f_i)}
\end{aligned}
\tag{D.8}
$$

(D.9)

Where e_{nif} is the noise floor level, f_f is the $^1/_f$ corner frequency, f_1 is 0.01 Hz (simply a very low-frequency to avoid divide by 0 errors, 0.01 Hz is used by the references followed[163,167]), f_{zf}, f_{pf} and f_i are pole frequencies, C_i is the overall input capacitance, C_s is the stray capacitance and f_c is the op-amp crossover frequency. Many of these values are calculated in Equation set D.6. f_{pf} is also the bandwidth of the signal.

A special case can occur with very large feedback resistances (as is true in the scenarios discussed in this report) where $f_{zf} < f_f$ or $f_i < f_{pf}$. In these cases e_{noe2} or e_{noe4} can result in imaginary numbers which do not have physical meaning. In these situations the result should simply be set to 0 as that frequency region no longer exists. This is the standard approach to this situation in the literature. In the case where e_{noe4} is imaginary, phase compensation is likely required. For each design below the various noises are calculated and presented.

D.2.3 Modifications to Accommodate Post-TIA filter

One of the primary advantages to the DEV2 circuit was the inclusion of a $\Delta - \Sigma$ ADC with an integrated finite impulse response (FIR) filter. For the sampling rate of 1000 sps (discussed in Section 4.6.1) the low pass FIR filter has a bandwidth of 732 Hz. Analysis of the data-sheet suggests that the filter roll-off is roughly 15 $^{\text{dB}}/_{\text{octave}}$ at 732 Hz, increasing in slope around 2 kHz before settling at about -60 dB suppression beyond 6 kHz. This attenuates the majority of the region 4 and 5 input voltage noise which spans from the signal bandwidth f_{pf}(1.59-32 Hz for these designs) to the unity gain crossover frequency f_c (1.3 MHz-15 MHz depending on the op-amp). Therefore, there needs to be a method to take this filter into account.

The approximate approach taken here was to introduce a new f_i and f_c value to take into account the effect of the

filter. f_i is the boundary between regions 4 and 5 where the noise begins to roll off. This was set to the filter bandwidth of 732 Hz. f_c is normally the unity gain bandwidth based on the typical 6 $\mathrm{dB}/_{\mathrm{octave}}$ roll-off of the op-amp open loop gain. Here, a new, effective f_c was calculated be determining the new unity gain point assuming a 15 $\mathrm{dB}/_{\mathrm{octave}}$ filter. This was done by first calculating the number of decibels of gain between f_{zf} and f_{pf}, then determining the number of octaves above 732 Hz are required to counteract that. This gives $f_{i,new}$ and $f_{c,new}$ which can then be used in the same equations as above.

$$f_{i,new} = 732Hz \tag{D.10}$$
$$f_{c,new} = \frac{\log_2(f_{pf} - f_{zf}) \times 6}{15} \times f_{i,new} + f_{i,new}$$

While it should be noted that this is vast simplification of the filter, the estimated frequency for the DEV2 circuit to overcome 23 dB of noise gain is 1.8 kHz. This is only slightly above the 23 dB threshold of the filter performance in the ADS1248 datasheet. Thus, this approach is approximately valid for this situation.

D.3 Calculation Results and Modifications to the Model

Table D.1 summarises the results of the electronic designs described in Chapter 4 based on the equations above with no filter added. The following parameters were estimated: For PDE no assumptions on the calculation were needed, though the input capacitance of the TLV272 op-amp had to be extracted from Texas Instrument's TIA design tool. For DEV1 the op-amp input capacitance was assumed to be the same as the LMP7721 used in DEV2. This is a relatively safe assumption as both chipsets are CMOS-op-amps from TI with very low input bias currents. The calculated noises and bandwidths are not very sensitive to this parameter. No assumptions were made with the DEV2 calculation, though the input capacitance had to be extracted from an application demonstration.[170] As per Chapter 4, the key assessment factor is the minimum detectable optical power P_{min}. This is defined as the optical power required to reach a signal to noise ratio of 3, with the noise assessed after averaging. In this appendix, the noise is assumed to be the estimated noise by the model divided by $\sqrt{n}$ where n is the sampling rate (SRATE). This corresponds to the expected noise reduction of perfectly white noise by a moving average filter with a time period of 1s. The estimated P_{min} values here are better than expected as the model does not take into account other sources of noise and assumes a noise reduction by the moving average that is typically much better than was practically achieved.

	Parameter	PDE	DEV1	DEV2
Components	Op Amp Used	TLV272	LMC6082	LMP7721
Op Amp	Noise Floor ($^{nV}/_{\sqrt{Hz}}$)	35	22	7
	f_f Corner Frequency (Hz)	100	140	100
	Crossover Frequency f_c (MHz)	3	1.3	15
	Input Bias Current (fA)	1000	10	3
	Input Capacitance C_i (pF)	11.6	14	14
Feedback	Feedback Resistor R_f (GΩ)	0.1	1	10
	Total Feedback Capacitance (C_f+C_s) (pF)	1001	21	1
Frequency Components	f_{zf} (Hz)	1.57	4.59	1.17
	f_{pf} (Hz)	1.59	7.58	15.92
	f_i (kHz)	2965.63	780.00	1000.00
e_{noe} Components	e_{noe1} (μV)	0.46	0.44	0.47
	e_{noe2} (μV)	0.00	0.00	0.00
	e_{noe3} (μV)	0.00	0.05	0.24
	e_{noe4} (μV)	60.97	32.38	105.00
	e_{noe5} (μV)	8.23	33.14	492.39
Noise Breakdown	e_{noe} (μV)	61.53	46.34	503.47
	e_{nor} (μV)	1.62	11.17	51.17
	e_{noi} (μV)	0.09	0.20	1.55
	e_{no} (μV)	61.55	47.66	506.06
Circuit Gain	TIA Gain ($^{V}/_{A}$)	10^8	10^9	10^10
	Second Stage Gain ($^{V}/_{V}$)	7.27	11.72	2
Predicted Performance	Estimated Noise n_{TIA} (μV)	447	559	1012
	SRATE (Hz)	$\approx$ 160	$\approx$ 1950	1000
	Estimated Processed Noise (μV)	35.37	12.65	32.01
	Estimated P_{min} (fW)	438	9.71	14.40

Table D.1: Table of calculation parameters and results estimating TIA noise. The estimated performance of PDE is quite poor due to a poorly optimised gain distribution. Changes implemented in DEV1 without modifying any of the schematic design demonstrates the need to perform this analysis. DEV1 and DEV have very comparable P_{min}s in the 100's of fW, with a slight edge to DEV1. However, this does not take into account any post-TIA filtering. This is done in Table D.2 below, which is more representative of the DEV2 circuit.

Analysis of the PDE circuit suggests that the TIA components were not well optimised for this application. Specifically, the input voltage noise, e_{noe} is over an order of magnitude higher than the Johnson noise (61.53 μV vs. 1.62 μV). This input voltage noise is almost entirely in region 4 of the spectrum between f_{pf} at 1.59 Hz and f_i at 3 MHz, frequency space unused by the actual signal. This circuit could thus support much higher bandwidth with minimal changes to noise, or much higher gain while decreasing the feedback capacitance to maintain the same bandwidth. As discussed in Chapter 4, Section 4.7, the latter is a better solution for CE applications. This circuit could also have benefited greatly from a post-TIA filter. Assuming perfectly white noise, this results in a P_{min} of 438 fW, much above the required 56 fW requirement detailed in Chapter 4. From this analysis it was clear design changes were required.

Analysis of the DEV1 circuit shows vastly improved theoretical performance as compared to the PDE circuit. This is especially significant as both circuits were based on the exact same schematic and layout, demonstrating the need for this level of analysis for optimisation. In the DEV1 circuit, both the Johnson (e_{nor}) and input voltage noise (e_{noe}) are comparable at 11 μV and 46 μV respectively. The Johnson noise is a minimum noise for a given feedback resistance and thus considered a "base" noise for the design. Having a comparable e_{noe} suggests a well-chosen op-amp and well-set bandwidth for the application. The predicted P_{min} for this design is 9.71 fW after a 1950 point moving average assuming white noise originating entirely from the TIA circuit. This 9.71 fW is below the target of requirements detailed in Chapter 4, suggesting a practical implementation of the circuit might meet the detection goals.

Analysis of the DEV2 circuit without the filter compensation from the ADC demonstrates the difficulty in selecting a good op-amp for a given design. The DEV2 circuit should, in general perform, better than the DEV1 circuit due to a higher TIA gain (as the Johnson limited SNR of a circuit scales with $\sqrt{R_f}$) regardless of which op-amp used. Instead the DEV2 circuit without the ADC is expected to perform slightly worse. This is due to the much higher unity gain crossover frequency of the LMP7721 op-amp as compared to the LMC6082 op-amp used in DEV1. Thus, despite lower input bias currents and a much lower noise floor, this design actually has more noise due to stretching the input voltage noise regions 4 and 5 over wider bandwidth; for DEV1, region 4 spans 780 kHz and region 5 spans 520 kHz while for DEV2 these regions span about 1 MHz and 14 MHz respectively. The logical response here would be to target a low unity gain BW amplifier for these applications. However, the typical input bias current for such designs is much higher than the LMP7721 used for this circuit, which would lead to higher environmental susceptibility.[166] Therefore, the approach used here was to utilise post-TIA filtering to remove the high frequency noise. This was provided by the $\Delta - \Sigma$ ADC in the DEV2 circuit which had an integrated FIR filter. Therefore, to properly assess the DEV2 design the calculation adjustment presented above in Section D.2.3 must be done.

Table D.2 shows the results for 4 circuits assuming the 732 Hz filter from the ADS1248 $\Delta - \Sigma$ ADC was applied. These include the DEV2 design, the DEV2 design but replacing the op-amp with the LMC6082 used in the DEV1 circuit, the DEV1 circuit assuming this new ADC was applied and a new high-end op-amp from Analog Devices for comparison purposes.

Parameter	**DEV2**	DEV2, opamp change	DEV1	DEV2, opamp change
Op Amp Used	**LMP7721**	LMC6082	LMC6082	ADA4530
Noise Floor ($^{nV}/_{\sqrt{Hz}}$)	**7**	22	22	14
$^{1}/_{f}$ Corner Frequency (Hz)	**100**	140	140	200
Crossover Frequency f_c (MHz)	**15**	1.3	1.3	2
Input Bias Current (fA)	**3**	10	10	1
Input Capacitance C_i (pF)	**14**	14	14	11
Feedback Resistor R_f (GΩ)	**10**	10	1	10
Feedback Capacitance C_f (pF)	**1**	1	21	1
f_{zf} (Hz)	**1.17**	1.17	4.59	1.46
f_{pf} (Hz)	**15.92**	15.92	7.58	15.92
$f_{c,new}$ (Hz)	**1835**	1835	943	1741
e_{noe1} (μV)	**0.47**	0.48	0.44	0.69
e_{noe2} (μV)	**0**	0	0	0
e_{noe3} (μV)	**0.24**	0.76	0.05	0.39
e_{noe4} (μV)	**2.81**	8.83	0.99	4.50
e_{noe5} (μV)	**4.37**	13.74	0.67	6.69
e_{noe} (μV)	**5.22**	16.36	1.27	8.10
e_{nor} (μV)	**51.17**	51.17	11.17	51.17
e_{noi} (μV)	**1.55**	2.83	0.20	0.89
e_{no} (μV)	**51.46**	53.79	11.24	51.81
TIA Gain ($^{V}/_{A}$)	**10^{10}**	10^{10}	10^{9}	10^{10}
Second Stage Gain ($^{V}/_{V}$)	**2**	2	11.72	2
Estimated Noise (μV)	**104**	109	132	105
Sampling Rate sps	**1000**	1000	1950	1000
Estimated Processed Noise μV	**3.29**	3.44	2.98	3.32
Estimated P_{min} fW	**1.48**	1.55	2.29	1.49

Table D.2: Table of calculation parameters to estimate the TIA noise assuming a 732 Hz FIR filter from the ADS1248 ADC is applied to the output as in the DEV2 circuit. The bolded first column is the DEV2 circuit actually built and tested, while other columns are used as comparisons using various op-amps. Also compared was the DEV1 circuit with the filter added. Of these options, the LMP7721-based DEV2 has a slight performance edge due to having the lowest noise floor, though all designs are approximately the same due to Johnson noise domination.

Analysis of Table D.2 shows that the FIR filter has a very notable effect on the predicted circuit performance by effectively suppressing the high-frequency input voltage noise. This substantially reduces the impact of using a high unity gain bandwidth amplifier for low-bandwidth applications. Based on this calculation, the DEV2 circuit is expected to perform nearly 6.5x better than the DEV1 circuit from Table D.1 with a P_{min} of 1.48 fW assuming white noise and no other noise sources. This low P_{min} suggests it is highly feasible to practically implement a sub-56 fW detector as per the requirements in Chapter 4.

Table D.2 also includes some other circuits for comparison. For example, the DEV1 circuit with the filter applied was

analysed. This showed a substantial improvement though not as drastic an improvement as for DEV2. As discussed above, the DEV1 circuit noise had substantial input voltage and Johnson noise components. Since the low pass filter does not address Johnson noise at all (Johnson noise bandwidth is the same as the signal bandwidth), the relative improvement of the DEV1 circuit was not as much as for the DEV2 circuit. After filter application, the noise is dominated by the Johnson noise which scales with $\sqrt{R_f}$ as compared to a signal scaling of R_f. Thus, the DEV1 circuit is expected to be poorer performing due to having a lower TIA feedback resistance. This is illustrated by the analysis of a hypothetical design where the DEV2 components are used, but with the DEV1 LMC6082 op-amp. This change (despite a drop in sampling rate) still shows improved performance over what is predicted for DEV1 plus filter, as expected. Comparing the DEV2 circuit with the LMP7721 and LMC6082 op-amps, the LMP7721 outperforms due to having a lower noise floor. Of the op-amps surveyed for this project, the LMP7721 has the lowest input voltage noise of any sub-pA input bias current device. Thus, this makes it the best option for any application with high-frequency filtering (such as this one).

Table D.2 also compares the circuit performance of the DEV2 circuit if the op-amp were upgraded to the ADA4530 op-amp, a new high-end option from Analog Devices that was released after the design of DEV2. At first glance, this op-amp would be expected to have improved performance due to having a lower unity gain crossover frequency (and less input voltage noise). However, since in the DEV2 circuit the high-frequency component is limited by the FIR filter this benefit is not realised. Furthermore, since the input current noise is negligible, the reduction in input bias current also has no effect on the design (though it could lead to a minor improvement in environmental sensitivity). The final P_{min} estimated is almost exactly the same as the LMP7721 based circuit, though slightly higher due to a slightly higher (2x) noise floor. Overall, the change is negligible. Since the ADA4530 costs nearly 5x as much as the LMP7721 it is recommended that the DEV2 circuit stick with the latter.

Appendix E

Materials and Methods for Instrument Demonstrations

This appendix briefly describes the details of the application demonstrations from Chapter 5.

E.1 CMOS-based Instrumentation Demonstration

E.1.1 Contributions

In this work I was responsible for the design and fabrication of the microfluidics and optics as well as the data processing and presentation. The DNA sample preparation, agarose preparation and separation protocol were developed by Madeline H. Couse. The CE separation itself was performed primarily by Tianchi Ma. The CMOS microelectronic design was performed by the Elliott group at the University of Alberta with David L. Sloan providing troubleshooting and software for operating this micro electronic iteration.

E.1.2 Reagents

Genomic DNA was isolated from lymphocytes of individuals (obtained with informed consent) using a QIAamp DNA Blood Maxi Kit (QIAGEN, Canada), and solubilised in low TE (pH 8.0). PCR buffers and polymerase were from Invitrogen Canada. Primers were from Eurofins MWG Operon, USA. Agarose III was from Amresco Canada (#X174-100G). 10X TBE buffer was prepared to 0.89M Tris (tris (hydroxymethyl) aminomethane) (BioShop, Canada), 0.89M boric acid (EMD Chemicals, Canada), and 25 mM EDTA (Ethylenediaminetetraacetic acid)(BioShop, Canada). 10X TBE was diluted to 1X and 0.2X with Milli-Q water.

E.1.3 Sample Preparation

The test analyte was prepared by PCR. A primer pair was designed to amplify a region of the beta-2-microglobulin gene (β2M). The forward primer (5'- GTACTCCAAAGATTCAGGTTTACT -3') is unlabeled, while the reverse primer (5'- ACGGCAGGCATACTCATCTTTTTCAG-3') is labelled with Alexa Fluor 532. The 236 bp product was amplified in a 25 mL PCR reaction with 0.2 μM forward and reverse primers, 1X PCR buffer, 2 μM $MgCl_2$, 200 μM dNTPs, 0.2 $\frac{\mu g}{\mu L}$ BSA, 5 Units of Taq DNA polymerase, and 3 $\frac{ng}{\mu L}$ of genomic DNA template. (All concentrations are for the final concentration in 25 uL) The amplification was achieved through a thermal cycling protocol involving an initial 2 minutes at 94 ^{o}C, followed by 35 cycles of 94 ^{o}C for 10 seconds, 60 ^{o}C for 20 seconds, and 72 ^{o}C for 20 seconds.

E.1.4 LOC Fabrication

The CE chips were made according to the Gen 1 milled channels described in Section 2.2. Briefly, they were made from 1.5 mm PMMA (Acrylite-FF, Evonik Industries) using a CNC milling machine (MicroMill DSLS 3000, MicroProto Systems). Channels were 381 μm deep, and 381 μm wide, milled with a 2 flute carbide endmill (101-210, Sowa Tools). After milling the channels the piece was removed. Outer chip dimensions were cut with a Universal Laser VLS2.3 CO_2 laser with vector cuts at 20% power, 5% speed at 1000 PPI. The laser ablated exterior was smoother than a milled exterior cut allowing for better light coupling into the chip. After ablation, the PMMA chip was rinsed with Milli-Q water, and then dried by passing air over the top and bottom surfaces. The bottom surface (with open channels) was then sealed with PCR tape (Thermo Scientific, AB1170). Using this method a batch of 4 microfluidic chips could be manufactured in less than 1 hour for less than $2 material cost.

E.1.5 Optics Instrumentation

This application used the OPT1 optics from Section 3.8.1 and pictured in Figure 3.14 which consists of two side-illuminating blue LEDs run at 30 mA (WP710A10QBC/G), Kingbright Company LLC) that provide most of the excitation power and a small, third blue LED (SMP2-SBWC, Bivar Inc) facing directly into the collection optics run at μA levels to offset the baseline into the linear regime of the CMOS ADC as described in Section 4.2.

A practical implementation of the optics module faced a notable alignment challenge as it required the optics to align to both the CMOS microelectronics as well as the PMMA microfluidics. The fluidic-optics alignment was enforced by fabricating a holding piece from PVC that the microfluidic chip press-fit into, holding the channel above the collection lens. The PVC layer also contains a space for the emission filter (Acrylite 2C04, Evonik Industries) and the two side-illuminating LEDs. The CMOS-optics alignment was more difficult. Briefly, a PMMA holder chip was fabricated that contains a GRIN lens and press-fits to the DIP package the CMOS microelectronic chip is wire-bound inside. Multiple microscope measurements were made to iteratively align the GRIN hole to the CMOS photodiode. This PMMA holder chip also contained 4 $^1/_8$" dowels press fit to it that were used to align other optical layers to it, including the PVC layer that aligns to the fluidics. An image of the assembled instrument was shown in Figure 5.1.

E.1.6 Electronic Instrumentation

This application had two sources of electronic instrumentation. The optical detection was provided by the CMOS microelectronic chip as described in Section 4.2. This consisted of a photodiode, integrator set to 26.2 ms, an ADC with 14 effective bits and an SPI interface. A microcontroller (Parallax Propeller prototype board) provided the SPI and a custom program in C# implemented by David Sloan logged the photodiode data. The LED currents were set with a constant current source IC (LT3092, Linear Technologies). Two sources were used, one set to 30 mA for the side-illuminating LEDs and one set to a few μA for baseline offset. The high voltage was supplied externally by a commercial instrument termed the μTK (Microfluidic Toolkit, Micralyne). This high voltage module was more advanced, allowing for online monitoring of the voltage and current which was not possible with this early CMOS demonstration. This allowed for biochemical troubleshooting. Separations of the same DNA product on the commercial system were also done such that the optical detection could be directly compared.

E.1.7 Experimental Protocol

To load the chip with sieving matrix, the chip was placed tape side down on a steel block heated to 50^{o}C. Using a syringe, 2% agarose in 1X TBE was injected into the buffer waste well. The agarose was allowed to gel for 2 minutes in a humid environment, then for 15 minutes in 1X TBE. Excess gel in the wells was subsequently removed, and replaced with 1X TBE. An equilibration run was performed for 600 s across the injection channel at a field of approximately 35 $\frac{V}{cm}$ (50 V applied) and 600 s across the separation channel at a field of approximately 26 $\frac{V}{cm}$ (60 V applied). 1X TBE was aspirated from all the wells and replaced with fresh 1X TBE in the buffer waste, sample waste, and buffer wells. A mixture of 1 μL of PCR product diluted in 0.2X TBE was pipetted into the sample well. This gives a sample stacking ratio of x5.

The microfluidic chip features an inject-separate technique per Figure 1.3 in Section 1.2.2. In this demonstration detection occurs 11 mm from the intersection as in.[96] Injection fields of approximately 42 $\frac{V}{cm}$ (70 V applied) and separation fields of approximately 43 $\frac{V}{cm}$ (100 V applied) were used.

To directly compare this IP-CMOS instrument to the commercial instrument a fluidic chip was prepared as above and loaded into the CMOS-based instrument. After 3 separations the chip was removed from the IP-CMOS and a fourth separation was done on the μTK. Thus exactly the same sample was run on both systems with the same voltage program on the same day directly after one another.

E.1.8 Data Processing

Data was processed using a python program. Due to differing injection times, the x-value of the primer peak was first set to 0 seconds. This also corrected for any time delay in beginning IP-CMOS data acquisition through the C# program and starting the HV program on the μTK. Next, a linear baseline was determined from data up to 20 seconds before the primer peak and data 100 seconds after the primer peak (i.e. after the product as well). A linear function was fit to the baseline to remove any linear drift as well as set the baseline to 0. At this stage the noise was assessed

for the raw data as being the standard deviation for all data in the last 50 seconds of the baseline. This region was chosen as it excluded the time point when the HV switched from the injection to separation channel (this switch can introduce noise, particularly in the μTK). A 30 point moving average was applied to suppress time domain noise with minimal interference with peak shape. This averaging corresponds to 0.15 seconds on the μTK and 0.79 seconds on the IP-CMOS. Since the peaks are approximately 6 seconds in width, this averaging is not considered significant. The post-processing noise was then calculated from the same region as before. The product peak height and full width at half max were then calculated. A LOD estimation was made by assuming that the conversion of primer to product in the PCR reaction matched the area under the curve ratio between the primer and primer-dimer peaks and the product peak for injection 3. This ratio was 3. We therefore estimate that $\frac{3}{4}$ of the 200 nM of primers in the PCR were converted to product giving a product concentration of approximately 150 nM. The LOD was adjusted for the sample stacking by multiplying by a factor of 5, then adjusted for well dilution by dividing by a factor of 10. This gives an LOD value representative of the minimum fluorescent signal the instrument could detect. It should be noted that in Hall et al.[48] the reported LOD was 2x as this adjustment was not made (instead, the LOD was reported for the sample concentration that could be detected with this protocol). This change was made here to make it consistent with the calculations. The results are shown in Table 5.1.

E.2 Automated Enzymatic Digest Demonstration

E.2.1 Contributions

This demonstration was a group effort with a number of contributors. For the microfluidics, the valve structure was provided by Tianchi Ma, though I developed the membrane material used in this work. I also provided the design and fabrication of the CE microchannels as well as the test chips used in this demonstration. The molecular biology aspects were provided by Madeline H. Couse which included DNA sample preparation, agarose preparation, separation protocol development and the CE separation itself. Optics were designed, developed and fabricated by myself. Victor Shadbolt provided the majority of the electronic design including the circuits used to produce HV, switch the pneumatics and provide the photodiode detection. The pneumatic system was designed and developed by myself in collaboration with Hirad Raisi. The physical box the instrument was contained in was designed and built by Hirad Raisi. Software was based on initial code by Daniel Pinto Ramos and Victor Shadbolt that interfaced with the electronics that I modified to implement the pumping and CE program.

E.2.2 Reagents

Genomic DNA was isolated from blood from individuals heterozygous or homozygous wild-type for the C282Y and H63D HFE mutations (obtained with informed consent) using a Gentra Puregene Blood Kit (QIAGEN, Canada), and solubilised in a low Tris-EDTA (TE) buffer of 10 mM Tris with 0.1 mM EDTA, pH 8.0, 36 . PCR buffers and polymerase were from Invitrogen Canada. Primers were from Eurofins MWG Operon, USA. Agarose III was from Amresco Canada. 10X Tris-Borate (TB) buffer was prepared from 0.89 M Tris (tris (hydroxymethyl) aminomethane) (BioShop, Canada) and 0.89 M boric acid (EMD Chemicals, Canada), and was diluted to 1X and 0.1X with Milli-Q

water. The SnaBI and BClI restriction enzymes with their corresponding buffers, CutSmart T M buffer and NE Buffer 3.1 respectively, were from New England Biolabs Ltd. (Ipswich, MA, U.S.A).

E.2.3 Sample Preparation

Samples were prepared using PCR.

For the C282Y analysis (exon 4): The forward primer (5- CTGGCAAGGGTAAACAGATCC -3) is unlabeled, while the reverse primer (5- CCCCTAACAAAGAGCAGATCCT -3) is labelled with AF532. The 436 bp product was amplified in a 25 μL PCR reaction with 0.4 μM forward and reverse primers, 1X PCR buffer, 2 mM $MgCl_2$, 200 μM dNTPs, 0.2 μg/μL BSA, 5 Units of Taq DNA polymerase, and 3 ng/μL of genomic DNA template, obtained from individuals with either the homozygous wildtype (+/+) and heterozygous for the C282Y mutation (+/-). The amplification was achieved through a thermal cycling protocol involving an initial 2 minutes at 95 ^{o}C, followed by 40 cycles of 95 ^{o}C for 15 seconds, 61 ^{o}C for 15 seconds and 72 ^{o}C for 30 seconds.

For the H63D analysis(exon 2): The forward and reverse primers were 5-CATACCCTTGCTGTGGTTGTGATT-3 and 5-TCAGAGCAGGACCTTGGTCTTTCC-3 respectively, with the latter labelled with AF532. The 234 bp product was amplified in a 10 μL PCR reaction with 0.4 μM forward and reverse primers, 1X PCR buffer, 2 mM MgCl 2 , 200 μM dNTPs, 0.2 μg/μL BSA, 2 Units of Taq DNA polymerase, and 1.2 ng/L of genomic DNA template, obtained from individuals with either the homozygous wildtype (+/+) and heterozygous for the H63D mutation (+/-). (All concentrations are the final concentration in the reaction) The amplification was achieved through a thermal cycling protocol involving an initial 2 minutes at 94 ^{o}C, followed by 34 cycles of 94 ^{o}C for 10 seconds, 62 ^{o}C for 20 seconds and 72 ^{o}C for 20 seconds. After amplification the products were held at 72 ^{o}C for 10 min and then cooled from 95 ^{o}C to 65 ^{o}C at 0.1 ^{o}C/s.

E.2.4 RFLP analysis

The C282Y mutation in exon 4 of the HFE gene sequence introduces a TACGTA palindromic site, rendering amplification products containing the mutation detectable by digestion with the *Sna*BI restriction enzyme. *Sna*BI digestion of our 436 bp C282Y (+/-) PCR product should yield two DNA fragments, a labelled 158 bp fragment and an unlabeled 278 bp fragment (undetected as the fluorescent label was only on one primer), while products derived from wild-type sequences will not be digested. Prior to exposure to the restriction enzyme, we would therefore expect to detect a single product peak following the primer peak in our C282Y (+/-) PCR product. Post-digestion, we expect to detect two product peaks; one peak will be the 436 bp wildtype (undigested sequence), and the other peak will be the 158 bp digested C282Y fragment. Because the C282Y mutation is a single base pair mutation, a single-stranded amplicon containing the C282Y mutation could anneal with either a wild-type strand or a strand bearing the mutation. After the denaturation stage of PCR with the heterozygous C282Y sample as template, the four denatured strands of the PCR product will reanneal randomly to produce C282Y homoduplexes, wild-type homoduplexes, and C282Y heteroduplexes. The *Sna*BI enzyme will only digest C282Y homoduplexes since only these contain the palindromic cut site. We would therefore expect a peak representing digested product that is one-quarter the area of the original product,

although relative peak heights might also be complicated by injection artefacts. In the case of a homozygous wild-type sample, no digestion would occur and the pre- and post- enzymatic activity results would be the same (i.e. 2 peaks). For H63D analysis the BClI enzyme was used to recognise the 5'-TGATCA-3' site. This occurs only when neither strand contains the H63D mutation (i.e. wild-type DNA only). In the case of cleaving, the 234 bp PCR product is cut into a 162 bp unlabelled fragment and a labelled 72 bp fragment. There are three situations that can occur. In the case where only wild-type DNA is present in the sample, 100% of the product DNA will be cleaved by the enzyme. This electropherogram will have 2 peaks: one primer and one very short 72 bp product. In the second situation, the sample is homozygous H63D mutated. This results in no digestion and the electropherogram will have 2 peaks: one primer and one long 234 bp product. Finally, in the third situation where the sample has a heterozygous H63D mutation the enzyme will only cut some of the DNA (wild-type homoduplexes). This results in three peaks: a primer peak, a short 72 bp product peak at roughly $^1/_4$ of the undigested product peak height and a longer 234 bp product which is undigested. This is the opposite of the C282Y analysis with the *Sna*BI enzyme where digestion occurs only on strands that are C282Y homoduplexes. However, for both exons a three peak electropherogram indicates the presence of a heterozygous mutation. Both wild-type and heterozygous samples were tested. Since the third peak in either exon that comes from a heteroduplexes is expected to be $^1/_4$ the signal of an undigested PCR product, the heterozygous mutation presents the most challenging detection for both exons.

E.2.5 LOC Fabrication

Microfluidic chips with the same "neck" style design as in Figure E.1 above and previously discussed in Figure 3.15. In contrast to previous work, these chips were made with a combination of micromilling and laser ablation. The electrophoresis section of the chip had channels milled using the generation 2 micromilled channels from Section 2.2.3. These channels were 254 μm wide and 254 μm deep and were cut with a inexpensive PCB router. This allowed for smaller channels than the generation 1 milled fluidics used for the demonstration in Section 5.2, though the channel roughness was much higher. In comparison to the laser ablated fluidics, the milled channels have more surface area due to being a square profile as compared to the gaussian profile of the ablated channel. This was hypothesised to increase the adhesion of the agarose gel to the chip to reduce the noodling phenomenon. While not explicitly verified, over the course of 14 months of on-going use in the Glerum molecular biology lab for routine DNA sizing no noodling was observed. In this application, the mill also cut-out the microfluidic chip to ensure the channel was well aligned to the centre of the chip "neck". After cutting out the chip, the fluidic valving subsection was then ablated into the design. Patterning of the valving subsection was done using an Universal Laser VLS 2.3 CO_2 laser as previously demonstrated.[96] The fabrication was a two step procedure. First channels were engraved using a vector cut at 18% power and 25% speed at 1000 PPI. This creates a channel that was triangular shape with a maximum width of approximately 200 μm and a depth of approximately 500 μm. The vias for the valves were cut with 5 vector cut passes of 18% power, 25% speed at 1000 PPI. This maintains the aspect ratio of the via through the entire sheet of PMMA. The wells and external dimensions were vector cut with 20% power, 5% speed at 1000 PPI. This was a through cut that goes through the PMMA. Chips were then annealed for up to 8 hours at 80 ^{o}C, rinsed with DI water and dried with clean dry air. Channels were then capped with PCR tape (AB1170, Thermo Scientific). In comparison to previous fabrication methods, this method was slower due the fact that the laser ablation processing could not be done in batches due to the chip being cutout in the milling step. This was necessary, however, to ensure alignment

between the milling and laser ablation steps, and the throughput was still at roughly three chips in half an hour of on-hand labour.

The membrane was made from a piece of nitrile as discussed in Appendix A, Section A.2.2. Due to issues sourcing very thin nitrile at reasonable cost, a segment of a lab glove was used (KC300, Kimberley-Clark). This segment was first flattened overnight by a heavy weight and then patterned in the VLS 2.4 CO_2 laser with settings of 5.1% power, 25% speed, 300% PPI and a focus of 0.1 mm. Patterning was extremely minor, including only two small holes to allow the alignment dowels through and a small, roughly aligned cutout to prevent the membrane from touching the wells. The membrane and chip were assembled directly before use.

E.2.6 Pneumatics Instrumentation

The instrument used a single mini-style pneumatics block (Section A.2.4) with 5 positions, giving 5 potential valves to toggle. The working pressures were +138 kPa to -75 kPa. A rudimentary instrument with vacuum and pressure regulators (IRV10-N07BG and AR20-N02B-Z-A, SMC Pneumatics) and air pumps (D2028D, Airpo) was made to supply these pressures from a 12 V line for semi-portable applications.

Pumping was executed by toggling three valves in a peristaltic motion. The time delay between valve actuations was 200 ms, and the estimated volume moved per pump cycle was 0.5 μL

E.2.7 Optics Instrumentation

The optics used for this application were the OPT2 optics described in Section 3.8.2. The excitation optics included two blue LEDs side-illuminating the sample as in Figure 3.16 presented previously. Laird 2424 Blue was used as an excitation filter for both LEDs. The emission light was collected by a 0.23 pitch GRIN lens arrangement with an Acrylite 2C04 emission filter. There was no pinhole in this optical arrangement.

One difference between this optics instrumentation and those previously is that the piece that holds the microfluidic chip, LEDs, excitation filters and the collecting GRIN lens was milled from aluminum, a change enabled with improved fabrication techniques. There were a number of disadvantages to the PVC that needed to be addressed. First and foremost, the PVC was a poor conductor of heat. As discussed in Chapter 4, LED stability is dependent on its thermal environment and encasement in a good conductor allowed the LED to reach equilibrium temperature faster. Further, the PVC was quite soft and there was a concern that repeated use of a PVC optics jig would eventually lead to a loss in alignment.

The manifold was also adjusted at this time. Previously, the manifold was opaque PVC to prevent leakage light entering the system. However, PVC was deemed too soft to properly form the pressurised chambers required for the valving system. Thus a PMMA manifold was built. This manifold contained the electrodes for CE (nickel) and o-rings for the valve operation. A picture of the optics was shown in Figure 5.3a

E.2.8 Electronic Instrumentation

The HV for this instrument was provided by the initial discrete HV module detailed briefly in Appendix A, Section A.1.2 and in the thesis of Victor Shadbolt.[161] This featured a 50-300 V HV source and 4 HV switches. The pumping and valving was provided by the old style pneumatic switching electronics in Appendix A, Section A.2.5, with 5 valve toggles. The PDE detection electronics were used. These electronics were described in Section 4.4 and were the first to feature on-board voltage regulation, an on-board 12-bit ADC and a two stage TIA. The computer interface for all these modules was provided by a LabJack U6 microcontroller controlled with a program designed in Python with the labjackpython library. The detection electronics operated over SPI, while the pneumatic and HV electronic modules used DIOs for switching and the LabJack DAC for setting the HV output. The optics were probed at approximately 160 Hz.

E.2.9 Experimental Protocol

Fluidic chips were prepared for use in the following manner. The microfluidic chip was first filled with 2.5 % agarose in 1xTB buffer. In comparison to other work, the EDTA was removed from the running buffer to encourage higher enzymatic activity. The wells in Figure E.1a were filled with the contents in Table E.1 for either Exon2 or Exon 4 analysis.

The automated enzymatic process is shown in Figure E.1. After filling the well, the nitrile membrane was carefully placed over the $^{1}/_{8}$" dowels such that it did not interfere with any of the wells. The PMMA manifold was then placed over the same dowels and screwed down with two 4-40 machine screws. The lid of the unit was then closed and all remaining steps were performed by the software. First the sample was filled with the components of Buffer Well 1 with 30 pump stroke cycles, followed by the contents of Buffer Well 2 with 20 pump stroke cycles. It is noted that this over pumps the wells, though it was found that with this overpumping the channels could be reliably self-primed and emptied into the sample well. Ultimately, this results in a dilution of 3 μL in 17 μL for C282Y (1:5.7) and a dilution of 2 μL in 18 μL for H63D (1:9). A pre-digestion separation was done with an inject-separate technique with an injection voltage of 70 V (50 $^{V}/_{cm}$) and a separation voltage of 200 V (100 $^{V}/_{cm}$). This was found to have superior resolution at short distance as compared to lower fields. The injection time was 175s for exon 2 and 200s for exon 4 analysis and the separation time was 140s. The difference in injection times was due to the shorter nature of the exon 2 product. After the pre-digestion separation the contents of the enzyme well were emptied into the sample well with 20 pump cycles and the instrument was left to digest for 30 minutes to guarantee sufficient digestion of the sample. The sample concentration after dilution was 1:6.3 for C282Y and 1:10 for H63D. After digestion a second separation was done with the same fields and voltages as the pre-digestion run. A comparison of the pre- and post-digestion electropherograms can be used to diagnose the presence of a mutation. Both wild-type and heterozygous mutated H63D and C282Y samples were run (4 total samples).

Well	Contents for Exon 4 (C282Y) Analysis	Contents for Exon 2 (H63D) Analysis
SW, B, BW	10 μL 1x TBE	10 μL 1x TBE
Sample Well	3 μL Test Sample	2 μL Test Sample
	7 μL 0.1x TB	8 μL 0.1x TB
Buffer Well 1	3 μL Milli-Q Water	4 μL Milli-Q Water
	0.5 μL CutSmart buffer	0.5 μL NE Buffer
	1 μL 1x TB	1 μL 1x TB
Buffer Well 2	2.5 μL 0.1x TB	2.5 μL 0.1x TB
Enzyme Well	1 μL *Sna*BI	2 μL CblI
	1 μL 0.1x TB	

Table E.1: Table of well contents for exon 2 and exon 4 analysis. Well identification is in Figure E.1, thought the water well was replaced with Buffer Well 2.

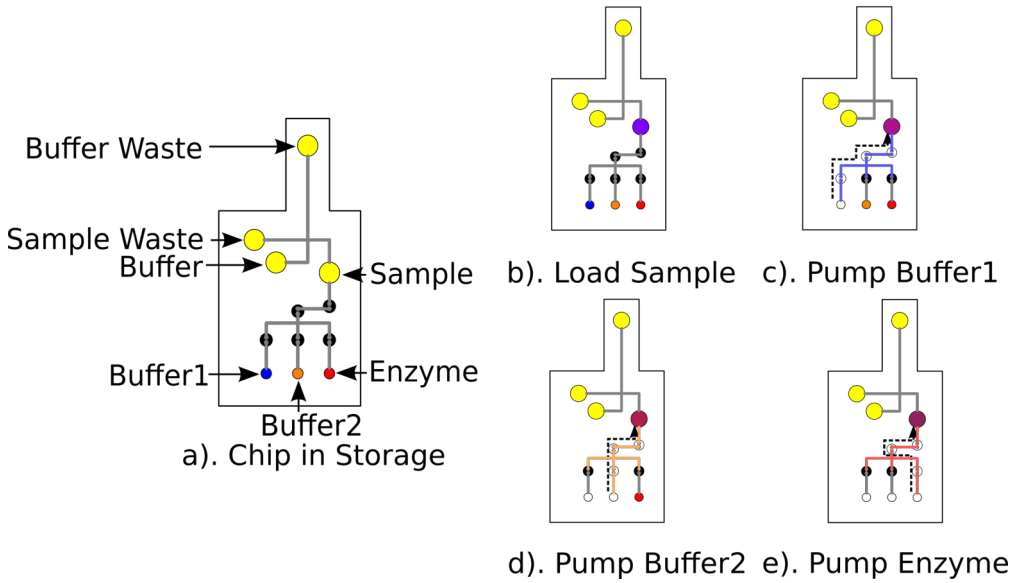

Figure E.1: Diagram of the analysis process. Actuated valves are clear while closed vales are black. a). A fluidic chip is first stored with with buffer in the buffer waste, sample waste, buffer and sample wells . b). The sample well buffer is then removed and replaced with sample . The system automatically pumps water c). and buffer d). into the sample well through peristaltic action using three valves. After mixing an inject-separate is done. e). The enzyme is then mixed with the sample. After 10 minutes of digestion a second inject-separate is done

E.2.10 Data Processing

Prior to plotting some basic data processing was done. Firstly, the injection time was subtracted from the x-values such that only the separation time is shown. Secondly, a 100 point moving average was applied to reduce noise. The sampling was done at approximately 160 Hz (rigorous timing was not implemented for this system) and as such the averaging does not interfere with electrophoretic peaks. Linear drift was removed by fitting a linear line using data from 25s -35s before and 120s-130s after injection. This linear line avoided selecting any peaks while also avoiding

fitting the transient baseline change associated with LED warming up in the first 20s due to LED thermal effects. Noise was quantified by calculating the standard deviation of the baseline after drift correction from 120s to 130s after injection. Finally, curves were offset for display purposes (0.03 V for exon 4, 0.015 V for exon 2).

After initial processing the peak heights were measured and presented in Table 5.2. To determine the LOD of the instrument, the sum of the signal of the primer and product peaks was taken. Next the total fluorophore concentration in the well was estimated based on the dilutions in Table E.1. This was used to estimate a signal per nM of fluorophore. The LOD was then calculated from the worst noise found in Table 5.2 to give the ultimate value. When calculating the average LOD, only the pre-digestion runs were counted. The pre-digestion experiments had a sample concentration that was comparatively simpler and thus assumed to be freer of injection artefacts. This is shown in Table 5.3.

E.2.11 Estimated Performance

Using the calculation infrastructure, the OPT2 optics module's performance can be estimated as shown in Table 3.11. These optics were expected to collect 380 fW of optical power per nM of end-labelled fluorophore, with a baseline rejection of 4.06×10^4. This value, combined with the performance of the PDE detection electronics, which have a P_{min} of 2600 fW as discussed in Section 4.4, results in an expected LOD of 6.8 nM. The spot-size was estimated to be 323 μm. This analysis, unfortunately, was not done prior to the implementation of the instrument as it is clear from this analysis that this instrument should not have been expected to meet the application relevant requirements.

E.3 State of Art LED-Photodiode CE Optical Detection Demonstration

E.3.1 Contributions

This demonstration was executed primarily by myself. This included microfluidic design and fabrication, optics design and fabrication, software development (due to a change in microprocessor), modifications of the instrument box to accommodate changes and execution of the CE testing protocols. The DNA sample preparation was provided by Chanel Polenz while the testing protocol was largely based on previous work by Madeline H. Couse. The instrument was housed in the same physical box as previously used, designed and built by Hirad Raisi. Victor Shadbolt's HV circuits were used for the CE separation. As described in Section 4.5, the detection electronics leveraged the same PCB that Victor designed but were modified extensively by myself for improved performance.

E.3.2 Reagents

Genomic DNA was isolated from lymphocytes purified from control individuals (obtained with informed consent) using a QIAamp DNA Blood Maxi Kit (QIAGEN, Canada) and solubilised in low TE buffer (pH 8.0). PCR buffers and polymerase were from Invitrogen Canada. Primers were from Eurofins MWG Operon, USA. Agarose III was from Amresco Canada. 5 X Tris-Borate-EDTA (TBE) buffer was prepared from Tris (tris (hydroxymethyl) aminomethane)

(BioShop, Canada), boric acid (EMD Chemicals, Canada) and EDTA (BioShop, Canada) and was diluted to 0.5 X with Milli-Q water.

E.3.3 Sample Preparation

The test analytes were either serial dilutions of PCR primer or a mixture of two different DNA samples. The DNA samples were the HFE exon 2 (234 bp) and exon 4 (436 bp) PCR products, the PCR's for which are described in Section E.2 above. The diluted primer sample was made by mixing all of the PCR components for an exon 2 PCR together, except the Taq polymerase and genomic DNA template which were replaced with Milli-Q water. Dilutions of 40 nM, 4 nM and 0.4 nM with 1x TBE were made for testing.

E.3.4 LOC Fabrication

The microfluidic chips used here were produced entirely via micromilling of PMMA (Acrylite FF, Evonik Industries as before). The channel geometry was the generation 3 micromilled channels from Section 2.2 and the general chip geometry was the same "neck" style design previously used as shown in Figure 3.15. These channels were 254 μm wide and 254 μm deep, milled with a standard endmill as described previously. In comparison to previous microfluidics used to demonstrate the instrument in Section 5.3 above, these channels had lower channel roughness, making them more optically clear. The smoother channel was also hypothesised to improve the CE separation stability, though this hypothesis was not confirmed. The one change was an extension of the separation channel from 11 mm to 17 mm. Channels were capped with PCR tape (AB1170, Thermo Scientific) as before. In comparison to the microfluidic chips made for the RFLP analyses, this design did not feature any valving. However, the chip size and format was the same and the valving and pumping could be readily integrated as before.

E.3.5 Optics Instrumentation

The optics used were the OPT3 optics described in Section 3.8.3. Briefly, this consisted of two side-illuminating blue LEDs, filtered by Rosecolux Sapphire Blue excitation filters. The new excitation filter was both thinner and had a higher optical density than the filter used in Section 5.3 allowing for an increase in excitation power due to improved coupling efficiency of the LED to the sample. The emission collection system was as before consisting of a lens arrangement with 2x 0.23 pitch GRIN lenses with a layer of Acrylite 2C04 as an emission filter in between. On the output of the second GRIN a pinhole was placed as an aperture. This pinhole was fabricated in the same procedure as the rest of the assembly to ensure placement accuracy and consisted of a 200 μm diameter hole cut with a PCB router through aluminised tape that was approximately 20 μm thick. As shown in Table 3.11, this reduced the spot-size from 323 μm to 152 μm. This change was considered a crucial component to the instrument performance as it reduced the spot-size to be less than the width of the channel, improving the baseline and ensuring the CE resolution was not affected by the optics module.

The entire optical assembly was made from aluminum to ensure robust placement and heat sinking of the LED and

channel. The manifold was made in two layers, with an aluminum base and a PMMA top. The PMMA top held the CE electrodes (nickel as before) and prevented the aluminum manifold from creating short circuits. In comparison to the all-PMMA designs previously used, the introduction of aluminum made this manifold more structurally sound and limited leakage light entering the system.

E.3.6 Electronic Instrumentation

The HV for this instrument was again provided by the initial discrete HV module designed by Victor Shadbolt and detailed in Appendix A, Section A.1.2 briefly and in his thesis.[161] The main change related to the detection electronics, which were the DEV1 design detailed in Section 4.5. This was the first detection electronic module that I became involved in and included key upgrades over the previous designs including an improved op amp, higher gain, more optimised gain distribution and air-wiring of the input stage. The microcontroller was changed to a BeagleBone Black Rev. A. This microcontroller was used to control the detection electronics over SPI, as well as external DAC (MCP 4902) to provide an analogue voltage to set the high voltage. The rest of the HV module was controlled with digital outputs. The optics were probed at 1950 Hz. These changes improved the instrument LOD by a factor of 21 as detailed in Sections 4.4 and 4.5 and addressed the signal stability issue identified above in Section 5.3.

E.3.7 Experimental Protocol

PMMA chips were first milled, cleaned, annealed and capped with PCR tape. Next, the channels were filled with 2.5 % agarose. Briefly, agarose was dissolved in 0.5 X TBE buffer and held for 1 hour at 80 ^{o}C. The agarose was then thoroughly vortexed and microwaved briefly (30s) to ensure full melting of the polymer. Subsequently, the agarose was left to sit at 80 ^{o}C for 5 minutes prior to chip loading. PMMA microchips were placed on a 60 ^{o}C hot block and agarose was gently pushed through the channels with a 1 mL syringe. Chips were left to slowly cool to room temperature in a humid environment for 10 minutes, inspected, then placed into a jar of 0.5 X TBE for storage. The agarose was stored overnight in a refrigerator at 4 ^{o}C and used the next day. This protocol is available in the SI and is considered the most robust agarose protocol used in the course of this project.

The CE running protocol was representative of clinical use of this standard analysis method. It begins with preparing the fluidic chip, which was stored immersed in buffer. The chip was first removed from the buffer and all buffer not in the wells was dried off with a Kimwipe. The agarose in the wells was then removed with a 200 μL pipette tip. After agarose removal, the well was filled with 10 μL of 0.5 X TBE buffer and placed into the ME system. Alignment of the chip to the optics was enforced by the chip and holder geometry. The upper manifold was lowered onto the chip. The manifold was aligned to the holder with 2 0.125" dowel pins along with 2 4-40 screws. The screws secure the manifold down and ensure the electrodes make contact with the bottom of the wells. The total system alignment was within 50 μm, with tighter alignment between the channel and the optics. The software was setup to flush the channels by injecting at 58 V (61 $\frac{V}{cm}$) for 100 s and separating at 166 V (64 $\frac{V}{cm}$) for 480 s. The manifold was then released and the buffers in the SW, B and BW were all emptied and replaced with 10 μL 0.5 X TBE. The S well was emptied and replaced with the sample. For the LOD test, 1 μL of dummy PCR mix was added to the S well with 9 μL of 0.5 X TBE for a 10 μL sample. For the DNA separation test, 1 μL each of both PCR products described above was

added to 8 μL of 0.5 X TBE to make the 10 μL sample. This represents a 1:10 dilution of each analyte. After adding the sample, the manifold was replaced prior to separation. The injection time was 80 s at 33 V applied (35 $\frac{V}{cm}$). The separation parameters were set to 166 V for 300 s. The software automatically inserted a 20s warmup time allowing for the LED junction temperature to stabilise prior to each run. Data were collected with a sampling rate of 1950 Hz.

E.3.8 Data Processing

The resulting electropherograms were processed with a standard data processing algorithm. The algorithm first discounts all pre-separation signal. Next any linear drift was removed with a single linear trend. It has been noted that LED output light decreases even at a stable current due to junction warming effects[81] and this process accounts for this effect. After the first 20s of the LED being on, the LED warming drift was linear on the time scale of an electrophoretic separation. This drift was removed by first fitting a linear trend to the first 80s of the separation and subtracting this trend from the whole signal. This also corrects for the baseline. Next a moving average was applied that corresponds to 1s of acquisition time (1950 points). This removes time domain noise not associated with the signal. The total process was very similar to that done previously.[48] After data processing, the baseline noise was 0.15 mV and the LOD was considered to be the concentration of fluorophore that gives a signal to noise ratio (S/N) of 3, i.e. a signal of 0.45 mV, adjusted for the dilution factor of 1:10.

E.3.9 Estimated Performance

Table 3.11 details the fluorescence model estimation results for this design. The expected signal from a 1 nM sample was 250 fW with a baseline rejection of 2.1×10^6 and a spot-size of 152 μm. Combining these results with the DEV1 electronics, which have a LOD of 122 fW as detailed in Section 4.5, results in an expected LOD of 488 pM. Thus, this instrument was expected to meet the 1 nM LOD requirement for these large channels. Again, resolution was considered a secondary objective as the basis on agarose sieving matrices suggests a poorer than 10 bp resolution should be expected as per Ugaz et al..[60]

Appendix F

Next Generation Instrument Usage Guide

F.1 Design

F.1.1 Specifications

The input specifications for the next-generation system are presented in Table 5.6. The performance specifications are presented in Table 5.7.

Parameter	Nominal Value	Maximum Value	Interface	Notes
Digital Input	-	-	USB-B Female	Connects directly to BeagleBone Black
Input Voltage	+12 V	+13 V	Wall wart	+12 V feeds directly to HV relays and HV supply
Input Current	2 A	-		
Input Pressure	138 kPa	206 kPa	$^1/_8$ OD shark-bite	Pressure - vac not to exceed 206 kPa
Input Vacuum	-60 kPa	-206 kPa	$^1/_8$ OD shark-bite	
Heater Voltage	+12 V	40 V	Banana Plug	Voltage limited by transistor used (TIP29)

Table F.1: Input specifications for the next-generation system

Module	Parameter	Nominal	Notes
Valves	Number of Valves	24	$^1/_{16}$ barbed fitting. $^1/_{16}$ ID tubing
	Simultaneous Valves Open	0 - 10	10 Valves = 1.5 A, maximum supported by cabling
	Actuation rate	10 Hz	300 Hz is valve maximum.
High Voltage	Output Voltage	50 V - 300 V	Operating below 50 V can result in less accurate voltage setting
	Voltage Set Accuracy	2%	
	Minimum Current Measurement	0.5 μA	
	Maximum Current Measurement	118 μA	
	Current Measurement Noise	152 nA	
	Current Measurement Rate	500 Hz	
Thermal	Thermal Measurement Accuracy	2.2^o	Thermocouple accuracy with no calibration.
	Temperature Reading Increment	0.25^oC	
	Heater Current	3 mA - 1000 mA	3 mA off-current can be avoided by cutting power to heater
	Controller Update rate	1 kHz	
Optics	LED supply 1	0 - 56.6 mA	Typ. LED = 30 mA
	LED supply 2	0 - 126 mA	Can be used as a heater as well.
	Sampling rate	5sps - 2000 sps	Typically 1000 sps
	Transimpedance Gain	$2-128\times10^{10}\frac{\text{V}}{\text{A}}$	Set with ADS1248 PGA. Typically 2
	Bandwidth	8-32 Hz	Calculated in Section 4.6
	P_{min}	42 fW	Calculated in Section 4.6
	LOD (estimated)	0.75 nM	Calculated in Section 3.8.4
	Spot Size (estimated)	134 μm	Calculated in Section 3.6.3

Table F.2: Table of performance specifications for the next-generation LOC system.

F.2 Electronic Implementation

The electronics used in the next-generation instrument were discussed previously in Chapters A and 4 and are similar to those used in previous instruments. However, previous designs developed in the Backhouse group have exhibited issues with serial communication, specifically sporadic dropping of bits and potential transmission line reflections. Other communication issues have resulted from fragile, easily broken connections between boards and there have been issues with erroneous connections being made due to no standard having been set within the lab. For example, the application detailed in Section 5.4 used two different DB15 cables to perform connections, with the two cables having different pinouts. Further, the connections contained a mixture of digital I/O, SPI, power and analog signals leading to a high chance that a wrong connection would destroy components. Finally, previous designs have used very large, bulky connectors that take up space and prevent more miniaturised devices. This in turn led to longer communication lines and increased risk of error. To address this, I have standardised the current instrument on flat

flexible cable (FFC) connectors. These connectors are an industry standard with robust terminations and a very small form factor. The standardised pinout of these connectors is briefly discussed in Section F.2.1.

In order to use these FFC connections I have developed a cape for the BeagleBone Black microcontroller. This cape plugs directly in the the microcontroller and also contains voltage regulation and digital buffers for a standard pinout detailed below and robust communication. The design details and usage of this interface board are shown in Section F.2.2. Finally, the designs detailed in Sections A.1.2, A.2.5 and 4.6 were implemented on two main PCBs to be compatible with the FFC connections. These boards are briefly discussed in Sections F.2.3 and F.2.4.

F.2.1 Electrical Connections

The instrument standardises on a 30-pin FFC connector. This gives plenty of pins for control of the various boards, while also ensuring that they can be readily separated into primarily analogue and primarily digital sections with the intention of reducing noise on the regulated analogue lines. Each connector contains a series of ”NC” lines, a series of ”GPIO” lines, the SPI communication lines, 3 power rails and ground. The ”NC” lines are unused pins that are connected to be common between all FFC connectors. This allows for sending signals between boards should the need arise. Further, NC5 and NC6 can be connected to the UART1 serial communication lines on the BeagleBone Black, thus enabling an alternative communication mode than SPI. The ”GPIO” lines are general-purpose digital lines from the BeagleBone Black that are configured as outputs. These lines are unique per connector and are typically used as chip selects. There is also a ”Return” pin. This is a digital input to the BeagleBone Black that is used on the detection board to time the data acquisition. Finally, there are 3 power rails used. The Digital Power rail is typically the 3.3V power output from the microcontroller and is used to power all digital chips and ensure that all of the logic is the appropriate level. A 12 V rail is included. This is the unregulated power input into the instrument and is used for relatively insensitive purposes (i.e. powering the HV relays) or high current applications (i.e. powering the solenoid valves). Finally, a 10 V line from a linear regulator is used. This is a cleaner source used for more sensitive analogue applications like powering the optical detection board. The pin identity and usage is written on the PCB and is shown in the tables below. Note that the HDMI needs to be disabled prior to use. A guide for setting up a BeagleBone Black Rev. C for usage with this cape is included in the SI. Table F.3 maps the BeagleBone Black digital pins to each connector while Table F.4 details the usage of the FFC pins for the two main boards.

Pin Identity	Connector 1	Connector 2	Connector 3
Output Enable	P8_7	P8_18	P8_34
Input Enable	P8_8	P8_17	P8_38
Return	P8_11	P8_30	P8_37
GPIO1	P8_9	P8_28	P8_36
GPIO2	P8_16	P8_32	P8_39
GPIO3	P8_14	P8_29	P8_40
GPIO4	P8_10	P8_26	P8_33
GPIO5	P8_12	P8_27	P8_35
GPIO6	P8_15	P8_31	P8_41

Table F.3: Table of the unique BeagleBone Black pins used for each of the three interface board connections

Pin Number	Identity	Fluidics Board	Detection Board	Notes
1	NC 6	None	None	Can be connected to UART1_TX with jumper
2	NC 5	None	None	Can be connected to UART1_RX with jumper
3	NC 4	None	None	
4	NC 3	None	None	
5	NC 2	None	None	
6	GND	GND	GND	
7	12 V	12 V	12 V	Unregulated input from wall wart.
8				
9				
10	GND	GND	GND	
11	10 V	10 V	10 V	Regulated 10 V line on Interface Board
12				
13	GND	GND	GND	
14				
15	Digital Power	Digital Power	Digital Power	Powered through BeagleBone Black
16	GPIO 6	CS Valve Switching	None	
17	GPIO 5	None	CS 125 mA Source	
18	GPIO 4	5V Logic Enable	CS 65 mA Source	
19	GPIO 3	CS HV Switch	None	
20	GPIO 2	CS HV set DAC	ADS1248 START	
21	GPIO 1	CS Current Read ADC	CS ADS1248	
22	Return	None	ADS1248 DRDY	
23	GND	GND		
24	MISO	MISO		
25	GND	GND		
26	MOSI	MOSI		
27	GND	GND		
28	CLK	CLK		
29	GND	GND		
30	NC 1	None	None	

Table F.4: Standardised 30-pin FFC connector pin identification

F.2.2 Microcontroller Interface

In order to use the FFC connectors with the BeagleBone Black, an interface board was designed. This board plugs directly into the microcontroller and can be considered the lab's "cape" used to enable the board to readily be connected to both optics and fluidics control electronics. The interface board contains 3 identical FFC connectors that can be

interchangeably used for fluidics or detection boards described below. The board also contains a 10 V, 1 A linear regulator to clean the wall wart power supply for sensitive applications. In order to avoid the communications errors from previous instruments, each digital line is buffered twice: once on the interface board and once on the slave board. Thus, there are three digital buffers used (one for each connector). Finally, to avoid cross-talk between boards MISO lines, each connector has an independent return buffer as well. This buffer can be enabled/disabled with a BeagleBone Black digital line. Thus whenever a board is being used the return communication for all other boards is disabled. An overview of the interface board functions and connections is shown in Figure F.1 and detailed board and schematic files are available in the SI.

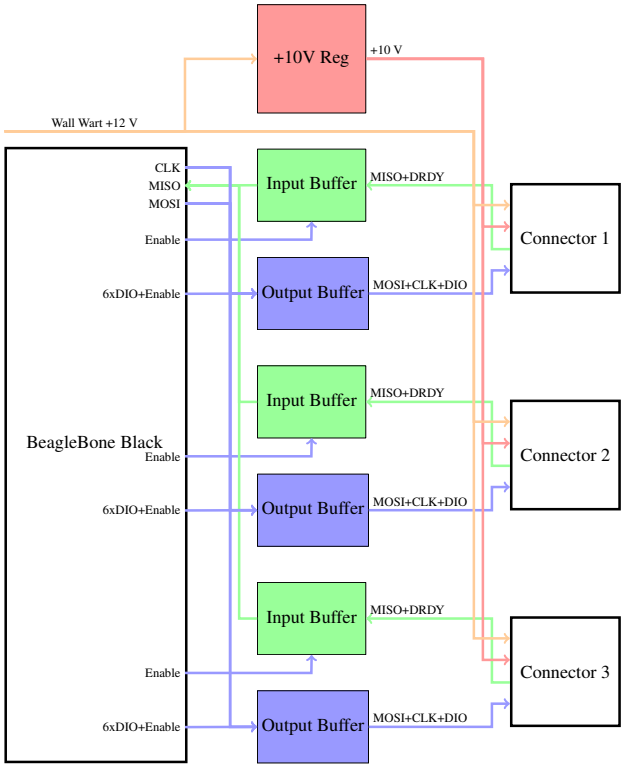

Figure F.1: Overview of the functionality of the next-generation system interface board. The board features 3 FFC connectors. Each connector features an input and output buffer for improved signal reliability, a shared 12 V, 2.5 A line from the wall wart for high power applications and a shared regulated 10 V, 1 A line for low-noise applications. Each connector also has a digital power rail (not shown) provided by the microcontroller. One other feature of the input and output buffers is the ability to toggle these buffers with Enable pins. This allows the user to deactivate unusued connectors and prevent corruption of the digital signals. The interface board plugs directly into the BeagleBone Black microcontroller as a ”cape”. This enables facilitated and reliable connection of the various electronic modules.

F.2.3 Fluidics Control Board

A singular PCB was designed to incorporate both the HV and pneumatic fluid actuation functions. This was done not only to make the best designs from Sections A.1.2 and A.2.5 compatible with the FFC connections, but also to simplify the instrumentation for future fluidic instruments and save space. Design details and performance metrics

can be found in the aforementioned Sections and is described here briefly. In terms of HV control, the board contains 2 switchable HV lines that can be controlled stably from 50 V to 300 V and 2 switchable ground lines with low-side current measurement from 0.5 μA to 118 μA. These lines are optimised for short channel CE separations that our group has specialised in for quite some time. For pneumatic valve control, the instrument contains 24 addressable 5 V lines that can be used to control 24 miniature solenoid valves as used in the pneumatics blocks described earlier in Section A.2.4. The board supports up to 2 A of current drawn through this 5 V line, or 13 concurrently actuated valves. It is not recommended to push the regulator limits due to thermal considerations, though the instrument has been tested with 7 simultaneously open valves for extended periods of time with no issues. It should be noted that the most strenuous protocol that we have developed for requires only 4 simultaneously actuating valves.

F.2.4 Detection Board

The detection PCB was designed to implement the DEV2 detection electronics as well as two stable, low-noise current sources. The DEV2 detection electronics design and performance is discussed in more detail in Section 4.6. In short, it contains a very high gain transimpedance amplifier with a high end ADS1248 24-bit ADC. The PCB optimised this design for very low parasitic capacitance including removal of solder-mask and a robust guard ring as outlined in a Texas Instruments recommended guide.[170] This was accompanied with two implementations of an Analog Devices application note for a very low noise current source[171]: one implementation with a 22.1 Ω output resistor to set currents between 0 and 56.6 mA and one with a 10 Ω resistor to set currents between 0 and 126 mA. These current sources can either be used to power LEDs or future low power heaters.

F.2.5 Thermal Instrumentation

The next-generation instrument contains the ability to read temperatures through a thermocouple, set a current up to 1 A through a heater and perform a PID control of the resulting system as detailed in the discussion of the current state of the thermal infrastructure in Section A.3.7. Currently, this functionality is implemented on protoboard and contained within the box. Communication with the thermal subsystem is over the serial interface previously described, which is connected to UART2 on the BeagleBone Black.

The thermal control circuit can be toggled to either take power from the 12 V wall wart, or from an external power supply (up to 40 V, limited by the transistor used). This was due to the fact that as of writing no thermal design has been decided upon for future work, thus the instrument must support a wide variety of heater resistances. As a point of reference, the thermal system described in the thesis of Tianchi Ma[118] required 30 V with a maximum current of 400 mA. This instrument is capable of implementing that system as well as having expanded functionality for higher current or higher voltage heaters. Thermal measurements are performed with a micro thermocouple that has cold-junction compensation and can read temperature changes down to 0.25C.

F.3 Fluidic Chip Design

One of the primary tools that I developed for this instrument was an Asymptote file where the user has ready access to pairs that indicate the various alignment features on the instrument. This allows for very rapid design work and ensures that the fabricated chips align to the optics, valves and other features. The tool also includes three sample chips; a microscope slide sized CE chip that aligns to the alignment pins, a microscope slide sized PCR chip that aligns to the heater zone and works with previously fabricated manifolds and a large format chip with all alignment features patterned for future use. The Asymptote code used to generate these files d is available in the SI. The sample chips are discussed below.

F.3.1 Sample CE Chip

Figure F.2 shows a sample CE chip. This device is designed to be fabricated using the most recently developed fabrication process detailed in Section 2.4 where the chips are laser patterned, solvent bonded, flattened on the mill and finally cutout on the laser. This produces CE chips with small channels (75 μm deep), with a thin capping layer (85 μm) compatible with the optics described in Chapter 3. The chip is designed to be aligned to the optics using the alignment pin system above. As described in Section 5.5.3 and Figure 5.7 there are two methods of aligning microscope slide sized chips to the detection point: the alignment pins and the spring fit system. The spring fit system references the edge of the chip to the detection point, which requires the user align the outside of the chip to the channel. The two stage laser patterning (one patterning the channel, one cutting the outside of the chip) makes this difficult as any misalignment of the chip during the laser patterning will cause a misalignment to the optics. This misalignment is further exacerbated by the angular cuts of the laser, making edge alignment difficult. Thus, the alignment pin system is preferred as it will preferentially align the centre of the pin holes patterned and thus result in lower alignment error. Figure F.2 shows three different patterns. On the left is the fluidics layer, which contains the electrophoretic channels, wells and alignment pins. In this image the red indicates channels engraved to a depth of 75 μm and the blue indicates through-cuts through the PMMA. In the centre is the capping layer. This layer can be simultaneously patterned with the fluidics layer. These two layer are bonded together to seal the channels. The capping layer contains two ”Mill align holes”. These holes are used to align the CNC mill in the z-axis to the surface of the fluidic layer, enabling more accurate thinning of the cap. Finally, on the right is the cutout picture. This image is used to cutout the final chip from the sacrificial 0.25” boundary after the cap has been thinned on the CNC mill. The outside is in black for alignment reasons (and should not be cut), while the alignment pins are in red. These red lines should be engraved through the thinned cap, but not through the whole chip. This ensures that the alignment of the chip on the alignment pins is set with the holes cutout on the fluidics layer and thus guarantees alignment between the channel and the pins.

The chip contains two identical CE features in a cross, with a 4 mm channel connecting the sample, sample waste and buffer wells to the intersection and a separation length of 17 mm, with the detection point being 3 mm from the buffer waste well. Having two devices per chip accelerates the fabrication, though a longer chip could also be made for improved resolution. Also included in Figure F.2 is the chip capping layer. This layer also contains alignment pins (enlarged somewhat to reduce alignment tolerance) as well as 4 ”Mill align holes”. These holes go through the cap, but not the fluidics layer. This allows the user to set z=0 on the mill to the surface of the fluidics layer,and cut the top

layer to a specific thickness with high tolerance.

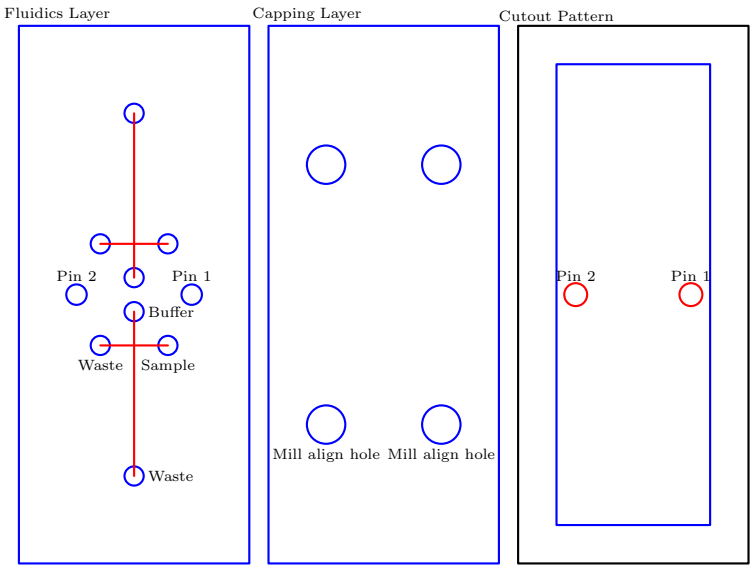

Figure F.2: A sample CE chip (left) and its capping layer (centre) and the picture for cutting out the chip after processing on the CNC mill (right). This chip fits over the alignment pins and contains two CE separation devices for inject-separate experiments. The device is designed to have the capping layer solvent bonded to the channels, then milled flat using the mill align holes to align the mill z-axis as per the fabrication procedure outlined in Section 2.4.

F.3.2 Sample PCR Chip

Figure F.3 shows a sample PCR chip. This device is designed such that the 4-40 and 6-32 screws align the chip to the centre of the heater zone in Figure 5.7, as well as with the previously made pneumatics manifolds. Thus, the design is compatible both with the next-generation system described here as well as all previous systems dating back to 2014. The chamber and valve placements are consistent with the thermal design established by Tianchi Ma in his thesis[118] and shown in Section A.3.8, notably a PCR chamber of 3.2mm x 3.2mm x 500 μm and a space of 4mm from the chamber centre to the start of the valve manifold, necessitating a valve to chamber distance of 1.016 cm. The fluidics layer (top left) is a CAD file where the blue lines indicate through cuts, the red lines indicate engraved channels and vias and the black diamond is a rastered chamber. Ultimately, the channels should be cut 75 μm deep and the chamber 2 mm. The capping layer (bottom left) is a relatively unpatterned layer to cap the channels and chambers. Note that for presentation reasons, the valves have been encircled with a small black circle, this (along with label text) is removed prior to processing. Much like the CE chip in Figure F.2, this cap is intended to be solvent bonded and CNC milled such that the cap is under 100 μm as described in Section 2.4. Again, the mill align holes can be used to accurately align the CNC mill to the fluidic layer for reproducible and thin caps. Finally, after solvent bonding and CNC processing the chip is cutout using the cutout pattern (right). This picture uses the black outer box to align the laser to the chip and contains a blue line (through cut) and small red circles around the alignment pins. These small red circles should be engraved $\approx$ 100 μm to cut through the cap. This ensures accurate alignment between the chip and the thermal instrument. The cutout pattern removes the sacrificial border around the chip. Note: if tape is being used for a capping layer as in Section 2.3.1 (not recommended), then the capping layer and cutout pattern are not needed.

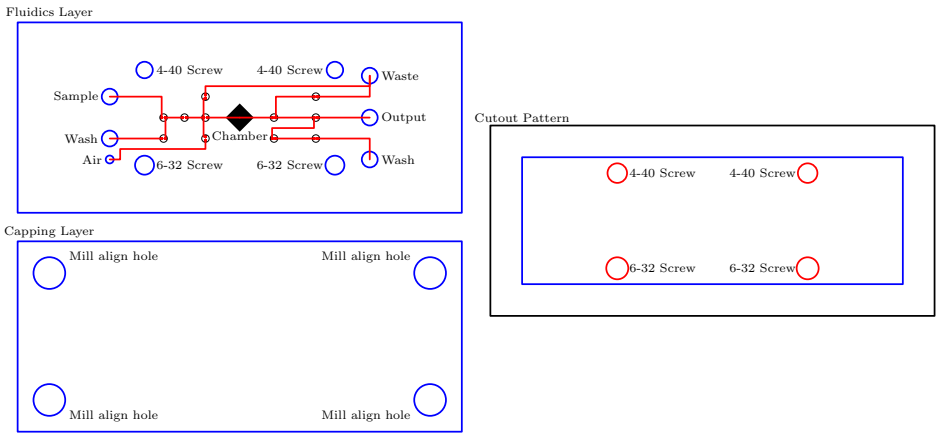

Figure F.3: A sample PCR chip. This chip has valves that align with the previously used manifolds and is thus backwards compatible with all pneumatic systems dating back to 2014. It, too is designed for the next-generation solvent bonding fabrication method outlined in Section 2.4. The fluidics layer contains all relevant fluidic features (channels, vias, wells and chamber), the capping layer is intended to solvent bond to the fluidics layer, capping the fluidic features. It contains mill align holes for aligning the CNC mill to flatten the cap to be consistent with thermal design rules. Finally, the cutout pattern is used to cut the final chip out, removing the sacrificial border.

The chamber is designed to be a diamond shape. This shape has been demonstrated in lab to be easier to fill with no air-bubbles than a circular well as the ”corners” of the diamond preferentially fill due to the slightly hydrophilic nature of the PMMA and the wicking of fluid into the corner angle. The process flow is as follows:

1. Load the chip into the system, add a membrane layer (preferably the thermoplastic elastomer discussed briefly in Section A.2.2) and manifold to create the valving system shown in Figure A.4
2. Fill Wash wells with buffer
3. Fill Sample well with sample and pump it from the sample well, through the chamber towards the waste well
4. Flush the input dead volume by pumping the left hand wash well through the top channel to waste
5. Flush the output dead volume by pumping the right hand wash well to the waste
6. Perform PCR
7. Use the Air well to push air into the chamber to empty the fluid to the Output well with no dilution

F.3.3 Large Format Chip

The instrument is designed to accommodate large 3inch x 3inch chips in the Large Format zone in Figure 5.7. This should give plenty of room for any future sample preparation protocols. Figure F.4 shows the current output of the microfluidics design tool for the large format chip, which contains all alignment holes and the outer dimensions. These holes are optional and the user can readily implement whatever manifold/alignment structure is needed.

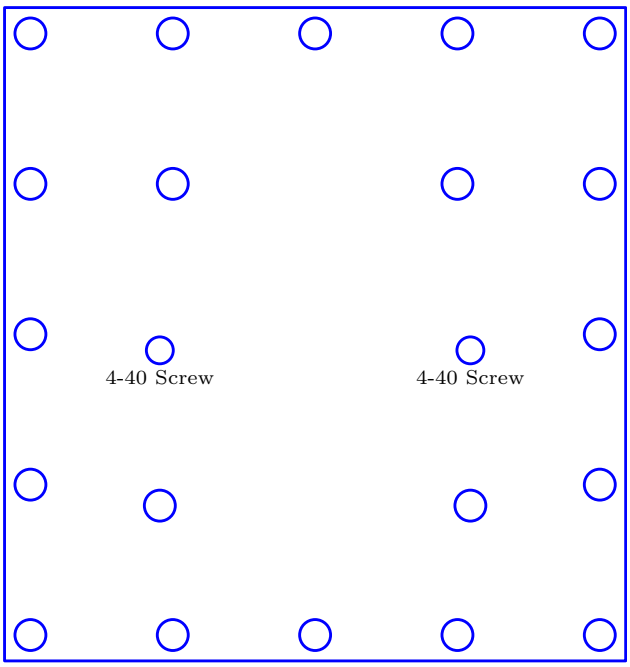

Figure F.4: A large format chip. This has all of the alignment holes (size 6 screw except where noted), though these may not be necessary given the ultimate design. This provides a base for future designs

F.4 Command Interface for the Next-Generation Instrument

I have implemented an easy to use python script that can run natively on the BeagleBone Black that can be readily reprogrammed to implement arbitrary fluidic protocols. This code title "EMC_BaseCode.py" is available in the SI. This code is quite long due to the large number of functions programmed in and the substantial initialisation required to implement them. However, it is designed such that there is an easy to use function to implement any arbitrary molecular biology protocol relating to pumping, valving, HV, thermal control or optical detection. These are implemented with a series of functions detailed here. Each command is detailed in terms of its syntax, its return and what the variables within mean.

F.4.1 Control Commands

These are commands used to prevent the various boards from having their MISO lines interfering with one another. The instrument has the ability to fully disable the MISO lines to any board. The two commands below are identical in their inputs, but will either enable the detection board while disabling the HV board or vice versa. Note that it is important that two boards are not simultaneously enabled as then the buffer outputs would attempt to drive each other, resulting in a board failure. Thus, these commands ensure that does not happen.

enablePD(pd_ie,hv_ie):

Returns: Nothing

enableHV(pd_ie,hv_ie):

Returns: Nothing

Parameter	Definition	Format	Default Value	Notes
pd_ie	PD board input enable	GPIO value, string	”P8_38	
hv_ie	HV board input enable	GPIO value, string	”P8_8”	

F.4.2 Stop Command

The disableall command stops all instrument activity. This includes turning off the HV, disabling the HV relays, turning off the thermal controller, turning off the heater current and turning off the LEDs.

disableall(pd_ie,hv_ie,hv_cs_dac,valve_cs,LED1,LED2)

Returns: Nothing

Parameter	Definition	Format	Default Value	Notes
pd_ie	Chip select, enable PD input	GPIO value, string	”P8_38	
hv_ie	Chip select, enable HV input	GPIO value, string	”P8_8”	
hv_cs_dac	Chip select, HV set DAC	GPIO value, string	”P8_16”	
valve_cs	Chip select, valve select	GPIO value, string	”P8_15”	
LED1	Chip select, LED1 set DAC	GPIO value, string	”P8_33”	
LED2	Chip select, ISRC set DAC	GPIO value, string	”P8_35	

F.4.3 Valving/Pumping Commands

These commands relate to the use of the valving and pumping. There are three commands developed. valvetest is a small piece of code for opening valves one at a time. This is useful in the prototyping and testing phase. valveswitch is a more useful command where it will toggle an arbitrary combination of valves. Finally, valvepump implements a peristaltic pump cycle for an arbitrary valve combination.

valvetest(cs,vnum)

Returns: Nothing

valvetest accepts a valve number from 0 to 24. A value of 0 will disable all valves. Valves 1-8 correspond to the valves on module V1, valves 9-16 correspond to those on module V2 and valves 17-24 correspond to those on module V3. This code supports only one open valve at a time, but its intuitive interface is good for testing to ensure all valves are operational.

Parameter	Definition	Format	Default Value	Notes
cs	Chip Select	GPIO value, string	”P8_15”	
vnum	Valve number	Integer from 0 to 24		0 turns off all valves. Otherwise opens valve vnum

valveswitch(cs,valves)

Returns: Nothing

valveswitch is very similar to valvetest above, but is extended in application to toggle an arbitrary number of valves. Here, the variable valves is no longer an integer between 0 and 24, but rather an integer between 0 and 16777215 ($2^{24}-1$), with each bit being assigned to a valve. Bits 1-8 (1-128) correspond to valves on module V1, bits 9-16 (256-32768) correspond to valves on module V2 and bits 17-24 (65536-8388608) correspond to valves on module V3. The advantage to this code is that multiple valves can be simultaneously toggled by passing a sum to the command. The integer valves is actually the integer passed to the 3 daisy chained 595 logic chips that control with valves are being actuated. It should be noted that the valves draw quite a bit of current (150 mA each) and thus users should refrain from toggling more than 5 valves for extended periods of time. It should also be noted that in the case of overcurrent, the system is protected, but valve reliability suffers and some valves may switch off without warning to relieve the current/thermal stress on the system.

Parameter	Definition	Format	Default Value	Notes
cs	Chip Select	GPIO value, string	”P8_15”	
valves	Valve number	Integer from 0 to 16777215		0 turns off all valves. Passes the integer to the 3 chained 595’s and opens associated valves

valvepump(cs,cyclenum,delay,v1,v2,v3,vopen)

Returns: Nothing. Prints status to terminal

The valvepump command implements a peristaltic pumping cycle of the type: v1, v1+v2, v2, v2+v3, v3, closed. This cycle repeats cyclenum times, with a time delay of delay between each step. There have been some applications we have devised that require multiple lines to be simultaneously pumped. This is supported with this code by entering a list as v1/v2/v3. Also supported is the ability to keep a valve open throughout the entire pump cycle. This is necessary for many applications, especially in the PCR chip in Figure F.3 where pumping sample to the waste well through the chamber requires 3 valves pumping and 2 valves to be held open. Valves to be kept open are entered into vopen. For example, the following code will execute 10 pump cycles where valves 6 and 22 (third to last valve on modules V1 and V3), 7 and 23 (second to last valve on modules V1 and V3) and valves 8 and 24 (last valve on modules V1 and V3) execute peristaltic pumping with a delay of 0.2 s with valves 12, 13 and 14 (middle three valves on module V2) being held open throughout. The code prints the pump cycle being executed and reports each cycle number.

```
valvepump(valve_cs,10,0.2,[6,22],[7,23],[8,24],[12,13,14])
```

Parameter	Definition	Format	Default Value	Notes
cs	Chip Select	GPIO value, string	”P8_15”	
cyclenum	Number of pump cycles to do	Integer		
delay	Time delay between valve actuations	Float, in seconds	0.2	
v1	1st valve(s) in pump	Integer from 1 to 24, can be list		For multiple valves to simultaneously pump, enter a list of integers
v2	2nd valve(s) in pump	Integer from 1 to 24, can be list		For multiple valves to simultaneously pump, enter a list of integers
v3	3rd valve(s) in pump	Integer from 1 to 24, can be list		For multiple valves to simultaneously pump, enter a list of integers
vopen	Valves to leave open during cycle	Integer from 1 to 24, can be list		For multiple valves to simultaneously pump, enter a list of integers

F.4.4 Heater Commands

The heater is accessed over serial commands as described in Section A.3.7, which here is executed using PySerial and UART4 on the BeagleBone Black. To simplify matters further, some functions have been developed to assist the user in interfacing with the thermal controller. There are four commands: iset which sets the current output through the heater, htrset which enables the PID controller and sets the temperature to some given value, pidsetup which sets the PID values and htrRead which reads back the thermal controller outputs.

icntrl(iset)

Returns: Nothing

This command sets the current output of the heater to the value iset, which is in mA. Minimum current to set is 0, maximum is 1000 mA.

Parameter	Definition	Format	Default Value	Notes
iset	Current to set	Value between 0 and 1000 (in mA)		

htrset(tset)

Returns: Nothing

Starts the PID controller with a set temperature of tset. At this point the controller will begin reporting back temperature values that can be read with the command htrRead. To stop the PID controller, execute the command:

```
ser.write("STOP \n")
```

Parameter	Definition	Format	Default Value	Notes
tset	Temperature to set	Value between 0 and 100 (in ^{o}C), one decimal place		

pidsetup(kp,ki,kd,errmax,imax)

Returns: Nothing

This command sends the appropriate serial commands to set each of the PID constants. Note that the controller has not yet been optimised.

Parameter	Definition	Format	Default Value	Notes
kp	Proportional constant for PID	Value, one decimal place	10	Dependent on heater system, unoptimised
ki	Integral constant for PID	Value, one decimal place	0	Dependent on heater system, unoptimised
kd	Derivative constant for PID	Value, one decimal place	0	Dependent on heater system, unoptimised
errmax	Maximum integral error allowed	Value, one decimal place	1200	Dependent on heater system, unoptimised
imax	Maximum current allowed	Value, one decimal place	1000	Dependent on heater system, unoptimised

htrRead()

Returns: [time, read temperature, set current, set temperature]

This command reads back the serial output of the thermal controller and returns the time the controller has been on a certain step (in seconds), the thermocouple read temperature (in ^{o}C), the set current (in mA) and the set temperature (in ^{o}C). The accuracy of this code is based on the thermocouple used. The resolution is 0.25C.

Note: To read the thermocouple without setting a heater, simply start the controller with a setpoint of 0C and run the htrRead() command.

Note: The sampling rate is nominal 500 Hz, though executing htrRead() does not need to fit 500 Hz as this code clears the serial buffer before reading both the running time and temperature.

F.4.5 High Voltage and Electrophoresis Commands

These commands relate to the use of the High Voltage (HV) module, which includes HV generation, HV switching and current reading. The target application is electrophoresis. There are two general purpose commands for the DAC and ADC used to set the high voltage and read back the HV current (set_MCP4902 and read_MCP3202 respectively). Hvset is a small function that contains calibration data to map the DAC value to the desired HV. Finally, HV_cntrl is a function to implement HV switching and setting for easy implementation of electrophoresis.

set_MCP4902(cs, channel, gain, shdn, v_set)

Returns: Nothing

This command sets the value for an MCP4902 or MCP4922 DAC. This DAC is one of the common DACs used in the lab, and has 12-bits which map to a reference voltage applied to the chip. On the fluidics control board, this DAC reference is set to 3.3 V, and the output is put through a non-inverting amplifier with a gain of 3 (thus mapping the DAC set value to 0-9.9 V). The Matsusada TS-0.3P HV power supply is DAC controlled with a line up to 10 V, hence the design. On the fluidics board, channel 1 of the DAC is used to control the HV. The DAC value required to get a given HV can be accessed with the command Hvset(voltage).

Parameter	Definition	Format	Default Value	Notes
cs	Chip Select	GPIO value, string	”P8_16”	
channel	DAC channel to set	Integer of 0 or 1	1	0 = CH0, 1 = CH1
gain	DAC gain	Integer of 0 or 1	0 (1x)	0 = 1x, 1 = 2x
shdn	Shutdown DAC	Integer of 0 or 1	1 (on)	0 = shutdown, 1 = not shutdown
v_set	Voltage to set	Integer from 0 to 4095		For HV board, mapped to 0-10 V applied to the HV supply. Use command Hvset(voltage) to calibrate.

Hvset(voltage)

Returns: integer for set_MCP4902

This function contains the calibration values that map the DAC value required to get a given HV from the Matsusada TS-0.3P HV power supply. The function accepts a float value up to 300 V, and returns the required integers to pass to the set_MCP4902 command. Note that voltages below 50 V are not as accurate, and voltages below 25 V do not work as per the Matsusada datasheet.

Parameter	Definition	Format	Default Value	Notes
voltage	Desired voltage	Float		Returns calibrated voltage as an integer between 0 and 4095 to pass to set_MCP4902

Hvset(voltage)

Returns: integer for set_MCP4902

This function contains the calibration values that map the DAC value required to get a given HV from the Matsusada TS-0.3P HV power supply. The function accepts a float value up to 300 V, and returns the required integers to pass to the set_MCP4902 command. Note that voltages below 50 V are not as accurate, and voltages below 25 V do not work as per the Matsusada datasheet.

Parameter	Definition	Format	Default Value	Notes
voltage	Desired voltage	Float		Returns calibrated voltage as an integer between 0 and 4095 to pass to set_MCP4902

read_mcp3202(cs,channel,diff)

Returns: 12-bit integer of the ADC read voltage

read_mcp3202 reads the value from the laboratory standard MCP3202 ADC. On the fluidics board, this ADC is used to read back the measured current on the HV line as per Section A.1.2, with channel 0 being connected to channel 1 and separation being connected to channel 0. The returned value is a 12-bit value which is mapped to the reference voltage. On the fluidics board the reference positive input is connected to 3.3 V, and the ground reference to -0.227 V. The measured voltage is the voltage drop across a 1 kΩ resistor, passed through a non-inverting amplifier stage with a gain of 27.8 $^{V}/_{V}$ and referenced to ground (0 V). Thus the current can be expressed as in Equation F.1

$$I = \frac{\frac{\text{ADC Read}}{4095} \times 3.527 - 0.227}{1000 \times 27.8} \tag{F.1}$$

Where ADC Read is the read ADC integer and I is the current in amps.

Parameter	Definition	Format	Default Value	Notes
cs	Chip Select	GPIO value, string	”P8_9”	
channel	ADC channel to read	Integer of 0 or 1		0 = CH0, 1 = CH1. Injection = 1, Separation = 0
diff	Enable differential measurement	Integer of 0 or 1	0 (single ended)	0 = single-ended, 1 = differential

HV_cntrl(cs_switch,cs_dac,mode,voltage)

Returns: Nothing

The HV_cntrl function provides both the HV setting and HV switching functionality for implementing electrophoresis. It requires two chip selects: one for the HV switching and one for the HV setting DAC described above. It also takes an input called mode. The mode can either be ”inj” for injection, ”sep” for separation or ”off”. ”inj” and ”sep” send the appropriate commands to enable either the HV and ground line for HV1 as marked on the box in Figure 5.7 or the HV and ground line for HV2 respectively, while ”off” appropriately turns off both the HV relays as well as the HV source.

When switching lines, earlier revisions of the board exhibited some interference on the SPI line that controls which relay enables while a large HV was being generated. This issue is avoided by rapidly turning off the HV generator, performing the relay switches, then re-enabling the HV generator rapidly. This is done automatically within this code. voltage is a float of the voltage to set. In the case that the voltage is below 25 V, the system is turned off. In the case that the voltage is over 300 it will be set to 300 (which is the maximum output of the Matsusada supply). Combining the read_mcp3202 command above, a CE inject-separate can be done as in the following sample code:

```
HV_inj=100 # Injection Voltage
time_inj=30 # Injection Time
HV_sep=300 # Separation Voltage
time_sep=60 # Separation Time
i=[] # variable to store injection currents
s=[] # variable to store separation currents
t=[] # variable to store experiment time
hvset=Hvset(HV_inj) # determine DAC value for injection

HV_cntrl(hv_cs_switch,hv_cs_dac,"inj",hvset) # set HV for injection
tstart=time.clock() # start timer

while time.clock()<time_inj:
        t.append(time.clock()-tstart)
        i.append(read_mcp3202(hv_cs_adc,1,0))
        s.append(read_mcp3202(hv_cs_adc,0,0))
        # record injection and separation currents as integer values.

hvset=Hvset(HV_sep) # determine DAC value for separation
HV_cntrl(hv_cs_switch,hv_cs_dac,"sep",hvset) # set HV for separation

while time.clock()<time_inj+time_sep:
        t.append(time.clock()-tstart)
        i.append(read_mcp3202(hv_cs_adc,1,0))
        s.append(read_mcp3202(hv_cs_adc,0,0))
        # record injection and separation currents as integer values.

HV_cntrl(hv_cs_switch,hv_cs_dac,"off",0) # Turn off HV
```

Parameter	Definition	Format	Default Value	Notes
cs_switch	Chip select of relay switching IC	GPIO value, string	”P8_14”	
cs_dac	Chip select of DAC	GPIO value, string	”P8_16”	
mode	Select mode of operation	String		Values of inj (HV1 out enabled), sep (HV2 out enabled), or off (all relays and HV source off)
voltage	Voltage to set	Float from 25 to 300 V		

F.4.6 Optical Detection Commands

These commands relate to the detection board, which includes setting the LED current (AD5452), initialising the sampling parameters for the ADC (ADS1248_init), calibrating the ADC (ADS1248_cal), setting the appropriate inputs to be read on the ADC (ADS1248_mux) and reading the ADC value (ADS1248_readonce)

AD5452(cs,dacset)

Returns: Nothing

The AD5452 command controls the AD5452 DAC used on the detection board to set the current output of the two current sources (labelled LED and ISRC). The DAC takes an integer between 0 and 4095, which is mapped to its reference voltage (1.25 V) to give the output voltage. This circuit then controls the current through the current source such that the voltage drop across the output resistor is equal to the DAC output. For the LED, this resistor is 22.1 Ω giving a full scale current of 56.6 mA and current steps of 13.8 μA. For the ISRC the resistor is 10 Ω giving a full scale current of 125 mA and a current step of 25.5 μA. Note that the LEDs typically used have a maximum specified current of 30 mA.

Parameter	Definition	Format	Default Value	Notes
cs	Chip Select	GPIO value, string	LED1 = ”P8_33”	Current source between 0 and 56.6 mA
			ISRC = ”P8_35”	Current source between 0 and 125 mA
dacset	Set voltage output of DAC	Integer from 0 to 4095	LED1: 30 mA = 2170	Integer/4095 is mapped to the current source range

ADS1248_init(cs,ainp,ainn,vrefen,vrefset,gain,srate)

Return: Nothing. Breaks on error. Prints multiple lines detailing status

The ADS1248_init command initialises the ADS1248 chip for use. This includes setting the reference voltage, setting the state of the internal reference, setting the programmable gain amplifier (PGA) gain, setting the sampling rate and setting the analogue inputs. This code creates and sends the appropriate mux commands based on the values provided in the table below. For the gain and sampling rate, only certain values are supported by the chipset. The code will round down the gain to the nearest value, and select the nearest sampling rate to the value entered. The code will print to the terminal the inputs that are given. If an invalid input is given, the code will break and return an error message. After sending the mux commands to the ADS 1248 chip, the BeagleBone will then attempt to read all the ADC's registers. If the register read back does not correspond to the code sent, it will flag an error and stop. The user should then ensure and double check the board connections and power supply.

Note that it is best practices to run a calibration code (below) after changing the gain or sampling rate.

Parameter	Definition	Format	Default Value	Notes
cs	Chip Select	GPIO value, string	”P8_36”	
ainp	Positive ADC channel	Integer from 0 to 7	5	
ainn	Negative ADC channel	Integer from 0 to 7	4	
vrefen	Enable Vref	Integer from 0 to 3	1 (on)	0 = off, 1 = on, 2 or 3 = powersave mode
vrefset	Set reference voltage	Integer from 0 to 3	2 (Internal reference)	0 = REF0, 1 = REF1, 2 = internal reference, 3 =output internal reference to REF0
gain	Set the gain	Value from 0 to 128	2 (enables internal PGA)	Code will automatically round gain down to nearest viable value (1, 2, 4, 8, 16, 32, 64, 128)
srate	Set the sampling rate	Value from 5 sps to 2000 sps	1000	Code will automatically round to nearest viable rate (5, 10, 20, 40, 80, 160, 320, 640, 1000, 2000)

ADS1248_cal(cs,drdy,vmin1,vmin2,vmax1)

Return: Nothing. Breaks on error. Prints multiple lines detailing status

The ADS1248_cal command runs all of the ADS 1248 calibration commands one by one. This includes calibrating the self offset, the system offset and the gain. To do so, the chip requires two different analogue inputs tied to the negative voltage rail, and one tied to the positive voltage rail. These are vmin1, vmin2 and vmax1 respectively. As in the initialisation code, this code prints to the terminal what it is doing, and flags an error in the case the sent and read registers do not match. Finally, it will output the FSC and gfactor. These are values read from the gain calibration. The gfactor should be close to 1, if it is very far off this might indicate a problem with the ADC.

A calibration should be run on every power cycle, as well as whenever the gain or sampling rate is changed according to the ADS 1248 datasheet.

Parameter	Definition	Format	Default Value	Notes
cs	Chip Select	GPIO value, string	”P8_36”	
drdy	Data ready pin	GPIO value, string	”P8_37”	
vmin1	ADC channel tied to negative rail	Integer from 0 to 7	2 (enables internal PGA)	
vmin2	ADC channel tied to negative rail	Integer from 0 to 7	3	
vmax1	ADC channel tied to positive rail	Integer from 0 to 7	7	

ADS1248_mux(cs,ainp,ainn)

Return: Nothing. Breaks on error. Prints multiple lines detailing status

The ADS1248_mux command sends the minimal mux bits to change the set analogue inputs to read on the ADS 1248 chip. This is useful as it avoids touching the gain and sampling rate and thus means that a calibration does not need to be done. As with other ADS 1248 commands, it will read back the registers set and break if there is any error detected.

Parameter	Definition	Format	Default Value	Notes
cs	Chip Select	GPIO value, string	”P8_36”	
ainp	Positive ADC channel	Integer from 0 to 7	5	
ainn	Negative ADC channel	Integer from 0 to 7	4	

ADS1248_readonce(cs)

Return: ADC reading specified by ADS1248_init or ADS1248_mux as a list of 3 8-bit integers

The readonce command sends 3 NOP commands to the ADS1248 chip and reads back the 3 8-bit values output by the ADC. The voltage level can be reconstructed by summing the return bits to form a 24-bit value. This value can be converted to a voltage reading based on the reference used. This command should be run inside of a while or for loop with an if statement for a standardised sampling rate as in the sample code below:

```
while 1: # Ensures loop waits for DRDY to be brought low
        if GPIO.event_detected(drdy): # Detects DRDY brought low
                x=ADS1248_readonce(ads_cs) # Single reading of ADC
                sig=((x[0][0] & 0x7F) << 16) + ((x[1][0] & 0xFF) << 8)+x[2][0] # Sum bits
                voltage_reading=float(sig)/(2**23-1)*2.048  # Assumes internal reference
```

Parameter	Definition	Format	Default Value	Notes
cs	Chip Select	GPIO value, string	”P8_36”	